Université de Montréal

Thermal stability of sub-Arctic highways: Impacts of heat advection triggered by mobile water flow under an embankment

Par

Lin Chen

Département de géographie

Faculté des arts et des sciences

Thèse présentée aux Études Supérieures et Postdoctorales

en vue de l'obtention du grade de

Philosophiæ Doctor (Ph.D.)

en géographie

1er septembre 2020

Université de Montréal

Département de géographie /Faculté des arts et des sciences

cette thèse intitulée

Thermal stability of sub-Arctic highways: Impacts of heat advection triggered by mobile water flow under an embankment

Présenté par

Lin Chen

A été évalué(e) par un jury composé des personnes suivantes

James King
Président-rapporteur

Daniel Fortier
Directeur de recherche

Jeffrey M. McKenzie
Codirecteur

Oliver Sonnentag
Membre du jury

René Therrien
Examinateur externe (pour une thèse)

RÉSUMÉ

Les infrastructures de transport est essentielle au maintien et à l'expansion des activités sociales et économiques dans les régions circumpolaires. À mesure que le climat se réchauffe, la dégradation du pergélisol sous les remblais a entraîné de graves dommages structuraux à la route, entraînant une augmentation importante des coûts d'entretien et une réduction de la durée de vie des infrastructures. Pendant ce temps, l'advection de chaleur déclenchée par les écoulements d'eau souterrains peut altérer le bilan énergétique du remblai et du pergélisol sous-jacent et modifier le régime thermique des remblais routiers. Cependant, peu de recherches ont été effectuées pour comprendre la synergie entre les processus thermiques de surface et souterrains des remblais routiers des régions froides. L'objectif de cette recherche était de comprendre les interactions thermiques entre l'atmosphère, le remblai routier, les écoulements d'eau et le pergélisol dans le contexte du changement climatique. Cette base, de connaissances est nécessaire pour la conception technique, l'entretien des routes et l'évaluation de la vulnérabilité des infrastructures.

Les travaux de recherche ont permis de développer de nouvelles méthodes d'analyse thermique pour caractériser et identifier le rôle de l'advection thermique sur le changement de température d'un remblai routier expérimental au Yukon (Canada) en termes d'intensité, de vitesse et de profondeur de l'impact thermique. Les résultats montrent que l'augmentation de la température due aux flux de chaleur advectifs déclenchés par l'écoulement d'eau peut être jusqu'à deux ordres de grandeur plus rapide qu'en raison du seul réchauffement atmosphérique.

La recherche a ensuite présenté un bilan énergétique de surface pour quantifier la quantité d'énergie entrant dans le centre et la pente du remblai avec des épaisseurs et des propriétés de neige variables. Le tout a été appuyé par des observations géothermique de plusieurs années et une grande quantité de données météorologiques. Les résultats illustrent que le bilan énergétique de surface est principalement contrôlé par le rayonnement net et moins par le flux de chaleur sensible. Le flux de chaleur transmis à la pente du remblai diminue de façon

exponentielle avec l'augmentation de l'épaisseur de la neige et diminue de façon linéaire avec l'installation du couvert de neige et la longueur de la période d'enneigement.

De plus, un modèle de bilan énergétique de surface et un modèle cryohydrologique entièrement couplé ont été développés pour étudier l'impact thermique de l'advection de chaleur associée à l'écoulement de l'eau souterraine sur le dégel du pergélisol et le développement de taliks (c.-à-d. zone perpétuellement non gelée dans les zones de pergélisol). Le modèle couplé a réussi à reproduire la tendance à la hausse du plafond du pergélisol (erreur absolue moyenne <0,2 m) au cours de la période 1997-2018. Les résultats montrent que l'advection de chaleur a fourni une source d'énergie supplémentaire pour accélérer le dégel du pergélisol et a doublé le taux d'augmentation de l'épaisseur de la couche active 0,1 m·a^{-1} à 0,19 m·a^{-1}, par rapport au scénario où aucun écoulement d'eau ne se produit. Le talik s'est initialement formé et développé en fonction du temps sous l'effet combiné des écoulement d'eau, de l'isolation de la neige, de la construction de la route et du réchauffement climatique. Le débit d'eau souterraine a relié des corps isolés de talik et a amené le remblai de la route dans un état thermique irréversible, en raison de la rétroaction de l'eau liquide (effet de chaleur latente) piégée dans le talik.

Ces résultats montrent l'importance de l'advection de chaleur induite par l'écoulement d'eau sur le régime thermique de la sous-couche (c.-à-d. la couche de matériau de remblai) et du sous-sol (c.-à-d. le matériau natif sous un remblai) du remblai lorsque le remblai routier intercepte le drainage local. De plus, les résultats obtenus soulignent la nécessité de coupler les processus thermiques de surface et souterrains dans le but d'évaluer la stabilité thermique des routes subarctiques.

Mots-clés : Pergélisol, Bilan énergétique de surface, Isolation de la neige, Advection de chaleur, Infiltration des eaux de surface, Écoulement de l'eau souterraine, Processus thermiques couplés de surface et souterrains, Initiation et développement de Talik, Autoroute de l'Alaska, Réchauffement climatique.

ABSTRACT

Transportation infrastructure is crucial to maintaining and expanding the social and economic activities in circumpolar regions. As the climate warms, degradation of the permafrost causes severe structural damages to the road embankment, leading to large increases in maintenance costs and reductions in its lifespan. Meanwhile, heat advection triggered by mobile water flow can alter energy balance of the embankment and underlying permafrost and modify the thermal regime of road embankments. However, little research has been done to understand the synergy between surface and subsurface thermal processes of cold region road embankments. The overall goal of this research was to elucidate thermal interactions between the atmosphere, the road embankment, mobile water flow, and permafrost within the context of climate change. This knowledge is needed for engineered design, road maintenance, and infrastructure vulnerability assessment.

The research first used new thermal analysis to characterize and identify the role of heat advection on temperature change of an experimental road embankment, Yukon, Canada in terms of magnitude, rate and thermal impact depth. It shows that soil temperature increase due to advective heat fluxes triggered by mobile water flow can be up to two orders of magnitude faster than due to atmospheric warming only.

The research then presented a novel surface energy balance to quantify the amount of ground heat flux entering the embankment center and slope with varying snow depth and properties, supported by multi-year thermal and meteorological observations. My results illustrate that the surface energy budget is mainly controlled by net radiation, and less by the sensible heat flux. The ground heat flux released at embankment slope exponentially decreased with the increase of snow depth, and was linearly reduced with earlier snow cover and longer snow-covered period.

A fully integrated surface energy balance and cryohydrogeological model was implemented to investigate the thermal impact of heat advection associated with subsurface water flow on permafrost thaw and talik (i.e., perennially unfrozen zone in permafrost areas) development. The integrated model successfully reproduced the observed increasing trend of the active layer depth

(mean absolute error < 0.2 m) over the 1997-2018 period. The results show that heat advection provided an additional energy source to expedite permafrost thaw, doubling the increasing rate of permafrost table depth from 0.1 m·a^{-1} to 0.19 m·a^{-1}, compared with the scenario where no water flow occurs. Talik formation and development occurred over time under the combined effect of subsurface water flow, snow insulation, road construction and climate warming. Subsurface water flow connected isolated talik bodies and triggered an irreversible thermal state for the road embankment, due to a local feedback mechanism (latent heat effect) of trapped, unfrozen water in talik.

These findings elucidate the importance of heat advection induced by mobile water flow on the thermal regime of embankment subbase (i.e., a layer of fill material) and subgrade (i.e., the native material under an embankment) when the road embankment intercepts the local drainage. Furthermore, the obtained results emphasize the need to couple surface and subsurface thermal processes to evaluate the thermal stability of sub-Arctic roads.

Keywords: Permafrost, Surface energy balance, Snow insulation, Heat advection, Surface water infiltration, Subsurface water flow, Coupled surface and subsurface thermal processes, Talik initiation and development, Alaska Highway, Climate warming.

TABLE OF CONTENTS

VIII

x

LIST OF TABLES

LIST OF FIGURES

LIST OF SYMBOLS AND ABBREVIATIONS

SYMBOLS

A_a	Mean amplitude of air temperature (°C)
a	Regression coefficient (-)
A_b	Mean amplitude of ground temperature (°C)
b	Regression coefficient (-)
c	Regression coefficient (-)
C_a	Apparent heat capacity (J·kg^{-1}·°C^{-1})
C_w	Heat capacity of water (J·m^{-3}·K^{-1})
Cs	Heat capacity of snow (J·m^{-3}·K^{-1})
d	Regression coefficient (-)
d_g	Ground depth (positive downwards) (m)
d_r	Inverse relative distance Earth-Sun (-)
d_s	Snow thickness (m)
FDD_a	Sum of freezing degree-day of air (°C·days)
FDD_g	Sum of freezing degree-day of ground (°C·days)
G_{sc}	Solar constant (117.5 MJ·m^{-2}·day^{-1})
g	Gravity (m·s^{-2})
J	Number of the day in the year between 1 (1st January) and 365 (31st December)

J_A	Supplementary heat flux (W·m⁻²)
K	Hydraulic conductivity (m·s⁻¹)
K_r	Relative permeability (-)
$\underline{\underline{K}}$	Permeability tensor
L_f	Latent heat of freezing (J·kg⁻¹)
L_v	Latent heat of vaporization (J·kg⁻¹)
m	Number of independent variables
N	Number of the data points
n_f	Freezing n-factor (-)
n_t	Thawing n-factor (-)
p	Pressure (kg·m⁻¹·s⁻²)
P_{rain}	Daily rainfall (m·daily⁻¹)
q_p	Pore water inflow at a boundary (kg·m⁻³·s⁻¹)
q_w	Water flux (m³)
Q_a	Extra-terrestrial radiation (W·m⁻²)
Q_c	Ground heat flux through the snow cover and ground (W·m⁻²)
Q_{LW}^{in}	Incoming long-wave radiation (W·m⁻²)
Q_{LW}^{out}	Outgoing long-wave radiation (W·m⁻²)

Q_{net}	Net solar radiation absorbed at the surface (W·m^{-2})
Q_p	Rainfall heat (W·m^{-2})
Q_{SW}^{in}	Incoming solar radiation (W·m^{-2})
Q_{SW}^{out}	Outgoing solar radiation (W·m^{-2})
Q_h	Sensible heat flux (W·m^{-2})
Q_v	Heat flux of vapor exchange from the surface (W·m^{-2})
Q_0	Stored energy (W·m^{-2})
R^2	Coefficient of determination (-)
R	Thermodynamic vapor constant (J·kg^{-1}·K^{-1})
r_v	Resistance to vapor exchange (day·m^{-1})
S_L	Saturation of liquid water (%)
S_w	Total water saturation (%)
S_i	Saturation of ice (%)
S_{op}	Specified pressure storativity
S_{wres}	Residual liquid saturation (-)
t	Time (hour)
t_{max}	Maximum duration of simulation period (day)
t_p	Period of oscillation and of the ground (day)

T_a	Air temperature (°C)	
T_{dp}	Dew-point temperature (°C)	
T_g	Ground temperature (°C)	
T_f	Freezing point (°C)	
T_{ti}	Soil temperature at the initial time step (°C)	
T_{tf}	Soil temperature at the final time step (°C)	
T_s	Temperature of snow (°C)	
T_{sub}	Soil temperature at the bottom of a soil layer (°C)	
T_w	Temperature of the recharge water (°C)	
T_0	Mean annual air temperature (°C)	
T_m	Average value of the ground surface temperature and air atmosphere (°C)	
T^*	Temperature of the inflowing water (°C)	
TDD_a	Sum of thawing degree-day of air (°C·days)	
TDD_g	Sum of thawing degree-day of ground (°C·days)	
U	Wind speed (m·s^{-1})	
$\underline{v}$	Groundwater velocity vector (m·s^{-1})	
ΔT	Surface offset (°C)	
Δt	Model time step (hour)	
$\Delta T_{surf\text{-}a}$	Temperature difference between the ground surface and the atmosphere (°C)	

α_g	Ground albedo (-)
α_s	Snow albedo (-)
ω_s	Sunset hour angle (-)
δ	Solar decimation (°)
φ	Latitude (radian)
ρ_v	Saturation vapor density (kg·m^{-3})
ρ_a	Saturation vapor density at the dew-point temperature (kg·m^{-3})
ρ_w	Water density (kg·m^{-3})
ρ_s	Snow density (kg·m^{-3})
ρ_i	Ice density (kg·m^{-3})
ε	Porosity (-)
θ_u	Unfrozen water content (%)
μ	Viscosity of liquid water (kg·m^{-1}·s^{-1})
Ω	Impedance factor (-)
ψ	Total hydraulic head (m)
ψ_g	Gravitational potential (m)
ψ_m	Matric potential, which result from capillary forces (m)
ψ_T	Temperature potential (m)

ψ_p	Pressure head (m)
ψ_s	Osmotic forces (m)
ε_0	Corresponding random error
ξ	Deviation convergence tolerance for solvers iteration
ζ_a	Rate of AT increase ($°C·a^{-1}$),
γ	Heat exchange coefficient ($J·m^{-2}·s^{-1}·K^{-1}$)
∇T	Temperature gradient ($K·m^{-1}$)
λ	Thermal conductivity ($W·m^{-1}·K^{-1}$)
λ_a	Thermal diffusivity of air ($W·m^{-1}·K^{-1}$)
λ_g	Thermal diffusivity of ground ($W·m^{-1}·K^{-1}$)
λ_s	Thermal diffusivity of snow ($W·m^{-1}·K^{-1}$)
β	Mean values of regression coefficients
φ	Phase shift (radian)

ABBREVIATIONS

ALT	Active layer thickness
AT	Air temperature
BC	Boundary condition
BC-RES	Beaver Creek - Road Experimental Site
FDD	Freezing degree-day
GST	Ground surface temperature
HBC	Hydraulic boundary condition
MAAT	Mean annual air temperature
MAE	Mean absolute error
MASR	Mean annual solar radiation
MBE	Mean bias error
MGT	Mean ground temperature
NG	Natural ground
PVC	Polyvinyl chloride
QTP	Qinghai-Tibet Plateau
RCP	Representative Concentration Pathway
RMSE	Root mean square error
SD	Standard deviation

SEB   Surface energy balance

SST   Snow surface temperature

TBC   Thermal boundary condition

TDD   Thawing degree-day

TID   Thermal impact depth

CONTRIBUTION OF AUTHORS

This thesis is composed of three manuscripts for which I am first author, but that are written in collaboration with several colleagues. I hold primary responsibility for the literature review, developing and calibrating the surface energy balance model, integrating the surface energy balance model with cryohydrogeological numerical model, designing and performing numerical simulations, analyzing and interpreting the simulated and observed data, and preparing the manuscripts for publication in the scientific literature and the doctoral dissertation. My supervisor, Prof. Daniel Fortier of the Département de géographie at the Université de Montréal, and co-supervisor, Prof. Jeffrey M. McKenzie of the Department of Earth & Planetary Sciences at McGill University are co-authors on all three manuscripts for their contributions to defining research scope and objectives, guiding the numerical simulations, contributing to the interpretation of results and revising the manuscripts and the doctoral dissertation. My internship advisor, Prof. Clifford I. Voss of the United States Geological Survey is included as a co-author on the manuscripts from Chapter 4 and 5 for his help in the development of the surface energy balance model and with editing the manuscripts.

The first manuscript (Chapter 3) was published in Hydrological Processes in 2020. Michel Sliger is included as co-author for contributing to fieldwork and scientific discussions.

The second manuscript (Chapter 4) has been accepted in Permafrost and Periglacial Processes in 2021.

The third manuscript (Chapter 5) will be submitted for publication to a peer-reviewed journal in 2021.

xxx

ACKNOWLEDGEMENTS

Chapter 1 - INTRODUCTION

1.1. BACKGROUND

In Arctic and sub-Arctic regions, transportation infrastructure has experienced severe structural damages due to the degradation of the underlying permafrost induced by climate warming and surface disturbance caused by construction (Nelson et al., 2001, Hjort et al., 2018, Streletskiy et al., 2019). Infrastructure damages caused by permafrost degradation includes severe settlements, longitudinal cracking, and surface movement (Wu et al., 2007, Doré et al., 2016). These processes largely increase maintenance costs, severely threaten the structural integrity of the infrastructure and reduce the lifespan of road embankments (Reimchen et al., 2009, Melvin et al., 2016). For instance, in Alaska, cumulative estimated expenses from the climate-related damage to infrastructure from 2015 to 2019 was about $4.2 billion for Representative Concentration Pathway (i.e., a greenhouse gas concentration trajectory adopted by the IPCC) 4.5 (RCP4.5; van Vuuren et al., 2011), while $5.5 billion for RCP8.5 (Melvin et al., 2016). Also, Larsen et al., (2008) proposed that climate change will add $3.6 - $6.1 billion to future costs for Alaska public infrastructure from 2008 to 2030.

For transportation infrastructure, its vulnerability to permafrost thaw is mainly a function of the thermal regime of embankment subgrade (i.e., the native material underneath a constructed road) and subbase (i.e., the layer of embankment fill material laid on the subgrade) (Cheng 2005a, Calmels et al., 2015, Doré et al., 2016). The temperatures of an embankment's subbase and subgrade are a function of the air temperature (AT), water infiltration, subsurface water flow, vegetation and seasonal snow cover deposited on the slope surface (Shen 1988, Goering 1998, Chen et al., 2018). Numerous studies have investigated the thermal interaction between embankments and underlying permafrost via field observations (e.g., Sheng et al., 2002, Wu et al., 2007, Malenfant-Lepage et al., 2010, Ma et al., 2012), numerical simulations (e.g., Goering and Kumar 1996, Lai et al., 2004, Fortier et al., 2011, Chen et al., 2018), and experimental models (e.g., Yu et al., 2004, Lai et al., 2009), indicating that high solar absorbability and large thermal conductivity of embankment material extensively increase the amount of atmospheric heat

entering underlying permafrost. Such additional energy absorption results in accelerating permafrost degradation at a fast rate (Cheng 2005b, Wu et al., 2007). Simultaneously, in order to stabilize embankments over degrading permafrost, much of the previous research estimated the thermal effectiveness of mitigation techniques aimed at increasing heat release and reducing subsurface heat penetration (e.g., Goering and Kumar 1996, Lai et al., 2004, Yu et al., 2004, Darrow and Jensen 2016, Chen et al., 2017b, Fortier et al., 2018). Additionally, mobile water flow, acting as a heat source (Bullard 1939, Harris and Corte 1992), can trigger heat advection and greatly modify the temperature distribution within the embankment subgrade and subbase (e.g., Lu and Ge 1996, McKenzie et al., 2007b). Recently, several studies have reported that subsurface water flow beneath a road embankment induced an advective heat flux and further undermined the stability of engineered structures (de Grandpré et al., 2012, Zottola et al., 2012, Zhang et al., 2017a, Mu et al., 2020b). However, the role of heat advection in accelerating the rate of permafrost thaw has not been quantified due to lack of long-term thermal monitoring. Additionally, the heat exchange between the atmosphere and the road embankment remains largely unknown, as the employed thermal boundary conditions (TBCs) neglected the coupling processes among the atmosphere (above ground surface), road surface, and the embankment subgrade and subbase (below ground surface). Therefore, to better understand surface and subsurface thermal processes of cold-regions road, it is imperative to investigate and quantify the amount of heat from the overlying air and radiative energy entering the underlying permafrost through embankment fill and impacts of heat advected by mobile water flow on the thermal stability of road embankments built on permafrost.

1.2. RESEARCH OBJECTIVES

Given the demonstrated importance of heat advection caused by mobile water flow under a road embankment built on permafrost, I aim to present new ways to characterize and identify advection dominance over conduction in terms of rate and magnitude of temperature change within the embankment. Subsequently, I aim to develop a novel surface energy balance (SEB) model to quantify the quantity of ground heat flux through the embankment fill. Additionally, I aim to fully integrate this novel SEB model into the SUTRA-ice code (a coupled heat transport and

water flow model) to investigate the impact of heat advection caused by mobile water flow on the thermal stability of road embankment built on permafrost.

Specifically, the objectives were:

- **Objective 1** is to quantify the magnitude and rate of heat advection triggered by mobile water flow through the embankment subbase and subgrade and under the road embankments with different surface cover types (Chapter 3)
- **Objective 2** is to develop, calibrate, and implement a novel SEB model of a road to investigate and quantify the quantity of energy entering the embankment subbase and subgrade (Chapter 4)
- **Objective 3** is to fully integrate the SEB model into the SUTRA-ice code and quantify the sensitivity of the simulated ground surface temperatures to meteorological forcings over the 1993-2018 period (Chapter 5)
- **Objective 4** is to use the integrated model to estimate the heat advection associated with subsurface water flow on permafrost degradation and talik development beneath an embankment in a context of climate warming (Chapter 5)

1.3. THESIS ORGANIZATION

Chapter 1 introduces the study background, objectives, and structure of the thesis. The authors' contributions are presented.

Chapter 2 presents a detailed literature review on the permafrost distribution, road embankment damages caused by permafrost degradation, and the thermal interactions between the atmosphere and the ground. Heat transfer during the freezing and thawing processes are also discussed.

Chapter 3 addresses Objective 1 and identifies the magnitudes and rates of heat exchange induced by infiltrated surface water and subsurface water flow. Five experimental road sections along the Alaska Highway with nine-year soil temperatures and meteorological data were statistically analyzed. The thermal impact depths, magnitudes and rates of temperature change beneath five different surface cover types, including four embankment surfaces and one natural

ground surface adjacent to the embankment, were compared and discussed on the basis of the thermal deviation caused by the mobile water flow. This study aims to demonstrate the role of heat advection in accelerating the rate of permafrost thawing. Our findings have implications for subsurface hydrology research and applied hydrology for infrastructure across the permafrost regions. The results from our research are of interest beyond northern Canada, and are applicable in pan-Arctic settings (e.g., Dalton Highway and Taylor Highway, Alaska, US), in QTP (e.g., Qinghai-Tibet Highway and Railway, China), or undisturbed grounds (e.g., alpine meadow and aeolian sand in the QTP, China; polar desert in high Arctic regions). This chapter has been published as: Lin Chen, Daniel Fortier, Jeffrey M. McKenzie & Michel Sliger, 2020, Impact of Heat Advection on the Thermal Regime of Roads Built on Permafrost. Hydrological Processes. 34 (7), 1647–1664. DOI: 10.1002/hyp.13688.

Chapter 4 addresses Objective 2 and presents a novel SEB model of cold-regions roads to simulate the GSTs for different surface cover types with varying snow regimes and properties, supported by 10 years of thermal observations and large amounts of meteorological data from the Beaver Creek - Road Experimental Site (BC-RES) on the Alaska Highway. The characteristics of the GSTs and ground heat fluxes entering the embankment slope and center were investigated and compared for three different periods, including snow-free period (April 15th to October 17th), snow-accumulation period (October 17th to March 26th) and snow-melt period (March 26th to April 15th). The sensitivities of seasonal snowpack depth, timing and duration on the ground heat fluxes through the embankment slope were quantified. The conductive heat transfer model coupling the surface energy balance can be used to assess the vulnerability of underlying permafrost to road construction built in the areas where the subsurface water flow is insignificant. In addition, the outputs of the SEB model, either specified temperature or ground heat flux variations at the top surface, can be easily implemented as a TBC in geothermal model or cryohydrogeological models developed for different purposes. Examples include thermal interactions between an infrastructure (e.g., highways, railway, buried pipelines, or airstrips) and the underlying permafrost, the effect of climate change on cryohydrogeological processes, or the land surface - atmosphere interactions. This chapter has been accepted as: Lin Chen, Clifford I. Voss, Daniel Fortier & Jeffrey M. McKenzie, 2021, Surface Energy Balance of Sub-Arctic Roads

with varying Snow Regimes and Properties in Permafrost Regions, Permafrost and Periglacial Processes.

Chapter 5 addresses Objective 3 and 4 by fully incorporating the SEB model into the SUTRA-ice code to couple the individual energy processes at the top surface with thermal processes in the subsurface layer. I apply this coupled model to investigate and quantify the effects of heat advection caused by mobile water flow, snow insulation, and atmospheric warming on the permafrost degradation and talik development in permafrost regions, supported by long-term (1993-2018 on Alaska Highway) field observations. The uncertainty of reconstructed meteorological data was quantified. Additionally, hydrothermal processes beneath three surface cover types were simulated, including undisturbed vegetated NG, snow-covered embankment slope, and snow-free asphalt-paved surface of embankment center. The newly coupled model can be applied to a range of environmental issues in either the permafrost regions or the seasonal frozen areas, including engineering applications (e.g., thermal stability of roads in Alaska, US or on the QTP, China), climate-change scenarios, studies of hydrogeological processes or environmental concerns (e.g., spatiotemporal changes of permafrost, soil water dynamics). This chapter will be submitted for publication to a peer-reviewed journal in 2020: Lin Chen, Daniel Fortier, Jeffrey M. McKenzie & Clifford I. Voss, *to be submitted*, Talik Initiation and Development Trigger Irreversible Thermal State of a Sub-Arctic Road Embankment.

Chapter 6 presents a summary of the thesis and suggestions for future work.

1.4. ORIGINAL CONTRIBUTIONS TO NEW KNOWLEDGE

The thesis addresses the impacts of heat advection triggered by mobile water flow on the thermal regime of an embankment subbase and subgrade built on permafrost. The specific contributions to new knowledge are highlighted below.

(1) Impacts of surface water infiltration and subsurface porewater flow have been quantified in terms of thermal impact depth, magnitude, and rate of temperature change for the first time. Previous work has demonstrated the importance of heat advection, yet little data are available to support the role of heat advection in accelerating the rate of permafrost thaw. This study presented a novel way, based on temperature deviations, to characterize and identify the role of

heat advection in cold regions infrastructure dynamics. The infiltration of spring snowmelt causes a very rapid temperature increase in the road embankment, within just a few days. The infiltration of summer rainfall lowers near-surface temperatures, while simultaneously warming embankment fill materials at depth. The advection of heat due to pore water flow leads to warming rates that can be up to two orders of magnitude faster than by atmospheric warming only.

(2) A novel surface energy balance model with varying snow regimes and properties was developed for the determination of ground surface temperatures and the quantification of surface energy components for a road embankment for the first time. Employed approaches for the determination of the surface temperature of an asphalt pavement negate impacts of subsurface processes and effects of snow depth, timing, and duration. Based on a unique dataset of soil temperatures and meteorological measurements, a novel SEB model of cold-regions road was developed and validated. We demonstrated that the quantity of heat entering the embankment center and slope is mainly controlled by net radiation, and less by the sensible heat flux. In spring, lateral ground heat flux from the embankment center to the slopes leads to the earlier disappearance of the seasonal snow cover on the embankment slope. In winter, the insulation created by the snow cover on the embankment slope reduces conductive heat loss by three times compared with the embankment center where the snow is plowed. The ground heat flux released at the embankment slope exponentially decreases with the increase of snow depth and was linearly reduced with earlier snow cover and longer snow-covered period.

(3) A surface energy balance model, driven by meteorological data, was fully integrated into the modified SUTRA-ice code to couple surface and subsurface thermal processes for the first time. Previously employed SEB models were restricted to a one-dimensional vertical domain neglecting the impact of lateral ground heat flux induced by asymmetric geometry or uneven surface disturbance (e.g., water ponding and preferential snow accumulation), which are not suitable for understanding the multi-dimensional thermal interactions of the atmosphere-road-permafrost systems. We fully coupled our novel SEB model into the SUTRA-ice code to include the inter-annual variations of climate and subsurface processes. The integrated model had a good performance to predict the GSTs and reproduced the trend of permafrost warming and thawing

6

under the combined effect of the snow cover and subsurface water flow. The simulated GSTs were most sensitive to the snowpack thickness, followed by solar radiation and AT. The empirical equation relating AT and solar radiation reduce the required input of meteorological variables. The integrated model can be applied in other regions given sufficient meteorological data and land surface characteristics.

(4) A fully coupled heat transport and water flow model, integrating surface and subsurface thermal processes, was used to investigate and quantify impacts of heat advection on permafrost degradation and talik development for the first time. Numerous geothermal models with specified TBCs have been used to investigate the thermal interaction between a road embankment and the underlying permafrost within the context of climate warming. However, the quantification of heat advection on talik development and its feedback on permafrost degradation has not been studied methodically. This study demonstrated that heat advection triggered by subsurface water flow provided an additional energy source to expedite permafrost thaw and doubled the increasing rate of permafrost table depth from 0.1 m·a^{-1} to 0.19 m·a^{-1}, compared with the scenario where no water flow occurs. Talik initially formed and developed over time under the combined effect of water flow, snow insulation, road construction and climate warming. Talik formation created a new thermal state of road embankment, resulting in acceleration of thawing of the underlying permafrost, due to the latent-heat feedback of trapped unfrozen water.

Chapter 2 - LITERATURE REVIEW

2.1. PERMAFROST AND CLIMATE CHANGE

2.1.1. Permafrost distribution

Permafrost, defined as ground (i.e., soil, rock and included ice and organic material) that remains at or below 0 °C for at least two consecutive years, constitutes about 23-25 % of the world's exposed land surface (Anisimov and Nelson 1996, Davis 2001), with about 15 % of all permafrost occurring within Canada (Baranov and Tsytovich 1959, Smith et al., 2010), shown in Figure 2.1a. More than 50 % of the Canadian landmass is underlain by permafrost (Heginbottom et al., 1995). In addition, permafrost can be categorized into four types according to its spatial occurrence: continuous permafrost (90 - 100 % presence), discontinuous permafrost (50 - 90 % presence), sporadic permafrost (10 - 50 % presence), and isolated patches permafrost (0 - 10 % presence) (Vandenberghe et al., 2014).

Permafrost thickness varies from a few metres to hundreds of metres and its temperature ranges from close to 0 °C to much lower than -10 °C (Romanovsky et al., 2010). The presence of permafrost is broadly controlled by the climate system (Smith and Riseborough 1996, Cheng 2004, Lewkowicz et al., 2012). The permanently frozen grounds are most common in Earth's high latitudes (Throop et al., 2012, Aalto et al., 2018) and in regions with high altitudes (e.g., Qinghai-Tibet Plateau, QTP), where the mean annual AT (MAAT) is below 0 °C (Wu et al., 2002, Zou et al., 2017, Mu et al., 2020a). However, details of the permafrost distribution differ greatly among sites (Cheng 2004, Aalto et al., 2018) due to the regional and local difference of surface cover types, snowpack, soil types, moisture contents and terrain conditions (Yi et al., 2007, Davesne et al., 2017, Karjalainen et al., 2019, Harris 1998). For instance, the desertification and aeolian sand cover greatly change the permafrost distribution in the QTP (Wu et al., 2017, Chen et al., 2020b). Also, wind-driven snow conditions control the spatial distribution of permafrost in mountainous areas (Harris and Pedersen 1998, Ishikawa and Hirakawa 2000, Davesne et al., 2017, Beniston et al, 2018).

Additionally, the active layer, a layer of soil on top of permafrost, experiences seasonal freezing and thawing processes over a year (French 2017), shown in Figure 2.1b. The thickness of the active layer ranges from several centimetres in high-latitude cold regions (e.g., high Arctic) to several meters in warmer regions (French 2017). When more heat accumulates beneath the ground surface and the heat release in winter is not enough to freeze back the active layer to permafrost table, talik (perennially unfrozen layers or bodies in permafrost areas) initiates and enlarges with time (Nelson et al., 2001, Connon et al., 2018). The talik formation is mainly triggered by the presence of river, water bodies, thick snowpack, fire, thermokarst lake and road construction (Shur and Jorgenson 2007, Rowland et al., 2011, O'Neill and Burn 2016, Roux et al., 2017, Connon et al., 2018, Sun et al., 2018b, Walvoord et al., 2019). Furthermore, in freezing or thawing active layer, the soil temperature is maintained near 0 °C for a considerable length of time (i.e., zero-curtain period) due to the effect of the latent heat (Outcalt et al., 1990).
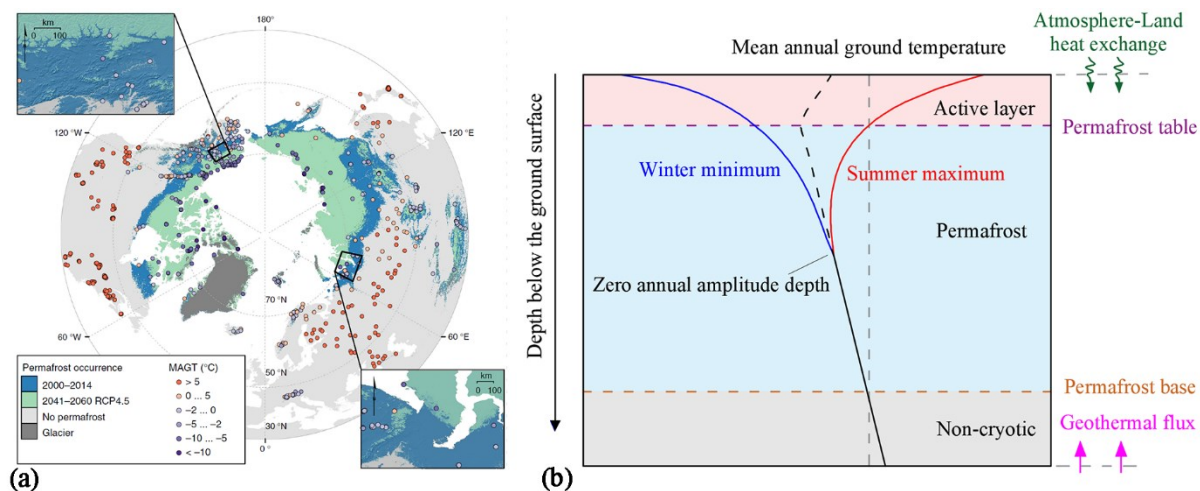
Figure 2.1. (a) Distribution of permafrost in the current (2000–2014) and future (RCP4.5 2041–2060, van Vuuren et al., 2011) climates, modified from Aalto et al., (2018); and (b) a typical temperature envelope for a permafrost region, modified from French (2017).

2.1.2. Global climate warming

The Earth's climate is changing at a global scale and a rapid pace (IPCC 2014). Global surface AT is projected to rise by an average of 1.0 °C for the RCP2.6 and 3.7 °C for RCP8.5, respectively, over the 21st century. Extreme precipitation events are projected to occur more intensely and frequently (Lewkowicz and Way 2019). Additionally, the surface AT in pan-Arctic areas warms by

approximately twice than the global mean (Lawrence et al., 2008a) due to the Arctic amplification, which include, but are not limited to, the soot on snow, the positive surface albedo feedback caused by melting Arctic sea ice, and heightened black carbon aerosol concentrations (Winton 2006, Serreze and Barry 2011, Pithan and Mauritsen 2014, Huang et al., 2017). The mean annual surface temperatures in Arctic regions are projected to increase by 4 ˚C to 7 ˚C over the 21st century (IPCC 2014).

2.1.3. Permafrost degradation

Climate change is causing permafrost warming and thawing at a global scale (Hinzman et al., 2005, Christiansen et al., 2010, Biskaborn et al., 2019). Permafrost temperatures have increased in most regions since the early 1980s (Biskaborn et al., 2019), shown in Figure 2.2. The global mean permafrost temperature increased by 0.29 ± 0.12 °C over the 2007-2016 period (Biskaborn et al., 2019). The pan-Arctic permafrost region is expected to warm at least at twice the global average during the 21st century (Lawrence et al., 2008a). Furthermore, in response to increased surface temperature and changing snow cover, the area of permafrost near the surface (upper 3.5 m) is projected to decrease by 37 % (RCP2.6) to 81 % (RCP8.5) by the end of 21st century (IPCC, 2014), shown in Figure 2.1.

Permafrost is highly vulnerable to climate warming. In northwestern Canada, Kwong and Gan (1994) documented a 120 km shift northward in the southern limit of permafrost in northern Alberta and southern Northwest Territories. Thibault and Payette (2009) found that the permafrost boundary has receded northwards by about 130 km in the James Bay area of Quebec. James et al., (2013) presented that the southern limit of permafrost appears to have shifted northward by at least 25 km in northern British Columbia and southern Yukon, northwest Canada. Furthermore, In Alaska, Osterkamp (2005) presented that over the 1977-2003 period, the magnitudes of the total warming at the surface of the permafrost were 3 to 4 ˚C for the Arctic Coastal Plain, 1 to 2 ˚C for the Brooks Range including its northern and southern foothills, and 0.3 to 1 ˚C south of the Yukon River, respectively. Similarly, on the QTP, Western China, Ran et al., (2018) demonstrated that the permafrost area has decreased by approximately 23.84 % over the 1960-2010 period, in response to the increasing AT rate of 0.04 ˚C·a[-1]. Nan et al., (2005) illustrated

that the permafrost area will shrink up about 13.5 % by 2050, under the projected AT increasing rate of 0.052 ˚C·a⁻¹. Additionally, in Northeast China, the areas of sporadic discontinuous and isolated patchy permafrost have reduced by approximately 35 % in the 1970s (Jin et al., 2007) and by 43 % from 1980 to 2000 (Zhongqiong et al., 2019). In addition, processes contributing to the permafrost thaw will increase the active layer thickness, result in the disappearance of permafrost, and ultimately lead to additional hydrological pathways.
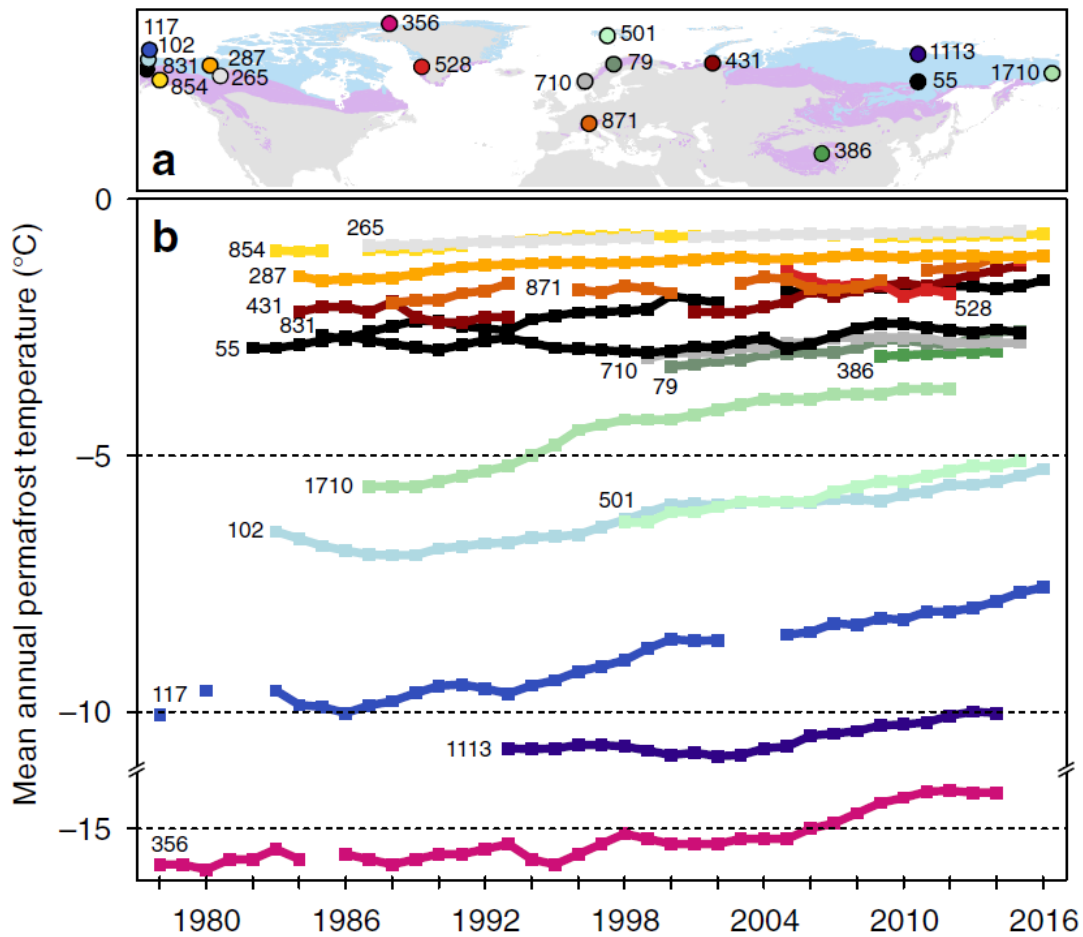
Figure 2.2. (a) Permafrost distribution and location of boreholes with long time-series data; and (b) Mean annual ground temperature over time, from Biskaborn et al., (2019). Note: in Figure 2.2a, the light blue area represents the continuous permafrost zone (> 90 % coverage) and the light purple area represents the discontinuous permafrost zones (< 90 % coverage).

2.2. SUBSIDENCE RISK OF INFRASTRUCTURE INDUCED BY THAWING PERMAFROST

Transportation infrastructure is crucial for the social and economic activities in circumpolar regions (Doré et al., 2016). Either air, road or railway transportation is essential to ensure the communication and linkages between northern communities (Beaulac and Doré 2006, James et al., 2013). For example, the Alaska Highway is the only terrestrial link between mainland Alaska and the contiguous United States (Calmels et al., 2015). About a quarter of the Alaska Highway is built on permafrost, which is typically ice-rich and at a temperature near the point of thawing (James et al., 2013, Calmels et al., 2015, Smith et al., 2017). Also, the Dempster Highway, built above continuous permafrost, is an important transportation route for northern communities in the Yukon and Northwest Territories (Burn et al., 2009, O'Neill and Burn 2016). Furthermore, about 550 km of Qinghai-Tibet Highway, connecting Xining to Lhasa, Western China, overlies the continuous permafrost, half of which is at a high mean annual ground temperature ranging from 0 to −1 °C (Cheng 2005a, Jin et al., 2008).

Degradation of near-surface permafrost (< 15 m depth) can pose a serious threat to transportation infrastructure, due to loss of the structural bearing capacity (Streletskiy et al., 2012, Hjort et al., 2018). Degradation of permafrost has already been related to numerous damages of infrastructure components (Larsen et al., 2008, Hong et al., 2014, Melvin et al., 2016, Shiklomanov et al., 2017, Suter et al., 2019). For instance, in Alaska, near-surface permafrost thaw was responsible for 38 % of infrastructure damages (Melvin et al., 2016). On the QTP, the damage ratio (length of damaged sections to the total length) was over 30 % for existing Qinghai-Tibet Highway (Cheng 2005a). Additionally, detrimental effects on engineered structures will be expected throughout the permafrost domain under climate warming (Melvin et al., 2016, Hjort et al., 2018). Hjort et al., (2018) demonstrate that, under a medium stabilization scenario RCP4.5, nearly 70 % of current infrastructure will be adversely affected by the thaw of near-surface permafrost by 2050 (see Figure 2.3). Also, they predicted that the one-third of pan-Arctic infrastructure are located in areas where thaw of near-surface permafrost can detrimentally affect the built environment (Hjort et al., 2018).
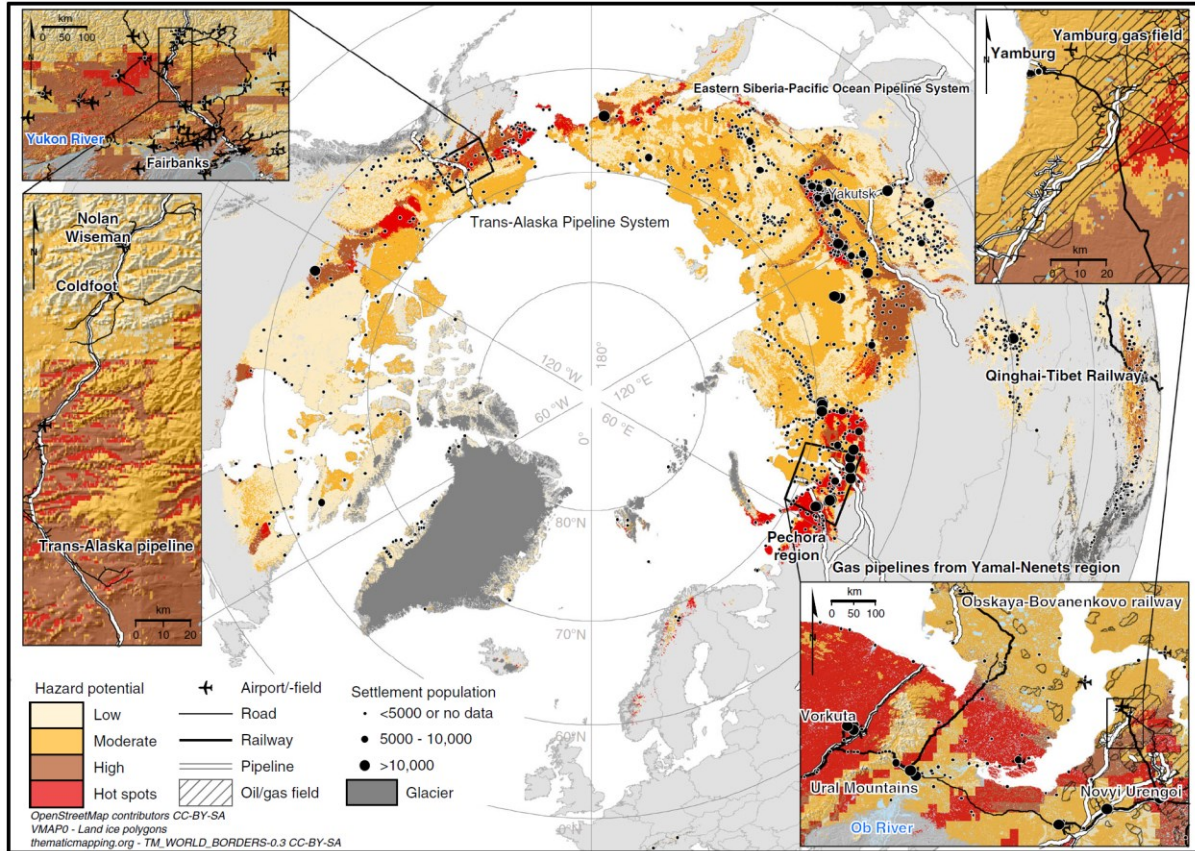
Figure 2.3. Pan-Arctic infrastructure hazard map with close-ups from central Alaska and northwestern parts of the Russian Arctic, from Hjort et al., (2018).

For transport infrastructure, the construction damages or removes the vegetation layer, alters the surface energy budget, and changes the heat exchange between the atmosphere and the natural ground (Wu et al., 2007, Calmels et al., 2015). In comparison to the thermal buffer effect of the vegetation layer (Yi et al., 2007), the low albedo of paved surface greatly increases solar energy absorption (Dumais and Doré 2016). In addition, the dry embankment material, with high thermal conductivity, largely favours the heat propagation downwards in the ground (Sheng et al., 2002). Furthermore, in snowy regions, road embankment acts as a snow fence, changes the wind profile, and creates vortex flows, which largely favors the snow accumulation at the embankment slope and toe (Fortier et al., 2011, O'Neill and Burn 2017). The thick snowpack insulates the heat exchange between the ground and the cold atmosphere in winter (Arenson et al., 2006, Fortier et al., 2011, Lanouette et al., 2015, O'Neill and Burn 2017). Therefore, surface disturbances including a thick snowpack cover and low-albedo embankment surface can result in

14
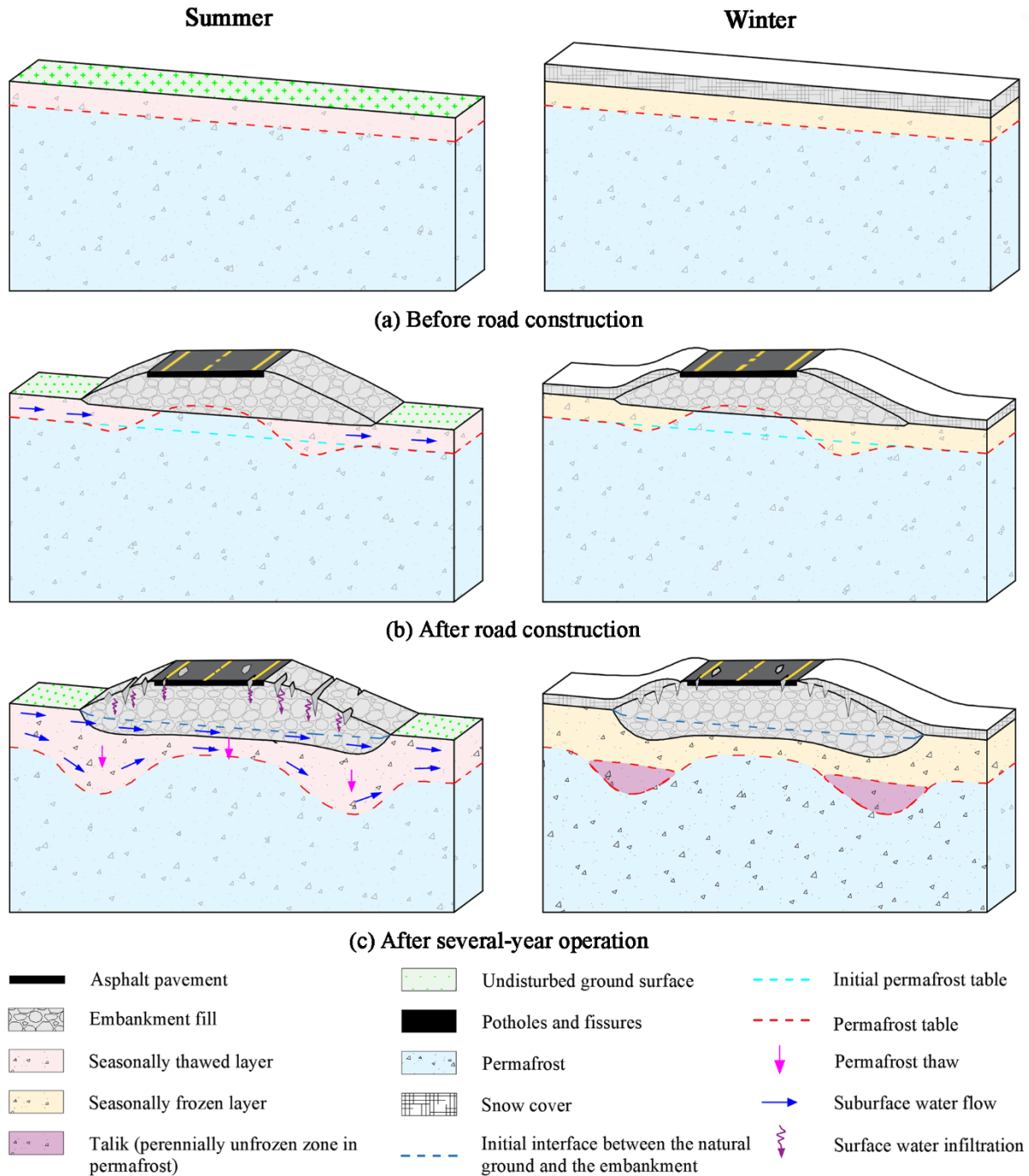
Figure 2.4. Thermal regime of natural ground (a) before road construction; (b) after road construction; and (c) road damages related to permafrost degradation after several-year operation.

the acceleration of permafrost degradation, further decreasing the structural integrity, and eventually cause road damages (Ma et al., 2009, de Grandpré et al., 2012, Malenfant-Lepage et al., 2012b, Calmels et al., 2015), conceptually shown in Figure 2.4. The road damages related to

permafrost thaw include longitudinal cracking, differential settlement, sinkholes and guardrail settlements.

2.3. HEAT EXCHANGE AT THE GROUND-ATMOSPHERE INTERFACE

In order to assess the vulnerability of permafrost to climate change and transportation infrastructure construction, it is essential to understand the energy exchange processes at the Earth's surface (Male and Granger 1981, Eugster et al., 2000, Hoelzle et al., 2001). The quantity of ground heat flux is determined by the energy budget of the ground surface (Eugster et al., 2000, Westermann et al., 2009), illustrated in Figure 2.5. The corresponding amount differs strongly among sites due to regional difference of surface cover types, surface temperature, and subsurface processes (Mittaz et al., 2000, Ling and Zhang 2004, Herb et al., 2008). Generally, the amount of heat exchange between the atmosphere and the natural ground is a function of solar radiation, turbulent heat fluxes by wind at ground surface, rainfall heat, and heat fluxes due to evaporation and condensation (Hwang 1976, Zhang et al., 2003, Walter et al., 2005).
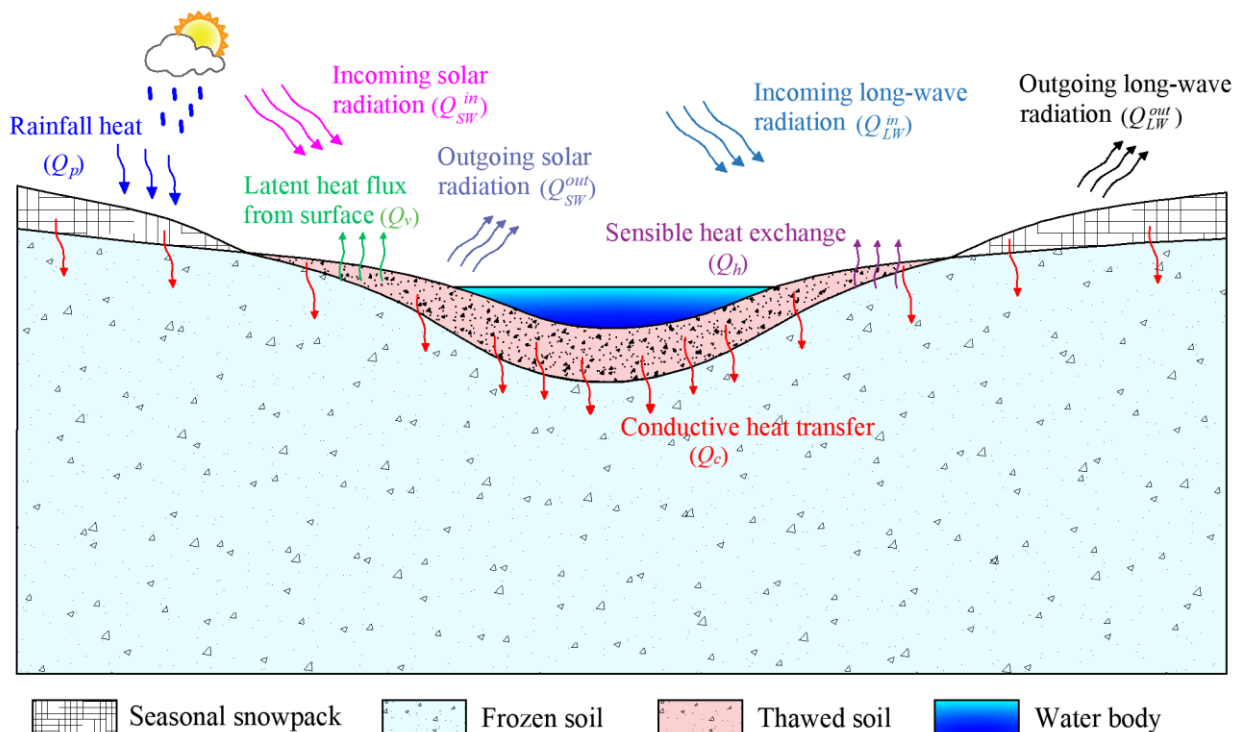
Figure 2.5. Schematic showing the heat exchange between the atmosphere and the ground in late spring when the snow starts to melt and the shallow ground thaws.

The quantification of the energy exchange processes at the Earth's surface is commonly investigated by either field observations or by land surface schemes (Riseborough et al., 2008). Firstly, the ground heat flux can be directly measured by self-calibrating ground heat flux plates (Zhang et al., 2017b, Boike et al., 2019, Chen et al., 2020b) or calculated by the Fourier's Law (Fourier 1822) using the measured soil temperatures at two depths (Sheng et al., 2002, Malenfant-Lepage et al., 2012b). For example, Boike et al., (2019) presented a public dataset collected in three Arctic sites (located at the Samoylov Island, Lena River delta, and northern Siberia), which is freely available through the PANGAEA data repository. The datasets provide meteorological information (e.g., AT, air pressure, humidity, precipitation, wind speed, and radiation), ground surface characteristics (e.g., surface albedo, vegetation type and density), and thermal and moisture status in the subsurface layer (e.g., soil temperature, soil moisture, ground heat flux, and water table) over the 2002-2017 period, which provides an opportunity to validate the land surface schemes (Boike et al., 2018, Boike et al., 2019). Similarly, there are several publicly-available open-access repositories providing measured GSTs and meteorological data in the Arctic, like Arctic Data Center (e.g., Wang et al., 2018b), AmeriFlux (e.g., Sadeghi et al., 2019), and Nordicana D (e.g., Fortier and Chen 2020b). Although direct measurements can provide reliable information to quantify the surface and subsurface thermal processes, observational data density in the Arctic areas or other cold regions is still low (Eugster et al., 2000, Boike et al., 2019). The site-specific dataset may be problematic for determination of energy exchange processes in other sites due to the different climate conditions and strong spatial heterogeneity, such as vegetation types and density, snow depth, soil stratigraphy, and topography. For instance, the effects of desertification and aeolian sand accumulation on permafrost degradation in the QTP remain much dispute, although extensive thermal observations have been conducted (e.g., Yang et al., 2004, Wu et al., 2017, Wang et al., 2019, Chen et al., 2020b). Additionally, this approach is difficult to predict the response of soil temperatures to the projected climate change and the change of surface cover types induced by human activity.

Alternatively, numerical models are valuable tools to understand the heat exchange between the atmosphere and the ground (Hwang 1976, Hoelzle et al., 2001, Walter et al., 2005). The TBCs are the primary key factor to numerically simulating the heat exchange processes in the subsurface

layer (Cichota et al., 2004, Riseborough et al., 2008, Harris et al., 2009). Typically, the TBCs can be classified into three categories: a specified temperature BC (named "Dirichlet BC"), a specified heat flux BC (named "Neumann BC"), and a weighted combination of temperature and heat flux (named "Robin BC") (Bruch Jr and Zyvoloski 1974, Lunardini and Varotta 1981). In this thesis, I mainly evaluated the performance of different approaches to obtain the TBCs, instead of discussing the deviations caused by the different TBC types (i.e., Dirichlet, Neumann, and Robin BCs), which has been documented in previous references (e.g., Miller 1979, Hansson et al., 2004, Qin et al., 2012, Roux et al., 2017). The approaches of determination of the heat transfer at the ground surface can be mainly classified into five categories: 1) analytical analysis method; 2) regionally calibrated empirical equations, including n-factor and adherent-layer theory methods; 3) regression analysis approach; 4) surface heat transfer layer, and 5) surface energy balance (SEB) model.

2.3.1. Analytical analysis method

As a first order approximation, the highest order of derivative in the series expansion (Yotsukura et al., 1973), AT variations can be considered as a sinusoidal oscillation with a period of one year (Carson 1963), shown in Eq. (2.1). Similarly, when the atmospheric heat is transferred by conduction, soil temperature follows an analogous behaviour (Carson 1963), although the decay of the amplitude of oscillation and its phase lag increase with depth, due to heat diffusion into the ground (Smith and Riseborough 1983, Smerdon et al., 2003). The soil temperature at a depth of z_g can be described as (Beltrami 1996):

$$T_a = T_0 + A_a \times \sin\left(\frac{2\pi}{365}t + \varphi\right) \tag{2.1}$$

$$T_g = A_g \frac{T_a}{A_a}\cos\left(-d_g\sqrt{\frac{\pi}{\lambda_g t_p}} - d_s\sqrt{\frac{\pi}{\lambda_s t_p}}\right) + A_g\sqrt{1-\left(\frac{T_a}{A_a}\right)^2}\sin\left(-d_g\sqrt{\frac{\pi}{\lambda_g t_p}} - d_s\sqrt{\frac{\pi}{\lambda_s t_p}}\right) \tag{2.2}$$

where subscripts of a, g, and s illustrate that air, ground, and snow, respectively; T_0 is MAAT (°C); φ is the phase shift (radian); A is the mean amplitude of temperature (°C); λ is the thermal diffusivity (m²·s⁻¹); t_p is the period of oscillation and of the ground (days); d_g and d_{snow} refer to the ground depth (positive downwards) (m) and snow thickness (m), respectively. Details about how

to derive the Eq. (2.2) and impacts of snow cover were documented in Beltrami (1996).In addition, the effects of land surface processes related to snow cover, soil freezing, and vegetation have been quantitatively analyzed (Smerdon et al., 2009, Hu et al., 2017).

Broadly, Eq. (2.2), an ellipse equation, represents a phase-space relation between the AT and the ground temperature, termed thermal orbits. As neglecting the non-conductive heat transfer, thermal orbits vary as a function of depths (z_g) and thermal diffusivity (k_s) (Beltrami 1996, 2001). Also, Luethi et al., (2016) adopted this approach to detect the thermal impact of snowmelt and rainfall infiltration.

2.3.2. Empirical equations

2.3.2.1. N-factor method

The n-factor method presents an empirical relation between the AT and ground surface temperature (GST) (Carlson 1952, Lunardini 1978, Klene et al., 2001). It has been used for more than 60 years in engineering studies (e.g., Lunardini 1978, Fortier et al., 2011, Zottola et al., 2012, Richard et al., 2015, O'Neill and Burn 2017), predictions of permafrost distribution (e.g., Nishimura et al., 2009), and hydrological research (e.g., Hayashi et al., 2007, Walvoord et al., 2019) to parameterize the temperature regime at the ground surface (Klene et al., 2001). The n-factor acts as an empirical alternative to account the influence of local factors (e.g., vegetation, snow, asphalt pavement) to the energy balance (Carlson 1952, Loranty et al., 2018). The thawing n-factor (n_t) is calculated by a ratio of the positive degree-day sum at the soil surface to that in the air, while the freezing n-factor (n_f) is a ratio of the negative degree-day sum at the soil surface to that in the air (Lunardini 1978, Riseborough et al., 2008). The GSTs are obtained using AT multiplied by the n-factor, expressed as:

$$T_g = \begin{cases} n_t \times T_a \;=\; TDD_g \big/ TDD_a \times T_a \\[2em] n_f \times T_a \;=\; FDD_g \big/ FDD_a \times T_a \end{cases} \qquad (2.3)$$

where TDD and FDD are the sums of thawing degree-day and freezing degree-day (°C days), respectively; the subscripts of g and a are for the ground and air, respectively. Klene et al., (2001)

and Karunaratne and Burn (2004) used the GST to divide the freezing and thawing seasons. However, in order to better investigate the impact of snow cover, Hinkel et al., (2008) and Lewkowicz et al., (2012) suggested to determine the start and end of the freezing and thawing seasons independently for the air and ground surface.

Table 2.1. Typical values of thawing and freezing factors for different surface cover types

	Thawing factor (n_t)	Freezing factor (n_f)	Reference
Asphalt surface	$2^{[2]}$ - $3^{[2]}$	$0.84^{[1], [3]}$ - $1.03^{[3]}$	[1] Carlson (1952);
Low-stature vegetation surface	$0.79^{[5]}$ - $0.98^{[5]}$	$0.2^{[5]}$ - $0.7^{[4]}$	[2] Lunardini (1978); [3] Berg (1985); [4] Hinkel et al., (2008);
Bare gravel/sand surface	$1.22^{[3]}$ - $1.53^{[3]}$	$0.62^{[1]}$ - $0.76^{[1]}$	[5] Way and Lewkowicz (2018);
Snow-covered surface	-	$0.2^{[5]}$ - $0.7^{[4]}$	

Note: the freezing factors of asphalt-paved surface and the bare gravel/sand surface are measured at specific sites, manually removing snow.

Additionally, the values of n_t and n_f differ greatly for the different surface cover types (Lunardini 1978, Riseborough et al., 2008, Throop et al., 2012). Broadly, the closer the values of n_t or n_f to 1.0, the similar the AT and GST. In contrast, the larger n_t and smaller n_f represent the greater buffering effect between the surface and the overlying atmosphere (Taylor, 1995). For example, dark asphalt absorbs more solar energy than most natural surfaces and thus yields high empirical thawing n-factor, usually between 2 to 3 (Lunardini 1978). While the snow layer impedes the heat loss in winter and produces low empirical freezing n-factor, usually between 0.2 to 0.7 (Klene et al., 2001, Way and Lewkowicz 2018). The typical values for the different surface cover types are detailed in Table 2.1.

2.3.2.2. Adherent-layer theory method

To simplify the BCs and represent the complex heat transfer at the surface, the annual surface temperature can be approximated by a sinusoidal function (Carson 1963) and the daily variations

of soil temperature are neglected with the boundary layer theory (Zhu 1988, Zhu et al., 1996), shown in the Figure 2.6.
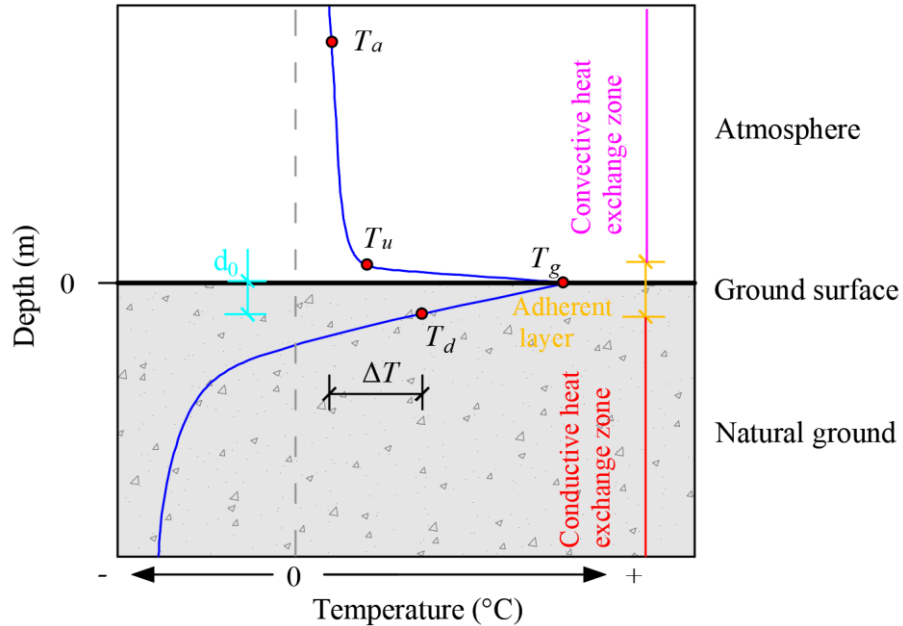
Figure 2.6. Schematic of the adherent layer theory method, modified from Zhu et al., (1996).

The adherent-layer theory demonstrates that the soil temperature (T_d) at a certain depth, defined as lower adherent layer thickness (d_0), is mainly affected by heat conduction, while impacts of non-conductive heat transfers (e.g., solar radiation and wind convection) can be neglected (Zhu et al., 1996, Bai et al., 2015, Zhang et al., 2017b). The values of d_0 are about 15 cm for the moist fine silt and clay, while about 20 cm for dry coarse sand, respectively (Zhu, 1988). The adherent-layer approach has been substantially used to predict the thermal regime of transport infrastructure (e.g., Lai et al., 2003, Chen et al., 2017b). The GST can be expressed as:

$$T_g = T_0 + \Delta T + A\sin\left(\frac{2\pi}{365}t + \varphi\right) + \varsigma_a \times t \tag{2.4}$$

where T_0 is the MAAT (°C), ΔT is the surface offset (°C) based on the boundary layer theory (Zhu, 1988), ς_a is the rate of AT increase due to climate change (°C·a^{-1}), A is the seasonal temperature amplitude (°C), t is the time (hour), and φ is the phase shift (radian).

A surface offset (ΔT) is adopted to represent the difference in absorbed shortwave radiation at different surface cover types. Based on the field observation in the QTP, the mean annual GST of

21

gravel/sand surface is 2.9 °C to 3.7 °C higher than AT, while the corresponding value for asphalt pavement is 4.2 °C to 6.8 °C greater, respectively (Zhang et al., 2017c; Zhu, 1988). Alternatively, Chou et al., (2008) presented an alternative way to calculate surface offset with incoming solar radiation, while Bai et al., (2015) and Tai et al., (2020) took into account effects of incoming solar radiation, thermal diffusivity and the heat-transfer coefficient of wind convection. The effects of sunny and shaded slope on the GST are considered with the azimuth angle of the sun, the slope angle and strike angle of embankment subgrade (Chou et al., 2008, Tai et al., 2020). The typical values of adherent layer thickness and surface offset are listed in Table 2.2.

Table 2.2. Adherent layer thickness and surface offset for different surface cover types obtained by adherent-layer theory

	Lower adherent layer thickness (m)	Surface offset (°C)	References
Moist fine soil surface	0.15[1]	2.0[1]	[1] Zhu, (1988);
Dry coarse soil surface	0.20[1]	2.9[1] - 4.0[5]	[2] Niu et al., (2008);
Vegetated surface	0.31[3]	2.2[3] - 2.5[2]	[3] Bai et al., (2015);
Concrete surface	-	4.7[1]	[4] Zhang et al., (2017b);
Asphalt surface	0.39[3] - 0.47[5]	4.2[4] - 6.8[4]	[5] Tai et al., (2020);

2.3.3. Regression analysis approach

Regression analysis is an alternative way to investigate the relationship between a dependent (i.e., T_g) and independent variables (e.g., T_a, snow depth, moisture, surface albedo, etc.), including linear regression (e.g., Gold 1967, Berg 1985, Shen 1988, Niu et al., 2008) and multiple linear regression (e.g., Gao and Stefan 1999, Qiu et al., 2003, Zhang et al., 2012, Park et al., 2018, Zhang et al., 2019). Gold (1967) demonstrated a linear relationship between the average monthly temperature and monthly totals of absorbed shortwave radiation. Similarly, Berg (1985) demonstrated that the average daily pavement surface temperature is related to the daily quantity of absorbed short-wave radiation and developed a family of lines for different wind speeds. Recently, Zhang et al., (2012) adopted a multiple linear regression method to obtain the

GST for different surface cover types, based on the outputs of regional climate models. The linear relationship relating the difference (ΔT) between air and surface temperature to absorbed short-wave radiation is expressed as (Gold 1967):

$$\Delta T = T_s - T_a = a + b \times \left(Q_{SW}^{in} - Q_{SW}^{out}\right)$$ (2.5)

where T_s and T_a represent the average daily GST and AT (°C), respectively; $Q_{SW}^{in} - Q_{SW}^{out}$ illustrates the total daily absorbed shortwave radiation (W·m^{-2}); while a and b are the regression coefficients (Berg 1974).

The multiple linear regression model is expressed by linear combination of more than two independent variables:

$$T_g = \beta_0 + \sum_{i=1}^{m} \beta_i x_i + \varepsilon_0$$ (2.6)

where, x illustrates the explanatory independent variables (e.g., AT, moisture, soil temperature at depth, maximum snow depth); β are the values of regression constant and coefficients; ε_0 is the corresponding random error; m is the number of independent variables. Alternatively, the coefficients (β_i) are estimated by the ordinary least square method, which finds the solution to minimize the residual sum of squares. Three types of hypothesis tests can be carried out for multiple linear regression models to determine whether the random error term (ε) is normally and independently distributed with a mean of zero and variance. The three hypothesis tests refer to (1) test for significance of regression; (2) t test, which checks the significance of individual regression coefficients (Zhang et al., 2012); and (3) F test, which examines the significance of a number of regression coefficients (Gao and Stefan 1999).

2.3.4. Surface heat transfer layer

To include the simulated ground temperature, Molson et al., (1992) developed a conceptual heat exchange layer to calculate a temperature-dependent ground heat flux (W·m^{-2}), which can be described as:

$$J_i = \gamma \left(T_a - T_g\right) + \left(q_w \cdot c_w \cdot \rho_w\right) \times \left(T_w - T_g\right) + J_A$$ (2.7)

where γ is heat exchange coefficient ($J·m^{-2}·s^{-1}·K^{-1}$), determined by the thermal conductivity and thickness of a conceptual surface heat transfer layer; T_a is the measured AT (°C); T_g is the simulated GST (°C), T_w is the temperature of the infiltrated water(°C); and J_A is a supplementary heat flux term ($W·m^{-2}$), representing net solar radiation (i.e., incoming solar radiation minus outgoing solar radiation) and evaporative heat loss(Ghias et al., 2017, Dagenais et al., 2020).

For the conceptual surface heat transfer layer, the calibrated value of the heat flux term (J_A) allows to consider the insulation/reflection effects of snow cover (Ghias et al., 2017, Dagenais et al., 2020). The heat exchange coefficient (γ) and calibrated heat flux (J_A) are typically determined through model calibration, while the corresponding value of J_A varies from about 3 to 30 $W·m^{-2}$ (Dagenais et al., 2020). Similarly, McKenzie et al., (2007b) used a specified AT with an underlying thermal boundary layer to obtain the specified GST. A heat transfer coefficient, defined as ratio of the surface-layer thermal conductivity and its thickness, was used to represent the effect of vegetation, which has been used in other cryohydrogeological modelling (e.g., Evans and Ge 2017, Lamontagne-Hallé et al., 2018). Additionally, Šimůnek et al., (1998) presented a similar approach to obtain a variable heat flux BC at the top surface, determined by a heat transfer coefficient multiplied with the temperature difference (Hansson et al., 2004).

2.3.5. Surface energy balance model

In order to consider the meteorological measurements, SEB models were proposed to implicitly calculate the energy fluxes and GSTs for different surface cover types by numerically solving the heat equations at the ground surface (Idso et al., 1975, Walter et al., 2005, Herb et al., 2008). The SEB model was driven by meteorological data and was solved iteratively for the surface temperature using the Newton-Raphson method (Hwang 1976). Generally, the near-surface energy balance is an integration of the effects of seasonal snow cover, soil properties, surface cover types, atmospheric temperature, slope aspect and angle (Zhang et al., 2003, Westermann et al., 2009, Yao et al., 2011, Glose et al., 2017). The SEB model requires an extensive amount of input data describing meteorological conditions, ground surface characteristics (e.g., surface albedo, emissivity and roughness), and subsurface soil temperatures (Hwang 1976, McFadden et al., 1998, Mittaz et al., 2000). The data set of meteorological variables includes AT, dew-point

temperature, cloud cover, wind speed, precipitation of snow and rainfall, and incoming solar radiation (Hoelzle et al., 2001, Pomeroy et al., 2007, Jensen and Allen 2016). Additionally, to include the subsurface processes, a combined model fully integrating the SEB model and heat conduction was developed to quantify impacts of snow cover layer on ground temperatures (Hwang 1976, Ling and Zhang 2003). The energy exchange between the ground surface and atmosphere is expressed as:

$$Q_{SW}^{in} - Q_{SW}^{out} + Q_{LW}^{in} - Q_{LW}^{out} + Q_p - Q_h - Q_v = Q_0 + Q_c \tag{2.8}$$

where Q_{SW}^{in}, Q_{SW}^{out}, Q_{LW}^{in}, and Q_{LW}^{out} represent incoming solar radiation, outgoing solar radiation, incoming long-wave radiation, and outgoing long-wave radiation (W·m^{-2}), respectively; the Q_h, Q_v, and Q_p illustrate sensible heat flux, heat flux of vapor exchange from the surface, and rainfall heat (W·m^{-2}), respectively; the Q_c and Q_0 are for the ground heat flux through the snow cover and ground, and the stored energy (W·m^{-2}) in the snowpack and the subsurface layer, respectively.

For a road embankment, the SEB model was firstly used to determine ground temperature and energy components of a paved surface of a road embankment (Berg 1974). The energy balance was restricted to a vertical dimension with neglecting the subsurface processes, snow regime variations, and the lateral heat transfer (Berg 1974). This approach has been extensively used for determination of daily maximum and minimum temperatures of the pavements (e.g., Solaimanian and Kennedy 1993, Hermansson 2004, Hall et al., 2011, Qin and Hiller 2014). In the regions without seasonal snowpack or where the snowpack is manually removed (e.g., pavement centerline), ground heat flux (Q_c) can be simplified by a percentage of absorbed solar radiation (Berg 1985, Dumais and Doré 2016) and maximum of daily pavement surface temperature linearly increases with solar absorption (Qin et al., 2017b). Additionally, Miller (1979) presented a SEB model integrated with a two-dimensional geothermal simulator to investigate thermal regime of Arctic and sub-Arctic embankments. Furthermore, Solaimanian and Kennedy (1993) estimated the sensitivity of pavement surface to the change of sub-soil thermal properties (e.g., thermal conductivity and heat capacity) and surface properties (e.g., albedo, emissivity). Also,

effects of color and texture on the surface temperature of an asphalt pavement has been investigated using SEB models (Berg 1985, Hall et al., 2011, Dumais and Doré 2016).

2.3.6. Limitation of previously employed thermal boundary conditions

Analytical analysis method can provide reliable soil temperatures at different depths for a homogenous material with simple TBCs, but its implication for a road embankment may lead to uncertain or even misleading results due to the multi-dimensional thermal processes. Furthermore, empirical relations and linear regression approaches (e.g., Berg 1974, Zhang et al., 2012) require a limited need for the input data, can produce quite reliable GSTs if well calibrated locally or regionally, and are easily employed as TBCs in a geothermal model. Similarly, the approach of surface heat transfer layer requires only several forcing variables to obtain GSTs and can easily be coupled with another thermal simulator, but the accuracy of prediction of GST is highly related to calibrated heat flux or calibrated heat transfer coefficient (e.g., Ghias et al., 2017, Dagenais et al., 2020, McKenzie et al., 2007b). Briefly, either empirical coefficients or fitting parameters are primarily applicable to specific areas and may be problematic for the determination of the surface thermal processes in other sites with different climate conditions or the prediction of the GSTs in a changing climate. More importantly, these approaches simply interrelate the air and ground temperature without considering individual energy transfer processes. Subsequently, to assess the geothermal response to climate change, the warming trend of ground surface is simplified by a linearly increasing rate of GST without the inter-annual and decadal variations. This assumption of the linearly increasing rate has been widely used in many studies on thermal stability of roads (e.g., Lai et al., 2003, Chen et al., 2017b), spatiotemporal changes of permafrost (e.g., Nishimura et al., 2009, Sheng et al., 2020), and hydrological processes (e.g., Bense et al., 2009, Kurylyk et al., 2015). The approach of linear increasing rate is easily applied, but it does not represent well the projected climate change (Chen et al., 2018) and may be problematic for prediction of geothermal and hydrological processes in long-term climate warming scenarios with either the change and shift of winter and summer precipitation, or the change of land surface processes.

Conversely, the SEB model can improve accuracy and versatility of TBCs by fully coupling nonlinear surface heat transfer effect and subsurface thermal processes (Miller 1979, Jordan 1991, Walter et al., 2005), including the effects of snow insulation, vegetation buffer effect, turbulent convection by wind, rainfall heat, solar radiation, and impact of subsurface water flow (Ling and Zhang 2004, Herb et al., 2008). Additionally, the SEB model can be fully integrated into another geothermal simulators to easily quantify the effects of various surface disturbances (McFadden et al., 1998, Herb et al., 2008) and allow the engineer to directly represent the configuration design in the model (Miller 1979, Dumais and Doré 2016). Although a full treatment of the SEB model requires extensive parameterization data to estimate the surface energy components at a specific site (McFadden et al., 1998, Hoelzle et al., 2001, Walter et al., 2005), the collection of meteorological data in recent decades enables us to develop, calibrate and validate a SEB model (e.g., Boike et al., 2019, Fortier and Chen 2020b).

For the cold-regions transportation infrastructure, knowledge gaps still exist in examining how the atmospheric energy enters the permafrost layer through the embankment subbase and subgrade. Firstly, the employed methods negate the thermal effect of surface water infiltration and the effect of subsurface processes on the surface temperatures. When a road embankment is built on the slope, there is commonly significant subsurface water flow beneath the embankments, which greatly influences the magnitude and rate of GST change. Secondly, although the snow insulation effect has been investigated by geothermal models by either alternative factor (e.g., Lunardini 1978, Fortier et al., 2011) or calibrated heat flux (e.g., Ghias et al., 2017, Dagenais et al., 2020), the impacts of snow depth, timing, and duration, and snowpack characteristics on the thermal regime of a road embankment have not been studied methodically. Thirdly, the previously employed TBCs were mainly restricted to the vertical dimension and addressed the vertical heat exchange with the atmosphere (Lunardini 1978, Zhu 1988, Hermansson 2004, Zhang et al., 2012, Dumais and Doré 2016). These approaches neglect the impact of lateral ground heat flux induced by asymmetric geometry (e.g., road embankment built on slope) or uneven surface disturbance (e.g., preferential snow accumulation). These employed approaches are not suitable for understanding multi-dimensional thermal processes of a road embankment. In the context of emerging scientific and societal questions related to permafrost

thaw and thermal stability of cold-regions transportation infrastructure, there is a need to fully integrate the SEB model into a geothermal model to include the surface and subsurface thermal processes and to quantify the vertical and lateral ground heat fluxes through the embankment subbase and subgrade.

2.4. FUNDAMENTAL HEAT TRANSFER PROCESSES IN SOILS

Permafrost is highly susceptible to external thermal changes (Smith and Riseborough 1983, Romanovsky and Osterkamp 1995). The thermal state of permafrost is mainly determined by the amount of energy entering permafrost bodies (Roth and Boike 2001, Romanovsky et al., 2010). In general, processes of heat transfer in the subsurface layer can be divided into three categories: conduction, convection, and radiation. Firstly, the rate of heat conduction through a material is proportional to the negative gradient in the temperature (Fourier 1822). Furthermore, heat convection entails the concurrent migration of both mass (either liquid water or water vapor) and energy (either sensible or latent heat) (Philip and De Vries 1957, Hinkel and Outcalt 1993). The amount of heat advected by mobile water in soils is a function of flow rate, porosity of soil media, and temperature difference between the water flow and the surrounding soils (Lu and Ge 1996, Kurylyk et al., 2016). Moreover, radiation is typically considered negligible because only at high temperatures (e.g., 600 °C) radiation can be significant in groundwater flow and heat transport studies (Ingebritsen and Sanford 1999).

In the active layer, heat transfer is complicated, including the heat conduction of soil particles and ice (Lunardini and Varotta 1981), the heat advection associated with the air flow and the mobile water flow, either in the liquid or in the vapor phase (Philip and De Vries 1957, Hinkel and Outcalt 1993, Hinkel and Nelson 2001), and the latent heat, which is the energy stored or released without change of soil's temperature over an extended period, named the zero-curtain period (Cook, 1955, van Everdingen, 1988). Additionally, in the permafrost zone, the heat transfer is primarily dominated by conductive heat transfer due to the low permeability of frozen soils (French 2017). Generally, the heat transfer models to estimate the subsurface thermal processes can be classified into two groups: 1) pure heat conduction, and 2) conductive and convective (heat advection) heat transfers.

2.4.1. Heat conduction

When lateral subsurface water flow is insignificant, the effect of heat advection triggered by water flow can be negligible, since the conductive heat transfer is two to three orders of magnitude greater (Taylor and Luthin 1978, Nixon 1991), or Peclet number much smaller than 1 (Putkonen 1998). When the mass (either liquid water or water vapor) transport processes is neglected, heat transport is predominantly conductive, described by the classic Fourier's Law (Fourier 1822). The subsurface thermal regime is mainly controlled by a combination of the GST variations and heat flow from the interior of the earth (Kelvin 1861, Gold and Lachenbruch 1973). The analytical and numerical analyses are employed to solve for the temperature distribution in heat-conduction problems with or without the phase change (Bruch Jr and Zyvoloski 1974, Comini et al., 1974). The conductive heat flux is calculated by:

$$q_c = -\lambda \nabla T \tag{2.9}$$

where, λ is the thermal conductivity (W·m^{-1}·K^{-1}), and ∇T is the temperature gradient (K·m^{-1}).

The typical analytical solutions for the one-dimensional conduction problem, including Neumann and Stefan problem, is only reasonable for a homogenous material with simple TBCs (Carslaw and Jaeger 1959, Cho and Sunderland 1969, Lunardini and Varotta 1981). The Stefan problem is a special case of the Neumann problem, when the temperature of a liquid is equal to the temperature of its environment. Stefan's equation is adopted to calculate thaw depth under a certain condition where no mobile water flow occurs (Lunardini and Varotta 1981). Neumann solution for the movement of a freezing front considers only two zones: a frozen and a thawed zone, while Lunardini solution divides this problem into three zones: fully frozen zone with only the residual amount of unfrozen water; mushy zone with both ice and water; and fully thawed zone (Lunardini and Varotta 1981). These exact analytical solutions for the one-dimensional heat propagation in a porous medium with time are widely used to test the accuracy of numerical simulations (e.g., Shen 1988, Romanovsky et al., 1997, McKenzie et al., 2007b, Tan et al., 2013).

Additionally, to involve complicated time dependent TBCs and non-linear physical properties, transient heat conduction problems are solved iteratively to obtain the soil temperatures (Comini et al., 1974, Shen 1988, Krabbenhoft et al., 2007). These heat conduction models are used to

simulate the thermal response of permafrost beneath transportation infrastructure to climate change (e.g., Shen 1988, Wu et al., 2006, Fortier et al., 2011, O'Neill and Burn 2017, Chen et al., 2018), as well as the heat exchange among the atmosphere-thermosyphon-embankment system in permafrost regions (e.g., Zhang et al., 2011, Ma et al., 2012, Chen et al., 2017b).

2.4.2. Conductive and convective heat transfer

Water movement in variably saturated soil is proportional to the hydraulic conductivity and hydraulic gradient (Van Dam and Feddes 2000, Šimůnek et al., 2005), and can be expressed by a general form of Darcy's law, which is proposed by Richards (1931). The Darcy flux (q_w) is calculated as follows:

$$q_w = -K(\psi)\nabla\psi \tag{2.10}$$

where $K(\psi)$ is the unsaturated hydraulic conductivity function, which also strongly depends on the water potential and properties of the porous media, while ψ is the total hydraulic head (m).

Water flow in soil is driven by the total hydraulic head (ψ), which mainly consists of the matrix potential (ψ_m , which results from capillary forces), gravitational potential (ψ_g), the pressure head (ψ_p), osmotic forces (ψ_s), and temperature potential (ψ_T) (Alvarez-Benedi and Munoz-Carpena 2004).

$$\psi = \psi_g + \psi_p + \psi_m + \psi_s + \psi_T \tag{2.11}$$

2.4.2.1. Heat transfer and water flow in unsaturated soils

When unsaturated soils are subjected to freezing-thawing processes, the driving force of moisture migration is composed of three components, including the ground temperature gradient (ψ_T), gradient of matric potential (ψ_g) and the gravity (ψ_m) (Philip and De Vries 1957, Harlan 1973, Taylor and Luthin 1978, Bronfenbrener 2009, Li et al., 2014). Philip and De Vries (1957) presented the mathematical equations of moisture movement in porous materials under a temperature gradient (ψ_T), including impacts of liquid water, water and air vapor flows, but neglecting the cytostatic pressure effects. Simultaneously, the ground temperature gradient (ψ_T)

can drive liquid water towards the freezing zone and promote formation of ice lenses at the freezing front (Thomas et al., 2009, Lai et al., 2014), which is not included in this thesis.

Furthermore, in the fully thawed zone, the unfrozen water content and hydraulic conductivity are highly nonlinear functions of the pressure head (Van Genuchten 1980). The soil volumetric moisture content and suction heat are related by the soil-water characteristic (soil moisture retention) curve (Williams 1964, Fredlund and Xing 1994). The shape of the nonlinear relationship greatly depends on the soil texture and soil pore size distribution (Alvarez-Benedi and Munoz-Carpena 2004), which can be presented by the commonly used models, such as Brooks and Corey (1966) and Van Genuchten (1980). Additionally, when the soils experience the freezing process, the unfrozen water content is determined by the soil-freezing curve (i.e., the relationship between the water saturation and temperature), including piecewise linear function (McKenzie et al., 2007b), exponential function (McKenzie et al., 2007b, Ghias et al., 2017), and power function (Lovell Jr 1957, Osterkamp and Romanovsky 1997). In the completely frozen zone, only residual unfrozen water exists.

Alternatively, the convective heat transport by water vapor and the latent heat of vaporization can alter the thermal regime of the shallow unsaturated zone (Kane et al., 2001, Saito et al., 2006). Water vapor movement is typically induced by thermal, pressure or osmotic gradients (Kane and Stein 1983, Kane et al., 2001, Saito et al., 2006). According to Fick's law, the rate of water vapor flow is proportional to the isothermal and thermal vapor flux densities (Noborio et al., 1996, Jiang et al., 2012). Zhang et al., (2016a) demonstrated via numerical simulation that the water vapor contributes to approximately 15 % of the water flux at the Beiluhe area in the QTP. Furthermore, the air flow in soils is not normally a significant thermal process, except in certain weather conditions (Saito et al., 2006, Zhang et al., 2016a). For example, after intense rainfall event, neglecting the soil airflow can cause an underestimation of evaporation by 33.3 % in the high permeability (2×10^{-3} m·s^{-1}) soil, and 53.3 % in the low-permeability (7.9×10^{-4} m·s^{-1}) soil (Zeng et al., 2011). However, over a year, the amount of heat advected by liquid water and water vapor, and the latent heat of water vapor diffusion only accounted for less than 5 % of the total ground heat flux from near (5 cm) surface to the depth of 2.2 m (Zhang et al., 2016a). For a road embankment, the energy fluxes contributed by water vapor and air flow are considered negligible

due to the low water content and low water storage capacity of the embankment fill (Doré and Mercier 2008).

2.4.2.2. Heat transfer and water flow in saturated soils

In saturated soils, the subsurface water flow is typically driven by the hydraulic gradient and density gradient (Voss and Provost 2010). The sediment compaction ($\psi_p = 0$) and free convection induced by water density gradients is usually neglected (Deming et al., 1992). Because the free convection due to buoyancy-induced motion of fluids is not an important heat-transfer mechanism in the active layer (Kane et al., 2001).

In cold regions, subsurface water flow can trigger heat advection, modify subsurface temperature (Bullard 1939, Lu and Ge 1996, Bense and Beltrami 2007), and accelerate permafrost thawing and warming in terms of magnitude and rate, compared to the scenario without water flow (McKenzie et al., 2007b, Jiang et al., 2012, Paquette et al., 2018). Rowland et al., (2011) compared two scenarios with and without near surface sub-permafrost groundwater flow by the ARCHY model, which indicates that stable permafrost thicknesses are two to five times greater in the absence of groundwater flow. Ge et al., (2011) illustrated through numerical simulation by SUTRA-ice code that heat advection triggered by subsurface water flow deepens the active layer thickness by a factor of three within 40 years, compared to the case without water flow. McKenzie and Voss (2013) presented via the SUTRA-ice code that advective heat transport could reduce the time to complete permafrost degradation by one-third compared to a situation without heat advection. Recently, based on the field observation at the Umiujaq, Nunavik, Canada, Dagenais et al., (2020) illustrated via the HEATFLOW/SMOKER code that groundwater flow transports warm water into the sub-permafrost aquifer and enhances permafrost thaw at a fast rate of 0.8 m·a^{-1}. Conversely, Kane et al., (1991) demonstrated that the 2 °C surface warming results in gradual increase (0.0044 m·a^{-1}, from 50 cm to 72 cm in 50 years) of the active layer thickness, consisting of 10 cm organic soil overlying mineral soils in Arctic-Alaska regions. Similarly, Sheng et al., (2020) presented that the projected permafrost thawing rate induced by atmospheric warming is about 0.14 m·a^{-1} from 2030 to 2050 under the scenario of RCP6.0 (AT

increasing rate of 0.023 °C·a^{-1}) in the Headwater Area of the Yellow River at the QTP, Western China.

For a linear transportation infrastructure, road alignment commonly intercepts the local drainage network, conceptually shown in Figure 2.7. Subsurface water flow beneath a road embankment has a detrimental effect on permafrost degradation. de Grandpré et al., (2012) demonstrated through short-term observation on the Alaska Highway that subsurface water flow in the thawed layer beneath a road embankment can trigger heat advection and enhance permafrost degradation. Périer et al., (2014) found through numerical simulation that water flow through the culvert (i.e., a pipe that allows water to flow under a road) warms the soil temperature in summer, although the rising magnitude is related to the temperature and rate of water flow. Zhang et al., (2017a) simulated the thermal regime of a riverbank built on ice-rich permafrost, indicating that water seepages increase permafrost thaw. Mu et al., (2020b) illustrated via long-term observation on Qinghai-Tibet Railway that water ponding adversely affects the cooling effect of the crushed-rock embankment. Similarly, subsurface water flow adversely affects thermal stability of a buried oil pipeline (e.g., Yu et al., 2014, Wang et al., 2016a, Wang et al., 2018a) and the foundation of a power transmission line tower (e.g., You et al., 2016) in permafrost regions. But the quantification of the heat advection caused by subsurface water flow remains largely unknown due to the uncertainty of water flow direction and rate, and thermal and moisture state of the media. To better understand the role of subsurface water flow on permafrost thaw, it is crucial to build a fully coupled heat transfer and water flow model to investigate and quantify the amount of energy advected by subsurface water flow.
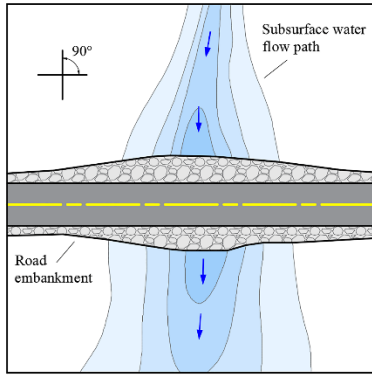
(a) Road embankemnt perpendicularly intercepting local drainage network
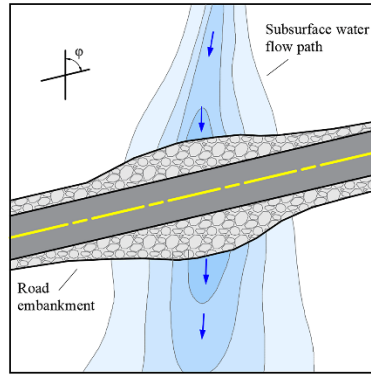
(b) Road embankemnt obliquely intercepting local drainage network
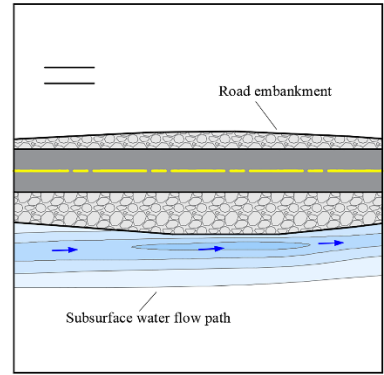
(c) Road embankemnt parallel to subsurface water flow path

Figure 2.7. Road alignment intercepting the local drainage network; (a) perpendicularly; (b) obliquely; and (c) parallelly.

Chapter 3 - IMPACT OF HEAT ADVECTION ON THE THERMAL REGIME OF ROADS BUILT ON PERMAFROST

Authors: Lin Chen, Daniel Fortier, Jeffrey M. McKenzie & Michel Sliger

CRediT author statement

Lin Chen: Conceptualization, Methodology, Field survey, Writing- Original draft preparation.

Daniel Fortier: Supervision, Field survey, Reviewing and Editing.

Jeffrey M. McKenzie: Supervision, Reviewing and Editing.

Sliger Michel: Field survey, Reviewing and Editing.

ABSTRACT

In northern regions, transportation infrastructure can experience severe structural damages due to permafrost degradation. Water infiltration and subsurface water flow under an embankment affect the energy balance of roadways and underlying permafrost. However, the quantification of the processes controlling these changes and a detailed investigation of their thermal impacts remain largely unknown due to a lack of available long-term embankment temperature data in permafrost regions. Here, we report observations of heat advection linked to surface water infiltration and subsurface flow based on nine years (from 2009 to 2017) of thermal monitoring at an experimental road test-site built on ice-rich permafrost conditions in southwestern Yukon, Canada. Our results show that snowmelt water infiltration in the spring rapidly increases temperature in the upper portion of the embankment. The earlier disappearance of snow

deposited at the embankment slope increases the thawing period duration and the temperature gradient in the embankment compared to the natural ground. Infiltrated summer rainfall water lowered the near-surface temperatures and subsequently warmed embankment fill materials down to 3.6 m depth. Heat advection caused by the flow of subsurface water, produced warming rates at depth in the embankment subgrade up to two orders of magnitude faster than by atmospheric warming (heat conduction). Subsurface water flow promoted permafrost thawing under the road embankment and led to an increase in active layer thickness. We conclude that the thermal stability of roadways along the Alaska Highway corridor is not maintainable in situations where water is flowing under the infrastructure unless mitigation techniques are used. Severe structural damages to the highway embankment are expected to occur in the next decade.

GRAPHICAL ABSTRACT
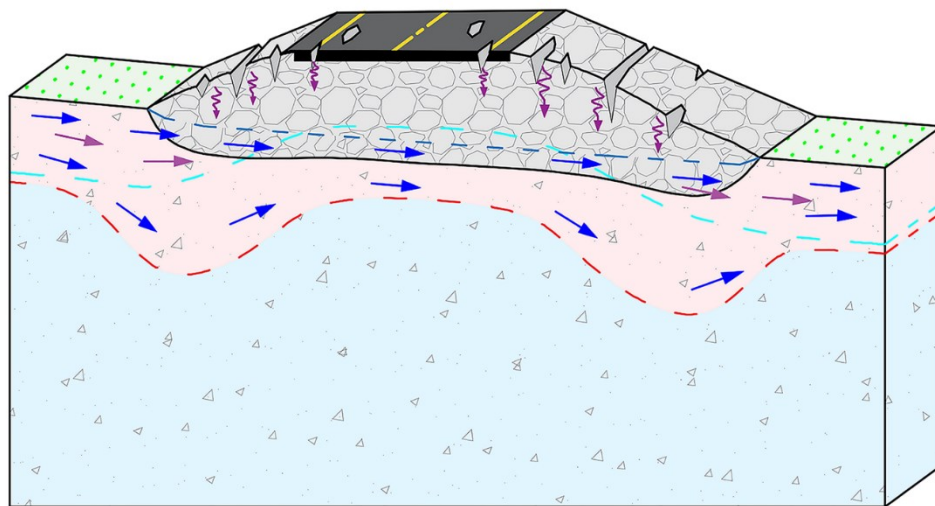
▬	Asphalt pavement	– – –	Initial interface between natural ground and embankment
▨	Embankment fill	– – –	Initial permafrost table
▨	Active layer	– – –	Permafrost table
▨	Permafrost	→	Initial suburface water flow
▨	Ground surface	→	Suburface water flow
▨	Potholes and fissures	↯	Surface water infiltration

Our manuscript presents three important novel findings:

1) The infiltration of spring snowmelt causes a very rapid temperature increase in the road embankment, within just a few days.

2) The infiltration of summer rainfall lowers near-surface temperatures, while simultaneously warming embankment fill materials at depth.

3) The advection of heat due to pore water flow through subsurface water flow leads to warming rates that can be up to two orders of magnitude faster than by just atmospheric warming.

3.1. INTRODUCTION

In northern regions, transportation infrastructure experiences severe structural damage due to the degradation of the underlying permafrost (Hjort et al., 2018), leading to large increases in maintenance costs and reductions in the lifespan of road embankments (Cheng 2005a, Reimchen et al., 2009). The temperatures within a road embankment's subbase (i.e., a layer of fill material) and subgrade (i.e., native material under an embankment) are a function of air temperature, solar radiation, turbulent flux of latent and sensible heat, and heat conduction through the embankment material (Hall et al., 2011, Dumais and Doré 2016, Zhang et al., 2017b). The thermal regime of infrastructure can be modified and cooled by mitigation techniques used in or on the embankment (Goering and Kumar 1996, Lai et al., 2003, Doré et al., 2016, Chen et al., 2018). Water infiltration and subsurface water flow through and under an embankment can also alter the thermal regime of roadways (de Grandpré et al., 2012, Zottola et al., 2012, Fortier et al., 2016). An unanswered but important question in the field of permafrost transportation engineering is understanding how the thermal regime of embankments, with porous aggregate and macropores, are affected by not only heat conduction but also heat advection through surface water infiltration and subsurface flow.

Observations of ground temperatures show that the infiltration of snowmelt and rainfall alters soil temperatures in Arctic and sub-Arctic regions (Hinkel et al., 2001, Kane et al., 2001, Luethi et al., 2016) and on the Qinghai-Tibet Plateau (QTP) (Wen et al., 2014, Zhang et al., 2016a, Liu et al., 2019). In the spring, snowmelt water infiltration causes a rapid temperature increase of the upper portion of the ground (Hinkel et al., 2001, Kane et al., 2001). In late summer, rainfall infiltration is effective in transferring sensible heat to depth and may warm or cool soils by several degrees (Hinkel and Outcalt 1994, Hinkel et al., 1997, Kane et al., 2001, Westermann et al., 2011, Wen et al., 2014, Sjöberg et al., 2016, Zhang et al., 2016a). The thermal impacts of water infiltration are higher in coarse sediments with greater hydraulic conductivity than in organic and fine grained soils with lower hydraulic conductivity (Kane et al., 2001, McKenzie and Voss 2013). Surface cover types, such as vegetated or bare gravel/sand embankments, change the hydraulic and TBCs of road embankment surfaces, but their impact on surface water infiltration, subsurface

flow, and the thermal regime of the embankment and underlying permafrost has not been studied methodically.

In summer, the shallow ground thaws and subsurface water is readily able to flow. Subsurface flow triggers heat advection which modifies ground temperatures and the extent of this temperature change is a function of flow rates, hydrogeologic properties, and regional climate (McKenzie et al., 2007a, Woo 2012, Ghias et al., 2018, Huang et al., 2019). Paquette et al., (2017) observed that in polar desert conditions, snowmelt water flowing through water tracks has a cooling effect on the subsurface and restricts the extent of active-layer deepening. Similar behaviour has been reported for subsurface flow in cold-room simulations when air temperatures were higher than water temperatures (Veuille et al., 2015). Conversely, many studies demonstrate that the permafrost thaw rate can be enhanced by heat advection linked with subsurface water flow (Fortier et al., 2007, McKenzie et al., 2007b, Kurylyk et al., 2016, You et al., 2016). For transportation infrastructure, most of the previous studies neglected the cryohydrogeolocial processes beneath infrastructure and mainly focused on how the atmospheric heat enters the underlying permafrost (Wu et al., 2007, Dumais and Doré 2016). Linear transportation infrastructure commonly crosses local water systems. Subsurface water flowing through embankment subgrade loses heat to the surrounding soils. The heat advected in mobile subsurface water can significantly alter the thermal regime of permafrost to melt ground ice and trigger differential subsidence that damage the structural integrity of roadways (de Grandpré et al., 2012, Zottola et al., 2012, Mu et al., 2018). Additionally, the thermal impact of subsurface water flow represents one of the largest sources of uncertainty when predicting the response of permafrost geosystems to climate change or the impact of infrastructure on the permafrost thermal state. But the quantification of the heat advection caused by subsurface water flow remains largely unknown due to a lack of available long-term embankment temperature data in permafrost regions.

Our study addresses the question: what is the impact of infiltration and subsurface water flow on the thermal stability of a road embankment subbase and subgrade? The two objectives of the present study are to quantify the thermal impact of snowmelt water and rainfall infiltration and to evaluate the potential impact of subsurface water flow on permafrost degradation. We

hypothesize that: 1) the ground warming caused by water movements (heat advection) can be several orders larger than that caused by just atmospheric warming without flow (heat conduction); 2) the thermal impact depths (TIDs) caused by infiltrated snowmelt and rainfall are controlled by the surface cover conditions; and 3) subsurface water flow can accelerate permafrost degradation under an embankment in permafrost regions.

3.2. SITE, MATERIAL, AND METHODS

To achieve these objectives, the nine-year (2009 - 2017 on Alaska Highway) records of in-situ meteorological measurements and ground temperatures at four different sections of the Beaver Creek Road Experimental Site (BC-RES) were analyzed. The sections refer to the natural ground, a bare (unmitigated) embankment slope, a vegetated embankment, and an embankment covered by a shed. For each section, statistical analysis was computed on the time-series and a novel approach of thermal analysis, based on temperature deviation, was adapted to detect, quantify and interpret the heat transferred by water movements in the embankment subbase and subgrade. The natural ground served as a reference to evaluate the effects of water movement on the thermal regime of the road embankments overlying permafrost, while the embankment covered by a shed was used as a reference for comparison with the other two sections, as water infiltration cannot occur under the shed.

3.2.1. Environmental context and site description

In 2008, BC-RES was constructed to test twelve mitigation techniques designed to study how best to prevent permafrost degradation from affecting the Alaska Highway, the main transportation link in Yukon and the only terrestrial link between Alaska and the contiguous USA (Reimchen et al., 2009, Malenfant-Lepage et al., 2012a, Stephani et al., 2014) (Figure 3.1). The Beaver Creek region, southwestern Yukon, is in the Klondike Plateau of the Western Boreal Cordillera (Statistics Canada 2018) (Figure 3.1a, 3.1b). The regional permafrost is discontinuous, and potentially composed of a thick and ice-rich sedimentary overburden (Brown et al., 2001), especially in lowlands (Rampton 1971).

(a) Map of Canada

(b) Map of Yukon Territory

(c) Satellite image of the Beaver Creek study region

(d) Falso-color satellite image of the BC-RES study site
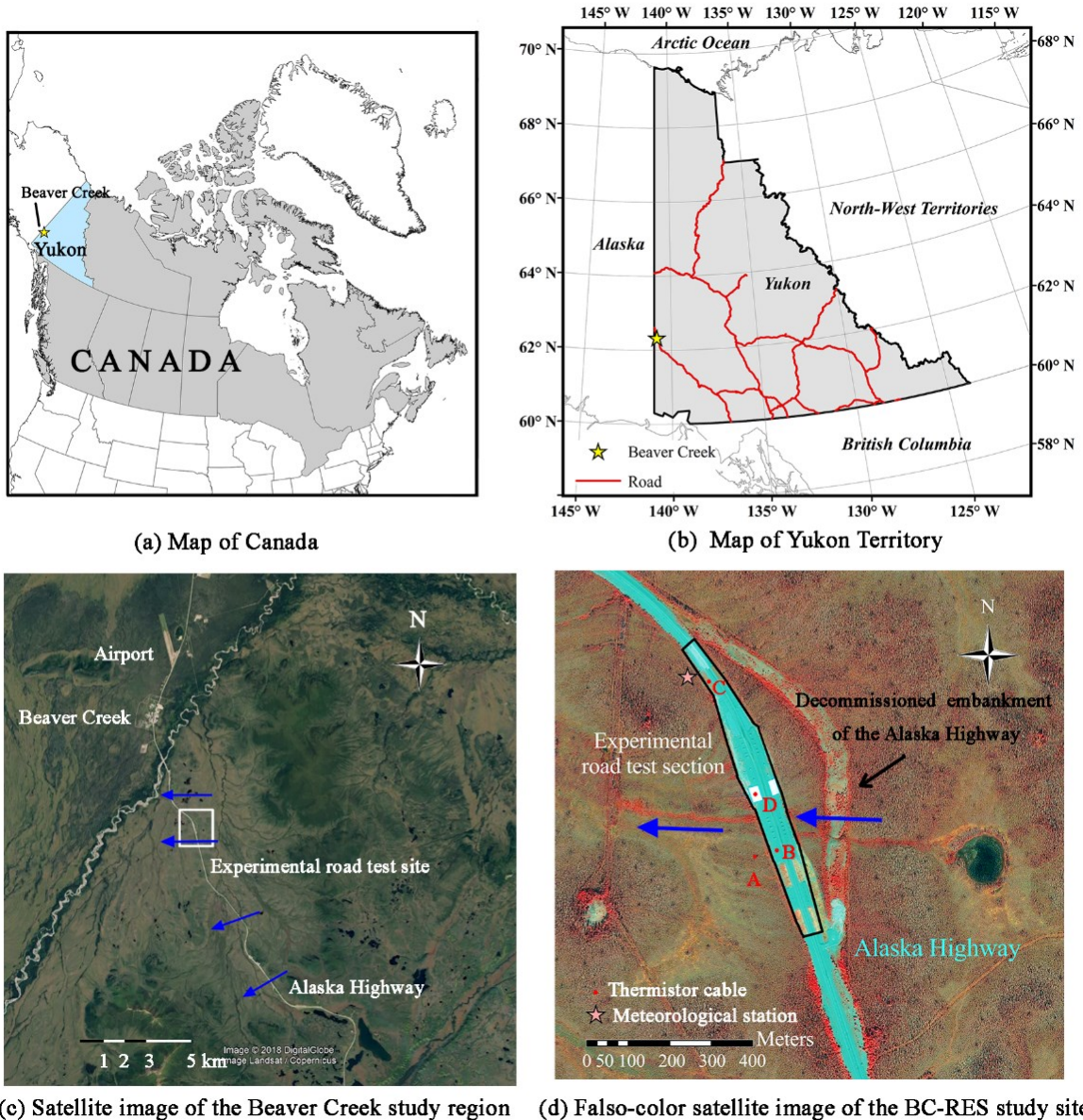
Figure 3.1. Location of the study site (62° 20' N, 140° 50' W). (a) Map of Canada showing the location of the Beaver Creek, south-western Yukon, with a yellow star; (b) map of Yukon Territory showing the location of the Beaver Creek study site with a yellow star (modified from Natural Resources Canada, 2014); (c) satellite image of Beaver Creek study site (Google Earth, August 3, 2010); and (d) false-color satellite image of experimental road test section near Beaver Creek (WorldView II image, taken August 4th, 2010 at 21h30). The road embankment crosses the local drainage. Note: In Figure 3.1c, A ~25 km section of the Alaska Highway intercepts the local drainage network. The blue arrows indicate the direction of regional hydrologic gradient. The white box indicates the region shown in Figure 3.1d; In Figure 3.1d, the blue arrows indicate the location of water tracks (i.e., preferential shallow subsurface flow paths). The black arrow indicates the location of the decommissioned embankment of the Alaska Highway. The red dots, labelled A, B, C and D, represent the location of thermistor cables of the natural ground,

41

unmitigated embankment section, grass-covered embankment section, and shed-covered embankment section, respectively. The pink star represents the location of the meteorological station.

The mean annual air temperature (MAAT) measured at Beaver Creek airport (62° 24' N, 140° 52' W, elevation: 649.00 m above sea level), 8 km away from the BC-RES, for the period from 1981 - 2010 was -4.9 °C, with average AT of -25.2 °C in January and 14.1 °C in July (Figure S3.1) (Environment and Climate Change Canada 2018). Snowfall begins in September, and snowmelt starts in April (Environment and Climate Change Canada 2018). Mean annual precipitation (1981-2010) is 417 mm, of which 300 mm falls as rain (Figure S3.2) (Environment and Climate Change Canada, 2018). The precipitation from June to September accounts for about 70 % of the total precipitation in a year. The thawing and freezing indices (yearly air temperatures above and below freezing) represent an average of 1537.7 thawing degree-days (TDDs) and 3321.8 freezing degree-days (FDDs) respectively (1981-2010) (Environment and Climate Change Canada 2018).

The local environment is a wetland complex constituted by patches of spruce-lichen mineral slope marsh, shrub-tussock basin fen, and spruce-shrub-sphagnum channel fen (Sliger 2016). The surrounding soils normally range from a static cryosol (upslope) to an organic cryosol (in lower areas). The active layer thicknesses vary between 0.40 m when the organic mat is thicker (> 20 cm) to more than 1.20 m when the organic mat is thin (< 20 cm). A silt layer and organic paleosols that are several meters thick are buried below the actual soil (Stephani et al., 2014, Sliger 2016). The permafrost temperature at 8 m depth beneath the ground surface is about -2.2 °C (mean value from 2009 to 2018). The water-table elevation follows the natural topography. The water flow occurs mostly in the subsurface and especially in water tracks (i.e., preferential subsurface flow paths) that can be observed on Figure 3.1c and 3.1d (lighter tone vegetation aligned perpendicular to the slope) (de Grandpré et al., 2010, Sliger 2016).

The experimental road is paved and built on porous, low-saturation embankment fill (68% sand and 28% gravel) lying directly on the natural ground (Doré and Mercier 2008). It is underlain by ice-rich, degrading permafrost (de Grandpré et al., 2012, Stephani et al., 2014, Sliger 2016). Its alignment is sub-perpendicular to the natural ground's slope gradient and therefore intercepts the local drainage network (Figure 3.1c). The water table beneath the road embankment is

calculated by linear interpolation of the water table depths at the upstream side and at the downstream side. The maximum elevation change of natural surface across both sides of the embankment is 2.5 m with an average of 1.5 m (Stephani 2013). Hydraulic and thermal properties of the embankment fills, peat, and silt are presented in the Table S3.1.

The BC-RES was divided into four different sections, including an undisturbed natural ground (Figure 3.2a), a 50-m long sand and gravel embankment section (Figure 3.2b), a 50-m long grass-covered section of the same embankment materials (Figure 3.2c), and an additional 30-m long section of embankment covered by a 1-m high shed (Figure 3.2d). The vegetated section has a thin cm-thick layer of organic material supporting the growth of 30-cm tall grasses. The thermal performance of the shed was reported by (Fortier et al., 2018). Additional technical details about each test case are available in (Stephani 2013) and (Malenfant-Lepage 2015).

3.2.2. Measured climate data and soil temperature

The measurements used in this study include AT and rain precipitations at hourly intervals, and temperature profiles of natural ground and embankment subgrade and subbase at 4-hour intervals (see details in the Table S3.2).

The AT record started in October 2008 and is measured by a shielded AT probe (Campbell Scientific, resolution of 0.01 °C, accuracy of ± 0.1 °C) installed in a solar radiation shield located 2 m above the ground surface about 30 m from the road. The precipitation record started in October 2012 and is measured at the same location by a tipping bucket (TE525WS, manufactured by Texas Electronics and distributed in Canada by Campbell Scientific, resolution of 8.25 ml, accuracy of 1.0 %). The snow thickness survey was conducted just before the snowpack started to melt during winter 2012, using a graduated pole.
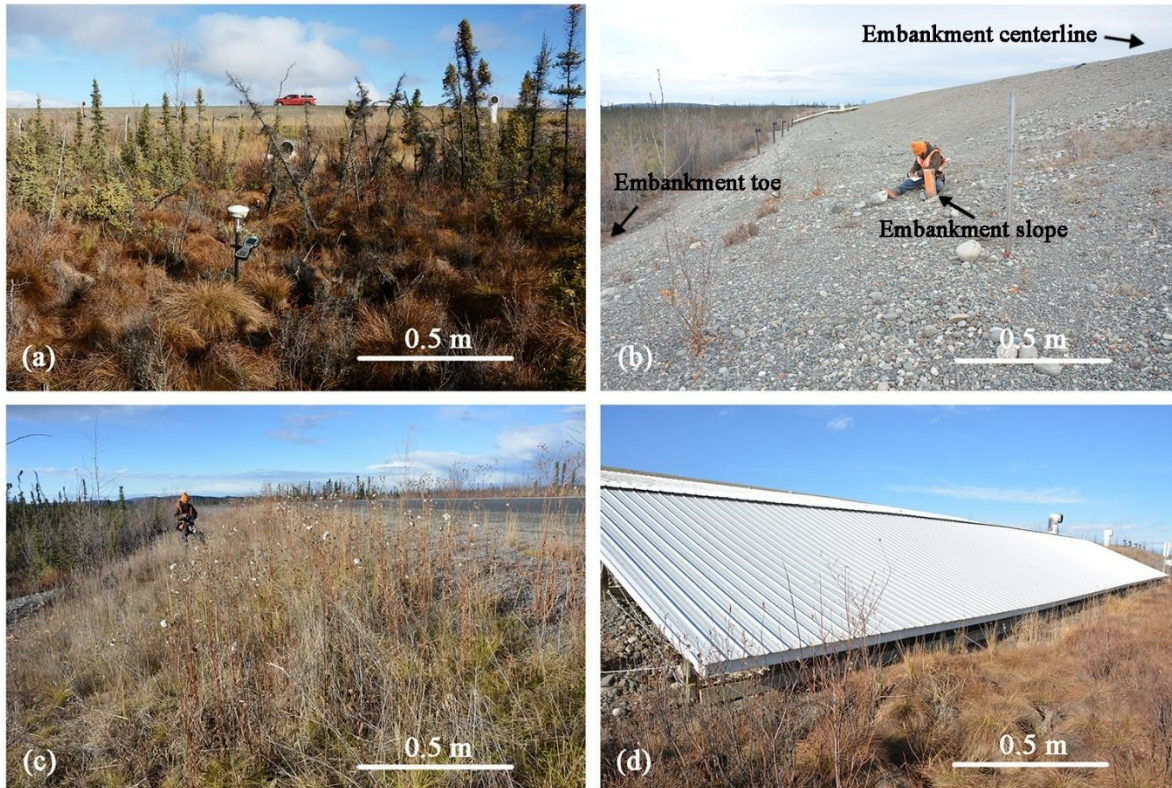
Figure 3.2. Beaver Creek road test section with different surface cover types. (a) Muskeg (natural ground); (b) unmitigated embankment; (c) vegetated embankment; and (d) shed-covered embankment.

The record of all the ground temperature profiles started in 2008. They were measured at each site using a thermistor string (custom-made). The thermistor strings in the embankment are installed in 15-m deep boreholes located at the mid-distance in the slope of the embankment facing the south-west. The thermistor string in the natural ground (8 m depth) is 30 m from the southwestern roadside. All the thermistors strings were placed inside a casing of polyvinyl chloride filled with silicone oil to prevent air convection in the hole and to provide effective contact with the ground. The sensors used to measure ground temperature have an accuracy of ± 0.1 °C between -10 °C to 10 °C and ± 0.2 °C through the rest of the operating range, -50 °C to + 30 °C. All the sensors are wired to an external datalogger (CR1000, Campbell Scientific) for the control and record.

3.2.3. Thermal analysis of infiltrated water and subsurface water flow

In this study, we used marked ground temperature deviation, in comparison to the smooth temperature change (Figure 3.3a) observed in the previous several days, to detect the infiltrated surface water and subsurface water flow (Anderson 2005, Yoshioka et al., 2015). When water movement (vertical infiltration and lateral flow) occurs at a given depth, the ground temperature can change rapidly due to heat advection and has a thermal departure from the smooth sinusoidal variation that would result from heat conduction into the embankment (Beltrami 1996, Lu and Ge 1996, Kurylyk et al., 2017) (Figure 3.3b, 3.3c, 3.3d, and 3.3e). The thermal impact depth (TID), relative to the ground surface, is defined as the maximum depth where a step temperature change is observed for a given thermistor string (Figure 3.3a).
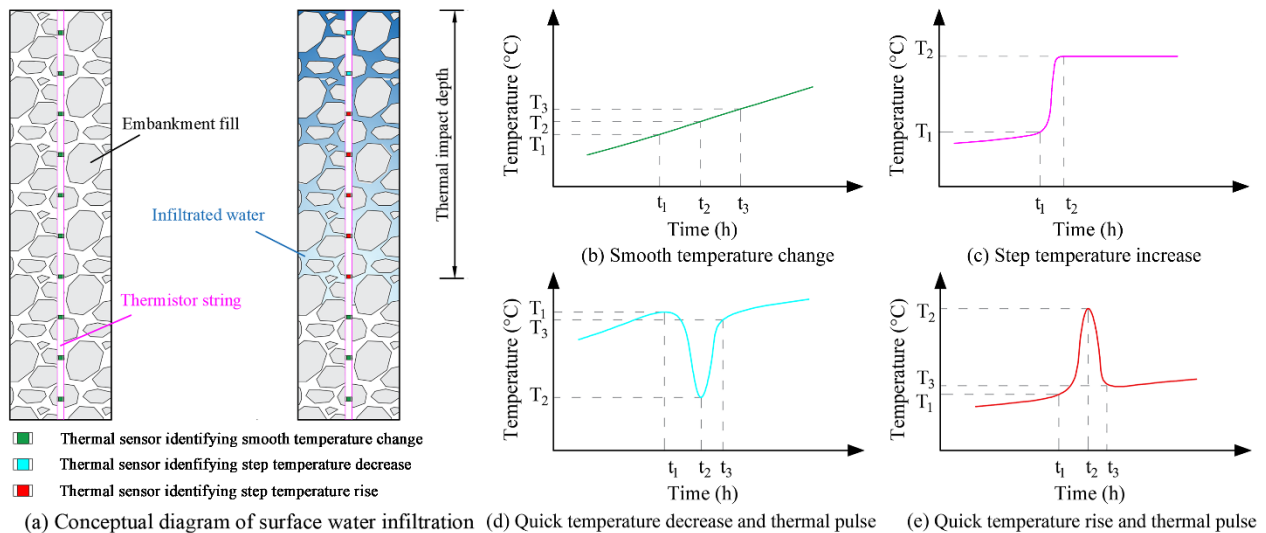
Figure 3.3. (a) Examples of soil temperature variations triggered by seasonal atmosphere warming, top-down water infiltration, and subsurface water flow; (b) Smooth temperature change caused by atmosphere warming; (c) step temperature increase caused by snowmelt water infiltration, generally followed by a zero-curtain period; (d) step temperature decrease, indicative of rainfall infiltration; and (e) step temperature rise due to rainfall infiltration and subsurface water flow.

3.2.3.1. Detection of surface water infiltration

Ground temperature variations were used to illustrate the thermal response of embankment subbase and subgrade to the infiltrated surface water (Figure 3.3). The mean and standard deviation (SD) values of the rate and magnitude of temperature change over the 9-year period are listed in the tables to quantify the impact of water infiltration. Furthermore, soil

45

temperatures, measured at the depth of 0.3 m, 1.4 m and 2.0 m under the embankment slope, are used to quantify the impact of water infiltration at depth, while the 0.3 m depth (first temperature sensor of the thermistor cable) soil temperatures are used to analyze the thermal response of near-surface natural soils to water infiltration.

During the spring, the onset of snowmelt was detectable by a step-rise of the ground surface temperature (GST) to 0 °C over several days (Figure 3.3c) (Hinkel et al., 1997, Kane et al., 2001, Lanouette et al., 2015). The date of the complete snowpack disappearance is identified as the time when the ground surface temperature rises above 0 °C, generally after a brief zero-curtain period. The zero curtain refers to the effect of latent heat in maintaining temperatures near 0 °C over extended periods during soil freezing or thawing (Cook 1955, van Everdingen 1988). In fall, the date of the snowpack onset was identified by the slight diurnal oscillation of the GST due to the thermal insulation created by snow (Teubner et al., 2015). Snow thickness along the embankment was measured in 2012 and this year is used to illustrate and quantify the impact of snowmelt water infiltration on embankment temperature. The inter-annual variability of step temperature rise for four cases were detailed in the period from March 1st to May 31st.

In summer, the thermal response of subsurface soils to rainfall infiltration can be identified by a sudden temperature change in comparison to subsurface temperature before and after the rainfall events (Wen et al., 2015, Yoshioka et al., 2015). During the rainfall event, the soil temperatures suddenly decrease to a lower point or increase to reach a high point (i.e., thermal pulse) in a short period of time (Figure 3.3d and e). Available rainfall data (Table S3.2) associated with a larger magnitude of ground temperature change are used to illustrate the impact of rainfall infiltration on embankment temperature. Furthermore, where no water infiltration occurs, the soil temperature change is primarily controlled by heat exchange between the dry embankment subbase and the atmosphere. Thus, the coefficient of determination (linear regression) of air-ground temperatures was used as an indicator of infiltrated water's impact of shed-covered and shed-free surface. The R-squared value was calculated as the squared correlation between the air temperatures and soil temperatures at the depth of 0.3 m in summer (June to August) over the 9-year period. If the R-squared value approaches 1, it indicates that the shallow (0.3 m depth)

ground temperatures experience a good correlation with AT and there is no temperature deviation due to surface water infiltration.

3.2.3.2. Detection of subsurface water flow

To identify and assess the impact of subsurface water flow during the summer, high temperature rise rate (i.e., quick temperature increases against time) and reversed thermal gradient (i.e., temperature increase with depth instead of a normal temperature decrease with depth) beneath the water table are used as a diagnostic tool (Figure 3.3e). The ratios of the thermal gradient and the rate of temperature increase between the step and smooth temperature changes against time are used to assess difference between heat conduction and heat advection. The statistical metrics (mean and SD) of magnitude and rate of temperature rise caused by water flow are presented to illustrate the thermal characteristics of the subsurface water flow over the 9-year period. The TID caused by the subsurface water flow was calculated with reference to the interface between the embankment and the natural ground. The location of the interface was obtained from Stephani (2013).

The year 2015, with the largest temperature changes during the period of record, is used to illustrate the thermal impact of subsurface water flow. Similar phenomena in other years are presented in the supporting information (Figure S3.3). Due to the inter-annual variations of AT and precipitation, box-plot graphs were used to display the daily temperature change rate over the 9-year period with a five-number summary: minimum, first quartile, median, third quartile, and maximum. The daily temperature change rates were computed by splitting the year into a freezing and thawing period, which were based on the negative and positive soil temperatures at the 0.3 m depth.

The statistical metrics (mean and SD) of active layer thickness (ALT) and ground temperature at a depth of 0.9 m was calculated to compare the difference of water flow on permafrost thawing and warming between the natural ground and embankment subbase and subgrade. The depth of the permafrost table (0°C isotherm) was estimated using kriging interpolation with linear semi-variogram model (Trochu, 1993) of the thermistor string data for each site.

3.3. RESULTS

3.3.1. Thermal impact of snowmelt water infiltration

Figure 3.4 shows that surface temperatures of the shed-covered embankment had a strong diurnal variation, continuously in phase with atmospheric temperature throughout the entire year, and experienced a smooth temperature increase in the spring. The temperatures of unmitigated gravel/sand embankment experienced a quick increase from -5 °C up to 0 °C over several days at the end of March (Figure 3.4b and d). Further, its temperature showed a diurnal variation only a few days after the onset of snowmelt (Figure 3.4d). Similarly, step temperature rises were observed for the vegetated embankment (Figure 3.4e) and natural ground (Figure 3.4f), followed by a long (more than one month) zero-curtain period before a diurnal variation.
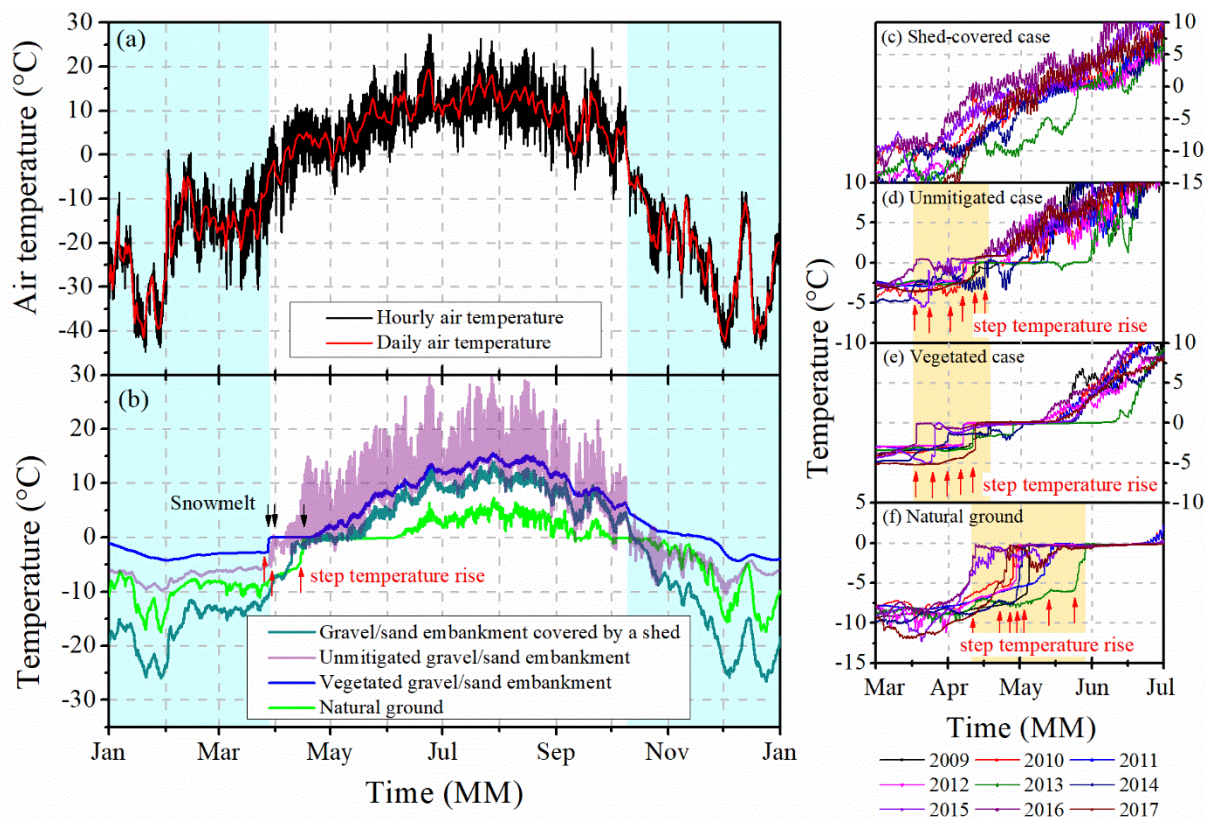
Figure 3.4. (a) Hourly and daily air temperature (AT) variation; (b) 4-hour interval soil temperatures variations at the depth of 0.3 m in 2012; 4-hour interval soil temperature variations from 1st March to 31st May over the nine-year period for (c) shed-covered case; (d) unmitigated case; (e) vegetated case; and (f) natural ground. The blue zone indicates that the air temperature

is below 0 °C. The yellow zone illustrates the detected snowmelt periods. The red arrows represent the detected infiltration events.

Table 3.1 presents the timing and duration of the seasonal snowpack derived from the ground surface temperature. For both unmitigated and vegetated cases, the mean starting dates of the step temperature rise were March 26th, with a range from Mid-March to earlier April over the 9-year period. For the unmitigated embankment, the snow disappeared, on average, 3 weeks after the onset of snowmelt. For the vegetated embankment, the duration of snow disappearance was delayed by about 2 weeks in comparison to the unmitigated case. For the natural ground, the starting date of the step temperature rise was delayed by approximately two weeks compared to the embankment slope. The date of snow disappearance was, on average, seven weeks after the onset of snowmelt.

Table 3.1. Timing and duration of the seasonal snowpack at the borehole site derived from the ground surface temperature measured over the 2008-2017 period.

		Natural ground	Unmitigated gravel/sand embankment	Vegetated gravel/sand embankment
Onset (dd-mm)	Max	03-May	01-Apr	01-Apr
	Min	01-Apr	13-Mar	14-Mar
	Mean	11-Apr	26-Mar	26-Mar
	SD	12	7	6
Melt (dd-mm)	Max	09-Jun	07-May	16-May
	Min	27-May	04-Apr	22-Apr
	Mean	03-Jun	17-Apr	30-Apr
	SD	5	11	7
Duration (day)	Max	69	30	46
	Min	32	5	25
	Mean	53	19	35
	SD	14	9	8

The TID, magnitude, and rate of temperature rise differed among the four cases (Table 3.2). For the unmitigated gravel/sand embankment, the TID was deeper on average by 1.5 m compared with the other cases. The maximum TID was 3.6 m, about three times larger than the maximum of the other cases. The temperature increase rate for the unmitigated gravel/sand embankment was also larger, about 0.82 °C·hour^{-1} near the surface and 0.32 °C·hour^{-1} at a depth of 2 m. The

magnitude of temperature rise was strongly linked to the mean ground temperatures (MGT) in winter (December-February) (R^2 = 0.94). The magnitude of soil temperature increase of the natural ground was larger, about 5.2 °C near the surface (SD = 0.9 °C, n = 9).

3.3.2. Thermal impact of rainwater infiltration

For the natural ground, the 0.3-m-depth soil temperatures decreased quickly after rainfall events (Figure 3.5a), while soil temperatures at depth remained stable (Figure 3.5b). Moreover, as expected, the subsurface soils under the shed (Figure 3.5c) did not respond to rainfall infiltration.

Embankment fill's temperatures of the other three cases responded quickly to rainfall events. For the unmitigated gravel/sand embankments, a cooling occurred near the surface, but a warming occurred at depth after the rainfall events (Figure 3.5d and Figure 3.5e). Soil temperatures at 0.9 m depth rose by 1.0 °C, corresponding to a 50.8 mm precipitation on June 28-30th 2013, although the largest magnitude of temperature rise was 7.0 °C at a depth of 2.1 m (Figure 3.5e). Over this rainfall event, the maximum TID reached a depth of 3.6 m, which resulted in a quick warming by 1.7 °C in 8 hours (Figure 3.5e). Also, the heat propagation rate caused by infiltrated rainfall water was about 35 cm·h^{-1}. Similarly, the temperatures of the subsurface soil of the vegetated embankment increased slightly after rainfall events, although with a smaller amplitude and at lower rates.

The thermal characteristics of rainfall infiltration over the 9-year period are listed in Table 3.3. The TIDs for rainfall were 3.1, 1.9 and 0.3 m for the bare gravel/sand embankment, vegetated gravel/sand embankment, and natural ground, respectively. The magnitude of temperature changes and MGT were larger for the bare gravel/sand embankment, lower for the vegetated gravel/sand embankment, and lowest for the natural ground. For both sections of bare and vegetated embankment, the magnitude and rate of temperature increase at the 2 m depth were larger than that at the 1.4 m depth.
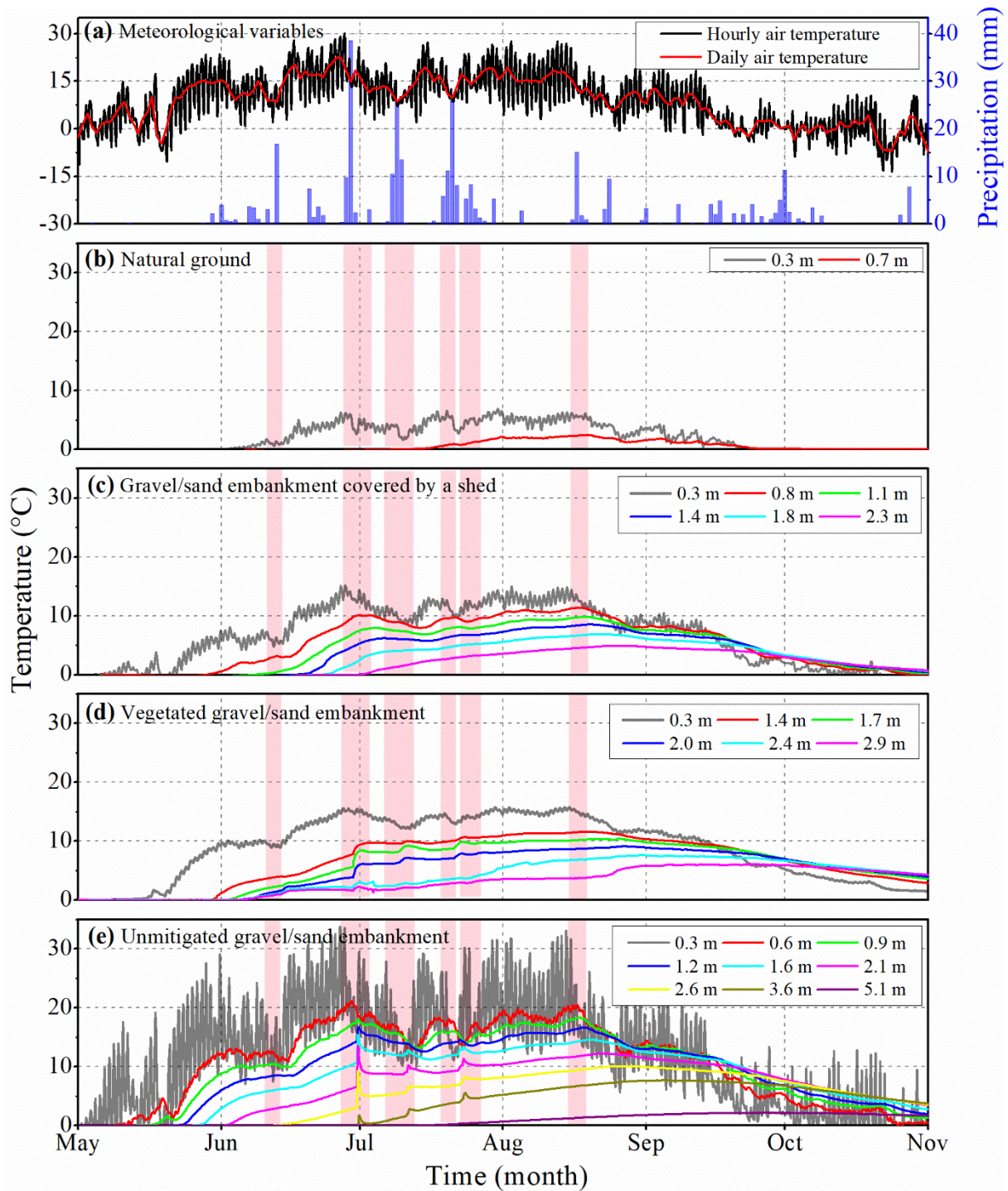
Figure 3.5. Variations of air temperature, daily precipitation and soil temperature during snow-free season, 2013. (a) Air temperatures and daily precipitation; (b) natural ground temperature; (c) shed-covered gravel/sand embankment temperature; (d) vegetated gravel/sand embankment temperature; and (e) unmitigated gravel/sand embankment temperature. The pink column represents the detected infiltration events.

51

Table 3.2. Thermal characteristic of snowmelt water infiltration over the nine-year period (TID: thermal impact depth; MGT: mean ground temperature; SD: standard deviation).

	Thermal Characteristics		Natural ground	Unmitigated gravel/sand embankment	Vegetated gravel/sand embankment
	TID (m)	Max	0.7	3.6	2.4
		Min	0.3	2.1	0.1
		Mean ± SD	0.7 ± 0.1	2.9 ± 0.7	1.3 ± 1.0
		n	9	9	9
0.3-m depth	Magnitude (°C)	Max	6.7	6.1	5.2
		Min	3.9	2.6	1.4
		Mean ± SD	5.2 ± 0.9	4.7 ± 1.3	2.8 ± 1.1
	Rate (°C·hour^{-1})	Max	1.26	1.33	1.11
		Min	0.30	0.47	0.35
		Mean ± SD	0.56 ± 0.30	0.82 ± 0.36	0.62 ± 0.25
	MGT (°C)	Max	-7.5	-6.1	-3.0
		Min	-11.6	-15.1	-6.7
		Mean ± SD	-9.3 ± 1.7	-9.5 ± 2.9	-4.6 ± 1.3
2.0-m depth	Magnitude (°C)	Max	0	2.4	1.5
		Min	0	1.0	0.2
		Mean ± SD	0	1.7 ± 0.5	0.6 ± 0.6
	Rate (°C·hour^{-1})	Max	0	0.51	0.07
		Min	0	0.15	0.02
		Mean ± SD	0	0.32 ± 0.13	0.03 ± 0.02
	MGT (°C)	Max	-3.6	-1.3	0.2
		Min	-6.2	-3.3	-0.3
		Mean ± SD	-4.5 ± 0.9	-2.1 ± 0.7	0.0 ± 0.2

The near-surface temperatures (0.3 m depth) had a large decrease of up to 5.2 °C on average (n = 27) after a rain event. The magnitude of temperature decrease for the natural ground and the vegetated embankment were about 0.9 °C and 1.3 °C, respectively. Their decreasing rates were smaller, less than 0.16 °C·h^{-1}. The decreasing magnitude for the unmitigated embankment was four times larger, with a decreasing rate of more than 1.5 °C·h^{-1} (SD = 0.83 °C·h^{-1}, n = 31). The

magnitude and rate of temperature change were smaller compared with that for the near-surface temperature. The maximum increasing rate was 0.3 °C·h^{-1} for the unmitigated embankment.

3.3.3. Thermal impact of subsurface water flow

Figure 3.6 presents one noteworthy event of soil temperature change observed at a depth of 0.6 m to 4.1 m from June 4 to June 20, 2015. Prior to this period, the soil below the embankment was gradually warming. On that occasion, there was a quick increase of ground temperature, rising by 5.1 °C in 4 days from 4th June to 7th June (Figure 3.6a). After this time, the thermal gradient reversed, and the soil temperature decreased slightly by 3 °C in 13 days (Figure 3.6b).

Furthermore, soil temperatures at depths of 2.6 m to 5.6 m exceeded the usual summer maximum (mid-October), by 1.4 °C (Figure 3.6c). Conversely, soil temperatures elsewhere in the embankment increased gradually and the magnitude of daily temperatures change was significantly smaller at about 1 °C.

Figure 3.6d and e illustrate the variations of daily temperature change rates with depth over the 9-year period. In the thawing period, the mean value of temperature change rate varied at the range of 1.7 °C·day^{-1} to 3.1 °C·day^{-1}. An obvious departure of temperature change rate was observed at depth from 0.6 m to 6.0 m. The maximum departure was observed at the depth of 1.6 m and the corresponding value was about 6.5 °C·day^{-1}, which was twice greater than that at the near surface. By contrast, in the freezing period, the temperature change rates were much smaller, about 1.2 °C·day^{-1}, and the amplitudes of temperature change rate reduced with depth.

The vertical thermal gradient and increasing rate of soil temperature below the embankment slope in 2015 are detailed in Table 3.4. One conspicuous feature is that the rate of step temperature increase is about two orders of magnitude greater than the smooth value at the depth of 1.1 m and 4.1 m, while the thermal gradients experienced a relatively slight change with ratios (relationship between the step values to smooth values) ranging from 0.5 to 2.3 over the whole year. The step temperature increasing rate was larger than that during the smooth period, on average by 4 °C·d^{-1}. The largest ratio for the temperature rising rate was up to 220 at the depth of 1.1 m, and its ratio for the vertical thermal gradient was smaller, about 0.5.

53

Table 3.3. Thermal characteristic of rainfall infiltration on the natural ground and the embankment slope (TID: thermal impact depth; MGT: mean ground temperature; SD: standard deviation).

	Thermal characteristics		Natural ground	Unmitigated gravel/sand embankment	Vegetated gravel/sand embankment
	TID (m)	Max	0.3	3.6	2
		Min	0.3	2.1	1.7
		Mean ± SD	0.3 ± 0	3.1 ± 0.6	1.9 ± 0.1
		n	31	31	31
0.3-m depth	Magnitude (°C)	Max	-0.3	-0.6	-0.6
		Min	-2.6	-12.7	-2.3
		Mean ± SD	-0.9 ± 0.6	-5.2 ± 3.6	-1.3 ± 0.6
	Rate (°C·hour^{-1})	Max	-0.06	-0.43	-0.03
		Min	-0.76	-3.25	-0.09
		Mean ± SD	-0.16 ± 0.14	-1.55 ± 0.83	-0.06 ± 0.02
	MGT (°C)	Max	2.6	15	12
		Min	1.8	12.8	9.7
		Mean ± SD	2.2 ± 0.3	13.6 ± 0.8	10.7± 0.8
1.4-m depth	Magnitude (°C)	Max	0	3.6	1.02
		Min	0	0.3	0.16
		Mean ± SD	0	1.3 ± 0.9	0.46 ± 0.25
	Rate (°C·hour^{-1})	Max	0	0.86	0.07
		Min	0	0.03	0.01
		Mean ± SD	0	0.23 ± 0.19	0.03 ± 0.02
	MGT (°C)	Max	-0.8	7	8.3
		Min	-1.4	5.6	6.4
		Mean ± SD	-1.0 ± 0.2	6.1 ± 0.4	7.4 ± 0.7
2.0-m depth	Magnitude (°C)	Max	0	6.1	1.36
		Min	0	0.2	0.55
		Mean ± SD	0	2.0 ± 1.5	0.86 ± 0.24
	Rate (°C·hour^{-1})	Max	0	1.63	0.06
		Min	0	0.02	0.01
		Mean ± SD	0	0.30 ± 0.35	0.04 ± 0.02
	MGT (°C)	Max	-1.3	4.5	6.1
		Min	-2.1	3.3	4.7
		Mean ± SD	-1.7 ± 0.3	3.8 ± 0.4	5.3 ± 0.5

Figure 3.6. Temperature variations with depth at the embankment slope. (a) Increase of ground temperature. The red arrow presents the quick temperature increase in 4 days; (b) reversed thermal gradient and soil temperature decrease. The blue arrow illustrates the decrease of soil temperature over 13 days; (c) thermal envelope in 2015; and temperature change rate (d) in the thawing period and (e) in the freezing period, respectively, over the 9-year period. Note that the depth is relative to the interface between the natural ground and embankment material. The summer maximum was calculated without considering soil temperature variations over the period from 4 to 20 June 2015. The pink colour zones illustrate the saturated unfrozen soil beneath the water table.

The thermal characteristics of the summer subsurface water flow over the 9 years period are detailed in Table 3.5. The maximum TID was 4.5 m with an average depth of 2.8 m. Subsurface water flow caused a quick and considerable increase of the soil temperature, rising on an average by 2.2 °C with an increasing rate of 0.13 °C·h^{-1}. The maximum warming magnitude and rate were 6.4 °C and 0.65 °C·h^{-1}. This thermal impact lasted during the whole summer, by an average of 4 months.

Table 3.4. Thermal gradients and temperature increasing rates of embankment subgrade in 2015.

Depth (m)	Thermal gradient (°C·m⁻¹)			Temperature increasing rate (°C·d⁻¹)		
	Step	Smooth	Ratios	Step	Smooth	Ratios
0.1				0.06	0.24	0
	11.5	13.8	0.8			
-0.2				0.64	0.10	7
	13.0	13.0	1.0			
-0.6				3.72	0.02	162
	6.3	7.3	0.9			
-1.1				5.05	0.05	220
	4.9	2.6	0.5			
-1.6				4.11	0.03	147
	1.7	3.2	0.5			
-2.6				2.68	0.03	89
	1.1	1.7	0.6			
-4.1				1.09	0.02	57
	1.7	0.8	2.3			
-5.6				0.01	0.01	1
	0.1	0.1	1			
-7.1				0.00	0.01	0

Note: The depth is measured from the interface between the embankment and the natural ground. The smooth temperature increasing rates and thermal gradient were calculated without taking into consideration the period from 4th to 20th June 2015. While the step values were calculated according to the period from 4th to 20th June 2015. The ratio represents the relationship between the step values to smooth values.

Table 3.5. Thermal characteristics of subsurface water flow under the embankment slope (TID: thermal impact depth; SD: standard deviation).

	TID (m)	Duration (days)	Magnitude (°C)	Rate (°C·h⁻¹)
Max	4.5	164	6.4	0.65
Min	1.5	106	0.2	0.01
Mean ± SD	2.8 ± 1.0	132 ± 17	2.2 ± 1.5	0.13 ± 0.12
n	14	14	58	58

Table 3.6 shows the thermal characteristic of the embankment subbase at a depth of 0.9 m below the natural ground from 2009 to 2017. For the natural ground, the ALT remained nearly stable, at about 1 m, over the nine-year period. The ground temperatures varied at the range of -12.4 °C to 1.2 °C, with an average of -2.5 °C. The ALTs under the embankment centerline were shallow

and varied between 1 and 1.4 m. Conversely, the mean ALTs under the embankment slope (2.8 ± 0.5 m) and toe (2.6 ± 0.5 m) were close to three times as deep as that in the natural ground, and the maximum value was 3.2 m at the embankment slope in 2017. Also, the mean annual ground temperatures at 0.9 m depth were 1.5 °C, 1.0 °C, and -0.2 °C, for the embankment toe, embankment slope, and embankment centerline, respectively. The mean annual ground temperatures below the embankment subbase and subgrade were about 3.0 °C higher than that below the natural ground.

Table 3.6. Thermal characteristics of the embankment subbase at a depth of 0.9 m below the natural ground over the nine-year period. (ALT: active layer thickness; SD: the standard deviation).

		Natural ground	Embankment toe	Embankment slope	Embankment centerline
ALT (m)	Max	1.1	2.9	3.8	1.4
	Min	1.0	1.9	2.3	1.0
	Mean ± SD	1.0 ± 0.0	2.5 ± 0.4	3.3 ± 0.6	1.3 ± 0.1
Soil temperature (°C)	Max	1.2	11.2	3.2	0.5
	Min	-12.4	-4.1	-0.3	-0.9
	Mean ± SD	-2.5 ± 0.3	1.6 ± 0.2	0.5 ± 0.3	-0.2 ± 0.1

3.4. DISCUSSION

The thermal analyses of the Beaver Creek - Road Experimental Site (BC-RES) demonstrate that water movement through the embankment adversely alters the thermal state of the embankment and underlying permafrost. In the discussion we first addressed heat advected due to the top-down infiltration of surface water and discussed the differences and similarities of the thermal impact of infiltrated water between an embankment and the natural ground. For the embankment itself, we compared the difference between a bare porous gravel/sand standard embankment, a vegetation-covered gravel/sand embankment, and a gravel/sand embankment covered by a shed (not submitted to rain/snowmelt water infiltration). Finally, we discussed the thermal impact of lateral subsurface water flow on permafrost degradation.

3.4.1. Thermal impact of infiltrated surface water

Our observations demonstrate that the ground temperature can be used as an indirect tracer to detect water infiltration and flow in embankment subbase and subgrade through the temperature deviation at the surface and subsurface (Figure 3.4 and Figure 3.5). Surface water infiltration changed the subsurface energy balance and reversed the thermal gradients within the embankment in spring and summer. The soil properties (Table S3.1) and surface cover types largely influenced the temperature change rate and TID (Table 3.2 and Table 3.3), when the seasonal snowpack was completely melted (Table 3.1).

3.4.1.1. Heat advected by the infiltrated water flow

In the spring, infiltrated snowmelt water enhances the downward ground heat fluxes and causes a quick increase of temperature (up to 0 °C) at depths, followed by a long zero-curtain period in the natural ground and the vegetated embankment (Figure 3.4). The heat released by infiltrated snowmelt water accelerates the warming rate of the embankment subbase and subgrade. The zero-curtain period observed at the near surface, caused by large amounts of water accumulated within the top-soil layer, is consistent with the field observation in taiga and tundra terrain (Hinkel and Outcalt 1994, Hinkel 1997, Kane et al., 2001). In comparison, the reference embankment covered by the shed does not receive any heat from the infiltration of snowmelt.

In summer, two types of soil temperature behavior triggered by infiltration of rainfall water were observed: a significant cooling near the surface and a steep warming at depth (Figure 3.5). The average increasing rates of temperature of subsurface soils are 0.3 °C·h^{-1} after rainfall events, which is two orders of magnitude greater than that without rainfall infiltration (less than 0.06 °C·h^{-1}) (Figure 3.5 and Table 3.3). Moreover, the relatively high hydraulic conductivity (Figure S3.1) of embankment material enhances the infiltration rate and results in faster heat propagation rate. For the unmitigated embankment (unfrozen thermal diffusivity of 1.5×10^{-7} m^2·s^{-1}), the heat propagation rate (maximum 25.7 cm·h^{-1}) caused by infiltrated rainfall water is one order of magnitude faster than conductive heat transfer by atmospheric warming (several centimeters per hour) (Figure 3.5e). Terzaghi (1952) and Hinkel & Outcalt (1994) also suggested that the mean conductive propagation rate, given a typical thermal diffusivity of 5.0×10^{-7} m^2·s^{-1}

for unfrozen soil, is only 8.3 cm·h^{-1}. Furthermore, unlike thermal conduction due to a thermal gradient, the magnitude of temperature rise due to advective heat flux does not diminish with depth. Over the rainfall events, the magnitude of temperature rise caused by the infiltrated water at a depth of 2.1 m was several times larger than that observed at 0.9 m depth (Figure 3.5e). The soil temperature deviation linked with water infiltration agrees with thermal analyses done in the unfrozen zone that show infiltrated surface water are able to alter subsurface temperature (Kane et al., 2001, Fujii et al., 2009, Rutten et al., 2010, Yoshioka et al., 2015, Liu et al., 2019).

3.4.1.2. Difference between the natural ground and embankment's slope

In winter and spring, the timing and duration of the seasonal snowpack differed between the embankment slope and the natural ground (Table 3.1 and Figure 3.4). At the BC-RES, the snowpack at the embankment slope typically melted earlier by an average of 2 weeks and disappeared faster by an average of more than one month (n = 9), in comparison to the natural ground (Figure 3.4). This is mainly attributed to the low albedo (0.15, Dumais & Doré, 2016) of snow-free surface of embankment fill material and asphalt. The low albedo of embankment surface enhances the absorption of solar radiation, in comparison to snow covered surfaces (albedo: 0.6 ~ 0.9) (Ling & Zhang, 2003; Dumais & Doré, 2016: study conducted at the test site).

The embankment fill material has a low water content (3.1 %) and a high thermal conductivity (frozen state: 1.45 W·m^{-1}·K^{-1}; and unfrozen state: 0.83 W·m^{-1}·K^{-1}) (Table S3.1), which is favourable to lateral heat transfer to the embankment slope and faster melting. Additionally, the low water content reduces the duration of the zero-curtain period (Figure 3.4), which also facilitates the temperature increasing rate in the embankment. This effect is further enhanced by the high hydraulic conductivity of embankment materials (Table S3.1) and the macroporosity created by fractures in the embankment, which can facilitate snowmelt water infiltration and reduce water stored on the embankment surface. As there is less water accumulated on and within the unmitigated embankment slope, the amount of heat required to warm the embankment is reduced. In comparison, for the natural ground a large amount of water is accumulated within the top peat layer overlying the silt (low hydraulic conductivity), which produces a zero-curtain period and significantly delays the ground warming by up to one month (Figure 3.4 and Table 3.1). Therefore, due to the direct exposure of the embankment slope surface to above freezing

air temperatures, the earlier disappearance of the seasonal snowpack accumulated at the ground surface increases the thawing period through the summer, rises the temperature gradient within the embankment, and finally leads to the underlying permafrost warming and thawing. Ishikawa (2003) and Ling and Zhang (2003) also demonstrated that the earlier disappearance of seasonal snowpack caused by increase of AT due to climate change increases ground warming in spring.

In the late summer, for the natural ground, the pre-existing near-saturated organic soil and low hydraulic conductivity of the underlying silt (Table S3.1) largely limit water infiltration and reduce heating at depth (about 0.3 m) (Table 3.3). Our results show that infiltrated rainfall water warms embankment fill materials at depths of up to 3.6 m, while lowering the near-surface temperature (Table 3.3). The macropores and low moisture content of embankment materials (Table S3.1) can be effective in absorbing moisture, facilitating infiltration, and transferring sensible heat to depth, although the extent of temperature change is a function of soil properties, and amount and intensity of infiltrated water. In comparison to the natural ground, the rate of temperature rise of unmitigated gravel/sand embankment is respectively about twice larger for the infiltrated snowmelt water and an order of magnitude for the infiltrated rainfall water at the depth of 0.3 m (Figure 3.4 and Figure 3.5). Similarly, for both the natural ground with sparse vegetation and asphalt-paved embankment surface in the QTP, Wen et al., (2014) and Wen et al., (2015) demonstrated that summer rainfall infiltration caused shallow subsurface soil cooling through thermal and moisture analysis, although the differences of surface cover types and soil properties was not included in their study.

3.4.1.3. Difference of surface cover types of embankment slope

The thermal response of embankment subbase to rainfall events differs in different surface cover types (Figure 3.5). The response of soil temperatures to rainfall events is more significant in dry coarse embankment fill (gravel/sand) without shed coverage and vegetation (Figure 3.5c and 3.5d).

For the unmitigated embankment, the thermal response of the embankment fill to rainfall is direct and immediate (Figure 3.5). The rate of temperature change is almost one order larger than the surface covered by vegetation (Table 3.3). The TID of unmitigated gravel/sand

embankment (3.0 m) is about twice larger than the vegetated embankment (Table 3.3). Vegetation layer and thin organic layer intercept the rainfall infiltration and store surface water, which limits the thermal impact of surface water infiltration. For example, a 1-cm-thick organic layer, with porosity of 0.7 and initial volumetric water content of 20 %, can hold about 0.5 mm of rainfall water against gravity drainage. Further, stored surface water markedly retards the surface warming (Figure 3.4), due to the high heat capacity of water. Also, vegetation buffers the contact between atmosphere and subsurface embankment material and reduces the daily amplitude of temperature in near-surface soils by about 2.6 °C in comparison to the unmitigated embankment (Figure 3.6d and 3.6e). Conversely, no thermal departure is observed at the subsurface temperature of the shed-covered embankment. Its subsurface temperatures exhibit a strong diurnal variation (Figure 3.4) and experience a good correlation with AT over the whole period (R^2 = 0.74). The main reason is that the shed-covered surface protects road embankment from surface water infiltration and its thawing and freezing processes are controlled by heat exchange with the atmosphere.

The observation data demonstrates that the TID response to rainfall water infiltration is largely limited to the active layer in the embankment subbase (Figure 3.5). Rainfall water cannot effectively infiltrate past the frost table in summer, although, following a few strong rainfall events, infiltrated rainfall water reached the frozen ground (Figure 3.5e). For example, the 50.8-mm precipitation event during 28th - 30th June 2013 resulted in a rapid warming of soil at the frost table by 1.7 °C in 8 hours, but in the embankment ground temperatures approached thermal equilibrium within one day. The heat advected by the infiltrated water may serve to melt pore-ice in the active layer instead of changing the temperature, even if soil temperature is below 0 °C, much lower than that of infiltrated water. As there is a small amount of water and a short contact time with the frozen ground, infiltration of rainwater was ineffective to thaw the ground at depth. There was no observed warming of soil (latent heat release during freezing) below the frozen front, indicating that very little infiltrated water refreezes back at the bottom of embankment material fills (Figure 3.5). Silt contains unfrozen water over a relatively wide range of negative temperature (Harlan 1973, Spaans and Baker 1995), due to its noticeable capillarity (Carsel and

Parrish 1988). This negative temperature range, where unfrozen water is present, may disable our method to track the advected heat.

3.4.2. Thermal impact of subsurface water flow

Warming rates caused by pore water flow (heat advection) can be 1 to 2 orders of magnitude larger than that caused by atmospheric warming without flow (heat conduction) (Table 3.4 and Table 3.5). When the embankment centerline thaws and the effective permeability increases, the flowing water increases the energy absorption of the underlying permafrost (Table 3.6), causes the short thermal pulse (with magnitude up to 6.5 °C) and leads to a reversed thermal gradient (up to 0.65 °C·h^{-1}) at depth (Figure 3.6). The heat advected by subsurface water flow causes temperature deviation at depth from the smooth temperature curve, which is normally dominated by heat conduction (Figure 3.6b). Over the period from June 4 to 20, 2015, the impact of vertical surface water infiltration can be excluded, due to the small amount of rainfall (0.5 mm·day^{-1}). By contrast, in the embankment subbase where no water flows, heat conduction plays a dominant role in transporting atmospheric heat from the embankment subbase to its subgrade (Figure 3.6a). Its temperatures experience a slight change, and no temperature departure is observed. Similarly, in the freezing period, the water movement was restricted by the low permeability of frozen soil and the energy transfer is mainly controlled by the vertical heat conduction process. The magnitudes of temperature change rate diminish with depth due to heat loss to the surrounding soil (Figure 3.6e). During the thawing period, subsurface water flow causes the deviation of temperature change rate (Figure 3.6d). The magnitude of temperature rise due to subsurface water flow does not diminish with depth. The thermal departure is used for interpretation of subsurface water flow, which agrees with theoretical analysis (Bredehoeft and Papaopulos 1965, Lu and Ge 1996) and field observation (Kurylyk et al., 2017). Furthermore, in addition to local subsurface water flow, the rate of warming is also enhanced by spring snowmelt water and summer rainfall which saturate the thawed soil. Warm water accumulates at the embankment toe and supports lateral flow in the active layer.

Subsurface water flow under embankments triggers strong advective heat fluxes, enhances the heat exchange between the embankment and the underlying permafrost, and finally leads to the

decrease of the permafrost table depth at a faster rate than where no water flow occurs (Table 3.6). The rate of ALT increasing under the embankment slope is about 20 times faster than in the natural ground, which is only on average of 0.01 m·a^{-1}. As the active layer beneath the road embankment deepens, thawed ice-rich permafrost will lead to ground and road subsidence. Road embankment subsidence, due to thawing of ice-rich permafrost and melting of buried ice wedges, creates a positive feedback to warming. Indeed, as coarse embankment material with large interstitial voids subsides, it increases the bulk permeability (Table S3.1) (the permeability of sand and gravel is much higher than for silt) and further enhances subsurface water flow (Figure 3.7). As more subsurface water flows through the embankment, the energy absorbed by the underlying permafrost increases, leading to additional permafrost thaw and more flow. The larger heat exchange rate can explain the relatively faster permafrost warming rate (0.08 °C·a^{-1}) and thawing rate (0.2 m·a^{-1}) at our study site. The measured increasing rates of ground temperature and active layer thickness linked with subsurface water flow are consistent with observation in Arctic gully system (Fortier et al., 2007) and support fast permafrost thawing rate caused by water flow, based on the hydrological modeling of conceptual hillslopes in permafrost regions (Bense et al., 2009, Ge et al., 2011, Kurylyk et al., 2016, Lamontagne-Hallé et al., 2018, Chiasson-Poirier et al., 2019).

Moreover, the coarse, permeable embankment material, built onto the natural ground, provides the preferential flow paths needed to enhance subsurface water flow. In this study, the road alignment is primarily perpendicular to the local hydraulic gradient (Figure 3.1b), but subsurface water flow is also possible sub-parallel to the road embankment. Further, the macroscopic heterogeneity and anisotropy of the subsurface can also control the direction of water flow (e.g., Mackay 1983, Paquette et al., 2017, 2018).

Overall, subsurface water flow causes a faster thawing rate of permafrost under the embankment. This process is strong enough to melt ground ice, followed by consolidation and thaw-induced embankment subsidence, the development of cracks, and surface depressions. The preferential flow paths also redistribute the temperature of embankment subgrade and subbase. The preferential subsurface water flow results in a faster thawing rate of frozen soil compared to where there is minimal water flow, which induces differential settlement of

embankment. Field investigation along the Alaska Highway shows that degrading permafrost has already led to severe structural damages to the highway such as deep longitudinal cracks, extended depressions, and unevenness in the road surface and embankments (de Grandpré et al., 2012, Stephani 2013, Calmels et al., 2015, Malenfant-Lepage 2015).
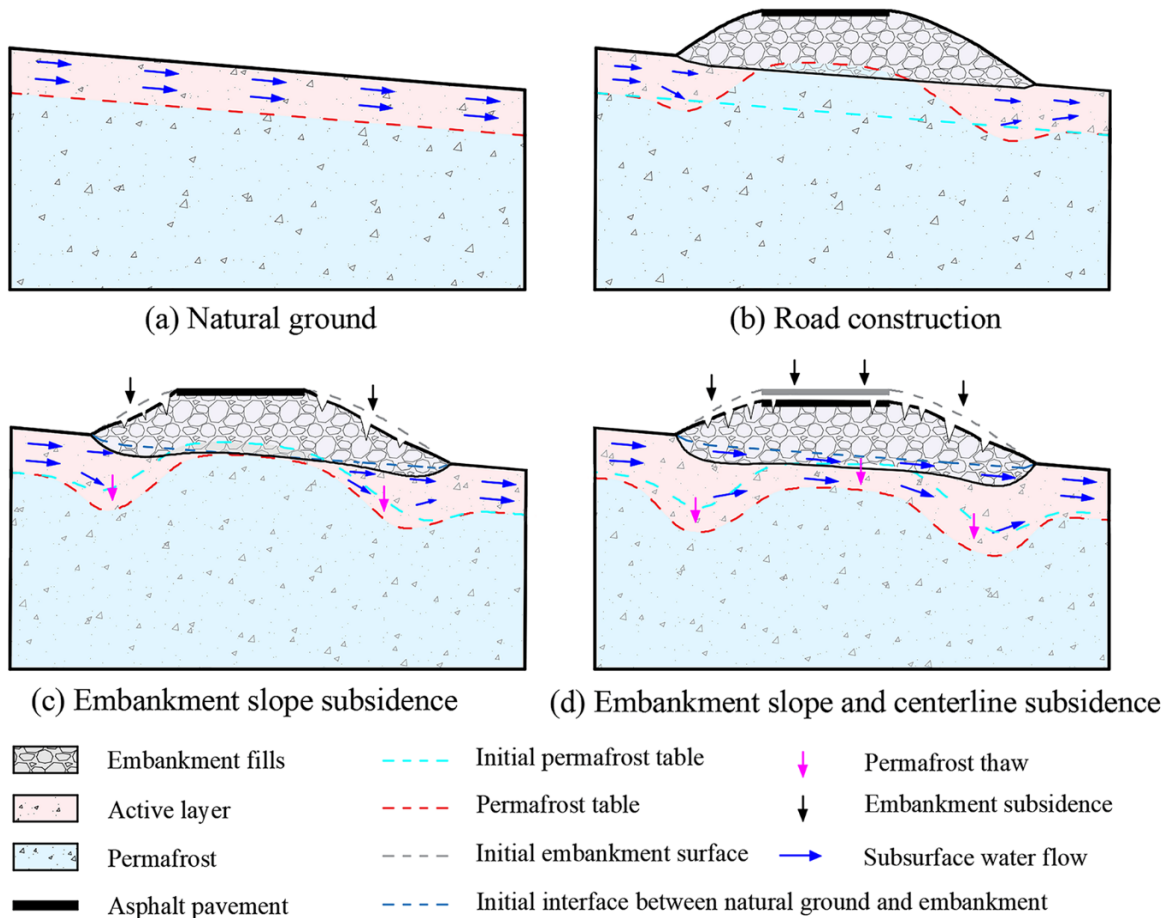
Figure 3.7. Conceptual diagram of permafrost degradation and subsurface water flow and the impact on the stability of road embankment. (a) Natural ground; (b) road embankment construction; (c) embankment slope subsidence caused by thaw of ice-rich permafrost after several-year operation; and (d) embankment slope and centerline subsidence after several-decade operation.

3.5. CONCLUSIONS

To the authors' knowledge, this study is the first to investigate and quantify the influence of seasonal surface water infiltration and subsurface water flow on the stability of embankment subbase and subgrade in a permafrost region. We classify the anomalous temperature gradients

associated with water flow into two categories: surface water infiltration, including spring snowmelt water and summer rainfall infiltration, and subsurface water flow. Evidence in support of heat advection water movement includes the rapid rate of ground temperature increase and decrease and reversals in the thermal gradient.

The infiltration of spring snowmelt causes a very rapid temperature increase in the road embankment, within just a few days. When large amounts of plowed snow are placed at the upstream side of embankment, lateral meltwater flow can warm the embankment subgrade.

The infiltration of summer rainfall lowers near-surface temperatures while simultaneously warming embankment fill materials at depth. In a changing climate, more frequent light rainfall may mitigate the thermal stability of road embankment when infiltrated water remains in the near surface. Conversely, more frequent heavy rainfall will adversely affect the thermal stability of a road embankment built on ice-rich warm permafrost, as water is able to percolate deeper and warm the embankment material.

Heat advection triggered by lateral subsurface water flow warms the soil, increases active layer thickness, melts ground ice, degrades permafrost and thus enlarges flow paths. The thaw-induced embankment subsidence eventually causes coarse high hydraulic conductivity sand and gravel to intercept the water table, which creates a positive feedback to warming by increasing subsurface water flow, increasing the energy absorbed by the underlying permafrost, and thus additional permafrost thawing over time.

The result of this pore water flow and heat flux is accelerated permafrost degradation and enhanced rates of destabilization of the overlying roadway embankment. The net result of these findings is that within the context of climate warming, we expect that permafrost under infrastructure will degrade faster than previously estimated in the coming decades due to increased subsurface water flow. With respect to northern infrastructure, such as roads, thaw-induced embankment subsidence will increase maintenance costs and reduce the lifespan of road embankment. The results from our research are of interest beyond Northern Canada, and are applicable to investigate the impact of mobile water flow on the thermal regime of pan-Arctic infrastructure (e.g., Dempster Highway, Canada, and Taylor Highway, Alaska, US), in the QTP (e.g.,

Qinghai-Tibet Highway and Railway, China), or undisturbed grounds (e.g., alpine meadow and aeolian sand in the QTP, China; polar desert in high Arctic regions). Additional engineered mitigation measures (e.g., culvert and ditch) need to be developed to accommodate subsurface water flow and control thaw settlement of embankment in permafrost areas. Our study suggests that further work of numerical simulation should consider the impact of surface and subsurface processes, such as precipitation infiltration and subsurface water flow.

3.6. ACKNOWLEDGEMENTS

3.7. SUPPORTING MATERIALS
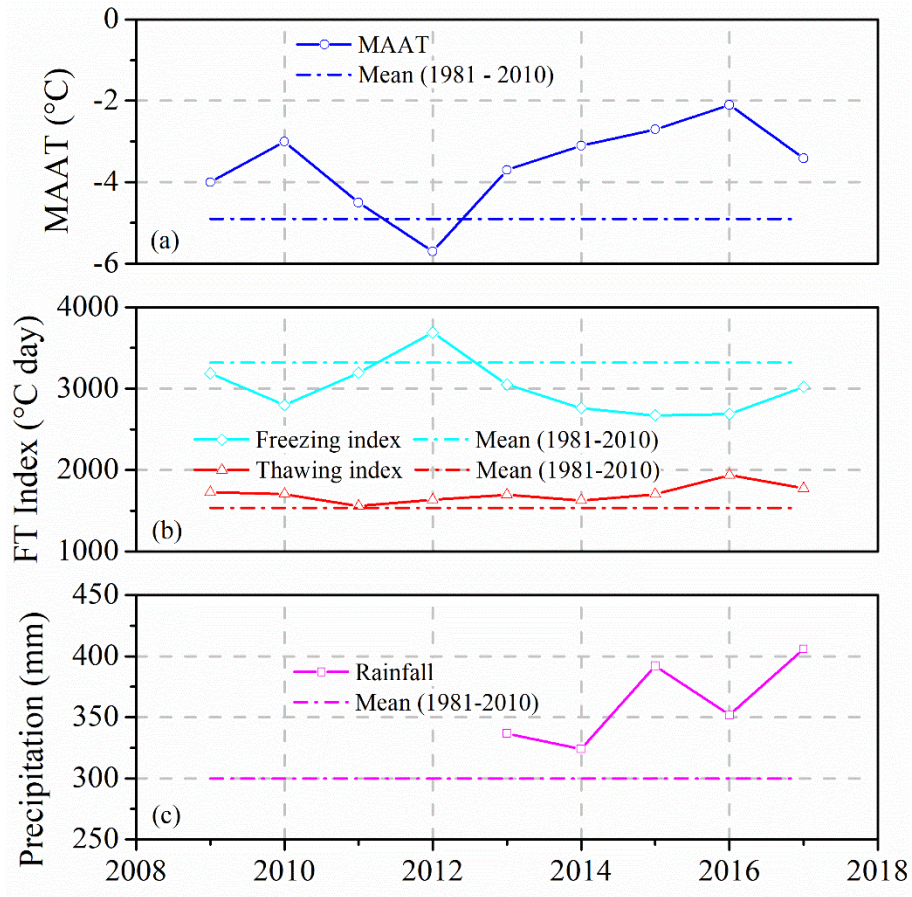
Figure S3.1. Meteorological data measured at the weather station near the Beaver Creek - Road Experimental Site (BC-RES). (a) Mean annual air temperature (MAAT); (b) Freezing/thawing index; and (c) Precipitation. The measured air temperature started in 2009, while the precipitation is only available starting in 2013. The dash dot lines represent the mean value over the period of 1981 to 2010 (Environment and Climate Change Canada, 2018).
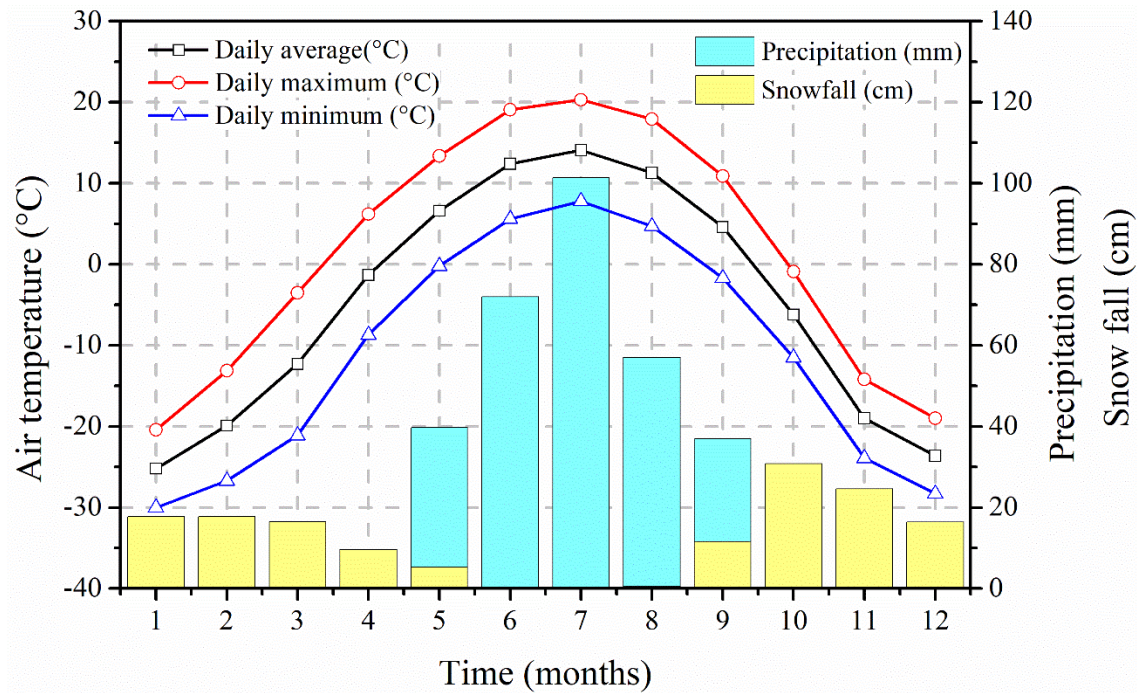
Figure S3.2. Meteorological data measured at the Beaver Creek airport weather station from 1981 to 2010 (62° 24' N, 140° 52' W, elevation: 649 m above sea level), 8 km away from the Beaver Creek - Road Experimental Site (BC-RES) (Environment and Climate Change Canada, 2018).
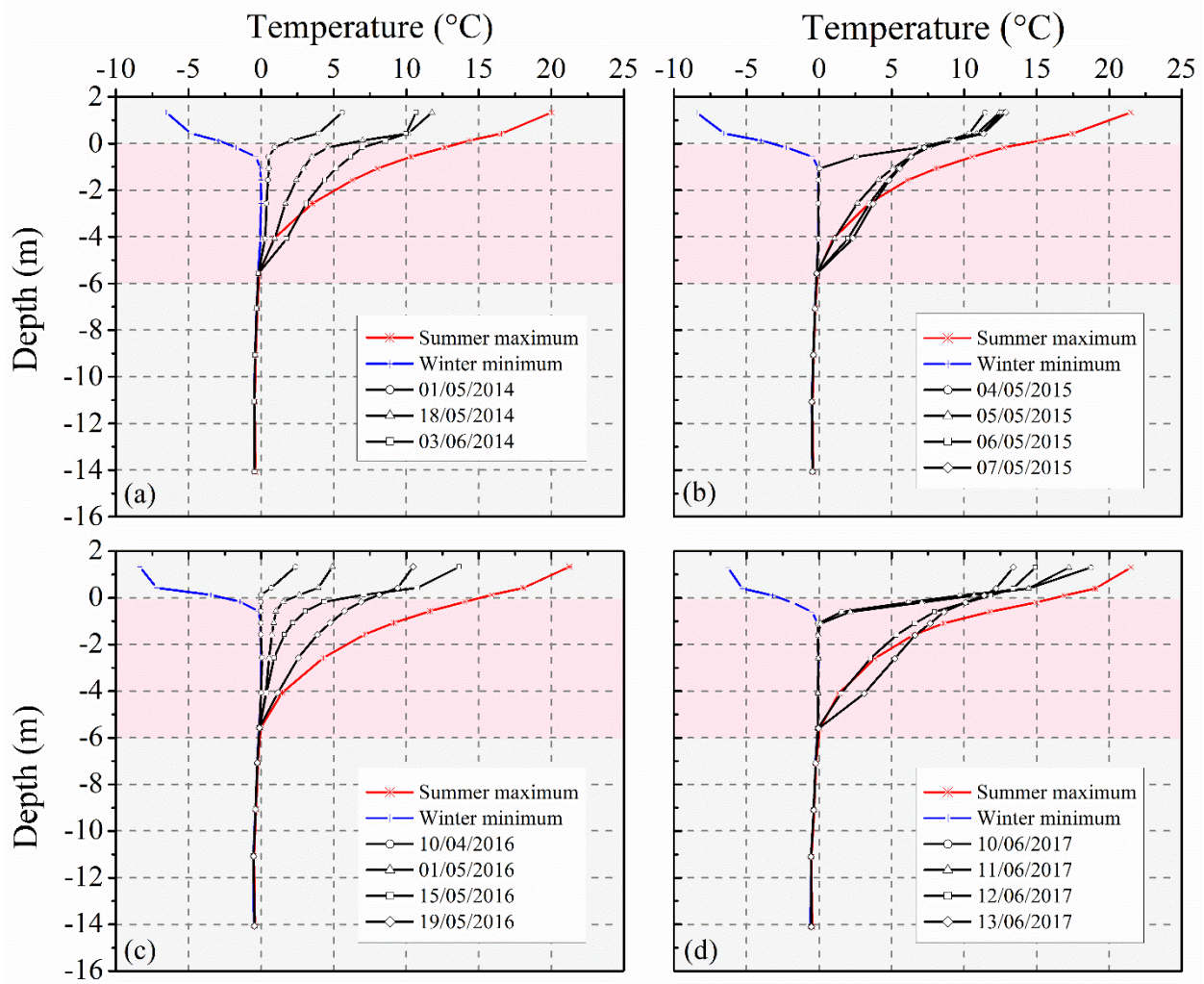
Figure S3.3. Thermal envelope in (a) 2014; (b) 2015; (c) 2016; and (2017). Note the depth is relative to the interface between the natural ground and the embankment material.

Table S3.1. Hydraulic and thermal properties of the embankment material, peat, and silt

	Embankment material (gravel/sand)	Organic soil (peat)	Mineral soil (silt)	Source
Porosity (%)	0.4	0.85	0.55	de Grandpré et al., 2012; Darrow et al., 2013; Sliger, 2016
Gravimetric water content (%)	3.1	358.2	49.8	Doré and Mercier, 2008; Darrow et al., 2013; Sliger, 2016
Unfrozen hydraulic conductivity (m·s^{-1})	5.04×10^{-5}	9.38×10^{-6}	3.33×10^{-6}	de Grandpré et al., 2012; Zottola et al., 2012; Darrow et al. 2013
Frozen hydraulic conductivity (m·s^{-1})	1×10^{-7}	8.7×10^{-7}	3.3×10^{-8}	Andersland and Ladanyi. 2004; Watanabe et al., 201
Unfrozen thermal conductivity (W·m^{-1}·K^{-1})	0.83	0.38	0.76	Zottola et al., 2012; Darrow et al., 2013
Frozen thermal conductivity (W·m^{-1}·K^{-1})	1.45	1.2	2	Zottola et al., 2012; Darrow et al., 2013

Table S3.2. Detailed information of sensors location in the Beaver Creek - Experimental Road Site.

Variable	Ground surface condition	Record period (mm/dd/yyyy)	Reporting interval	Resolution/ Accuracy	Location	Sensor depth/height (m)	Company
Air temperature (°C)	-	Oct./01/2008 - Jun./11/2018	Hourly	0.01 °C / ± 0.1 °C	Beside embankment toe	2 m above the surface	Shielded AT probe ; Campbell Scientific TE525WS; manufactured by Texas Electronics and distributed in Canada by Campbell Scientific
Precipitation (mm)	-	Oct./22/2012 - Jun./11/2018	Hourly	8.25 ml / 1.0 %		1 m above the surface	
Soil temperature in natural ground (°C)	Covered by taiga vegetation			± 0.1 °C between -10 °C to +10 °C;	30 m away from embankment	0.3, 0.7, 1.1, 1.5, 2.0, 3.0, 4.0, 5.0, 6.0, 8.0	Thermistor string;
Soil temperature of embankment subbase and subgrade (°C)	Covered by a 30-cm tall grass covered by a 0.5 m-high shed	Oct./01/2008 - Jun./11/2018	4-hour interval		Center of embankment slope	0.1, 1.4, 1.7, 2.0, 2.4, 2.9, 3.4, 4.4, 5.9, 7.4, 8.9, 10.9, 12.9, 15.9 0.1, 0.8, 1.1, 1.4, 1.8, 2.3, 2.8, 3.8, 5.3, 6.8, 8.3, 10.3, 12.3, 15.3 0.1, 0.6, 0.9, 1.2, 1.6, 2.1, 2.6, 3.6, 5.1, 6.6, 8.1, 10.1, 12.1, 15.1	
	Unmitigated (bare)			± 0.2 °C between -50 °C to +30 °C			
Data logger	-	-	-	-	Center of embankment slope	1 m above the surface	CR1000; Campbell Scientific

Chapter 4 - SURFACE ENERGY BALANCE OF SUB-ARCTIC ROADS WITH VARYING SNOW REGIMES AND PROPERTIES IN PERMAFROST REGIONS

Authors: Lin Chen, Clifford I. Voss, Daniel Fortier & Jeffrey M. McKenzie

CRediT author statement

Lin Chen: Conceptualization, Methodology, Software, Field survey, Writing- Original draft preparation.

Clifford I. Voss: Supervision, Software, Reviewing and Editing.

Daniel Fortier: Supervision, Field survey, Reviewing and Editing.

Jeffrey M. McKenzie: Supervision, Reviewing and Editing.

ABSTRACT

The surface energy balance (SEB) strongly influences the thermal state of permafrost, cryohydrogeological processes, and infrastructure stability. Road construction and snow accumulation, for example, affect the energy balance of the embankment and underlying permafrost. Herein, we use an experimental road section of the Alaska Highway, Yukon, Canada to develop a SEB model to investigate and quantify the surface energy components and ground surface temperature (GST) for different surface cover types with varying snow regimes and

properties. Simulated and measured ground temperatures (2008-2018 on Alaska Highway) are in a good agreement, and our results show that the quantity of heat entering the embankment center and slope is mainly controlled by net radiation, and less by the sensible heat flux. In spring, lateral ground heat flux from the embankment center to the slopes leads to earlier disappearance of the seasonal snow cover on the embankment slope. In winter, the insulation created by the snow cover on the embankment slope reduces heat loss by a factor of three compared with the embankment center where the snow is plowed. The simulated surface offsets (i.e., temperature difference between mean annual air temperature and mean annual GST) are 5.0 °C and 7.8 °C for the embankment center and slope, respectively. Furthermore, the ground heat flux released on the embankment slope exponentially decreases with increasing snow depth, and linearly decreases with earlier snow cover in fall and earlier disappearance of the seasonal snow cover in spring.

4.1. INTRODUCTION

Climate warming has led to an increase of surface temperatures (IPCC 2015) and concomitant accelerated permafrost degradation at a global scale (Biskaborn et al., 2019). The amplified Arctic warming of surface air, which is expected to be at least double the global average value (Miller et al., 2010, Huang et al., 2017), will adversely impact sustainable development of Arctic communities (Larsen et al., 2008), the surface and subsurface distribution of water resources (McKenzie and Voss 2013, Kurylyk et al., 2016), and stability of existing infrastructure overlying permafrost (Nelson et al., 2001, Hjort et al., 2018). Geohazard assessment, infrastructure risk-assessment, design and operating policy (Cheng 2005a, Anisimov and Reneva 2006, Obu et al., 2019, Yumashev et al., 2019) are required to evaluate how atmospheric warming will be transferred to the infrastructure and underlying permafrost. The thermal boundary condition (TBC) approach has been used to determine how heat propagates through infrastructure (Cheng 2005a, Wu et al., 2007, Doré et al., 2016, Chen et al., 2017b, Zhang et al., 2019), how it affects water resources dynamics (McKenzie and Voss 2013, Quinton and Baltzer 2013, Kurylyk et al., 2016, Evans and Ge 2017) and its impact on permafrost distribution (Ge et al., 2011, Way and Lewkowicz 2018) in cold regions. Surface disturbances, such as pavement construction, modification of snow deposition patterns, and water ponding, alter the surface energy balance (SEB) and simultaneously affect the thermal state of permafrost (Ling and Zhang 2004, Wu et al., 2007, Zhang et al., 2008b, O'Neill and Burn 2017, Chen et al., 2018, Jafarov et al., 2018, Luo et al., 2018, Zhang et al., 2018). Such surface changes have locally accelerated permafrost warming and thawing rates. Additionally, these changes have negatively impacted the thermal stability of transportation infrastructure in high-altitude and high-latitude permafrost regions. Reports of damaged infrastructure are numerous in circumpolar regions. Permafrost degradation adversely have affected infrastructure such as the Alaska, Taylor, Inuvik-Tuktoyaktuk and Dempster Highways in Alaska and Northern Canada (e.g., de Grandpré et al., 2012, Malenfant-Lepage et al., 2012b, Zottola et al., 2012, Darrow and Jensen 2016, O'Neill and Burn 2017, Kong et al., 2019), the Tasiujaq, Inuvik, Puvirnituq, and Iqaluit Airstrips in Canada (e.g., Fortier et al., 2011, Doré et al., 2012, Ghias et al., 2017), the Baikal-Amur and Trans-Siberian Railways in Russia (Kondratiev 2017). Similarly, many engineering challenges caused by permafrost thaw were found in Qinghai-

Tibet Plateau (QTP) Highway and Railway (e.g., Lai et al., 2003, Cheng 2004, Wu et al., 2007, Chen et al., 2018, Zhang et al., 2019), the Gonghe-Yushu Expressway (e.g., Dong *et al.*, 2019; Liu *et al.*, 2019) on the QTP, Western China, and the Mo'he Airstrip and Mobei Highway in Northeast China (Yu et al., 2012, Mao et al., 2019).

To simplify the complex heat transfer in an atmosphere-embankment-permafrost system, the TBC approaches in previous modelling studies are typically obtained by a specified ground surface temperature (GST) based on either the adherent-layer theory (i.e., annual GST can be approximated as a sinusoidal wave, which is a combination of surface offset and AT) (e.g., Zhu 1988, Li et al., 1998, Lai et al., 2004, Bense et al., 2009, Chen et al., 2018) or with an *n*-factor equation (i.e., a ratio of GST to air temperature, AT) (e.g., Lunardini 1978, Karunaratne and Burn 2004, Fortier et al., 2011, Kong et al., 2019). For the adherent-layer theory, a surface offset (i.e., temperature difference between mean annual AT and mean annual GST) is generally adopted to represent the difference in absorbed solar radiation by different ground surface cover types (Zhu 1988, Wu et al., 2007, Zhang et al., 2018). The suggested surface offsets of 6.5 °C and 4.0 °C (Zhu 1988) have been widely adopted to obtain the GSTs of asphalt-paved surface and gravel/sand surface, respectively, in heat transfer models simulating the interaction between the atmosphere, a road embankment and the underlying permafrost (e.g., Li et al., 1998, Lai et al., 2003, Wen et al., 2005, Zhang et al., 2005, Chen et al., 2018). Alternatively, GSTs predicted by the n-factor approach are also widely adopted to simulate the impact of different surface cover types, e.g., asphalt-paved or snow-covered surface, on the GSTs of a road embankment (Lunardini 1978). The value of the *n*-factor implicitly encompassed the impact of snow depth, snow thermal properties (Sturm and Johnson 1992, Sturm et al., 2002, Domine et al., 2016) and surface cover types (Lunardini 1978, Goodrich 1982, Richard et al., 2015). To couple the thermal processes on the top surface and in the subsurface, a SEB modelling approach, driven by meteorological data, has been proposed for the GST estimation of a road embankment (Solaimanian and Kennedy 1993, Hermansson 2001, Dumais and Doré 2016). When the conductive ground heat flux was simplified by a percentage of absorbed solar radiation and the snow cover was not considered, GSTs were linearly correlated with net radiation (Chou et al., 2012, Dumais and Doré 2016, Qin et al., 2017a).

For cold-regions transportation infrastructure, unresolved questions remain about understanding how atmospheric heat enters the seasonal snow layer, the embankment slope (i.e., the area from the edge of the road to the adjacent natural ground), the embankment center (i.e., the area between left and right shoulder of the road) and ultimately the underlying permafrost layer. Several limitations apply to the previously described TBCs. Firstly, the empirical relationships between GST and AT are site-specific and impractical over larger areas due to different regional climate conditions, such as AT variation, solar radiation, and snow depth. Also, projected GST variations (a sinusoidal wave) by the adherent-layer theory approach is not suitable to predict the GSTs of road embankments in Alaska and northern Canada, due to the seasonal presence of a thick snow cover. Secondly, previous TBC methods negate the feedback of subsurface processes on the SEB. It is assumed that the GST is known prior to simulating the ground temperature profiles and the thawing period of the predicted GST is fixed and consistent during the duration in which AT is positive. Thirdly, although impacts of snow insulation have been recognized in previous studies (Ishikawa 2003, Ling and Zhang 2004, Throop et al., 2012, O'Neill and Burn 2017, Jafarov et al., 2018, Way and Lewkowicz 2018), the thermal impacts of snow depth, timing, and duration on ground heat flux entering a road embankment are poorly understood.

Our study addresses the question: *what is the SEB of an embankment center and slope in permafrost regions with seasonal snow cover?* The objectives of the present study are to develop a novel SEB model to simulate the GST for different surface cover types with varying snow regimes and properties; to calibrate and validate the SEB model against the measured data from the Alaska Highway (2008-2018); to investigate the characteristics of the GSTs and ground heat fluxes entering an embankment center and slope; and to estimate the role of seasonal snowpack depth, timing and duration on the ground heat fluxes through the embankment slope. We achieve these objectives through a combination of field observations, a SEB model, and one-dimensional finite difference conductive heat transfer model with phase change. Furthermore, this SEB model can allow the user to directly represent the design configuration in the model and can be used to improve estimation of the ground surface temperature where direct measurements are not available.

4.2. STUDY SITE AND METHODS

We evaluated the SEB model, driven by the meteorological forcing, against field observations from the Beaver Creek - Experimental Road Section (BC-RES) (Figure 4.1). The SEB model has the following assumptions. Firstly, the embankment fill materials are highly compacted low frost-susceptible gravel/sand with low water content (2.3 % to 7.2 %) (Doré and Mercier 2008, Malenfant-Lepage et al., 2012a), so we assume that the air convection by wind in the embankment fill is negligible (Doré et al., 2016). In addition, the processes of cryosuction, ice segregation and ice lens formation are not considered. Secondly, as the embankment subbase (0.0 m to 1.6 m depth) at BC-RES is above the water table, the impact of lateral heat advection
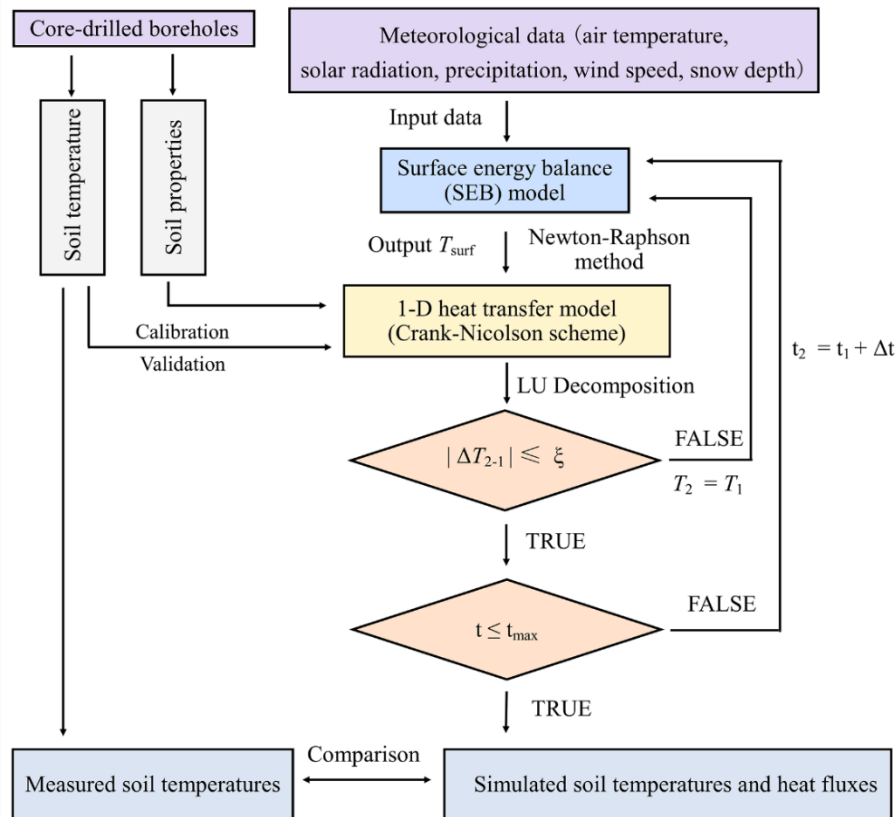
Figure 4.1. Flowchart depicting the flow data of surface energy balance (SEB) model and one-dimensional heat transfer model. The ξ is the deviation convergence tolerance (10^{-6}) for solvers iteration during temperature solution. T and t are temperature and time, while the subscripts 1 and 2 represent the results obtained at the previous and current time step, respectively. The Δt is the model time step and t_{max} is the maximum duration of the simulation period. The T_{surf} is the snow surface temperature (SST) when the snow layer is present, or the ground surface temperature (GST) when the snow layer is absent.

linked with subsurface water flow is not included. Thirdly, the heat advected by surface water infiltration is neglected, due to the small amount of water involved and the short length of time that water is in contact with the ground (Chen et al., 2020a). Only the energy released by temperature differences between rainfall and the ground surface is considered in this SEB model and the summer rainfall water is assumed to have the same temperature as the atmosphere. Fourthly, the impact of the slope aspect and angle are neglected due to small slope angle (less than 10 °) and thin embankment thickness (~ 1 m). The time step used in the modeling was one day, so diurnal variations were not included, which is due to using empirical equations to calculate long wave radiation and heat exchange coefficient by wind because these equations are based on daily data.

4.2.1. Study site

In the Beaver Creek area (south-western Yukon, Canada), a highway research facility with a road test section was constructed at km 1865 of the Alaska Highway in 2008 (Figure 4.2). The BC-RES was constructed to study the thermal performance of road embankments built on permafrost, with and without mitigation techniques, aimed to accommodate the impact of road embankment on permafrost (Reimchen et al., 2009, Kong et al., 2019). Details regarding soil stratigraphy and thermal monitoring at the BC-RES can be found in Reimchen et al., (2009), Malenfant-Lepage et al., (2012b), Coulombe et al., (2012), and Fortier *et al.* (2018). The Beaver Creek region is in the Klondike Plateau of the Western Boreal Cordillera (Statistics Canada 2018). The regional permafrost is discontinuous but widespread (50 - 90 % permafrost presence) and potentially composed of a thick and ice-rich sediments (Brown et al., 2001, O'Neill et al., 2019).

The mean annual air temperature (MAAT) from 1981 to 2010 is -4.9 °C at Beaver Creek airport (62° 24' N, 140° 52' W, elevation: 649.0 m above sea level, 8 km away from the BC-RES), with an average AT of -25.2 °C in January and 14.1 °C in July (Figure S4.1) (Environment and Climate Change Canada, 2018). The thawing and freezing indices represent an average of 1537.7 thawing degree-days (TDDs) and 3321.8 freezing degree-days (FDDs), respectively (1981-2010) (Environment and Climate Change Canada, 2018). Mean annual precipitation (1981-2010) is 417 mm, of which 300 mm falls as rain (Environment and Climate Change Canada 2018). Snowfall

begins annually in September and snowmelt starts in April in the undisturbed natural ground (Environment and Climate Change Canada 2018). Snow accumulated at the embankment slope disappears several weeks earlier than on the natural ground adjacent to the road (Chen et al., 2020a).
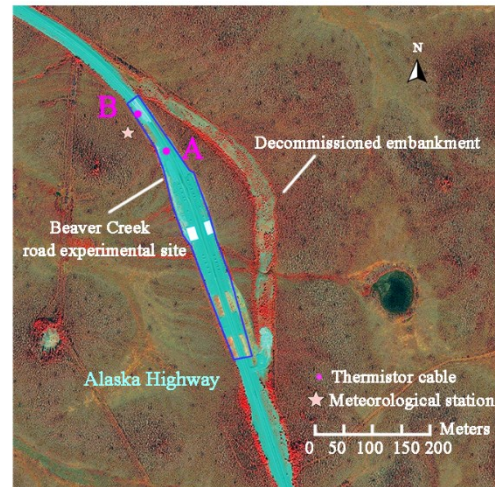
(a) Map of Yukon Territory   (b) False-color satellite image of BC-RES

(c) Asphalt-paved surface of embankment center   (d) Snow cover accumulation on embankment slope

Figure 4.2. (a) Map of Yukon Territory showing location of the Beaver Creek - Road Experimental Site (BC-RES) (62° 20' N, 140° 50' W) with a red star (modified from Natural Resources Canada, 2014); (b) false-color satellite image of experimental road test section at Beaver Creek (WorldView II image, taken August 4th, 2010 at 21h30); (c) photo of the asphalt-paved embankment center. The points A and B represent the location of the vertical thermistor cable of embankment center and slope, respectively; and (d) photo of embankment slope covered with snow in winter.

The embankment fill materials of the BC-RES are made of gravel and sand with low gravimetric moisture content (2.3 % to 7.2 %), lying directly on natural ground (peat over silt) (Doré and Mercier 2008). The embankment center surface is paved with asphalt (Figure 4.2c), while the

80

surface of the embankment slope is sand/gravel. Snow is plowed from the embankment center surface (Figure 4.2c), while a thick (~60 cm) snow layer remains on the embankment slope surface during winter and until the spring. Snow cover on the embankment slope is undisturbed and is not affected by the snow that is plowed from the road (Figure 4.2d).

4.2.2. Measured meteorological variables and soil temperatures

In 2008, a meteorological station was installed about 30 m from the road embankment at the BC-RES to provide hourly AT, rain precipitation, wind speed and direction, and incoming solar radiation data (Fortier and Chen 2020b). The dew-point temperature and humidity at the BC-RES were calculated by a fitting equation related to locally measured AT (Figure S4.1). Details about the climate measurement and sensors used are listed in Table S4.1. The snow thickness surveys were conducted just before the snowpack started to melt using a graduated pole in March 2010 and 2013. Additionally, the wind speeds were measured at the height of 3.5 m (Table S4.1), but the topography of the road embankment modifies the wind profile and affects the wind speed variations at the leeward and windward side (Brown et al., 2001, O'Neill et al., 2019). Thus, in order to quantify uncertainty, a range of ± 10 % (wind speed difference between embankment surface and measurements, based on a power law of wind profile, Irwin, 1979) of measured wind speed was selected. The GST deviations (difference of simulated GST between two cases with the modified and measured inputs) were calculated and presented in the supporting materials (Figure S4.3). The simulated results show that the variations (± 10 %) of wind speed had little impact on mean annual GST (mean ± SD = 0.04 ± 0.09 °C) (Figure S4.3). The maximum deviation was 0.26 °C in summer (mean ± SD = 0.14 ± 0.06 °C). The corresponding value in winter was smaller, only 0.07 °C (mean ± SD = 0.04 ± 0.01 °C).

Measured temperatures of the embankment subbase (i.e., a layer of fill material) and subgrade (i.e., the native material under an embankment) at multiple depths were available starting in October 2008 (Fortier and Chen 2020a). The thermistor strings were installed in 15-m deep boreholes located at the centerline of the road (snow-free) and in the slope of the embankment. Thermistors strings were placed inside a casing of polyvinyl chloride (PVC) filled with silicone oil to inhibit air convection in the hole and to provide effective contact with the ground. All the

sensors are wired to an external data logger (CR1000, Campbell Scientific). Details about each sensor's location are listed in Table S4.1.

4.2.3. Surface energy balance model

The SEB model was driven by the net radiation (Q_{net}), sensible heat flux (Q_h), heat flux of vapor exchange from the surface (Q_v), conductive ground heat flux through the snow and ground (Q_c), rainfall heat (Q_p), and stored energy (Q_0). The measurement of incoming solar radiation is available at the BC-RES, while the incoming and outgoing long-wave radiation are calculated with an empirical equation. In our approach, the heat flux is negative when the energy is lost from the embankment. The SEB is expressed as (Figure 4.3):

$$Q_{net} + Q_p - Q_h - Q_v - Q_c = Q_0 \tag{4.1}$$
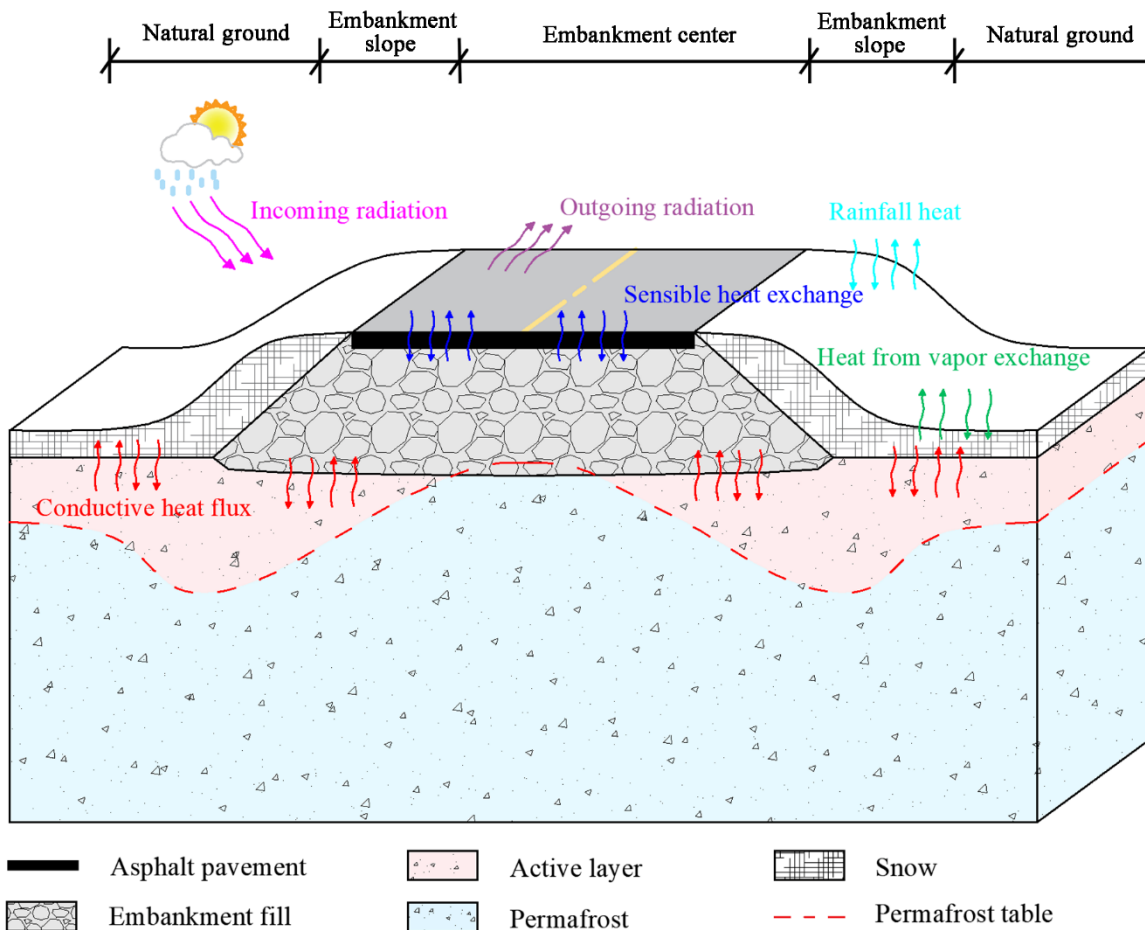
Figure 4.3. Schematic showing the primary components of the surface energy balance.

4.2.3.1. Net radiation

The net radiation (Q_{net}) of an embankment surface consists of net shortwave radiation (Q_s), incoming long wave radiation (Q_{li}), and outgoing long wave radiation (Q_{le}).

$$Q_{net} = Q_s + Q_{li} - Q_{le} \tag{4.2}$$

The net shortwave radiation (Q_s) absorbed at the surface can be expressed as:

$$Q_s = Q_{si} \times (1 - \alpha) \tag{4.3}$$

where incoming solar radiation flux (Q_{si}) is measured at the meteorological station, albedo (α) is a measure of the reflected solar radiation as a percentage of the incident radiation. The albedo can be modified at each time step to reflect the evolution of the albedo due to changing surface conditions. The albedo of paved embankment surface used in the SEB model was measured at the study site (Richard et al., 2015, Dumais and Doré 2016):

The temporal decay of snow albedo, α_{snow}, is approximated with an empirical relationship based on snow density (ρ_s, kg·m^{-3}) developed by Anderson (1976). When the snow density is larger than 450 kg·m^{-3}, the albedo during snowmelt can be calculated by linear (Ling and Zhang 2004, Anderson 1976) or exponential (Walter et al., 2005) functions.

$$\alpha_{snow} = 1.0 - 0.247 \times \left(0.16 + 110 \times \left(\rho_{snow} / 1000 \right)^4 \right)^{1/2} \quad 50 \leq \rho_{snow} \leq 450 \tag{4.4}$$

The incoming long wave radiation of the embankment surface is given by the following empirical equations (Satterlund 1979, Ling and Zhang 2004):

$$Q_{li} = 1.08 \times \left(1 - \exp\left(-\left(0.01 e_a \right)^{\frac{T_a + 273.15}{2016}} \right) \right) \times \sigma \times \left(T_a + 273.15 \right)^4 \tag{4.5}$$

$$\log_{10} e_a = 11.40 - \frac{2353}{T_{dp} + 273.15} \tag{4.6}$$

where T_a is the daily mean AT (°C), T_{dp} is daily dew-point temperature (°C), e_a is atmospheric vapor pressure (Pa), and σ is the Stefan-Boltzmann Constant (5.670367$\times$10^{-8} W·m^{-2}·K^{-4}).

The outgoing long wave radiation can be described using the Stefan-Boltzmann Equation (Solaimanian and Kennedy 1993, Walter et al., 2005):

$$Q_{le} = -\varepsilon \times \sigma \times \left(T_{surf} + 273.15 \right)^4 \qquad (4.7)$$

where ε is the emission coefficient of the surface (Campbell and Norman 2012), T_{surf} (°C) is the snow surface temperature (SST) when the snow layer is present, or the GST when the snow layer is absent.

4.2.3.2. Heat exchange by wind, rainfall, and vapor

The heat exchange by wind convection and free convection due to the temperature difference between the air and the ground surface is calculated as described by Solaimanian and Kennedy (1993):

$$Q_h = h \times \Delta T_{surf-a} \qquad (4.8)$$

where ΔT_{surf-a} is the temperature difference between the T_{surf} and AT, and the parameter h depends on the wind speed and the T_{surf}, as indicated by the following equation (Solaimanian and Kennedy 1993):

$$h = 698.24 \times \left(0.00144 \left(T_m + 273.15 \right)^{0.3} U^{0.7} + 0.00097 \left| \Delta T_{surf-a} \right|^{0.3} \right) \qquad (4.9)$$

where U is the wind speed (m·s^{-1}), and T_m is the average value of the AT and T_{surf} (°C).

The temperature of rainfall water is assumed to be the same as the atmosphere (T_a) and heat is added to the ground surface by lowering the rain's temperature to the surface temperature (T_{surf}) (Walter et al., 2005). Heat from rainwater is estimated as:

$$Q_p = C_w \times P_{rain} \times \left(T_a - T_{surf} \right) \qquad (4.10)$$

where C_w is the heat capacity of water (4186 kJ·m^{-3}·K^{-1}), and P_{rain} is the daily rainfall (m·daily^{-1}).

The daily heat fluxes due to vaporization and condensation are expressed by (Walter et al., 2005, Campbell and Norman 2012):

$$Q_v = L_v \times \left(\frac{\rho_v - \rho_a}{r_v} \right) \qquad (4.11)$$

Saturation vapor density at a temperature can be calculated with (Jensen and Allen 2016):

$$\rho = \exp\left(\frac{16.78T - 116.8}{T + 272.3} \right) \times \left(\frac{1}{273.15 + T} \times \frac{1}{R} \right) \qquad (4.12)$$

where L_v is the latent heat of vaporization (2 500 kJ·kg^{-1}), R is the thermodynamic vapor constant (0.4615 kJ·kg^{-1}·K^{-1}), ρ_v is assumed to be the saturation vapor density (kg·m^{-3}) at the GST, and ρ_a is the saturation vapor density (kg·m^{-3}) at the dew-point temperature (T_{dp}). The resistance to vapor exchange (day·m^{-1}), r_v, is obtained based on the turbulent eddy mechanisms (Walter et al., 2005, Campbell and Norman 2012).

4.2.3.3. Heat conduction through the snow and ground

Snow cover significantly changes the heat loss to the atmosphere (Goodrich 1982, O'Neill and Burn 2017). In our SEB model, appearance and disappearance of the snow cover and its thickness are described as input data as a function of time. Heat conducted through the snow and the ground is given by (Solaimanian and Kennedy 1993, Liston and Hall 1995):

$$Q_c = \left(T_{surf} - T_{sub} \right) \times \left(\frac{d_{fresh}}{k_{fresh}} + \frac{d_{old}}{k_{old}} + \frac{d_{hoar}}{k_{hoar}} + \frac{d_g}{k_g} \right)^{-1} \qquad (4.13)$$

where T_{surf} and T_{sub} represent surface and soil temperatures at the bottom of a soil layer (°C); k is the thermal conductivity (W·m^{-1}·K^{-1}); d is the thickness of snow or soil layer (m); subscripts of fresh, old, hoar, and g represent fresh snow, old snow, depth hoar, and ground, respectively.

The snow thermal conductivity, k_{snow} (W·m^{-1}·K^{-1}), was estimated by the correlation with its density (Yen 1965). We compared three empirical equations from Yen (1965), Anderson (1976) and Goodrich (1982), developed at study sites having similar climate conditions with the BC-RES (See Figure S4.2a). The differences of calculated values among three equations are less than 0.03 W·m^{-1}·K^{-1} (SD = 0.029), when the snow density ranges from 150 kg·m^{-3} to 550 kg·m^{-3}.

$$k_{snow} = 3.2217 \times 10^{-6} \times \rho_{snow}^2 \qquad (4.14)$$

The snow volumetric heat capacity, C_{snow} (J·m^{-3}·K^{-1}), is related to density (Goodrich 1982).

$$C_{snow} = 2.09 \times 10^{-3} \times \rho_{snow}$$

(4.15)

The snow density (kg·m^{-3}) is calculated by the following empirical equations (US Army Corps of Engineers 1956, Schmidt and Gluns 1991).

$$\rho_{snow} = \begin{cases} 67.92 + 51.25^{(T_a/2.59)} & \textit{for fresh snow} \\ \left(90 + 130 d_{snow}^{0.5}\right)\left(1.5 + 0.17 T_{snow}^{1/3}\right)\left(1 + 0.1 U^{0.5}\right) & \textit{for old snow} \end{cases}$$

(4.16)

where T_a is the daily mean AT (°C), d_{snow} is the thickness of snowpack (m), T_{snow} is the temperature of snow (°C), and U is the wind speed (m·s^{-1}).

4.2.3.4. Stored energy

The stored energy is related to the heat capacity of the soil layer and temperature changes during each time step. Soil volumetric heat capacities can be defined as the sum of the volumetric heat capacities of each component multiplied by their respective volumetric fraction (Lunardini, 1991).

4.2.4. One-dimensional heat transfer model with phase change

Heat conduction with the ice-water phase change is considered through (Lunardini 1991):

$$\frac{\partial}{\partial t}\left(\left(\rho C + \rho_i L_f \left(\frac{\partial \theta_u}{\partial T}\right)\right) T\right) = \frac{\partial}{\partial z}\left(k \frac{\partial T}{\partial z}\right)$$

(4.17)

where, C is the heat capacity (J·m^{-3}·K^{-1}), k is the thermal conductivity (W·m^{-1}·K^{-1}), L_f is the latent heat of freezing (J·kg^{-1}), and ρ_i is the ice density (kg·m^{-3}). The unfrozen water content (θ_u) as a function of temperature was calculated with a linear freezing function, because the sand/gravel embankment fill has low moisture content (Doré and Mercier 2008) and most of the water froze at -1°C (Watanabe et al., 2011).

The ground heat flux (Q_c) is negative when the energy is lost from the embankment, while the Q_c is positive during periods of new energy gain. The Q_c passing at the embankment surface is computed using Fourier's Law (Lunardini 1991):

$$Q_c = k \frac{T_{z_1} - T_{z_2}}{z_1 - z_2}$$ (4.18)

where T_{z1} and T_{z2} are soil temperature measured at the depth of z_1 and z_2, respectively. For the simulated cases, T_{z1} represents the simulated GST and the value of z_1 equals 0. While for measured cases, the T_{z1} and T_{z2} illustrate the measured soil temperatures at the depth of 0.3 m and 1.0 m, respectively, due to the lack of available measured GST.

4.2.5. Numerical solution methods

The SEB equation was solved using the Newton-Raphson method (Hughes 1977). The conductive heat transfer equation was solved using a Crank-Nicolson finite difference scheme, which is numerically stable (Hughes 1977). The mesh size of the conduction model is 0.1 m. The matrix was solved with *lower-upper* decomposition method in MATLAB (R2019a). The criterion used to stop each iteration cycle is when the difference of temperature between two interactions is less than 10^{-6} for every time interval.

4.2.6. Calibration and validation

The one-dimensional heat transfer model combined with the SEB model was validated with meteorological data and soil temperatures measured at the BC-RES. The measured relative humidity from the Beaver Creek airport was used to validate the accuracy of Eq. 4.6. The coefficient of determination of linear fitting equation between daily minimum AT and dew-point temperature was calculated with measured data from the Beaver Creek airport. The model was manually calibrated by adjusting model input values of the soil thermal properties and minimizing difference between simulated values and measured data. For the calibrated models, both top and bottom TBCs were set as specified temperatures measured by thermistors at depths of 0.1 m and 1.6 m, respectively. The validated model was run with the calibrated parameters (Table S4.2). The top TBC was provided by the SEB model. The simulated specified temperatures (outputs of SEB model) were set as TBC at the snow surface when a seasonal snow cover was present, while at the embankment surface when the snow cover was absent. The bottom boundary was set as specified TBC with the soil temperatures measured at 1.6 m depth.

The initiation temperatures were estimated using linear interpolation of measured data by the thermistors at depths of 0.1, 1.0, 1.3 and 1.6 m. The model calibration was carried out based on data for the period from October 2008 - April 2013, while the validation period was from April 2013 to April 2018 because the measured SEB inputs of rainfall and solar radiation were only available after October 2012.

To quantitatively evaluate the performance of the SEB model, the following metrics are calculated. The root mean square error (RMSE) was used to estimate the uncertainty in the simulation (Chai and Draxler 2014). The mean absolute error (MAE) was used to estimate the absolute difference between simulated and measured values (Karjalainen et al., 2019, Zhang et al., 2019). The standard deviation (SD) was used to quantify the extent of deviation of a set of data values (Karjalainen et al., 2019).

The model was also evaluated by comparing the simulated GST and thawing period against the measurements at the depth of 0.3 m below the embankment center. The GSTs during the period 2014-2017 were selected and compared by three approaches: the SEB model, n-factor method, and adherent-layer theory method. The thawing period was defined by the duration when the ground surface temperature was above the 0 °C. For the n-factor method, the thawing n-factor (n_t) was calculated by a ratio of the positive degree-day sum at the ground surface to that in the air, while the corresponding ratio of the negative degree-day sum was for the freezing n-factor (n_f) (Lunardini 1978, Lunardini 1991). The start and end of the freezing and thawing seasons were determined independently for the air and ground surface (Lewkowicz et al., 2012). In addition, for the adherent-layer theory method (Zhu 1988), the ground surface temperature variation was approximated by a sinusoidal function. The surface offset was the temperature difference between mean annual AT and GST over the 4-year period. Details about adherent-layer theory method can be found in the references (Lai et al., 2003, Zhang et al., 2018, Zhang et al., 2019).

4.2.7. Sensitivity analysis of snow depth, timing, and duration

The snow thickness was approximated using linear interpolation during the snow-accumulation period and the snow cover was assumed to be the same over the whole validation period (Figure 4.4a). The maximum thickness of the snowpack was set as 0.6 m, based on the snow survey using

a graduated pole in March 2013 (just before the snowpack started to melt). Also, the snow survey in 2010 showed that the average snow thickness along the test section was 0.5 m (SD = 0.078 m, n =109), which is close to observed maximum snow thickness (~ 0.6 m) in 2013 and therefore improved the confidence in the snow depth interpolation. Based on thermal analysis of the GST at the BC-RES (Chen et al., 2020a), we assumed that the snowfall started on October 17th (t_1) and snowmelt began on March 26th (t_2). The snow totally disappeared on April 15th (t_3). The duration of the snow-accumulation period was 160 days, while spring snowmelt lasted 20 days (Figure 4.4b). Moreover, in all simulations, the snow cover was treated as several layers, with meshed size of 0.04 m to 0.1 m. According to the snow survey, three snow layers overlaid the ground surface during the snow-accumulation period, including a thin fresh snow layer, a thick old snow layer, and a thin layer of depth hoar (Figure 4.4a). The thin (0.1 m) fresh snow layer overlaid the old snow layer until the snow-melt period, while the thin (0.14 m) depth hoar layer was formed after the first snowfall and lasted until the snow disappeared. The density of the depth hoar layer was set as constant of 218 kg·m^{-3} (SD = 23, n = 7), according to the snow survey conducted in March 2013. Also, Sturm and Johnson (1992) reported that the density of depth hoar ranged from 160 kg·m^{-3} to 240 kg·m^{-3}, which improves our confidence in the accuracy of our snow properties due to similar climate condition between Fairbank, Alaska and Beaver Creek, Yukon. Although the snow on the surface of the embankment center is removed mechanically, a superficial layer of ice and snow remains on the pavement throughout the winter (Dumais and Doré 2016). We changed albedo from 0.14 to 0.3 to represent this thin layer of snow and a superficial layer of ice on the pavement surface (Dumais and Doré 2016). The snow-free and snow-covered periods were assumed to be consistent with the period when the GST of the embankment center was positive.

A sensitivity analysis was used to study the effects of the snow depth, timing, and duration on the magnitude of ground heat fluxes through the embankment subbase and subgrade. During the sensitivity analysis, we changed one parameter at a time, while holding all others constant (Figure 4.4b).
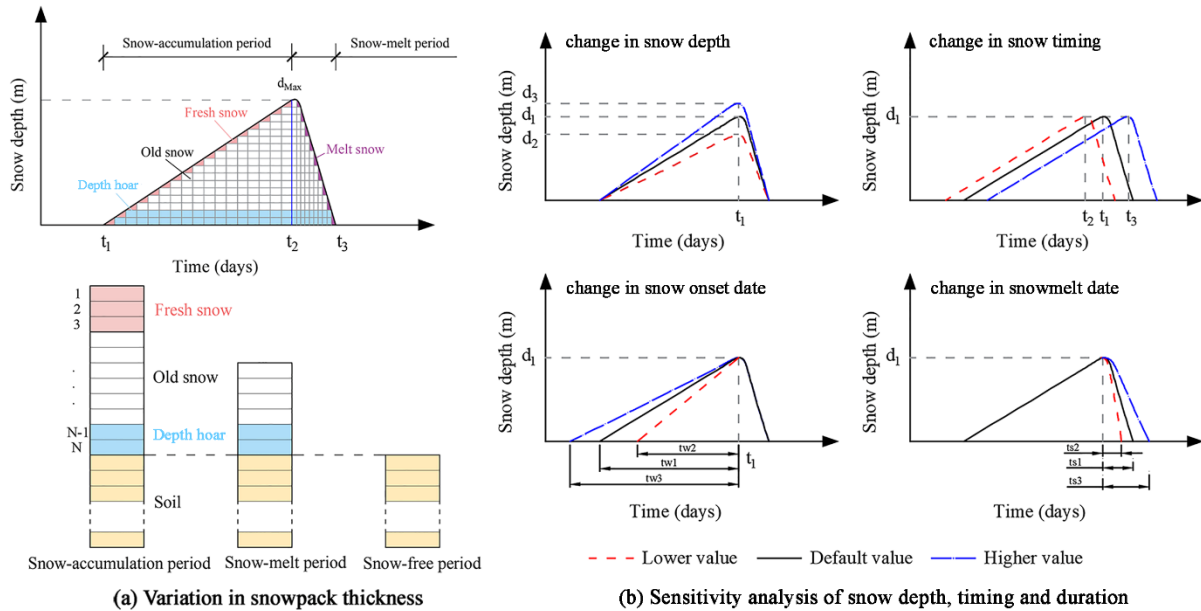
Figure 4.4. (a) Schematic description of variation in snowpack thickness for the snow-accumulation period in winter, snow-melt period in spring and snow-free period in summer, with snow grid cells numbered from j = 1, 2, 3… N; and (b) schematic snow distribution including snow depth, snow timing, snowpack onset date in autumn, and snowpack disappearance date in spring. The black line indicates the reference model (default value).

For the sensitivity analysis, all the simulations were run with the same input meteorological data from April 2013 - April 2018, except for the snowpack distribution. The reference model was run with a maximum snow thickness layer of 0.8 m without the formation of a depth hoar layer (Table 4.1). In Figure 4.4b, the minimum/maximum values of snow depth represented a thinner/thicker snowpack in comparison to the reference model. The change of snow timing indicated the temporal shift of the snow regime based on the reference model (Figure 4.4). The lower/higher value of the snowpack onset date illustrated that the snowfall started several days earlier or was delayed by several days. Changing the snowpack disappearance date shows the impacts of earlier disappearance of snowpack on the amount of ground heat fluxes through embankment slope in spring. Due to the inter-annual variations of input meteorological data, the box-plot graphs display the distribution of the data with minimum, first quartile, median, third quartile, and maximum. The linear and exponential fitting equations were calculated based on the mean value of the five years of data.

90

Table 4.1. Values used for the sensitivity analysis of snow depth, timing, and duration. The negative values of snow timing, snow onset, and snow disappearance indicate the delayed day in comparison to the reference model. The minimum/maximum values are based on the reference value.

Model parameters	Minimum value			Reference value	Maximum value	
Snow depth (m)		0.2	0.4	0.8	1.2	1.6
Advancing days of snow timing (days)	-16	-10	-5	0	5	10
Advancing days of snow onset (days)	-16	-10	-5	0	5	10
Advancing days of snow disappearance (days)		-10	-5	0	5	10

4.3. RESULTS

4.3.1. Measured climate data at the BC-RES

The mean daily ATs seasonally oscillated with an average of -3.0 °C, extending from a minimum of -38.4 °C in winter to a maximum of 22.6 °C in the summer (Figure 4.5a). The lowest monthly AT is in January, with an average of -19.2 °C, and the highest monthly AT is in July with an average temperature of 14.3 °C. The period of positive AT was less than half of the year, from early April to the end of September. The mean daily solar radiation had a normal distribution, with an average of 107.2 W·m^{-2} (Figure 4.5b). The summer values of solar radiation were particularly high, with an average of 191.2 W·m^{-2}, while the winter values (14.2 W·m^{-2}) had only 7.4 % of summer values. The mean annual wind speed was 1.1 m·s^{-1} (SD = 0.54 m·s^{-1}). The mean summer wind speed was 1.5 m·s^{-1}, more than three times the mean winter value (0.4 m·s^{-1}). The mean annual rainfall was 367.4 mm and nearly 70 % of rainfall was in summer from June to August. The dew-point temperatures, which were linearly related to the minimum daily AT (R^2 = 0.96, Figure S4.1a), experienced a similar trend with AT variations. The mean annual dew-point temperature (-7.7 °C) was 4.7 °C lower than the MAAT (-3.0 °C). The measured and simulated relative humidity from the Beaver Creek airport were in good agreement (R^2 = 0.99, Figure S4.1b) and the calculated relative humidity was on average 75 % at the BC-RES.
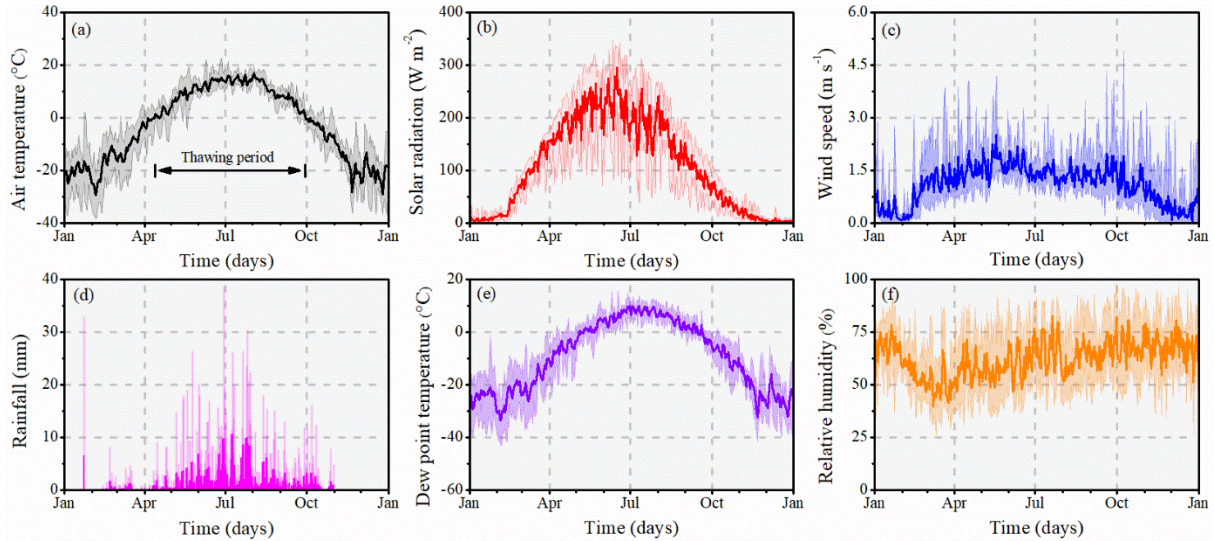
Figure 4.5. Daily meteorological data from Beaver Creek - Road Experimental Site (BC-RES) over the 5-year period from April 2013 to April 2018; (a) air temperature (AT); (b) solar radiation; (c) wind speed; (d) rainfall; (e) calculated dew-point temperature; and (f) calculated relative humidity. The calculated dew-point temperature and relative humidity were obtained using the fitting equations (Figure S4.1). The solid lines represent the mean value of the 5-year data. The light-colored zones illustrate the upper and lower envelope of the 5 years.

4.3.2. Measured soil temperature and ground heat flux variations

Figure 4.6a shows that the mean annual soil temperature (MAST) of the embankment center at 0.3-m depth was higher than the MAAT, by an average of 4.0 °C. The winter ΔT was smaller, only -1.4 °C, while the summer ΔT was -5.9 °C. In comparison, for the embankment slope, the MAST at the 0.3 m depth was 7.9 °C higher than the MAAT. When the surface was covered with snow during winter, the ΔT was higher, about -16.9 °C. In the spring, the value of ΔT decreased until the disappearance of the snow and then increased gradually to about 2.7 °C in summer.

Figure 4.6b illustrates the calculated ground heat flux through the embankment center between 0.3 m and 1.0 m depth, which had a seasonal variation, with a minimum mean value of -14.3 $W \cdot m^{-2}$ in winter and a maximum mean value of 11.3 $W \cdot m^{-2}$ in summer. The net annual ground heat flux was 34.8 $W \cdot m^{-2}$, and the direction of ground heat flux reversed around mid-March. In contrast, the ground heat flux through the embankment slope remained nearly constant in winter, with an average of -1.4 $W \cdot m^{-2}$, while its direction reversed at the beginning of April, increasing gradually in spring and reaching the maximum in summer (1.6 $W \cdot m^{-2}$). The net annual

ground heat flux through the embankment slope surface was 116.2 W·m^{-2}, more than three times higher than that of the embankment center (34.8 W·m^{-2}). The difference in ground heat fluxes between the embankment center and slope were -12.9 W·m^{-2} in winter and 9.8 W·m^{-2} in summer, respectively.
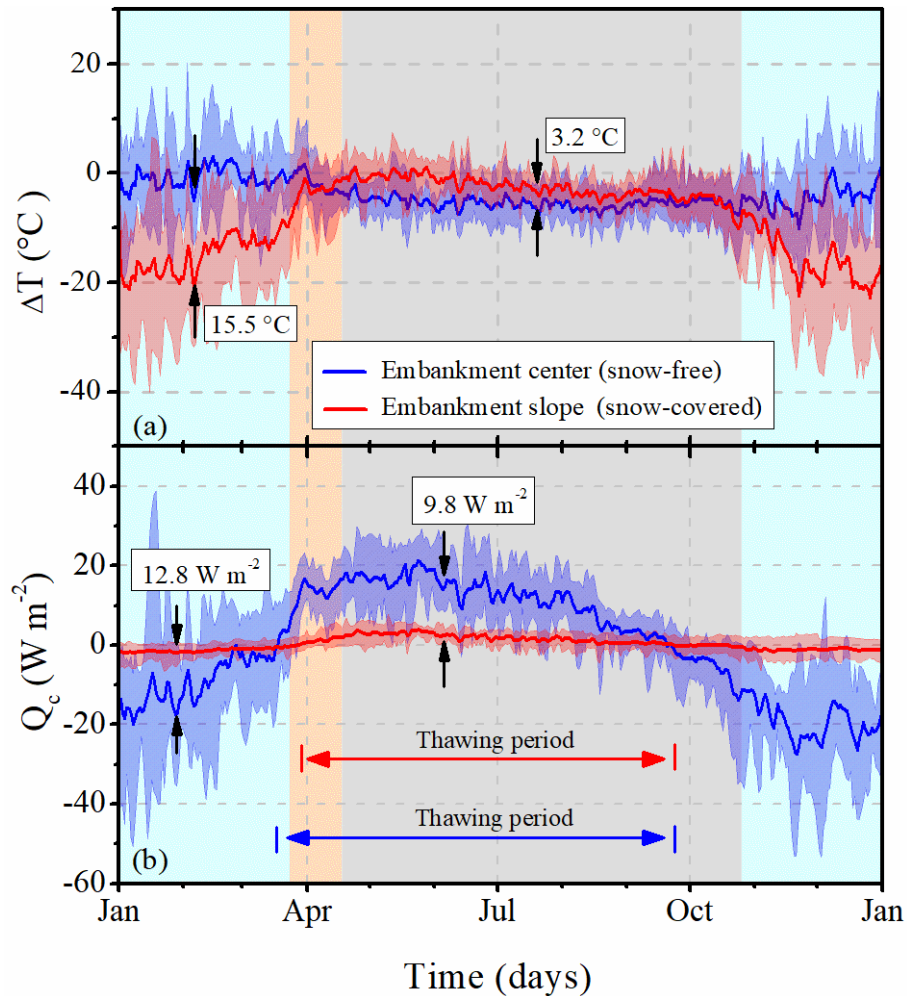
Figure 4.6. (a) Observed temperature difference (ΔT) between air temperature (AT) and the temperature at a depth of 0.3 m at the embankment center and slope over the 9-year period from 2009 to 2018; (b) Calculated ground heat fluxes passing through embankment center and embankment slope based on the soil temperatures between depths of 0.3 and 1.0 m. The light blue and red zone illustrate the max-min range of 5-year data of embankment center and slope, respectively. The color zones of blue, orange, grey represent the snow-accumulation, snow-melt, and snow-free periods, respectively. The temperature difference (ΔT) was negative when the AT was lower than ground surface temperature, and the ground heat flux (Q) was positive when direction of heat flux was downward to the ground. The differences of the simulated results between the embankment center and slope in winter and summer were shown in the graph.

4.3.3. Calibration and validation of SEB model

Calibration and validation results for the SEB model shown in Figure 4.7 indicate that the simulated soil temperatures were in good agreement (R^2 > 0.95) with observed values at depth. Over the calibration period, the MAEs were 1.0 °C at a depth of 1.0 m, and 0.5 °C at a depth of 1.3 m. The corresponding RMSEs were 1.2 °C and 0.6 °C, respectively. By contrast, in the validated period, the MAEs for the depth of 0.1 m, 1.0 m, and 1.3 m were -0.1 °C, -0.2 °C, and -0.1 °C, respectively, and their respective RMSEs were 2.7 °C, 1.2 °C and 0.7 °C. Furthermore, for the 0.1-m-depth soil, the MAE of the snow-accumulation period was 1.5 °C (RMSE = 1.3 °C), while the corresponding value of snow-free period was 2.1 °C (RMSE = 1.9 °C).
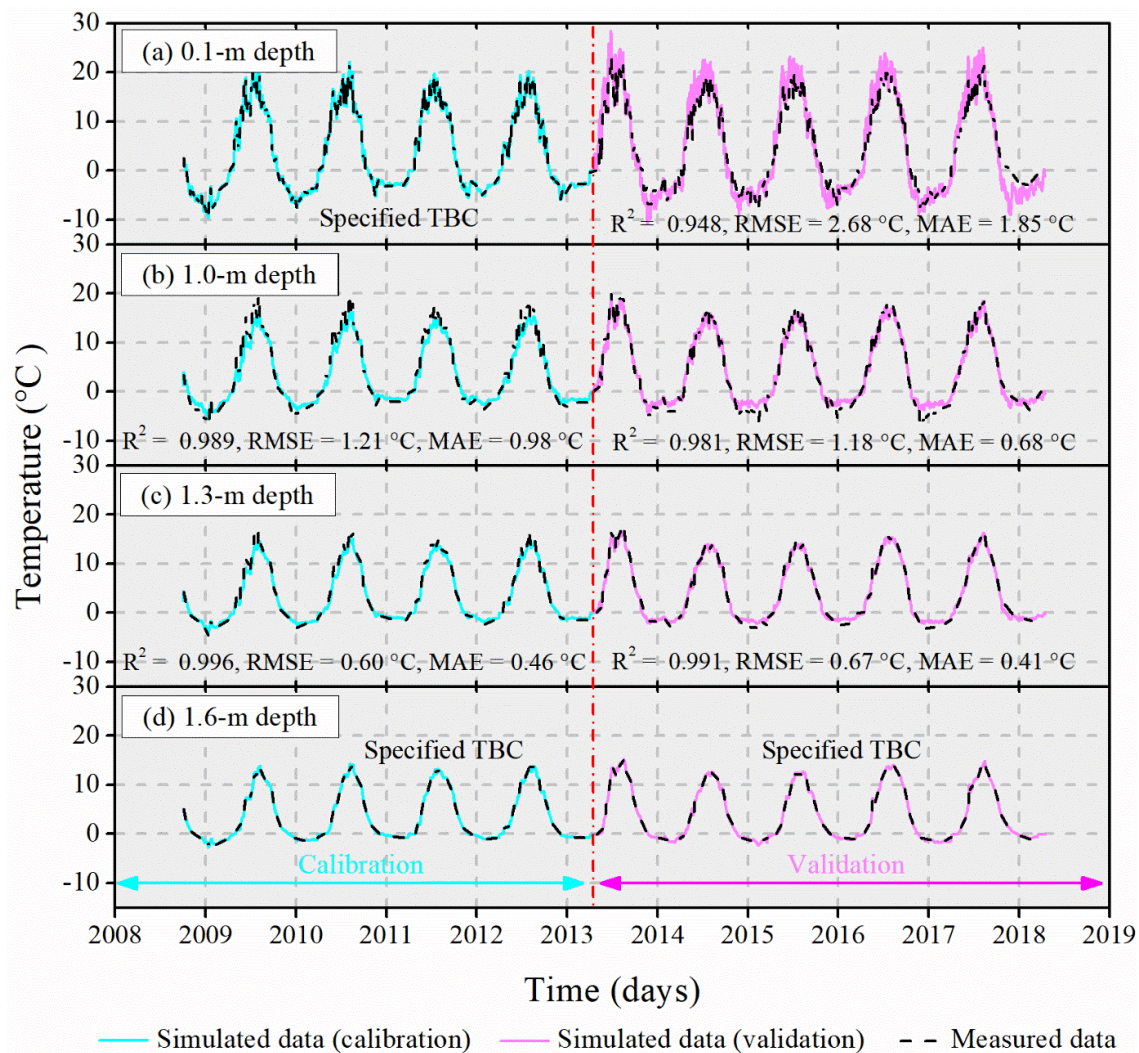
Figure 4.7. Comparison of measured and calculated soil temperatures below the embankment slope over a decade for the calibration period of October 2008 to April 2013, and for validation

period of April 2013 to April 2018; (a) at the depth of 0.1 m; (b) at the depth of 1.0 m; (c) at the depth of 1.3 m; and (d) at the depth of 1.6 m. The black line was the measured data, while the blue and pink lines were the simulated data in calibrated and validated models, respectively. Statistical metrics of root mean square error (RMSE), mean absolute error (MAE) are shown on the graphs.

4.3.4. Simulated SEB components of embankment center and slope

The simulated SEB components differed substantially between the embankment center and slope (Figure 4.8). For the embankment center, the mean annual net radiation was 11.3 W·m^{-2}. The net radiation in summer was 59.9 W·m^{-2}, about 1.5 times higher than in winter (-38.5 W·m^{-2}). The ground heat flux showed a similar seasonal trend, with the average value of ground heat flux in summer of 1.1 times higher than that in winter. The average value of sensible heat flux in summer was about 5 times higher than that in winter. The daily storage heat was between ± 10 W·m^{-2}. The heat fluxes transported by vapor exchange and rainfall were less than 5 W·m^{-2}.

Conversely, for the embankment slope, the net radiation was nearly constant in winter, increased quickly in the spring and reached a maximum in summer. The mean value of net radiation in summer was twice the winter value. The ground heat flux in the summer was more than 3 times larger than that of winter. However, the process of sensible heat exchange was stronger in the winter and its value was 1.9 times larger in comparison to the summer.

4.3.5. Simulated ground surface temperature and ground heat flux variations

Simulated surface temperature variations of snow, embankment slope and embankment center are shown in Figure 4.9. For the embankment center, the mean annual GST was 2.1 °C, about 5.0 °C higher than the AT. In summer, its GST was 11.4 °C higher than the AT, while close to the AT in winter. Conversely, the mean annual GST of the embankment slope was 7.8 °C higher than MAAT, with an average of 14.9 °C higher in winter and 6.0 °C higher in summer, respectively. Over the snow-covered period, the SST was much lower than both embankment slope surface and atmosphere, by an average of 26.5°C and 11.6 °C, respectively.
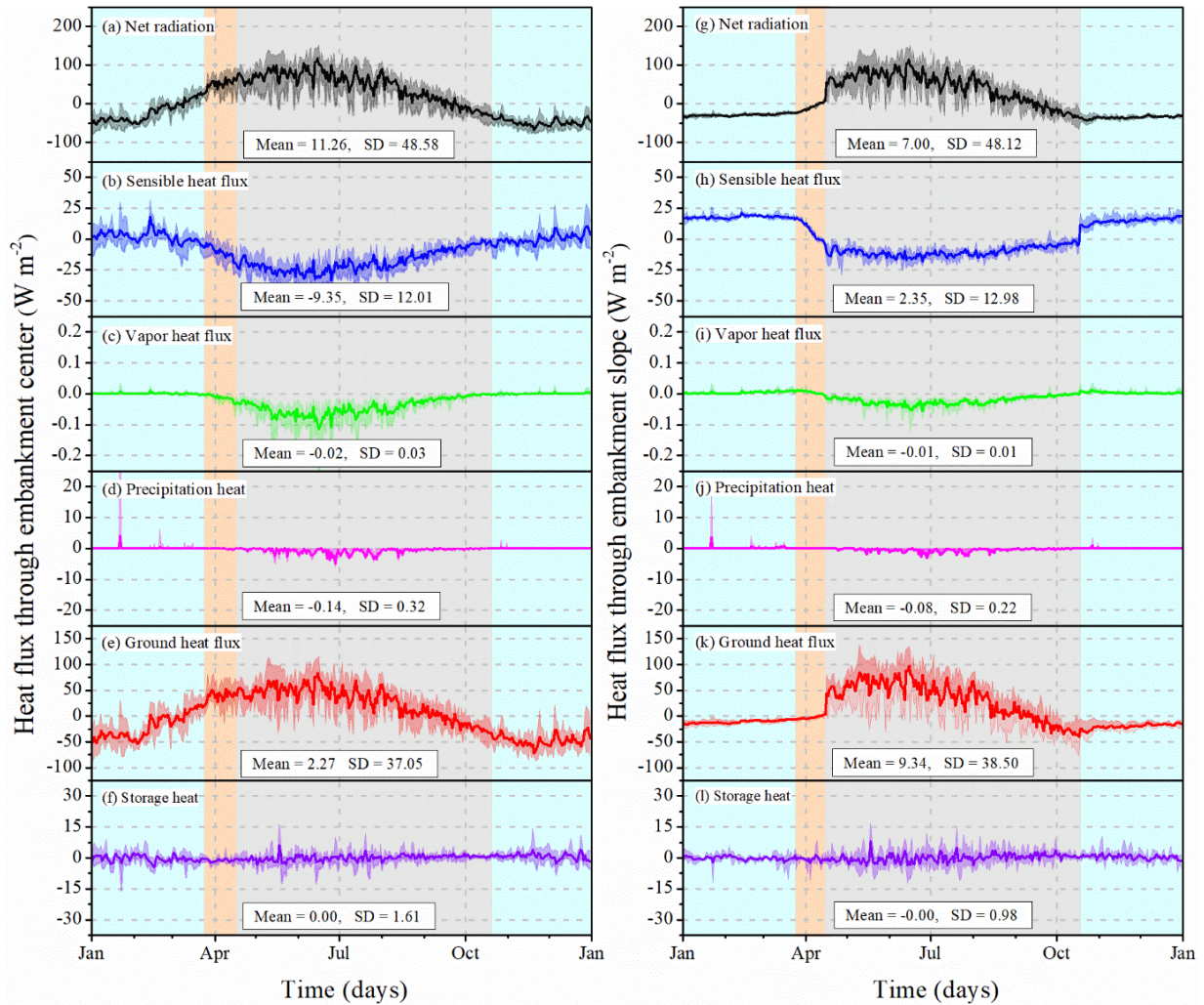
Figure 4.8. Surface energy balance (SEB) components at the embankment center (left) and slope (right) surface over 5-year period from April 2013 to April 2018; (a) and (g) net radiation; (b) and (h) sensible heat flux; (c) and (i) vapor heat flux; (d) and (j) rainfall heat; (e) and (k) ground heat flux; (f) and (l) heat storage. The dark color lines represent the mean value of 5-year data for embankment center and slope, respectively, with a range of MAAT from -2. 0 °C to -3.6 °C (Mean = -3.0 °C, SD = 0.65 °C), while light color lines illustrate the 5-year maximum and minimum values. The blue, orange, and grey zones represent snow-covered period, snow-melt period, and snow-free period, respectively. The heat flux was positive when its direction was towards the ground. Statistical values of mean and standard deviation (SD) are indicated on the graphs.
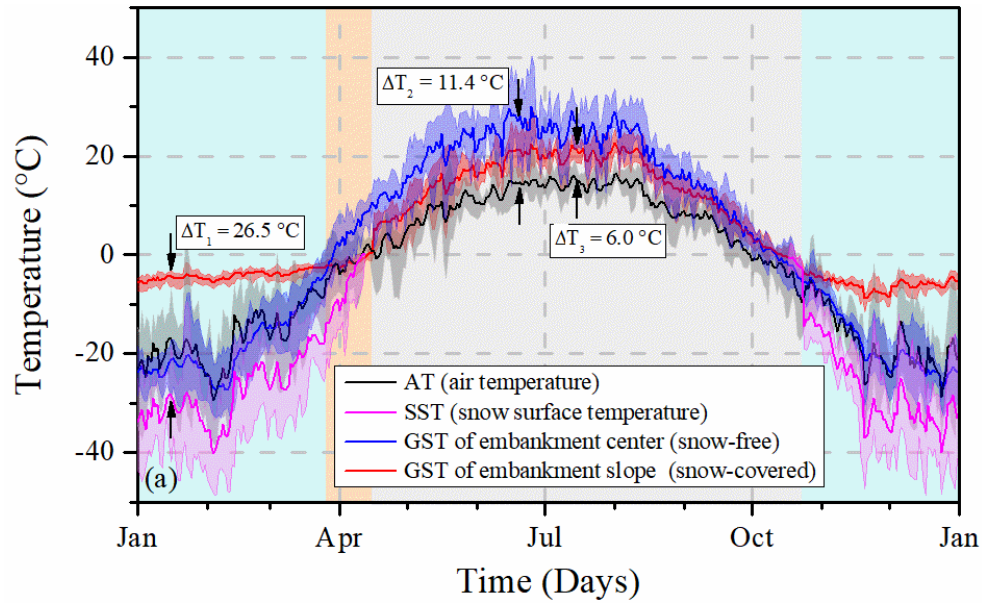
Figure 4.9. Surface temperature of the embankment center, the embankment slope, and the snow layer accumulated on embankment slope. The solid lines represent the mean 5-year values from April 2013 to April 2018 with a range of MAAT from -2. 0 °C to -3.6 °C (Mean = -3.0 °C, SD = 0.65 °C). The red, grey, and blue zone illustrate the range of the 5-year maximum and minimum. The ΔT_1 is the temperature difference between the embankment slope surface and the top surface temperature of the snow layer in winter. The ΔT_2 is the temperature difference between the embankment center surface and atmosphere in summer, while ΔT_3 represents the corresponding value of the embankment slope, respectively.

Figure 4.10a demonstrates the temperature difference between the atmosphere and the GST. The simulated GST at the embankment center was lower than the AT in winter and higher in summer, while the GST of the embankment slope was higher than AT during the whole year. In the summer, the embankment center was almost 5.5 °C warmer than that of embankment slope, while 17.5 °C colder in the snow-covered period. From Figure 4.10b, the annual net ground heat flux passing through the embankment center was 41.1 W·m^{-2}, with the total ground heat flux of -1050.6 W·m^{-2} in winter and 929.6 W·m^{-2} in summer. The thawing period was 186 days, starting from mid-March to mid-September. Over the snow-melt period, the net total ground heat flux was 190.8 W·m^{-2}. Conversely, for the embankment slope, the annual net ground heat flux entering the road embankment was 160.3 W·m^{-2}, almost 4 times higher than that of the embankment center. The corresponding total ground heat fluxes were -340.4 W·m^{-2} in winter and 536.6 W·m^{-2} in summer. The thawing period was only 155 days, from mid-April to mid-September.

97
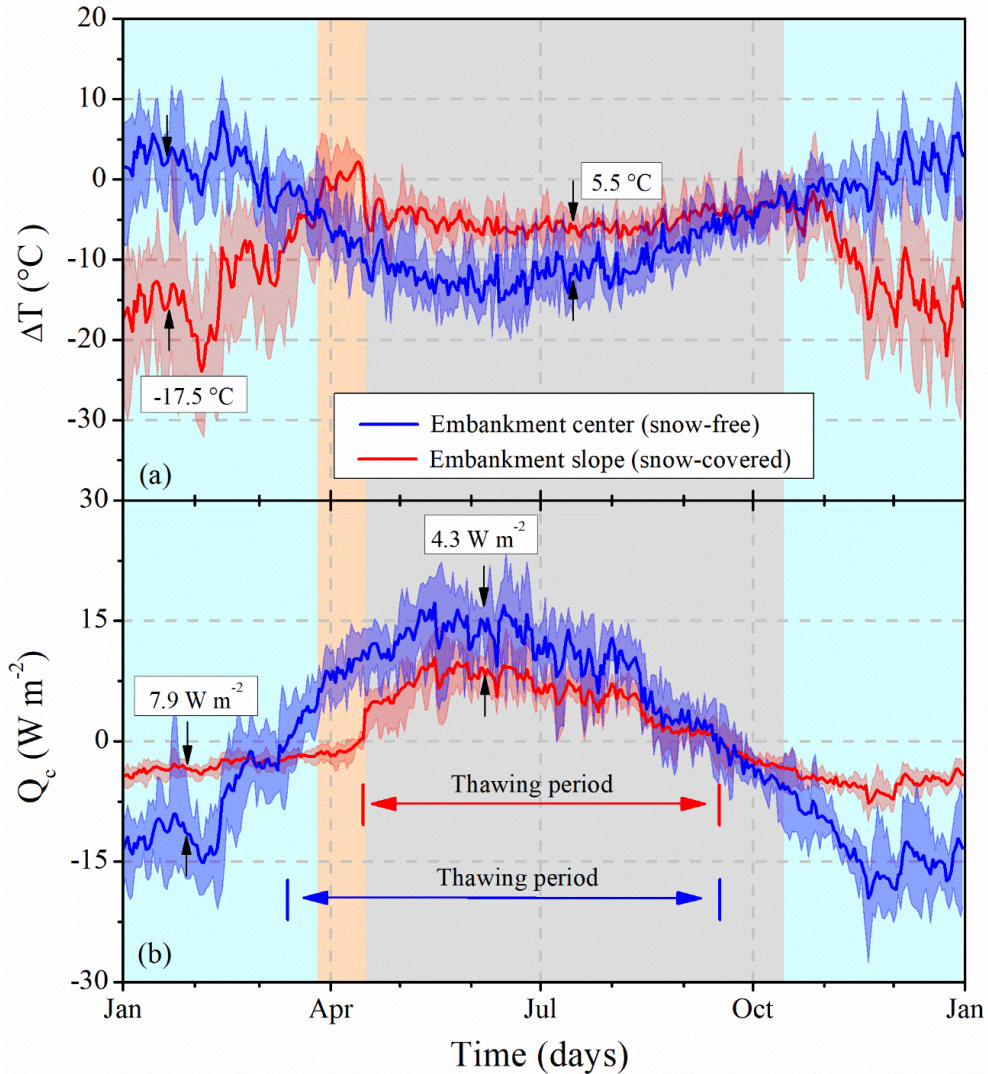
Figure 4.10. (a) Temperature difference (ΔT) of air and simulated ground surface of embankment center and slope; and (b) ground heat flux (Qc) of embankment center and embankment slope at the depth of 0.3 m. The solid lines represent the mean 5-year values from April 2013 to April 2018 with the range of MAAT -2.0 °C and -3.6 °C (Mean = -3.0 °C, SD = 0.65 °C), while the c zones illustrate the range of the 5-year maximum and minimum. The grey zone represents the snow-free period, and the blue zone represents the snow-covered period. The differences of the simulated results between the embankment center and slope in winter and summer were shown in the graph.

Figure 4.11 represented that the SEB model has the best performance (R^2 = 0.970) to predict the ground surface temperatures, in comparison to the n-factor (R^2 = 0.938) and adherent-layer approaches (R^2 = 0.945). Furthermore, for the SEB model, the MAE was 2.8 °C (RMSE = 3.3 °C), which is much lower than the values from other two approaches. Alternatively, the SEB model better predicts the near-surface thawing period. Compared to the field observations, the mean

value of the difference of thawing period was about 5 days for the simulated results by the SEB model (Figure 4.11), while the corresponding values for the n-factor and adherent-layer approaches were 24 days and 42 days, respectively.
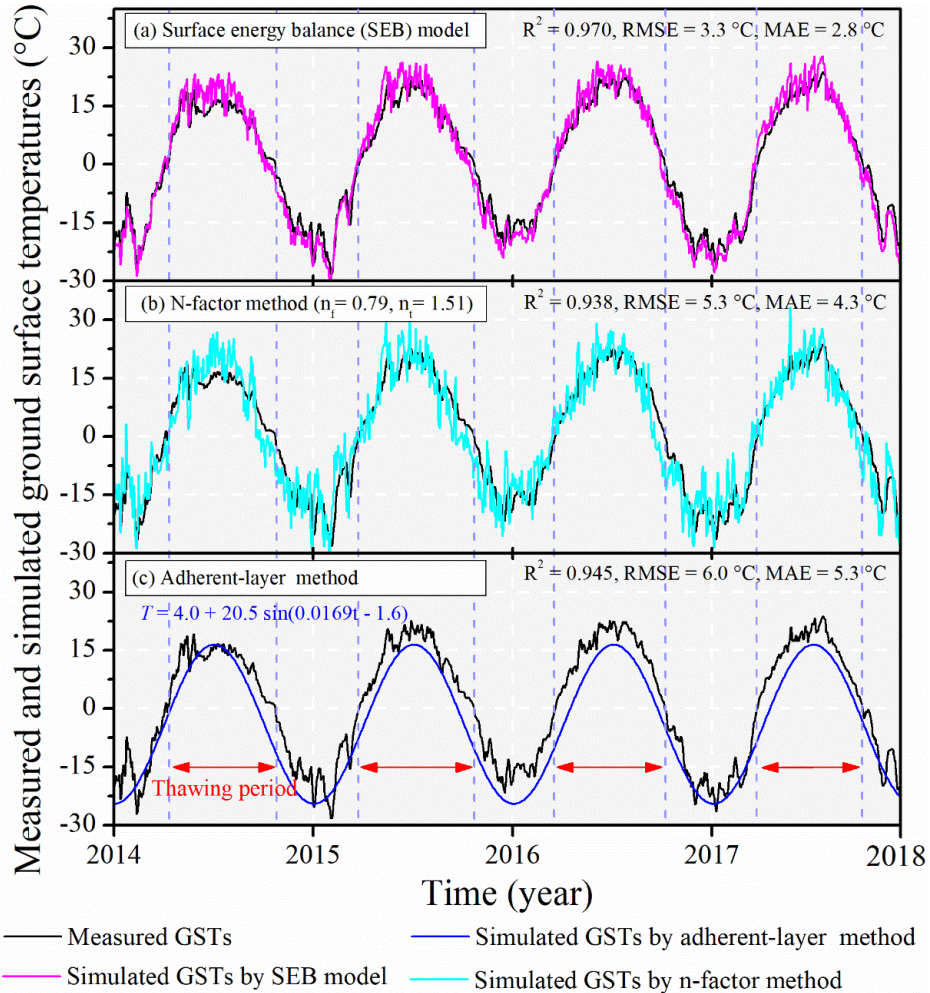
Figure 4.11. Measured and simulated ground surface temperature (GST) variations at the depth of 0.3 m below the embankment center over the 2014-2017 period, (a) surface energy balance (SEB) model, (b) n-factor approach, and (c) adherent-layer method. The blue dash lines represent the thawing period of near-surface (0.3-m depth) ground in each year. In Figure 4.11c, t is the Julian date, days from January 1st.

4.3.6. Impact of snow depth, timing, and duration on the amount of ground heat flux

Figure 4.12a indicates that the values of ΔT between the atmosphere and the embankment slope surface exponentially decreased with increasing snow depth. The difference of ΔT between snow

99

depths of 0.2 m and 1.6 m was 2.2 °C. Similarly, the values of ground heat flux exponentially decreased with the increase of snow depth (Figure 4.12b). The thickest (0.8 m to 1.0 m) snow layer insulates ground heat flux nearly twice as much as a thin (0.2 m) snow layer, which leads to a warmer embankment slope surface, by an average of 14.3 °C and 25.2 °C, compared with air and snow surface, respectively.
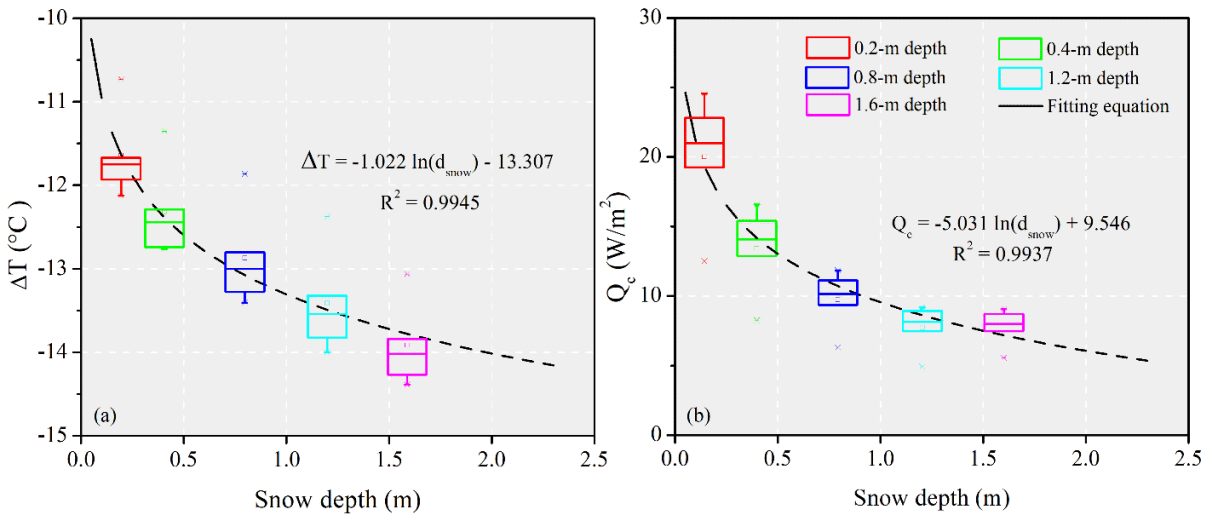
Figure 4.12. (a) Relation between snow depth (d_{snow}) and temperature difference (ΔT) between air and embankment surface; and (b) relation between snow depth and net ground heat flux through embankment slope. The MAATs were at the range of -2.0 °C and -3.6 °C over the 5-year period from April 2013 to April 2018 (Mean = -3.0 °C, SD = 0.65 °C). The values shown in the Figure 4.12b were the amount of ground heat flux released (negative) from the embankment slope surface during the snow-covered period.

The ground heat fluxes through the embankment slope were greatly affected by variations of snow timing, snowfall onset date and snowfall disappearance date, shown in Figure 4.13. Although the ground heat flux at the shallow surface varied in the 5-year period, the mean ground heat flux and snow timing were linearly correlated (R^2 = 0.997). Variations in 10 days of snow timing caused a change of surface heat flux by 3.5 W·m^{-2}. Similarly, the ground heat flux changed linearly with the onset of snow fall. Delaying the snow cover onset date by 10 days in autumn resulted in an increase in ground heat flux, while earlier snow onset leads to a decrease of ground heat fluxes. In addition, the ground heat flux in early spring was linearly associated with the snow-melt duration. A 10-day advance in snow disappearance resulted in a ground heat flux increase of 3.3 W·m^{-2}.
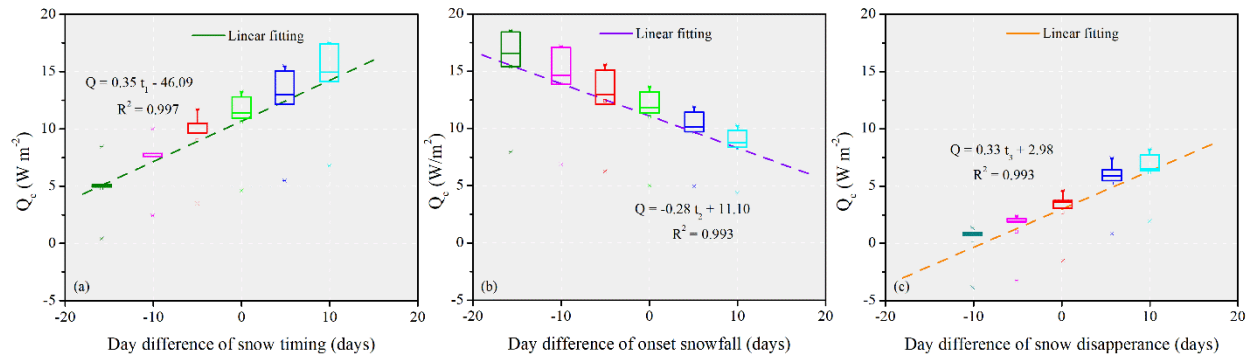
Figure 4.13. Relation between ground heat flux entering embankment slope and (a) snow timing; (c) snowfall onset date; and (d) snowfall disappearance date. The values shown in the Figure 4.13a and 4.13b were the amount of ground heat flux released (negative) from the embankment slope surface in the snow-covered period, while the corresponding values in Figure 4.13c were for the snow-melt period. Symbols are data and dashed lines show linear regression. The linear fitting equations were calculated based on the 5-year mean data.

4.4. DISCUSSION

By combining field measurements and numerical modelling, our study provides insights into how atmospheric heat enters a high latitude road embankment built on permafrost. In the discussion, we first evaluate the differences and similarities of SEB components and TBCs between embankment center and slope in different periods. Secondly, we compare different prediction approaches of GSTs, including SEB model, the adherent layer method, and the n-factor method. Thirdly, we discuss the thermal impact of the snow cover on ground heat flux at the shallow surface and the sensitivity analysis of snow depth, snow timing, and the date of snowfall and snow disappearance. Finally, we address the accuracy and uncertainty of the SEB model.

4.4.1. Differences and similarities of SEB components of the embankment center and slope

Our simulations illustrate that the heat entering a road embankment and heat loss to the atmosphere are mainly controlled by net radiation, followed by sensible heat flux, while the heat exchange controlled by vapor, rainfall and thermal storage are relatively weak (summarized in Table 4.2). The large amounts of negative net radiation in winter and positive net radiation in summer are mainly due to the amount of incoming solar radiation and the change in surface cover. In winter, in addition to the small amount of incoming solar radiation (~14.2 W·m^{-2}; Figure

4.5b), low AT (less than -20 °C) reduces the amount of incoming long wave radiation (Eq. 4.5, Figure S4.4). These processes result in an increase in heat loss from the embankment to the atmosphere. In spring, a quick increase in net solar radiation is due to the change in ground surface conditions from snow/ice-covered to snow/ice-free surfaces. Later in the summer, with a high amount of solar radiation (~191.2 $W \cdot m^{-2}$, Figure 4.5b), the low albedo of the asphalt-paved surface and bare gravel/sand surface increases the absorption of solar energy (Figure 4.8) and a high AT increases the amount of incoming long wave radiation (Figure S4.4).

The strong sensible heat exchange between the atmosphere and the embankment is largely associated with the high wind speed and large ΔT between the air and ground surface (Eq. 4.9). In summer, higher wind speed, with an average of 1.5 $m \cdot s^{-1}$, contributes to the higher value of sensible heat exchange for both the embankment center and slope (Figure 4.8). But, in winter, even if the wind speeds are much lower (Mean = 0.4 $m \cdot s^{-1}$), a large ΔT (about 10.9 °C) between the snow surface and the atmosphere leads to strong sensible heat exchange on the embankment slope.

The small amount of summer rainfall (Mean = 2.7 $mm \cdot day^{-1}$, Figure 4.5) minimizes the amount of heat carried by rainfall to the embankment, although the ΔT between rainfall (assumed to be equal with AT) and the ground surface is high (more than 6 °C) in summer. Also, the negative (upwards to the atmosphere) heat fluxes by rainfall in summer were mainly due to the higher GST in comparison to the rainfall temperature. A similar behavior has also been reported by Zhang et al., (2016a) and Zhang et al., (2016b). They demonstrated through thermal monitoring and modelling that the solar radiation and heat exchange between an embankment and atmosphere mainly contribute to heat entering the embankment in the QTP. Also, Zhang et al., (2016a) showed that heat convection by the liquid water and water vapor contribute to less than 5 % of soil heat flux at depth. Furthermore, our simulated net radiation variation patterns agree with simulations and measurements in Alaska (Ling and Zhang 2004), while the corresponding values are different from the observations of a road pavement in the Beiluhe region of the QTP (Zhang et al., 2018). In the QTP, the positive net radiation in the whole year is due to the absence of snow cover and high winter AT.

Table 4.2. Similarities and differences of heat exchange processes between the atmosphere and the embankment center and slope surface under different seasonal conditions. Note: ΔT represents the temperature difference between the ground surface and the atmosphere. The blue, orange, and grey zones represent the snow-covered period, snow-melt period, and snow-free period, respectively.

	Embankment center (Asphalt-paved surface)	Embankment slope (Gravel/sand surface)
Net solar radiation	Minimal net solar radiation	Similar to the embankment center
	Increasing amount of incoming solar radiation	High albedo (0.6~0.9) of snowpack reduces the solar radiation absorption
	Low albedo (0.14) increases the amount of solar radiation absorption	Low albedo (0.3) increases the amount of solar radiation absorption
Net long-wave radiation	Small ΔT (3.0 °C) reduces the amount of net long-wave radiation (negative)	High ΔT (-14.9 °C) rises the amount of net long-wave radiation (positive)
	Increasing ΔT increases the amount of net long-wave radiation (negative)	Decreasing ΔT reduces the amount of net long-wave radiation (negative)
	High ΔT increases the amount of net long-wave radiation (negative)	Similar to the embankment center
Sensible heat exchange	Low ΔT and low wind speed limits the sensible heat exchange	Large ΔT increases sensible heat exchange
	Increasing ΔT rises the amount of sensible heat exchange.	Decreasing ΔT reduces the amount of sensible heat exchange.
	High wind speed and large ΔT (positive) promotes heat loss	Compared to the embankment center, its value is smaller, due to the lower ΔT
Conductive heat transfer	Snow-free surface facilitates heat loss	Insulation created by the snow cover reduces heat loss
	Increasing heat flux transfers downward to the ground	Lateral ground heat flux transfers from the embankment center to the slopes
	Large amount of atmospheric energy transfers downward to the ground	Compared to the embankment center, its value is smaller, due to high albedo
Rainfall heat	Small amount of rainwater limits the heat exchange between the ground surface and the atmosphere	
Vapor heat exchange	Dry embankment fill limits the vapor heat exchange, and the high porosity and permeability of gravel/sand embankment fill favor the rainfall and snowmelt water infiltration and reduce the water accumulation in the near surface layer.	
Stored energy	Thin (0.3 m) soil layer and low water content (4%) reduce the amount of stored energy change at the shallow surface	

Our measurements and simulations illustrate that the magnitude of heat transported across the ground surface significantly differs between embankment center and slope in different periods of the year (Figure 4.6, Figure 4.8, and Figure 4.10). The difference in ground heat flux is mainly caused by ground surface processes. Firstly, during the snow-covered period, the low thermal conductivity of the snow layer reduces heat loss from the embankment slope to the atmosphere, even if the high albedo of snow decreases the absorption of solar radiation. In comparison, the snow-free surface at the embankment center facilitates heat loss to the atmosphere, at a rate more than three times higher than that of the embankment slope. Secondly, in the snow-melt period, snow cover insulates the embankment slope from the positive AT and reduces the thawing period by an average of one month. Whereas the embankment center surface is directly exposed to the positive AT, with additional solar radiation absorption (about 872.2 $W·m^{-2}$ over the snow-melt period). Thirdly, during the snow-free period, the low albedo of the asphalt-paved embankment center causes more than 16 % of incoming solar radiation to be absorbed, compared with the embankment slope. Over a year, the annual net ground heat flux through the embankment slope surface is more than four times larger than that at the embankment center (Figure 4.10). This may explain the rapid permafrost degradation (e.g., Fortier et al., 2011; Lanouette et al., 2015) and the formation of a talik (i.e., perennial unfrozen zone in permafrost areas) under the road embankment slopes (Kondratiev 2002, Fortier et al., 2011, Lanouette et al., 2015, Chen et al., 2017a, O'Neill and Burn 2017) in sub-Arctic regions where a thick snow cover is present in winter. During the snow-melt period, there is a positive ground heat flux passing through the embankment center, while the embankment slope is still frozen (Figure 4.10). The lateral ground heat flux from the embankment center to the slopes leads to the earlier disappearance of the seasonal snow cover on the embankment slope, which agrees with the observed data at the same site (Chen et al., 2020a). This process transfers the downward heat flux to the ground, contribute to higher soil temperature, accelerates permafrost warming and thawing, and contributes, in some cases, to tension stress and longitudinal cracking of the embankment (Figure 4.10b).

4.4.2. Comparison of different prediction approaches of ground surface temperatures

We compared the calculated surface offsets between the BC-RES (62° 20' N, 140° 50' W, elevation, 649 m above sea level) and Beiluhe Basin area (34° 82' N, 92° 92' W, elevation, 4600 m above sea level) in the QTP. Our simulated surface offset for the embankment center is 1.5 °C lower than the suggested value of 6.5 °C in the QTP by the adherent-layer method (Zhu 1988, Lai et al., 2004, Wu et al., 2007, Zhang et al., 2018), while the corresponding value for the embankment slope is 3.8 °C higher. The main reason for different surface offsets is associated with differences in regional climate. Firstly, the amount of solar radiation greatly differs between subarctic regions and the QTP. In winter, the amount of solar radiation at the BC-RES is only 25% that of the Beiluhe Basin area (Zhang et al., 2016b). Also, lower winter AT of the BC-RES facilitates heat loss from the embankment center (Figure 4.6) compared to the Beiluhe area, where the freezing index was 1779 FDD (Lin et al., 2019), only half of the BC-RES. In addition, its lower winter AT decreases the amount of incoming long-wave radiation (about 160 W·m^{-2}, calculated by Eq. 4.5), more than 10 % of that in the Beiluhe area (Zhang et al., 2016b, Zhang et al., 2018). Secondly, the snow cover layer at the BC-RES inhibits the heat exchange between the embankment and the atmosphere and acts as a thermal insulation for conductive exchange. Our study illustrates that a thick snow cover at the BC-RES causes a difference of temperature of about 4.0 °C for the gravel/sand surface of embankment slope, in comparison with measured values for the Beiluhe area, although the difference of the MAAT between two sites is less than 0.2 °C (Zhu 1988, Wu et al., 2007, Zhang et al., 2018). Thirdly, the wind-driven heat advection also changes the SEB and affects the GST. In winter at the BC-RES, wind condition (0.4 m·s^{-1}) limits the heat exchange process at the embankment surface, while the commonly strong wind in the QTP, (often more than 4.0 m·s^{-1}; Zhang et al., 2010), increases the heat loss from the embankment slope. Therefore, the TBCs related exclusively to AT variations by adherent-layer method are not practical to predict the GSTs for the different surface cover types when a thick snow cover is present, especially for the embankment slope in the sub-Arctic regions or tundra in high Arctic regions where a depth hoar layer is formed (Domine et al., 2016).

The patterns and magnitude of the GST variations are different from the AT variation and differ for the different surface cover types (Figure 4.9). The thawing period of the embankment surface is several weeks longer than the period of the positive AT (Figure 4.5, Figure 4.9a). Also, compared to the embankment slope, the quick and earlier warming of bare asphalt-paved surface is due to the large amount (~130 W·m^{-2}) of solar radiation absorption in spring (Figure 4.9a). Not coupling the individual energy processes at the top surface and thermal processes in the subsurface layer, the n-factor and adherent-layer approaches produce additional uncertainties of the predicted surface offset and thawing period (Figure 4.11). The n-factor approach controls the GST as a result of changes in the AT, which only amplifies or lowers the magnitude of the AT variations by freezing or thawing factors (Figure 4.11). Also, the thawing period of the predicted GST using the n-factor is completely fixed and consistent with the duration when AT is positive. Therefore, the n-factor approach totally ignores either the impact of the solar radiation variations, or the impacts of snow cover timing and duration on the thawing period. Similarly, sinusoidal function obtained adherent-layer approaches only represented the surface offset between mean annual AT and GST, and neglected the surface and subsurface thermal processes, resulting in the worst performance to predict the thawing period. The TBCs obtained by the n-factor and adherent-layer approaches are limited to simulate the advancing thawing of the asphalt-paved surface or delaying thawing of snow-covered surface (i.e., the shift of thawing period between AT and GST for the different surface cover types). Lacking to consider the individual energy heat transfer effect on the surface, the n-factor and adherent-layer approaches have a limited application on the projection of the impacts of the sunny and shady effect on the permafrost thermal state and the interaction of the surface flow, vadose zone, and groundwater flow. Similar conclusion was demonstrated about Advanced Terrestrial Simulator, which highlights the importance of coupling the surface/subsurface thermal processes in the permafrost thermal hydrology model (Jan et al., 2019).

Additionally, both the adherent-layer theory and the n-factor approaches cannot predict the SST. The simulated surface offsets agree with the measured temperature shift at the Tasiujaq airstrip in northern Quebec and at Alaska Highway in Beaver Creek, Yukon, Canada, when the ground was covered by a 1-m thick and 0.5-m snow layer, respectively, in 2015 (Lanouette et al., 2015).

The simple approximation of the same temperature between the snow surface and atmosphere underestimates the snow insulation factor (Kondo and Yamazaki 1990). This SEB model can predict the SST with inputs of the meteorological data and demonstrate that there is an offset between the SST and the AT. The simulated SST is 11.6 °C lower than the AT. This magnitude of temperature shift agrees with field observations (Brubaker et al., 1996, Raleigh et al., 2013, Domine et al., 2016), although this value varies over regional climates. Alternatively, this SEB model, taking into account variations of snow albedo, density and regimes, enables to investigate and quantify the impacts of surface and subsurface thermal processes, while the previously employed SEB model was mainly restricted to a vertical dimension and neglected the subsurface processes and snow regime variations (Hwang 1976, Solaimanian and Kennedy 1993, Williams et al., 2015, Dumais and Doré 2016).

4.4.3. Relation of simulated ground surface temperature and air temperature

Variations in depth, timing, and duration of the seasonal snow cover are critical to determine the ground heat flux through the embankment slope due to changes in surface conditions. Firstly, snow depth exerts the strongest influence on the GSTs and ground heat fluxes entering the embankment slope. The low thermal conductivity of snow reduces heat loss from the embankment to the atmosphere (Figure 4.12). The ΔT (difference between AT and GST) and ground heat flux are exponentially related to snow depth, which agrees with field observation at the Tasiujaq airstrip (Luetschg et al., 2008, L'Hérault et al., 2012, Lanouette et al., 2015). Secondly, delaying the snow cover onset date in autumn results in a decrease in ground heat fluxes entering embankment (Figure 4.13). Conversely, an early snow cover in autumn reduces the heat exchange between the ground surface and the atmosphere. Advancing the snow cover disappearance date in spring leads to an increase in downward ground heat fluxes to the embankment. Due to the direct exposure of the embankment slope surface to positive AT, the earlier disappearance of seasonal snowpack increases the thawing period, rises the ground heat flux entering the embankment, and finally contributes to the warming and thawing of the underlying permafrost. Stone et al., (2001), Ishikawa (2003) and Ling and Zhang (2003)

demonstrated that the earlier disappearance of seasonal snowpack caused by increase in the AT due to climate change increases ground warming in the spring.

4.4.4. Accuracy and uncertainty of SEB model

The SEB and heat transfer model in this study simulates the soil temperature variations under different surface cover types. The SEB model considers the long-wave and short-wave solar radiations, heat advected by wind, heat exchange by the difference in temperature and vapor between air and ground surface, rainfall heat, and heat conducted through the snowpack. The simulated and measured soil temperatures are in good agreement, but uncertainties in the snow regime (e.g., maximum snow depth, snow duration and timing) and the variability in snow thermal properties cause discrepancies in the calibrated and evaluated model. In the snow-covered period, the consistent presence of a fresh snow layer and the fixed variation of snow distribution mainly contribute to the large values of MAE (1.49 °C) and RMSE (1.30 °C) between measured and simulated data. Due to the lack of information on snow depth variations from 2013 - 2018, variations in snow depth were calculated using linear interpolation during the snow-accumulation period and remained the same in the 5-year period. The thin (0.1 m) fresh snow, thick old snow and thin (0.14 m) depth hoar layer are fixed in the whole snow-accumulation period. But the fresh snow layer does not consistently exist during the winter season and the thickness of depth hoar, which is highly insulative, varies locally. The fixed snow regime also contributes to the discrepancies between measured and simulated results due to a lack of inter-annual variation of snow depth, duration, and timing. On the other hand, in the snow-free season, high MAE (2.1 °C) and RMSE (1.9 °C) are likely caused by not considering of heat advection caused by surface water infiltration, such as spring snowmelt water and summer rainfall. In our SEB model, the rainfall heat only takes into consideration the amount of heat loss\absorption by changing the rainfall temperature to the GST, although the infiltrated surface water is able to transfer heat to depth and changes the thermal process in the subsurface (Kane et al., 2001, Wen et al., 2014, Yoshioka et al., 2015, Chen et al., 2020a). The variations (± 10 %) of wind speed had little impact on the mean annual GST (mean ± SD = 0.04 ± 0.09 °C) (Figure S4.3). The maximum deviation was 0.3 °C in summer (mean ± SD = 0.1 ± 0.06 °C), and the corresponding value in winter was smaller, only 0.1 °C (mean ± SD = 0.04 ± 0.01 °C).

4.5. CONCLUSIONS

To our knowledge, this study is unique as it quantifies the surface energy balance (SEB) for a road embankment center and slope in the permafrost regions with the seasonal snow cover. The ten-year thermal monitoring and large amount of meteorological data enabled us to develop, validate, and calibrate a SEB model. The SEB model simulates the ground surface temperatures (GSTs) for different surface cover types and surface energy components with varying snow regimes and thermal properties. Simulated and measured results are in good agreement, indicating that the SEB model can be implemented at a larger scale. Inter-annual variations of snow depth distribution in the SEB model would improve the accuracy of the SEB model.

Simulated mean annual GST of the embankment center is about 5.0 °C higher than MAAT (-3.0 °C), while that of the embankment slope is 7.8 °C higher. The heat entering a road embankment and heat loss to the atmosphere are primarily determined by a combination of the net radiation and sensible heat exchange between the embankment and the atmosphere.

The surface cover conditions (e.g., snow cover, snow depth and snow properties) are the critical factors determining ground heat flux through a road embankment. A thick snow accumulation on the embankment slope can negatively impact the thermal stability of infrastructure founded on permafrost, as snow reduces heat loss to the atmosphere in winter, resulting generally in an annual warming of the slopes. In a changing climate, earlier disappearance of the seasonal snow cover on the embankment slope, will increase the thawing period, warm the ground, and finally cause degradation of the underlying permafrost, with associated subsidence and infrastructure damages due to ground ice melting.

Our SEB model shows a better performance in predicting the GSTs and the thawing periods for different surface cover types and different climate conditions than the adherent layer method or the n-factor method. The collection of meteorological data in recent decades improves the confidence in the projection of energy flux and GST under a warming climate scenario. Conversely, lack of consideration of land surface processes (e.g., spatial variability in snow thickness and properties, or strong wind convection) largely limits the accuracy of the adherent-layer and n-factor methods.

The outputs of the SEB model, either specified GST or ground heat flux variations, can be implemented as a TBC in geothermal modelling software for different purposes, such as thermal interactions between an infrastructure and the underlying permafrost, or the effect of climate change on cryohydrogeological processes.

4.6. ACKNOWLEDGEMENTS

4.7. SUPPORTING MATERIALS

Figure S4.1. Linear fitting equation used for the surface energy balance (SEB) model; (a) relation of measured minimum air temperature and measured dew point temperature; and (b) relation of measured and calculated relative humidity, based on the Eq. (4.6). The measured data are from the weather station of Beaver Creek airport, 8 km from the study site. Data are available from Environment and Climate Change Canada (2018). The calculated relative humidity shows a good agreement with the measured data from Beaver Creek airport.
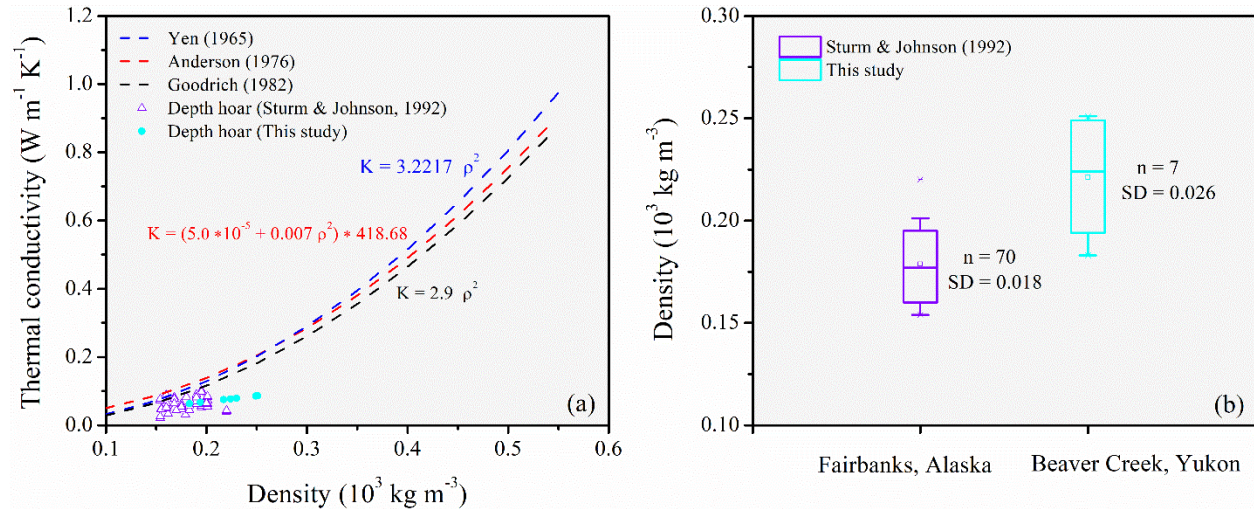
Figure S4.2. (a) Effective thermal conductivity of snow as a function of density; and (b) density of depth hoar. The red, blue, and black lines show the calculated thermal conductivity using the empirical equations of Yen (1965), Anderson (1976) and Goodrich (1982), respectively. The differences of calculated value between three equations are less than 0.03 W·m^{-1}·K^{-1}, when the snow density ranges from 150 kg·m^{-3} to 550 kg·m^{-3}. The measured density of depth hoar is close to the measured values in Fairbanks, Alaska, USA by Sturm & Johnson (1992), where the winter climate condition is similar to our study site. The n and SD represent the number of the sample and standard deviation, respectively.
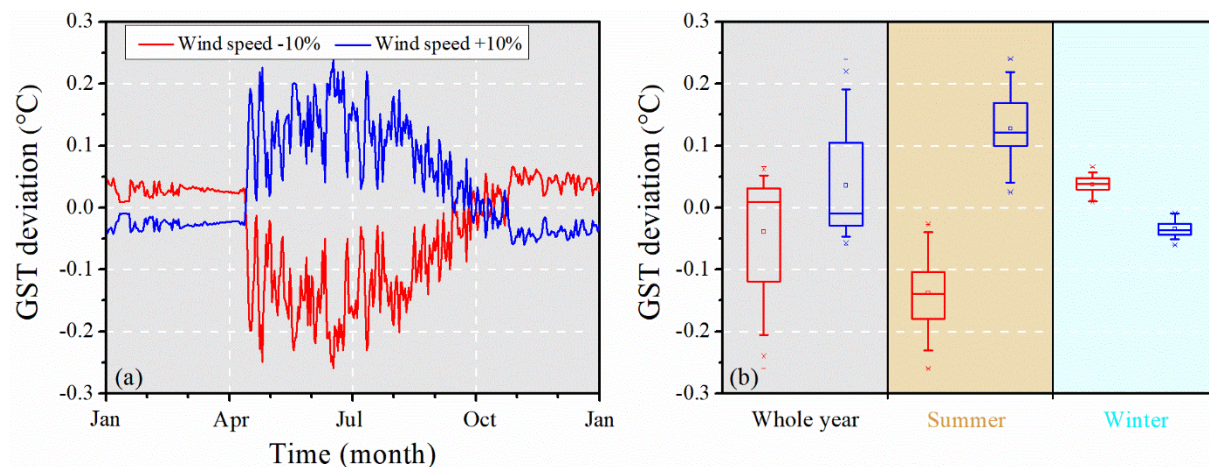
Figure S4.3. (a) Deviation of calculated ground surface temperature (GST) in 2014 caused by variable wind speeds at a range of ±10 %; and (b) Box-plot graphs of GST deviations in three periods, a whole year, summer and winter, respectively. The GST deviation displays the difference of simulated GST temperatures between two cases with the modified (±10 %) SEB inputs and the original inputs (Figure 4.5). The red line represents a wind speed decrease of 10 % of the measured values, while the blue line illustrates the case with 10 % higher winds, respectively. The box-plot graphs display the distribution of the data with minimum, first quartile, median, third quartile, and maximum.
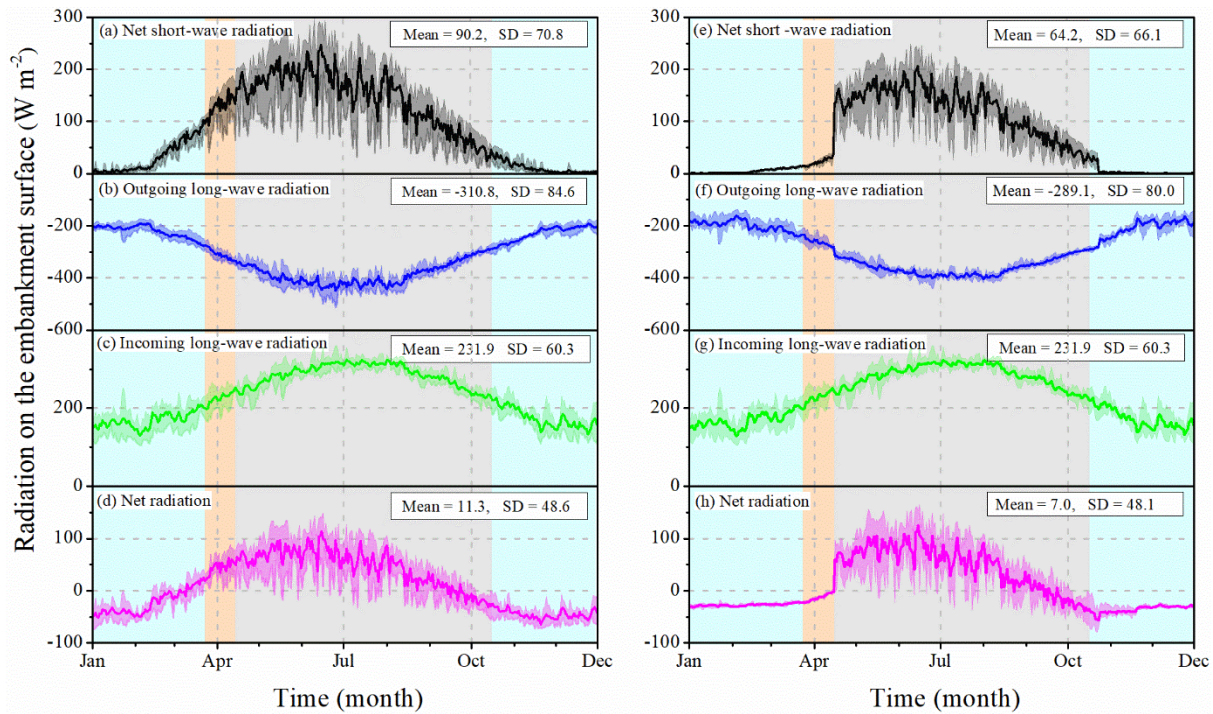
Figure S4.4. Short-wave and long-wave radiation at the embankment center (left) and slope (right) surface over 5-year period from April 2013 to April 2018; (a) and (e) net solar radiation; (b) and (f) outgoing long-wave radiation; (c) and (g) incoming long-wave radiation; (d) and (j) net radiation. The dark color lines represent the mean value of 5-year data for embankment center and slope, respectively, while light color lines illustrate the 5-year maximum and minimum values. The blue, orange, and grey zones represent snow-covered period, snow-melt period, and snow-free period, respectively.

Table S4.1. Detailed information of temperature and climate measurements in the BC-RES.

Variable	Location	Record period (mm/dd/yy)	Reporting interval	Resolution/ Accuracy	Sensor depth/height	Company	Source
Air temperature (°C)		10/01/08 - 06/11/18		0.01 °C / ± 0.2 °C	2 m above the ground surface	Air temperature probe; Campbell Scientific	de Grandpré et al., 2012; Malenfant-Lepage et al., 2012; Coulombe et al., 2012; Fortier et al., 2018
Wind speed (m·s^{-1})				0.0980 m·s^{-1} / ± 0.3 m·s^{-1}	3.5 m above the ground surface	Anemometer; Campbell Scientific	
Solar radiation (W·m^{-2})	5 m away from embankment toe		Hourly	± 2.5 %	3.0 m above the ground surface	SP Lite2 Pyranometer; Kipp & Zonen	
Rainfall (mm)		10/22/12 - 06/11/18		0.254 mm / 1.0 %	1 m above the ground surface	TE525WS; manufactured by Texas Electronics and distributed in Canada by Campbell Scientific	
Soil temperature (°C)	Paved-surface of embankment center	10/01/08 - 06/11/18	4-hour interval	± 0.1 °C between -10 °C to + 10 °C;	0.1, 1.0, 1.3 and 1.6 m below ground surface	Thermistor cable Geocryolab	de Grandpré et al., 2012; Fortier et al., 2018
	Bare-surface of embankment slope			± 0.2 °C between -50 °C to + 30 °C	0.3, 0.9, 1.2, and 1.5 m below ground surface		
Data logger	Center of embankment slope	-	-	-	1.5 m above the ground surface	CR1000; Campbell Scientific	de Grandpré et al., 2012

Table S4.2. Calibrated parameters of embankment materials used in the simulation.

Parameters	Unit	Value	Source
Embankment fill			
Frozen thermal conductivity	$W{\cdot}m^{-2}$	2.3	This study
Unfrozen thermal conductivity	$W{\cdot}m^{-2}$	2.0	This study
Frozen heat capacity	$J{\cdot}kg^{-1}{\cdot}°C^{-1}$	1105	This study
Unfrozen heat capacity	$J{\cdot}kg^{-1}{\cdot}°C^{-1}$	1565	This study
Density	$Kg{\cdot}m^{-3}$	1800	Zottola *et al.*, 2012
Gravimetric water content	%	4	Doré & Mercier, 2008
Melting point	°C	0	McKenzie *et al.*, 2007; Teng *et al.*, 2019
Phase change range	°C	-0.25	McKenzie *et al.*, 2007; Teng *et al.*, 2019
Asphalt			
Thermal conductivity	$W{\cdot}m^{-2}$	2.1	Solaimanian & Kennedy, 1993; Hermansson, 2001
Thermal capacity	$J{\cdot}kg^{-1}{\cdot}°C^{-1}$	920	Solaimanian & Kennedy, 1993; Hermansson, 2001
Density	$Kg{\cdot}m^{-3}$	2150	Darrow & Jensen, 2016
Gravimetric water content	%	1	Darrow & Jensen, 2016

Table S4.3. Nomenclature of symbols and terms used in the equations.

Nomenclature

Q	Heat flux, $W{\cdot}m^{-2}$	R	Thermodynamic vapor constant, $kJ{\cdot}kg^{-1}{\cdot}K^{-1}$
h	Heat transfer coefficient, $W{\cdot}m^{-2}{\cdot}C^{-1}$	r	Resistance to vapor exchange, $day{\cdot}m^{-1}$
P	Daily precipitation, $m{\cdot}daily^{-1}$	U	Velocity, $m{\cdot}s^{-1}$
C	Heat capacity, $J{\cdot}m^{-3}{\cdot}K^{-1}$	T	Temperature, °C
k	Thermal conductivity, $W{\cdot}m^{-1}{\cdot}K^{-1}$	ΔT	Temperature difference, °C
z	z axis, m	L	Latent heat in ice phase transition, $J{\cdot}m^{-3}$
t	Time, day	e	Vapor pressure
d	Thickness of snowpack, or soil layer, m		

Greek Letter

α	Albedo	σ	Stefan-Boltzmann constant, $W{\cdot}m^{-2}{\cdot}K^{-4}$
ε	Emission coefficient of the surface	ρ	Density, $kg{\cdot}m^{-3}$
ξ	Deviation convergence tolerance	ϑ	Water content, %

Subscripts

net	Net radiation	*g*	Ground
h	Sensible heat flux	*i*	Ice
c	Ground heat flux	*a*	Air
p	Rainfall heat	*dp*	Dew point
0	Stored energy	*fresh*	Fresh snow
si	Incoming solar radiation	*old*	Old snow
li	Incoming long wave radiation	*hoar*	Hoar snow
le	Outgoing long wave radiation	*w*	Water
surf	Surface	*v*	Vapor
f	Freezing	*u*	Unfrozen
r	Rainfall	m	Mean

Chapter 5 - TALIK INITIATION AND DEVELOPMENT TRIGGER IRREVERSIBLE THERMAL STATE OF A SUB-ARCTIC ROAD EMBANKMENT

Authors: Lin Chen, Daniel Fortier, Jeffrey M. McKenzie & Clifford I. Voss

CRediT author statement

Lin Chen: Conceptualization, Methodology, Software, Field survey, Writing- Original draft preparation.

Daniel Fortier: Supervision, Field survey, Reviewing and Editing.

Jeffrey M. McKenzie: Supervision, Reviewing and Editing.

Clifford I. Voss: Supervision, Reviewing and Editing.

ABSTRACT

The presence of talik (i.e., perennially unfrozen zone in permafrost areas) adversely affects the thermal stability of northern transportation embankments. However, the quantification of heat advection on talik development and its feedback on permafrost degradation have not been studied methodically. Based on long-term observations (1993-2018 on the Alaska Highway), we firstly incorporate a surface energy balance model in a coupled water flow and heat transfer model (SUTRA-ice model) to investigate and quantify the role of heat advection on the talik initiation and development under a road embankment. This novel approach enabled us to consider the inter-annual variations of climate and subsurface processes. This coupled model has a good performance ($R^2 > 0.93$) to simulate the 0.3-m depth soil temperatures (mean absolute error, MAE < 2.5 °C) and successfully reproduce the increasing trend (over the 25-year period) of

permafrost table depth (MAE < 0.2 m) and talik development, driven by the reconstructed meteorological data. The uncertainty of the reconstructed meteorological inputs causes a small deviation (less than 0.5 °C), and the simulated results are most sensitive to the snowpack depth, followed by solar radiation and air temperature. The observed and simulated results indicate that heat advection provides additional energy source to expedite the permafrost thaw and roughly double the increasing rate of permafrost table deepening from 0.1 m·a^{-1} to 0.19 m·a^{-1}, compared with a scenario without water flow. Talik initially forms and grows over time under the combined effect of the water flow, snow insulation, road construction and climate warming. The subsurface water flow connects two isolated talik (located the upstream and downstream sides, respectively), and develops new groundwater flow paths, which enlarges laterally and vertically with time. Talik formation creates a new thermal state of road embankment, resulting in acceleration of underlying permafrost degradation, due to the positive feedback of trapped unfrozen water. In a changing climate, mobile water flow will play a more important role in permafrost thaw and talik development under road embankment. Such processes will significantly reduce the long-term stability of embankments, increase maintenance costs, and very likely reduce the life cycle of the infrastructure.

5.1. INTRODUCTION

Permafrost is degrading at a global scale due to climate change (Huang et al., 2017, Biskaborn et al., 2019), especially in the Arctic regions (Lawrence et al., 2008b, Pithan and Mauritsen 2014). Amplified Arctic warming has increased average permafrost temperature by 2 to 5 °C since the 1980s (Hinzman et al., 2005, Osterkamp 2005, Jorgenson et al., 2006, James et al., 2013). The thawing permafrost substantially reduces the bearing capacity of the soil (Streletskiy et al., 2012), leading to potentially catastrophic situations for structures and roads (Hjort et al., 2018), which will increase maintenance costs and reduce the lifespan (Reimchen et al., 2009, Melvin et al., 2016). Under the scenarios of RCP8.5, the projected climate warming will add a big amount of additional costs, nearly $70 trillion in Arctic region by the end of the 21st century (Yumashev et al., 2019), and $5.5 billion in Alaska from 2015 to 2019 (Melvin et al., 2016). However, the effect of mobile water flow has not been taken account of assessing vulnerability of North transportation infrastructure to permafrost thaw.

Warming air temperature (AT) and surface disturbances due to engineering construction and maintenance alter the surface energy balance (SEB) (Chen et al., 2020a), increase the downward ground heat flux, and simultaneously lead to permafrost warming at a higher rate (Wu et al., 2007, Smith et al., 2010). When more sensibile heat accumulates beneath an embankment and the heat release from the ground surface in winter is insufficient to freeze back the active layer to permafrost table, a talik (perennially unfrozen layers or bodies in permafrost areas) initiates and develops with time (Nelson et al., 2001, Connon et al., 2018, Devoie et al., 2019). In addition to the increasing AT due to climate change (Buteau et al., 2004, Shur and Jorgenson 2007, Sippel et al., 2020), many local factors affect the talik initiation and development, including thick snow deposition (O'Neill and Burn 2016, Jafarov et al., 2018), fire (Shur and Jorgenson 2007, Zipper et al., 2018), water bodies (e.g., stream, river, and thermokarst lake) (Bradford et al., 2005, Roux et al., 2017, Gao et al., 2019), surfaces water infiltration (i.e., snowmelt and rainfall infiltration) (Westermann et al., 2011, Luethi et al., 2016), and subsurface water flow (Yoshikawa and Hinzman 2003, Rowland et al., 2011, Lamontagne-Hallé et al., 2018, Gao et al., 2019, Stephani et al., 2020). These surface and subsurface thermal processes increase the amount of net annual

ground heat flux transferred to underlying permafrost, cause additional permafrost thaw and eventually trigger the talik formation.

For northern infrastructure, construction removes the vegetation and replaces surficial materials by artificial materials (i.e., gravel/sand and asphalt) (Doré et al., 2016). Due to high-thermal conductivity and low albedo of artificial materials, more solar radiation is transferred downward underlying permafrost, resulting in talik development (Wu et al., 2010, Chen et al., 2021). Many observations recently present the formation of talik beneath or adjacent an artificial structure, such as the formation of isolated talik along the Qinghai-Tibet Plateau (QTP) Highway (Sheng et al., 2002, Wu et al., 2010, Mu et al., 2018, Sun et al., 2018a) and presence of talik under pile foundation of QTP Railway (You et al., 2017) in Western China. Similarly, reports of damaged infrastructure linked with talik are numerous in the circumpolar regions, such as an 8-m thick talik below the Mo'he airstrip (Mao et al., 2019) and a 3-m thick talik beneath the China-Russia Crude Oil Pipeline (Wang et al., 2016b, Li et al., 2018, Wang et al., 2018a) in Northeastern China, and talik formation under the Alaska Highway (Stephani 2013, Sliger 2016) and Dempster Highway in Northwestern Canada (O'Neill and Burn 2016).

Observations and numerical simulations demonstrate that the formation of talik affects the thermal, hydrological and biogeochemical processes in the surface and subsurface layer, and negatively affects overlying infrastructure due to increased drainage (Liljedahl et al., 2016, Tank et al., 2020). The thickening active layer lowers the water table and simultaneously reduces the surface moisture (Guan et al., 2010, Liljedahl et al., 2016), which will have an impact on soil strength (Ayers 1987, Carey and Woo 2002). Additionally, talik development enlarges subsurface water pathways (Lamontagne-Hallé et al., 2018) and changes the heat exchange processes between surface and subsurface layer (Rowland et al., 2011), which results in accelerated and irreversible permafrost thaw (Devoie et al., 2019). However, how talik initiates and grows over the time under a road embankment remains largely unknown due to lack of long-term observations. Also, effects of talik formation on the thermal state of road embankment has not been studied methodically.

Alternatively, the roles of conductive and advective heat transfer on the magnitude and rate of talik development are still unquantified under a road embankment. Although the importance of heat advection linked with subsurface water flow on permafrost degradation has gained recognition (e.g., Fortier et al., 2007, McKenzie and Voss 2013, Evans and Ge 2017, Dagenais et al., 2020), most previous studies neglected the advective heat transfer and adopted pure heat conduction to predict and evaluate thermal stability of road embankments (e.g., Fortier et al., 2011, O'Neill and Burn 2016, Chen et al., 2018). Moreover, for the previous described thermal boundary conditions (TBCs), the complex thermal interaction between the atmosphere and a road embankment is simplified by empirical equations, such as n-factor approach (i.e., a ratio of ground surface temperature, GST, to AT) (e.g., Lunardini 1978, Karunaratne and Burn 2004, Walvoord et al., 2019), and adherent-layer theory (i.e., annual GST can be approximated as a sinusoidal wave, which is a combination of surface offset and AT) (e.g., Zhu 1988, Lai et al., 2003, Chen et al., 2018). Briefly, these approaches negate the feedback of subsurface processes on the ground energy fluxes and do not consider effects of the land surface processes (e.g., the change of snow regime and surface cover types) and the inter-annual variation in the AT and precipitation. Although one-dimensional heat conduction model driven with the meteorological data was developed to investigate the shallow surface energy component (Solaimanian and Kennedy 1993, Hermansson 2004, Gui et al., 2007, Dumais and Doré 2016, Chen et al., 2021), impacts of lateral and vertical heat transfer on thermal regime of a road embankment are not investigated and quantified. To date and to our knowledge, no studies evaluate the thermal regime of a road embankment in a changing climate through a cryohydrogeological model coupled with SEB model.

Our study addresses the following question: "*what is the impact of heat advection linked with mobile water flow to the fast permafrost thaw and talik development under a sub-Arctic road embankment?*" The objectives of this study are (1) to integrate a SEB model into a groundwater flow and heat transfer model (SUTRA-ice model, originally developed by U.S. Geological Survey; Voss & Provost, 2010); (2) to reproduce observed 25-year (1993-2018) permafrost thaw and talik formation beneath a road embankment in Beaver Creek, Yukon, Canada; (3) investigate role of

heat conduction and heat advection via subsurface water flow in accelerating permafrost thaw and talik development; and (4) estimate the role of talik development on permafrost degradation.

We hypothesize that (1) a combined effect of snow insulation, water flow, road construction and climate warming contributes to the fast permafrost degradation and talik formation; (2) heat advection associated with water flow provides additional energy to expedite permafrost thaw; (3) formation of talik accelerates permafrost thaw and create an irreversible thermal state of permafrost. To achieve these objectives, a fully coupled heat transfer and water flow model integrated with the SEB model was developed and applied to address these questions using a 25-year record (1993-2018 on the Alaska Highway) of meteorological and ground temperature measurements.

5.2. STUDY SITE

In 1993, an experimental road was constructed to monitor the thermal state of permafrost under road embankment at Beaver Creek, southwestern Yukon, Canada (Figure 5.1a) (Doré et al., 2006). The Beaver Creek region is in the Klondike Plateau of the Western Boreal Cordillera (Statistics Canada, 2018). The study site is characterized by ice-rich, degrading permafrost, and significant subsurface water flow (de Grandpré et al., 2012, Stephani et al., 2014, Sliger 2016). Mean annual AT (MAAT, 19981-2010) at Beaver Creek is -4.8 °C, with a mean January temperature of -25.2 °C and a mean July temperature of 14.1 °C. The MAAT has been rising by 2.0 °C over 1981 to 2010 (Environment and Climate Change Canada, 2019). Mean annual precipitation (1981-2010) is 417 mm, of which 117 mm (28 %) falls as snow. Snowfall starts annually in September and snowmelt starts in April. The thawing and freezing indices (yearly ATs above and below freezing) represent an average of 1537.7 thawing degree-days and 3321.8 freezing degree-days respectively (1981-2010) (Environment and Climate Change Canada, 2019).

The Beaver Creek - Road Experiment Site (BC-RES) is located at km 1865 of the Alaska Highway (Figure 5.1b). The permafrost temperature below the undisturbed natural ground (NG) is about -2.2 °C at the 8 m depth (Stephani 2013). The local vegetation is the taiga biome, with stunted spruce, shrubs, tussocks, and mosses characterizing the area (Stephani 2013, Sliger, 2016). Peat deposit ranges from 0.2 m to 0.4 m in thickness overlying the sandy silt layer (Stephani 2013,

Sliger 2016). The active layer thickness is approximately 1 m (Stephani 2013). Subsurface water flow occurs preferentially in water tracks as can be observed on Figure 5.1 (lighter tone vegetation aligned perpendicular to the slope) (de Grandpré *et al.*, 2012; Sliger, 2016).

(a) Map of Yukon Territory

(b) False-color satellite image of BC-RES

(c) Vegetated natural ground (NG)

(d) Snow-covered embankmet slope

(e) Asphalt-paved embankment center
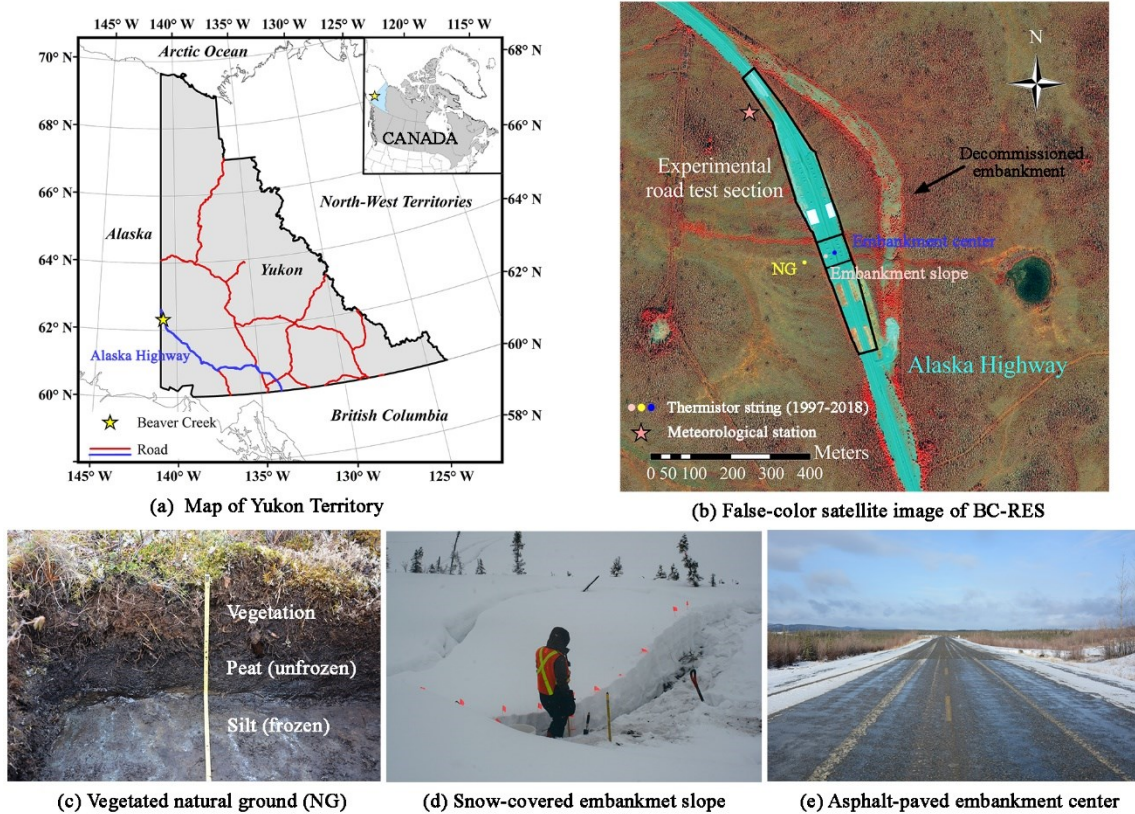
Figure 5.1. Location of the Beaver Creek - Road Experimental Section (BC-RES), south-western Yukon (62° 20' N, 140° 50' W). (a) Map of Yukon Territory showing the location of the BC-RES with a yellow star and roads with red lines (modified from Natural Resources Canada, 2014); (b) false-color satellite image of the experimental road test site near Beaver Creek (WorldView II image, taken August 4th, 2010 at 21h30), preferential subsurface water flow is identified by the lighter tone vegetation aligned perpendicular to the slope; (c) photo of soil pit of the undisturbed natural ground (NG) made in earlier October 2017. The pit location is near the thermistor string of the NG; (d) photo of thick (~ 60 cm) snow deposited on the embankment slope, taken in March 2013; and (e) photo of asphalt-paved embankment center, taken in earlier October 2017.

The previous road embankment (Figure 5.1b) at the BC-RES was decommissioned and relocated to the west in 1993 (Doré et al., 2006). Thermal monitoring started in April 1997 (yellow points, Figure 5.1b). The studied road embankment is a reference test section, which operates without any mitigation techniques. The road embankment has been experiencing severe damage due to the permafrost thaw and the maximum monitored settlement is 10 cm·month^{-1} in the summer (de Grandpré et al., 2012). During the reconstruction in 2008, removal of berms paralleling the

embankment revealed that the embankment material sunk into the NG due to permafrost degradation and isolated saturated talik developed under the embankment slope (Reimchen et al., 2009, Stephani 2013).

5.3. METHODS

To investigate the talik initiation and development beneath road embankment, the 22-year (1997-2018 on Alaska Highway) records of ground temperatures at the BC-RES were analysed. Three land cover types were monitored, modelled and compared. They referred to the undisturbed NG (snow-covered vegetated surface), embankment slope (snow-covered gravel/sand surface), and embankment center (snow-free asphalt-paved surface). The NG case served as a reference to evaluate the effect of snowpack accumulated on the ground.

Alternatively, we fully coupled a SEB model into the groundwater flow and heat transfer model (SUTRA-ice model, McKenzie *et al.*, 2007b; Voss & Provost, 2010) to simulate the interactions of the atmospheric energy and the road embankment subbase (i.e., a layer of fill material) and subgrade (i.e., the native material under an embankment). The spatiotemporal changes of temperature and water saturation were numerically investigated and quantified. And the feedback of the talik on the permafrost degradation was investigated by quantification of the mean annual soil temperature and sensible heat stored in talik. The *in situ* meteorological data was used to drive the SEB model and to obtain the TBCs. Missing meteorological data was reconstructed by the empirical equations and linear fitting equations with the nearest two weather station (about 4 km and 8 km from the BC-RES to the BC-YGT and the BC-airport, respectively). Over the 1993-2008 period, the ratio between days of missing data and day number of the year (365) was 22.4 % for the AT, 22.0 % for rainfall, and 33.2 % for the snow, respectively. Sensitivity analysis was used to quantify the uncertainties of the interpolated meteorological data to the projected GSTs.

5.3.1. Long-term field observations

Soil temperature records were consistently measured at multiple depths by a thermistor string since 1997, although the data was missing from January 1st to September 30th, 2008 due to road

reconstruction. The thermistor strings were installed in 8-m deep boreholes located at the centerline of the road, at the mid-distance in the slope of embankment facing the south-west (downstream side), and in the NG 30 m from the southwestern road side. All the sensors (accuracy of ± 0.1 °C between -10 °C to 10 °C and 0.2 °C through the rest of the operating range, -50 °C to + 30 °C) are wired to an external data logger (CR1000, Campbell Scientific) for the control and record. Additionally, the depth of the permafrost table, identified by 0 °C isothermal, was estimated using kriging interpolation with linear semi-variogram model (Trochu 1993) of the thermistor string data for each site. The latent heat effect was identified by the slowly decreasing rate of -0.2 °C and -0.4 °C isotherms over extended periods during the thawing soils. While, the snow insulation was detected by the smaller amplitude of GST variation, in comparison to winter AT variation (Chen et al., 2020a). Also, mid-October was chosen to locate the permafrost table, but mid-April was characteristic of the coldest conditions of underlying permafrost (Ives and Fahey 1971). The thickness of talik was determined by the distance between seasonal freeing depth and permafrost table in mid-April. The soil depth is relative to the NG surface. The negative value of soil depth represented that the soil is below the NG surface, while the positive value illustrated that the soil is located in the embankment, which is above the NG surface.

The dataset of the meteorological information at the BC-RES was available from 2008 to 2018 (Fortier and Chen 2020b). The meteorological station was installed in the right-of-way, about 30 m from the road embankment at the BC-RES, to provide hourly AT, rain precipitation, wind speed, and incoming solar radiation data. The measurements of AT and wind speed started in October 2008, while rainfall and solar radiation started in October 2012. The AT is measured by a thermistor (Campbell Scientific, resolution of 0.01 °C, accuracy of ± 0.2 °C) installed in a solar radiation shield located 2 m above the ground surface. The precipitation is measured at the same location by a tipping bucket (TE525WS, Campbell Scientific, resolution of 8.25 ml, accuracy of ± 1.0 %). The solar radiation is measured by pyranometer (Campbell Scientific, accuracy of ± 5 %). The wind speed is measured by an anemometer (Campbell Scientific, resolution of 0.0980 m·s^{-1}, accuracy of ± 0.3 m·s^{-1}).

5.3.2. Reconstruction of meteorological data

The missing meteorological data for the 1993-2008 period at the BC-RES was interpolated with data from BC-airport (62°24'37" N, 140°52'03" W, 649.0 m above sea level, 8 km away from the BC-RES), which provides the available dataset of daily meteorological measurements during the 1968-2014 period (Environment and Climate Change Canada, 2019).

5.3.2.1. Daily maximum, minimum, and mean AT

For the 1993-2008 period, we linearly interpolated the daily maximum, minimum, and mean AT of the BC-RES with the measurements at the BC-airport. The coefficients of linear fitting equation were calculated with the available data from the BC-RES and the BC-airport during the 2009-2014 period. Figure S5.1 illustrates that the measured daily maximum, minimum, and mean ATs at BC-RES were linearly related to the measured values at the BC-airport ($R^2 > 0.97$, RMSE < 2.6 °C, MAE < 2.0 °C).

5.3.2.2. Solar radiation

The solar radiation data over the 1993-2013 period were estimated by the empirical equation (Allen et al., 1998), due to the lack of direct measurements. Extraterrestrial radiation (Q_a) for each day of the year and for different latitudes can be estimated from the solar constant, the solar declination and the time of the year by the following empirical equation (Allen et al., 1998):

$$Q_a = \frac{G_{sc}d_r}{\pi}\left[\omega_s \sin\varphi\sin\delta + \cos\varphi\cos\delta\sin\omega_s\right] \tag{5.1}$$

where G_{sc} is solar constant (117.5 MJ·m^{-2}·day^{-1}) (Garnier and Ohmura 1968); d_r is the inverse relative distance Earth-Sun, $d_r = 1 + 0.033\cos(2\pi/365J)$; ω_s is the sunset hour angle, $\omega_s = \arccos(-\tan(\varphi)\tan(\delta))$; φ is the latitude (rad); δ is solar decimation (rad), $\delta = 0.409\sin(2\pi/365J - 1.39)$; J is the number of the day in the year between 1 (1st January) and 365 (31st December).

Solar radiation (Q_{SW}^{in}) is calculated by a function of diurnal temperature range (ΔT) and extraterrestrial radiation (Q_a) (Hargreaves and Samani 1982, Fan et al., 2018):

$$Q_{SW}^{in} = Q_a \times \left(a \times \Delta T^{0.5} + b \times \Delta T^{0.25} + c \times \Delta T + d \right) \tag{5.2}$$

where, a, b, c and d are empirical coefficients. The empirical coefficients of linear fitting equation between Q_{SW}^{in} and Q_a were calculated with the measured data from the BC-RES over the 2013-2018 period. In this study, the coefficients of a, b, c, and b were 0.341, -0.263, -0.016, and 1.279, respectively. Furthermore, the performance of three linear regression models were compared to calculate the daily solar radiation, shown in the Table S5.1. Eq. (5.2) was finally selected, due to a good performance with the high value of R^2 (0.91) and low values of RMSE (28.77 W·m^{-2}) and MAE (20.39 W·m^{-2}), shown in the Figure S5.2.

5.3.2.3. Rainfall

Over the 1993-2012 period, we assumed that the amount of rainfall in the BC-RES was the same with measurements at the BC-airport, due to high probability (larger than 80 %) of the consistent daily rainfall event and small deviation (less than ± 10 %) of total annual amount between two sites in 2013. Furthermore, the missed rainfall data in the years of 2006, 2007, 2008, and 2012 at the BC-airport was replaced by mean annual rainfall precipitation over the period of 1981-2010.

5.3.2.4. Snow depth

The long-term consistent measurements of snowpack were not available at the BC-RES. We used the measured snow depth variations at the BC-airport and the BC-YGT (62°22' N, 140°52' W, 663.0 m above sea level, 4 km from the BC-RES) to interpolate the snowpack regime at the BC-RES. Over the available period of snow depth measurement (1993-2008), the difference of maximum snow depth was less than 4 cm (Figure S5.3a) in the Beaver Creek area (Environment and Climate Change Canada, 2019). Also, the measurements show that the maximum snow depth was relatively stable (about 0.40 m) during 1993-2006, while varied greatly from 0.49 m to 1.1 m with an average of approximately 0.70 m over 2007-2014. Therefore, two snow conditions were used in all simulations. We run the simulations with the maximum snow depth of 0.4 m during 1993-2006, while 0.70 m during 2007-2018 (Figure S5.3b). Moreover, two snow surveys using a graduated pole in March 2010 and 2013 (just before the snowpack started to melt) shows that

the average of snow thickness was about 0.6 m (Stephani 2013), which improves our confidence in the interpolation of snow depth. The snow regime was presented in Figure S5.3.

5.3.2.5. Wind speed

Similarly, daily wind speed of the year during the 1993-2008 period was set the same as the mean values of daily wind speed over the 2009 - 2018 period. Because the mean annual wind speed varied at the range from 1.0 m·s^{-1} to 1.3 m·s^{-1}, with an average of 1.1 m·s^{-1} (SD = 0.1 m·s^{-1}, less than 10 %). Also, the variations (± 10 %) of wind speed, caused by the topography change, had little impact on mean annual GST (mean ± SD = 0.04 ± 0.09 °C) (Chen et al., 2021).

5.3.3. Numerical model and modelling approach

The methodology of modelling is illustrated in Figure 5.2. We fully integrated the SEB model, developed by Chen et al., (2021), into the SUTRA-ice code (McKenzie et al., 2007, Voss and Provost 2010). The meteorological data from 1993-2018 and the simulated soil temperatures at depth (outputs of the SUTRA-ice code) were used to drive the SEB model, while the TBCs of the SUTRA-ice code were provided by the SEB model (Figure 5.2). The performance of SUTRA-ice code integrated with the SEB model was evaluated by comparing the measured and simulated soil temperatures at depth. The validation period of integrated model from 2014 to 2018 was selected due to the available measurements of meteorological data.

3.3.2.1. Surface energy balance (SEB) model

The SEB model can simulate the surface temperatures and surface energy components with varying snow depth and properties (Chen et al., 2021). The SEB model was driven by the net radiation (Q_{net}), sensible heat flux (Q_h), heat flux of vapor exchange from the surface (Q_v), ground heat flux through the snow and the near-surface soil layer (Q_c), rainfall heat (Q_p), and stored energy (Q_0). The SEB is expressed as:

$$Q_{net} + Q_p - Q_h - Q_v - Q_c = Q_0 \tag{5.3}$$

The SEB model has been successfully developed, calibrated, and validated with 10-year field observations at the same study site and detailed description of sensitivity analysis of snow depth, duration and timing can be found in Chen et al., (2021). The energy balance in the SEB model was

fully coupled to the heat transfer equation in SUTRA-ice. The GSTs are used as the TBCs and affect the heat transport, while the subsurface temperatures influence the energy balance by changing the amount of the ground heat flux and stored energy (Figure 5.2). Additionally, the surface temperatures (purple nodes, Figure 5.2b) were calculated by balancing the energy components based on the inputted meteorological data and simulated sub-soil temperature (green nodes, Figure 5.2b). The distance between the ground surface node and the subsurface node depends on the meshed size and was calculated by their coordinates ($z = \sqrt{\Delta x^2 + \Delta y^2}$).
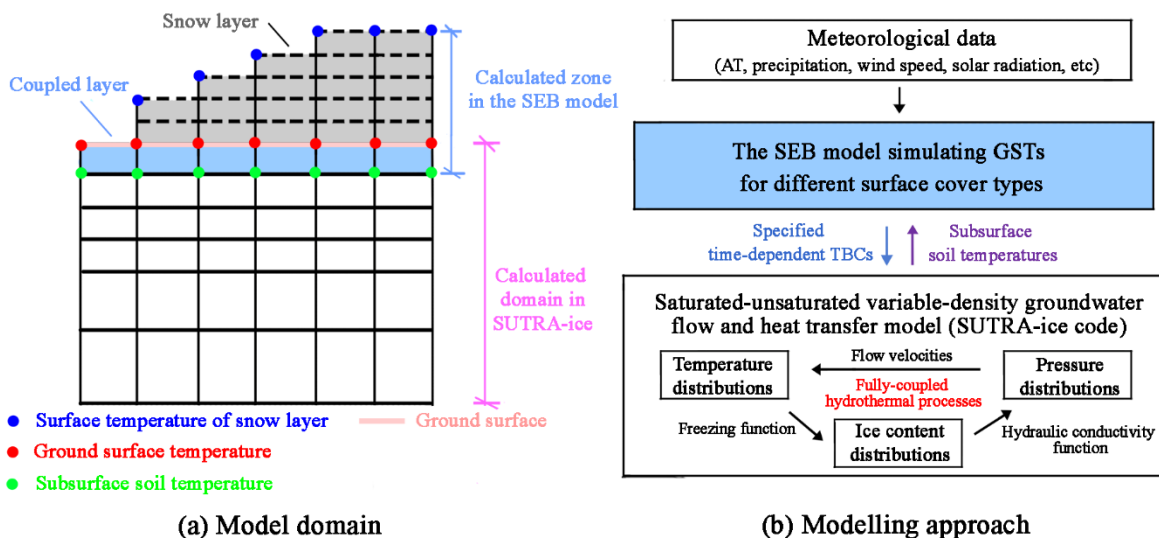
Figure 5.2. (a) model domain of SUTRA-ice code integrating surface energy balance (SEB) model; and (b) modelling approach of integrated model, driven by meteorological data.

Alternatively, the equation 5.3 was iteratively solved by Newton-Raphson iteration method. Because the radiation term (Q_{net}) depends on the fourth power of the surface temperature and the other terms depend on the first power (Hwang 1976). When snow cover is absent, the GST equals the surface temperature; when the snow is present, the GST was simulated by numerically solving heat conduction equation with dynamic freeze-thaw functionality (Chen et al., 2021). The outputs of the SEB model, either specified temperature or heat flux variations, were set as the time dependent TBCs. All parameters used in the model are listed in Table S5.2.

3.3.3.1. Saturated-unsaturated groundwater flow and heat transfer model

The modified SUTRA-ice code (McKenzie et al., 2007b, Voss and Provost 2010) was used to simulate the transient groundwater flow and heat transport in variably-saturated conditions with

129

freezing and thawing dynamics. It has been benchmarked against other coupled cryohydrogeological models from the *InterFrost* consortium (Rühaak et al., 2015, Grenier et al., 2018) and tested against the analytical solutions proposed by Lunardini (1986). The SUTRA-ice code has successfully simulated the effect of climate change on thermal and hydrological processes (e.g., McKenzie and Voss 2013, Kurylyk et al., 2016, Evans et al., 2018) and the feedback of permafrost degradation on the temporal shift of groundwater discharge (e.g., Ge et al., 2011, Lamontagne-Hallé et al., 2018, Walvoord et al., 2019).

Two coupled partial differential equations are used herein to represent the saturated-unsaturated groundwater flow and the transport of thermal energy in a subsurface environment. The detailed description of the governing equations can be found in Voss and Provost (2010) and details of BCs are documented in Provost and Voss (2019). Fluid movement in porous media where fluid density varies spatially is driven by differences in fluid pressure:

$$\left(S_L \rho_w S_{op} + \varepsilon \rho_w \frac{\partial S_L}{\partial p} \right) \frac{\partial p}{\partial t} + \left(\varepsilon \left(\rho_i - \rho_w \right) \frac{\partial S_i}{\partial T} + \varepsilon S_L \frac{\partial \rho_w}{\partial T} \right) \frac{\partial T}{\partial t} - \nabla \left[\left(\frac{\underline{\underline{K}} K_r \rho_w}{\mu} \right) . \left(\nabla p - \rho_w g \right) \right] = q_p \quad (5.4)$$

where S_L and S_i ($S_i = 1 - S_L$) are the saturation of liquid water and ice, S_{op} is the specified pressure storativity (Pa^{-1}), p is pressure (Pa), ε is porosity, t is time (s), ρ_w, ρ_i and ρ_s are the densities (kg·m^{-3}) of the liquid water, ice and solid matrix, respectively, T is temperature (°C), $\underline{\underline{K}}$ is the permeability tensor, μ is the viscosity of liquid water (kg·m^{-1}·s^{-1}), g is gravity (m·s^{-2}), q_p is pore water inflow at a boundary (kg·m^{-3}·s^{-1}), K_r is the relative permeability.

Energy transport in the porous media is governed by:

$$C_a \frac{\partial T}{\partial t} + \varepsilon S_L \rho_w c_w \underline{v} . \nabla T - \nabla . \left\{ \lambda \nabla T \right\} = Q_p c_w \left(T^* - T \right) \quad (5.5)$$

where C_a is the apparent heat capacity (J·kg^{-1}·°C^{-1}), ε is porosity, $\underline{v}$ is the groundwater velocity vector (m·s^{-1}), λ is the bulk thermal conductivity of the ice-water-solid matrix (W·m^{-1}·°C^{-1}), T^* is the temperature of the inflowing water (°C). In this study, the energy sources in the water and solid grains are equal to zero at the domain boundaries.

The apparent heat capacity (C_a) was equal to the weighted arithmetic average of the heat capacity of the matrix constituents plus latent heat effects during pore water phase change. Similarly, the bulk thermal conductivity was calculated by the weighted arithmetic average of the thermal conductivities of the matrix constituents (Farouki 1982).

$$C_a = \varepsilon \left(S_L \rho c_w + S_i \rho_i c_i \right) + \left(1 - \varepsilon\right) \rho_s c_s S_L + \varepsilon \rho_i L_f \frac{\partial S_L}{\partial T} \tag{5.6}$$

$$\lambda = \varepsilon S_w \lambda_w + \varepsilon S_i \lambda_i + \left(1 - \varepsilon\right) \lambda_s \tag{5.7}$$

where L_f is the latent heat of formation of ice. The c_i, c_w, and c_s are the heat capacities of ice, water and solid matrix, respectively. The SUTRA-ice uses three saturations: liquid water saturation (S_L), ice saturation (S_i), and air saturation (S_a). Total water saturation is the sum of S_L and S_i. Total water saturation (S_w) was related to the pore pressure (p) and was calculated with a piecewise-linear function:

$$S_w = \begin{cases} 1 & \text{for } p > p_{cent} \\ \left(1 - S_{wres}\right) \dfrac{p - p_c}{p_{cent} - p_c} + S_{wres} & \text{for } p_c \leq p \leq p_{cent} \\ S_{wres} & \text{for } p < p_c \end{cases} \tag{5.8}$$

where S_{wres} is the residual liquid water below which saturation is not expected to decrease (because fluid becomes immobile), p_c and p_{cent} are fluid capillary pressure (Pa) and entry capillary pressure (Pa), respectively. When pore pressure is larger than entry capillary pressure, p_{cent}, the void space is saturated ($S_w = 1$). When pore pressure is equal to or less than entry capillary pressure, air has entered the matrix and the void space is only partly fluid filled, $S_a = 1 - S_w$.

The liquid water saturation (S_L) varies as a function of temperature when the temperature is below the freezing point (T_0, °C) (Jame and Norum 1980) and was calculated by the exponential freezing function (Lunardini 1988).

$$S_L = \left(1 - S_{wres}\right) e^{-\left(\left(T - T_f\right)/m\right)^2} + S_{wres} \tag{5.9}$$

where T_f is the freezing point, usually 0 °C, m is a fitting parameter.

The relative permeability decreases with ice saturation until reaching a minimum permeability (10^{-5}) at residual liquid saturation (S_{wres}) and was calculated by an impedance factor approach (Lundin 1990).

$$K_r = 10^{-\Omega \ (1-S_L)}$$
(5.10)

where Ω is an empirically derived impedance factor. In this study, Ω equals to 10. Additionally, sensitivity analysis (Figure S5.5) suggested that the deviation of mean annual soil temperature caused by the linear and impedance-factor approaches was less than 0.2 °C (SD < 0.09 °C) at depth. Also, Evans and Ge (2017) presented that the coefficient (Ω) has a limited effect on the magnitude of warming and annual groundwater discharge. All parameters used in the SUTA-ice model were listed in Table S5.3 and Table S5.4.

3.3.3.2. Model domain and boundary conditions

The computational domain consists of four sub-domains, including asphalt, embankment fill, peat layer, and sandy silt layer, as described in Figure 5.3. The geometry corresponds to an asphalt-paved embankment with an upper surface width of 12.0 m, a height of 5.0 m, and 2:1 side-slopes. The top surface consists of a 10.0-m width asphalt-paved driving surface and 1-m width bare gravel-sand embankment shoulder. The porous, low-moisture embankment fill lies directly on the natural ground (Figure 5.3). The thickness of the peat layer is 0.4 m. The model domain is a 237 m long, and the thickness of the natural ground is 66 m. Additionally, the vertical mesh size of the computational domain coarsens with depth from 0.1 m in the peat layer to 3.0 m at the model bottom. The horizontal mesh size spacing increases from 0.2 m at the embankment subgrade to 2.0 m at the left and right sides.

The model simulation was run in three stage. The first stage generated the frozen ground with a specified temperature of -6 °C and a constant pressure of 0 Pa at the top surface of the NG, shown in Figure 5.3. The model was run for 1000 years to a steady state. In second stage, the model was driven by meteorological data from May 1st, 1992 to April 30th, 1993 for 100 years to reach a quasi-dynamic equilibrium with the active layer thickness of 1.0 m and the ground temperature of -2.5 °C at the 8-m depth, which is close to the observed values below the NG (Stephani 2013). The outputs of stage 2 were used as the initial temperature and pressure distribution of stage 3.

The initial temperature of embankment subgrade was set as the average summer AT (10.8 °C) in 1993, as the construction of the road started in 1993 summer. During stage 3, the model was driven by meteorological data from the 1993-2018 period. The time step sizes were 1 years for stage 1, and 1 day for stage 2, respectively. For the stage 3, to save the space and reduce the simulation time, we selected 8 hours as the time step as the simulated GST deviation caused by 8-hour and 6-hour time step was less than 0.05 °C.
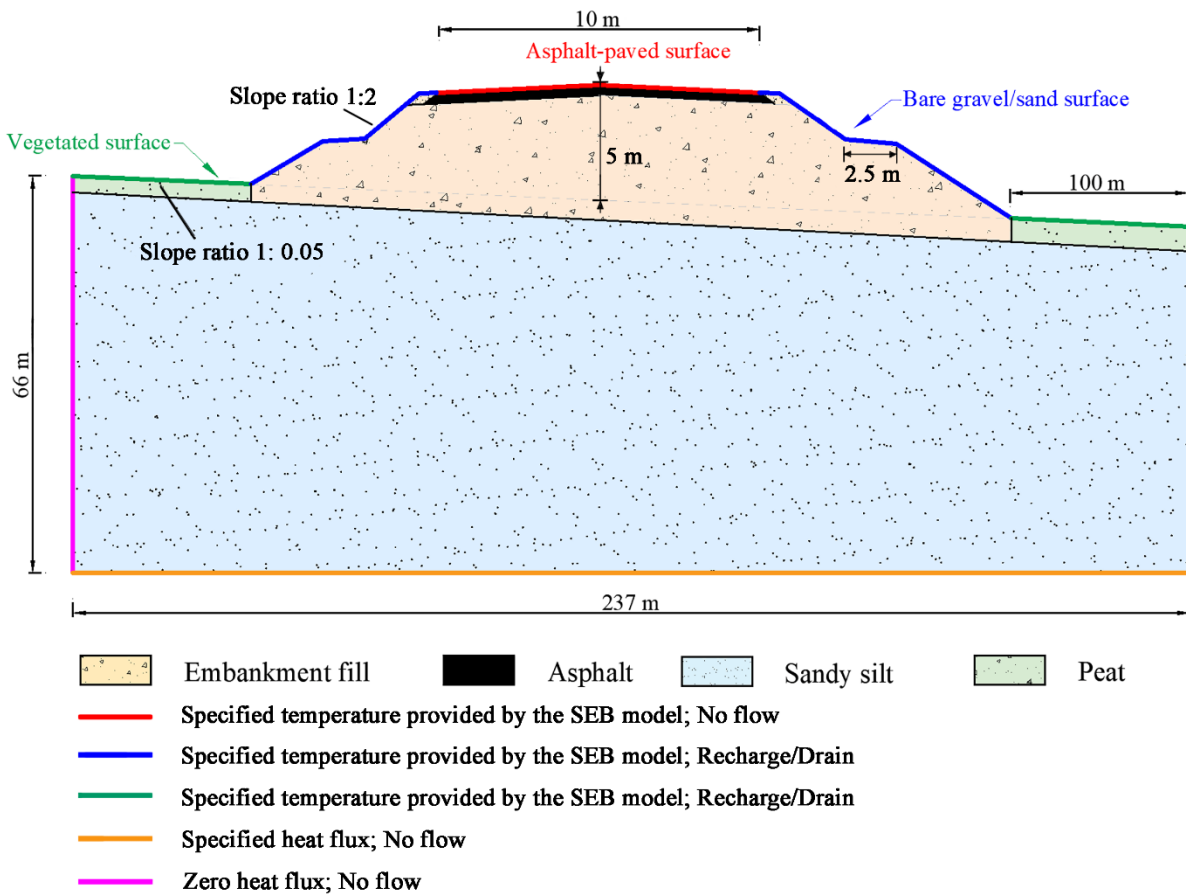
Figure 5.3. Two-dimensional model domain with temperature and hydraulic boundary conditions. Note that the model is not-to-scale.

For the TBCs, gain or loss of energy varies with the change of atmosphere and the land surface processes. To represent the complex heat exchange with the atmosphere at the top surface, the specified time-dependent TBC was estimated by the SEB model with inputs of independent variables of meteorological data. This novel TBC considered the effect of subsurface processes and inter-annual climate change, shown in Figure 5.3. Also, it allowed to simulate GST and surface

energy components with varying snow properties and depths (Chen et al., 2021). More details about the other TBC approaches were discussed in Chen et al., (2021). Additionally, an adiabatic BC was applied on both sides of the conceptual model. A heat flux representing the local geothermal gradient (0.08 W·m^{-2}; Grasby et al., 2011) is assigned across the bottom of the domain. The top embankment surface is asphalt-paved with an albedo of 0.13 in the snow-free period and 0.3 in the snow-covered period (Dumais & Doré 2016, Chen *et al*., 2021), while the top surface of embankment shoulder and embankment slope is bare and covered by gravel and sand (albedo 0.3, Hwang 1976).

For hydraulic BCs, the gain of fluid mass at the model surface was related to the recharge of rainfall and snowmelt water. The temperature of the inflowing water was always equal to the GST. Water may only exit the model at the NG surface or on the embankment sides, through the coupling of the time-dependent specified recharge boundary condition with a drain boundary condition. When the pressures of surface nodes were higher than 0 Pa (water table intercepts the top surface), the drain BCs allowed discharge (Figure 5.3). The loss of liquid water (discharge) varied linearly with pressure (Provost and Voss 2019). No flow boundaries were present at the vertical sides, representing the theoretical limits of a hydrogeological watershed, and at the bottom, representing the low-permeability bedrock at depth. The left and right boundary conditions were both set considerably far from the road embankment (100 m each), therefore limiting their potential effects on the modelling outcomes of interest for this study. The road pavement surface is also a no-flow boundary, as we consider asphalt to be impermeable.

3.3.3.3. Modelling strategy

To investigate the role of advective heat transfer on the permafrost degradation, two additional simulations with (scenario 2) and without (scenario 2) groundwater flow were performed and compared. The specified GST of scenario 2 was obtained by the SEB model with the same input of meteorological data of scenario 1. The thermal regimes in mid-October and mid-April of 2018 were selected to compare the difference of permafrost table depth and talik area between scenario 1 and 2. The difference of simulated soil temperatures (scenario 1 - scenario 2) is presented to investigate the role of the subsurface water flow on permafrost degradation.

Furthermore, the amount of sensible energy stored in the unfrozen zone and the mean soil temperature were used to quantify the feedback of talik development on permafrost degradation. Sensible heat storage in unfrozen water is expressed by (Dincer et al., 1997):

$$Q = \int_{T_{ti}}^{T_{tf}} m \, C_p dT = m \, C_p (T_{tf} - T_{ti})$$

(5.11)

where Q is the amount of heat stored (W), T_{ti} is the initial temperature, T_{tf} is the final temperature, m is the mass of heat storage medium, and C_p is the specific heat. In this study, the initial temperature (T_i) was set as the initial temperature at a certain depth at the beginning of the simulation, the mass (m) is equal to the volume ($\Delta x \times \Delta y \times \varepsilon$) of the pore soil multiplied by its saturation (S_L) and its density. In this study, the sizes of the rectangular grid at depth were the same with 0.2 m (Δx) width and 0.25 m (Δy) height.

5.3.4. Model performance and sensitivity analysis

To quantitatively evaluate the thermal performance of the SUTRA-ice code combined with SEB model, we selected five statistical criteria, including coefficient of determination (R^2), root mean square error (RMSE), mean absolute error (MAE), mean bias error (MBE), and standard deviation (SD). Due to available measurements of meteorological data and soil temperatures, we selected the validated period from May 1st, 2014 to April 30th, 2018 and compared the measured and simulated soil temperatures at multiple depths below three different surface cover types, including embankment center, embankment slope, and natural ground.

The RMSE was used to evaluate the uncertainty in the simulation (Chai and Draxler 2014). The MAE was used to estimate the absolute difference between simulated and measured values (Chai and Draxler 2014). The MBE is the average error representing the systematic error of a prediction model to under or over prediction (Kato 2016). The SD was used to quantify the extent of deviation of a set of data values (Newman 1939).

Alternatively, sensitivity analysis was used to quantify uncertainty of the interpolated meteorological data to the simulated GSTs by the combined code. The sensitivity analysis method changed one parameter at a time, while holding all others constant. For the AT, the uncertainty was quantified by comparison with: (a) simulations using raw measurement as a reference case;

and (b) simulations using the interpolated AT (Figure S5.1). Similarly, the uncertainty of solar radiation was quantified by comparison of measured values and interpolated data by an empirical equation shown in Figure S5.2. Additionally, the uncertainties of rainfall and wind speed inputs were quantified by comparison of measurements and average values of the measured data over the 2009-2018 period. The uncertainty of snow depth variations was quantified by changing a range of 0.12 m, determined by the deviation of snow depth along the test sections according to the snow survey in 2010 (Stephani 2013). Furthermore, the MAE and MBE of GST deviations were used to evaluate the uncertainty.

5.4. RESULTS

5.4.1. Reconstruction of meteorological data (1993-2018)

During the 1993-2018 period, AT gradually increased, rising at a rate of 0.072 °C·a^{-1} (Figure 5.4b).
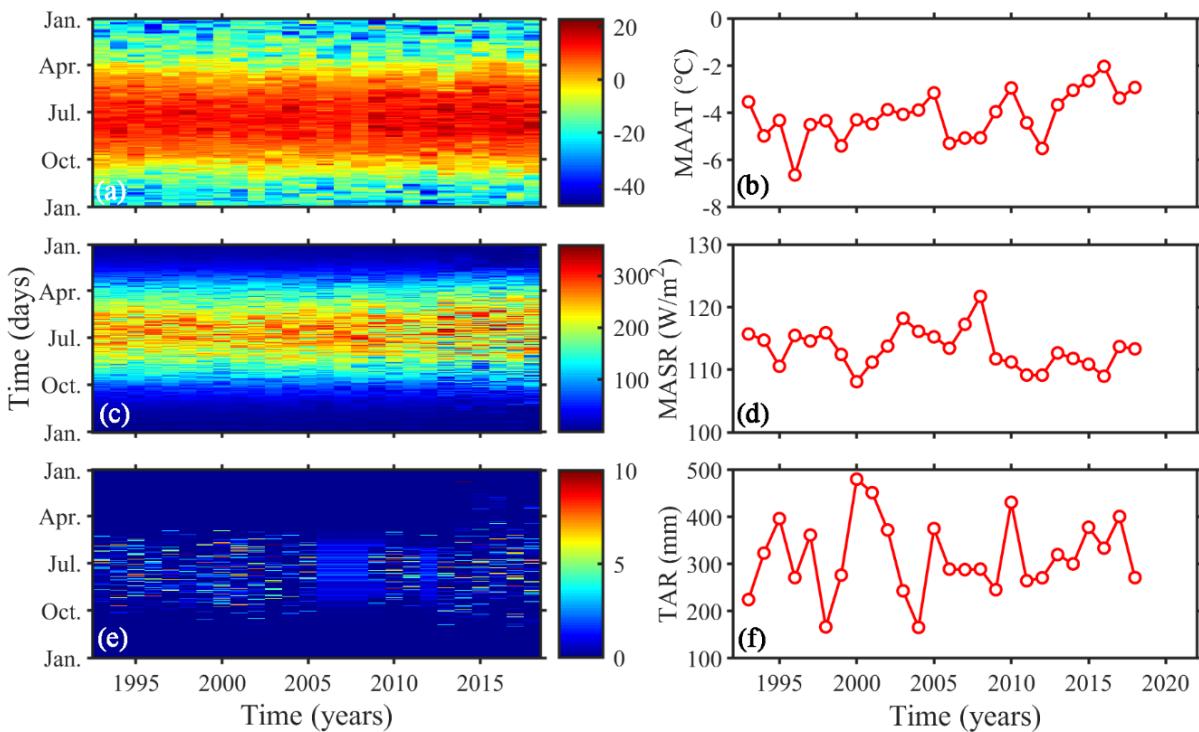
Figure 5.4. Reconstruction of climate data at the BC-RES over the simulated period from 1993 to 2018; (a) daily air temperature (AT) and (b) mean annual AT (MAAT) (°C); (c) daily solar radiation and (d) mean annual solar radiation (MASR) (W·m^{-2}); (e) daily rainfall; and (f) total annual rainfall (TAR) (mm). Note: the missing rainfall data of 2006, 2007, 2008, and 2012 was replaced by average daily rainfall over the 1981-2010 period; the data from 2013-2018 was measurements of meteorological station at the BC-RES.

Over this period, the MAAT was -4.1 °C. The thawing and freezing indices represented an average of 1449.0 thawing degree-days (TDD) and 2951.2 freezing degree-days (FDD), respectively. Mean annual solar radiation (MASR) remained relatively stable at an average of 113.4 W·m^{-2} (SD = ± 3.2 W·m^{-2}) (Figure 5.4b). The total annual solar radiation was 41374.4 W·m^{-2} (SD = ± 86.9 W·m^{-2}), in which summer radiation contributed to 46.9 % (19393.6 W·m^{-2}), while winter radiation was only 3.8 % (1591.2 W·m^{-2}), respectively. Mean annual rainfall precipitation exhibited a significant inter-annual variability, with an average of 302.2 mm (SD = 1.2 mm), of which 75 % falls in summer (Figure 5.4c).

5.4.1. Thermal observations (1997-2018)

For the NG (Figure 5.5a), the permafrost table, identified by 0 °C isothermal, remained stable at the depth of approximately 1.0 m (SD <0.05 m). The permafrost temperature below the NG was
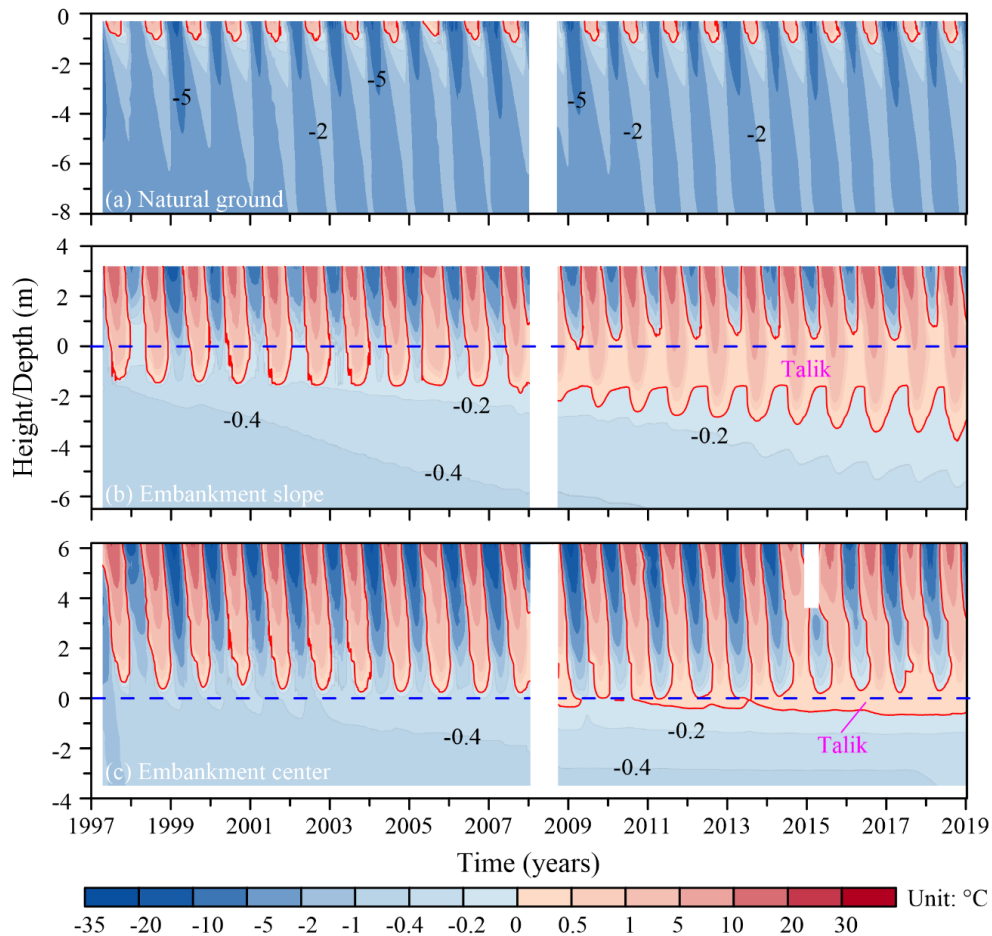
Figure 5.5. Measured soil temperature variations below the ground surface from 1997 to 2018; (a) natural ground; (b) embankment slope; and (c) embankment center. Note: the blue line

represents the interface between natural ground and embankment fill. The white column represents the missing data from January 1ˢᵗ to 30ᵗʰ September 2008.

-2.2 °C at a depth of 8.0 m. Conversely, for the embankment slope (Figure 5.5b), the permafrost table deepened from 1.3 m to 3.8 m, with an average increase of approximately 0.11 m·a-1. The increasing rate was not constant, with a relatively quick rate (0.17 m·a-1) during 2007-2018. In 2007, a 1.5-m-thick talik initially formed and grew gradually over the observed period. The soil temperature in talik reached a maximum of 7 °C in summer. Further evidence of permafrost warming was the -0.2 °C isotherm which was at a depth of 1.6 m in 2002 and was 3.8 m shallower than in 2018. Similarly, for the embankment center (Figure 5.5c), permafrost table increased by 1.2 m, with an increase rate of 0.054 m·a^{-1}. The permafrost warmed gradually by about 1.0 °C at the depth of 1.5 m. A 0.2-m thick talik initiated in 2012 and had enlarged to 0.8 m by 2018.

Figure 5.6 illustrate that soil temperature at the depth of 1.5 m below embankment slope increased at a rate of 0.048 °C·a^{-1}. The permafrost slightly warmed by 0.5 °C in the first decade of monitoring, reaching 0 °C in 2007, and completely thawed in 2008. After that, the soil temperature had a strong seasonal variation and its annual amplitude had quickly increased to 2.0 °C by 2013. In winter of 2008, the thawed soil did not completely freeze back and its temperature stayed around 0 °C. Similarly, permafrost temperature at the depth of 3.0 m experienced a gradual increase, rising at a rate of approximately 0.035 °C·a^{-1}.
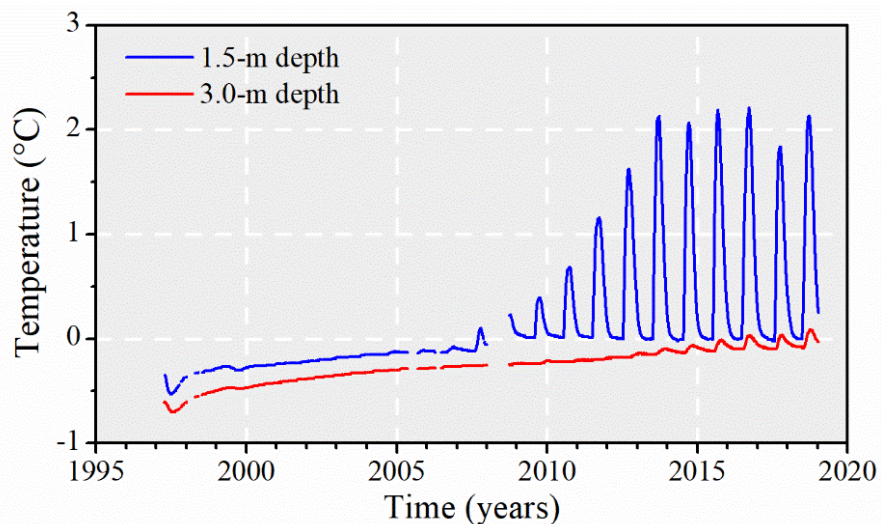
Figure 5.6. Measured soil temperature variations at the depth 1.5 m (blue) and 3.0 m (red) below the embankment slope from 1997 to 2018.

5.4.1. Model performance of SUTRA-ice model combined with SEB model

A comparison between simulated results and field measurements for three different surface cover types showed a good agreement ($R^2 > 0.93$) (Figure 5.7). The deviation between simulated and observed temperatures was largest at the top surface and gradually decreased with depth (Table S5.2). By comparison between simulated and observed GSTs, the MAEs were 1.0 °C for the NG, 1.8 °C for the embankment slope, and 2.4 °C for the embankment center, respectively. Also, the difference between measured and simulated mean annual GST was less than 0.5 °C for all three cases.
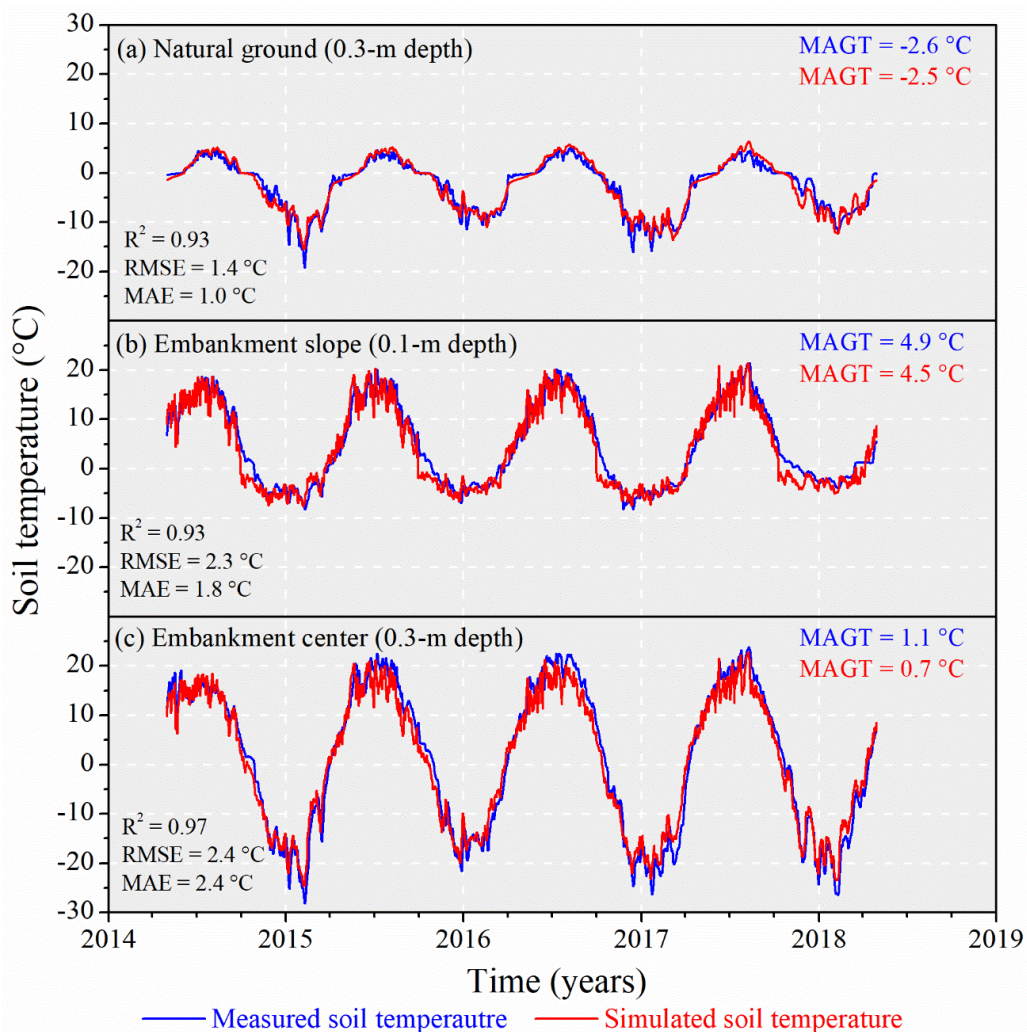
Figure 5.7. Simulated and measured soil temperatures below the different surface cover types. (a) 0.3-m depth below the embankment center surface; (b) 0.1-m depth below the embankment slope surface; and (c) 0.3-m depth below the natural ground from 2014-2019. Statistic values (R^2, RMSE, MAE) were shown in the graphs.

Additionally, the model is the most sensitive to snow depth (Table 5.1). The MBE ranged from 0.44 °C to -0.39 °C when the maximum snow depth varied ± 12 %. The next-most sensitive parameters are solar radiation and AT. Their MAEs and MBs were less than 0.4 °C. Finally, the model is least sensitive to changes in wind speed and rainfall.

Table 5.1. Sensitivity analysis of ground surface temperature (GST) to uncertainty of reconstructed meteorological data inputs.

Input parameters	Absolute perturbation	Sensitivity ranking	+ MAE (°C)	+ MBE (°C)	- MAE (°C)	- MBE (°C)
Maximum Snow depth	± 0.12 m	1	0.39	-0.39	0.44	0.44
Solar radiation	± 23.64 W·m^{-2}	2	0.38	-0.21	0.38	0.21
AT	± 1.28 °C	3	0.38	-0.10	0.28	0.00
Wind speed	± 0.54 m·s^{-1}	4	0.05	-0.02	0.06	-0.02
Rainfall	± 3.5 mm	5	0.00	0.00	0.00	0.00

5.4.2. Simulated permafrost thaw and talik development beneath road embankment

5.4.2.1. Simulated ground surface temperature (1993-2018)

The long-term GST data shown in Figure 5.8a indicates that the simulated mean annual GSTs below three surface cover types were much warmer than MAAT. The surface offsets were approximately 3.6 °C for NG, 9.1 °C for embankment slope, and 5.3 °C for embankment center, respectively (Figure 5.8b). Additionally, a significant ground warming occurred over the 2006-2018 period at a rate of 0.19 °C·a^{-1}, 0.14 °C·a^{-1}, and 0.24 °C·a^{-1} for the NG, embankment slope and center, respectively, which were about twice greater than that in 1993-2005. Additionally, the simulated thawing period of NG was approximately 20 days shorter than the duration of positive AT (Figure 5.8c). The corresponding values for embankment slope and center were about one week longer than the atmosphere.

Figure 5.8e illustrates daily specified GSTs for the SUTRA-ice simulation. In winter, the GST of embankment center was close to AT, while the surfaces of embankment slope and NG were much warmer than the atmosphere, about 16.1 °C and 10.9 °C higher, respectively. Conversely, in summer, the GST of the NG was nearly the same as the AT, while the surfaces of embankment center and slope were much warmer than the atmosphere, about 13.0 °C and 6.6 °C higher, respectively.
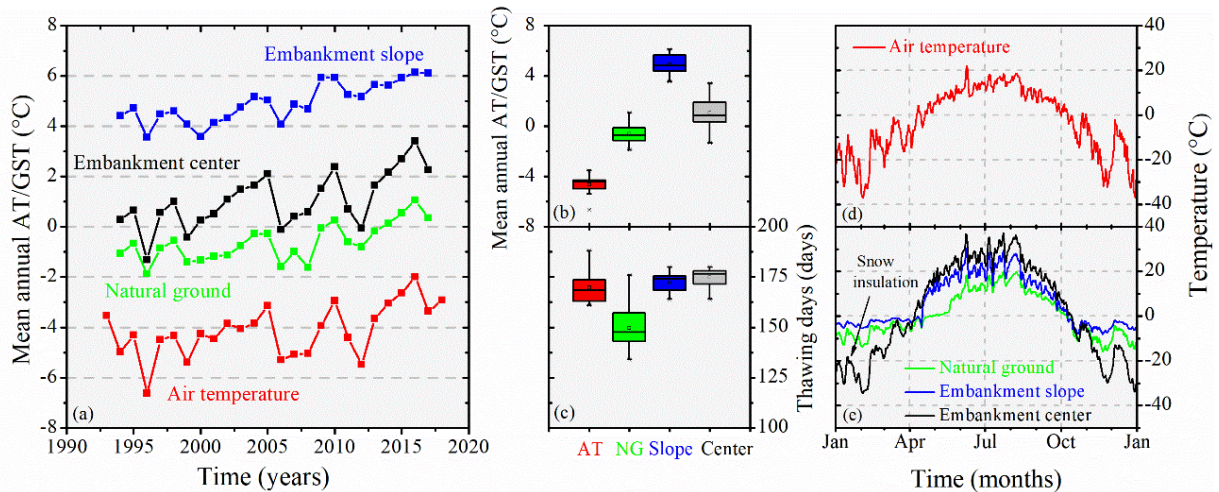
Figure 5.8. (a) Measured mean annual air temperature (AT) and simulated mean annual ground surface temperature (GST) for natural ground (NG), embankment center, and embankment slope, respectively for 1993-2018; statistical values of (b) mean annual GST and (c) thawing days over the 25-year period, mean values and standard deviations were represented with thick lines and error bars; and mean daily variations of (d) AT and (e) GST over the 25-year period.

5.4.2.2. Permafrost degradation and talik development

Figure 5.9a presented that soil temperature of the embankment subbase and subgrade exhibited an extremely asymmetric distribution. The difference between the upstream and downstream side of the embankment was about 5 °C for the soil temperature, while approximately 1 m for permafrost table depth. After road construction, the permafrost table at the embankment center was uplifted about 1.0 m above the NG surface. And, it was more than 2.0 m shallower at the embankment slope. With time elapse, permafrost degraded quickly and the depth of permafrost table rose by a maximum of 4.5 m. The temperature of the embankment subbase increased by an average of 3.5 °C from 3.0 °C in 1993 to 6.5 °C in 2018.

Figure 5.9b illustrated that a fast-growing talik initiated at the upstream side in 2003, enlarged laterally and vertically over time, and eventually expanded to the downstream side in 2008. By 2018, talik has grown more than three times larger than that in 2003. Furthermore, with the increase of permafrost thaw, more unfrozen water was accumulated beneath the embankment (Figure 5.9c). Since 2003, a saturated unfrozen zone had been located at the embankment slope and enlarged with time.
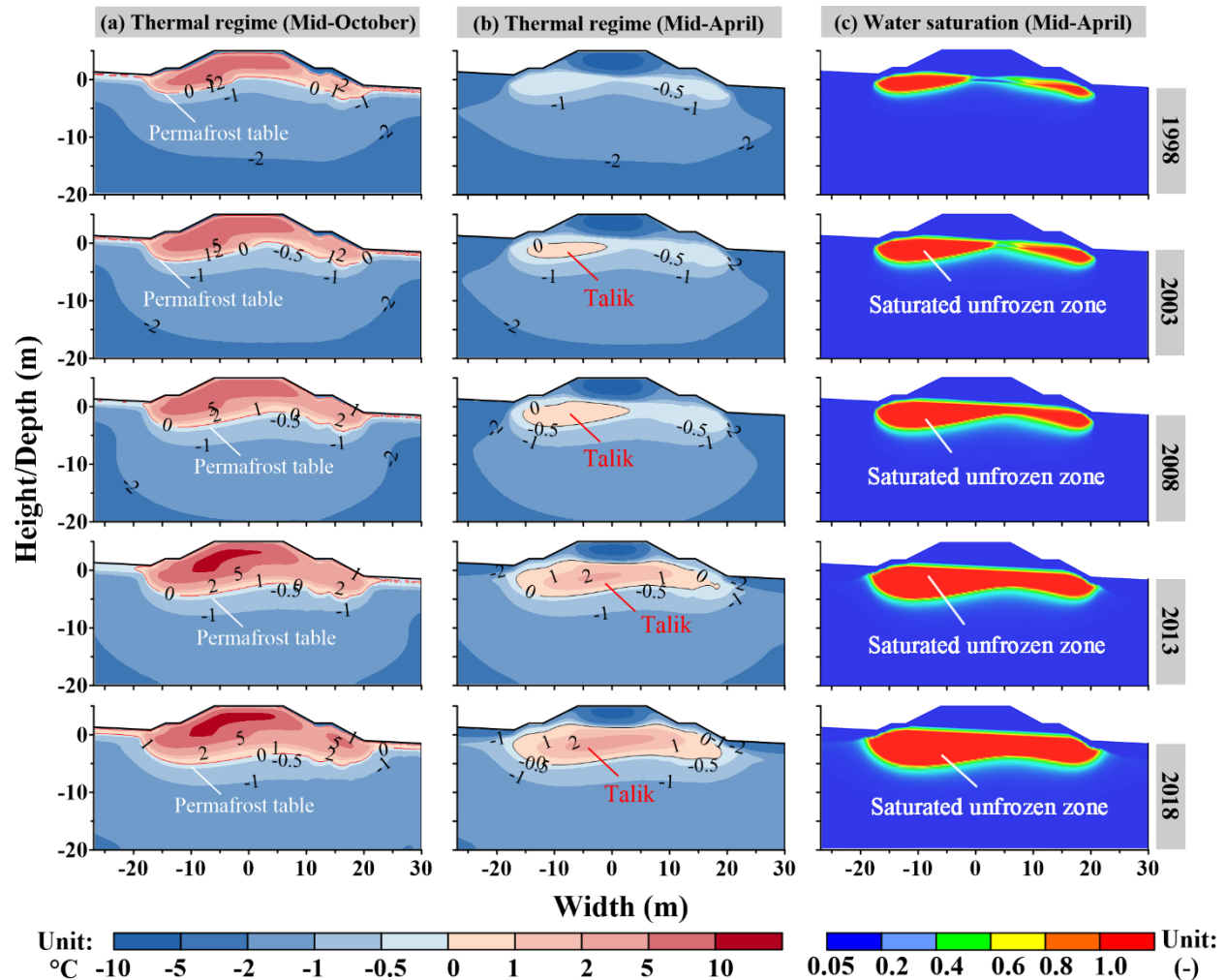
Figure 5.9. Simulated variations of (a) temperature distribution at Mid-October; (b) temperature distribution at Mid-April; and (c) water saturation at the 1998, 2003, 2008, 2013, and 2018. Note: mid-October was chosen to locate the permafrost table, but mid-April is characteristic of the coldest conditions of underlying permafrost.

Figure 5.10a presents the measured increasing depth of permafrost table from 1997 (1.3 m) to 2018 (3.8 m) at the downstream side. Similarly, the simulated depth of permafrost table experienced a similar increasing trend, at a rising rate of 0.14 m·a^{-1} from 1993 to 2018. The MAE

142

between the measured and simulated depth of the permafrost table was about 0.16 m. In contrast, permafrost thawed quickly at the upstream side, with an average rate of 0.19 m·a^{-1}. Moreover, the average of simulated talik thickness was about 2.1 m at the downstream side, which is similar to the observed value. In comparison, the talik thickness at the upstream side was much deeper, by an average of 1.4 m. By 2018, the talik thickness was 5.3 m, approximately twice larger than that at the downstream side (3.2 m).
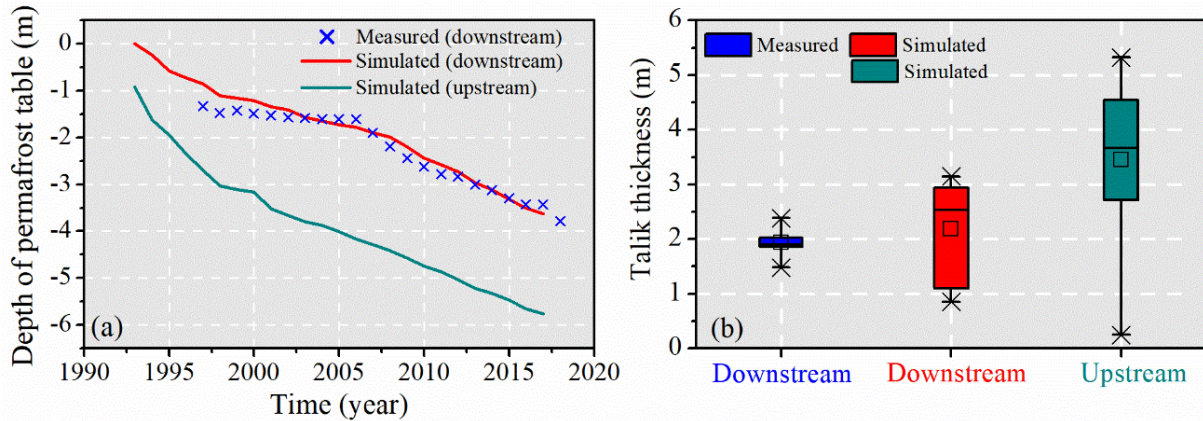
Figure 5.10. Simulated and measured (a) permafrost table depth versus time from 1993 to 2018; and (b) statistical analysis of talik thickness. The depth of the permafrost table was relative to the natural ground, mean values and standard deviations were represented with thick lines and error bars.

Figure 5.11a represents that permafrost at the depth 2.5-m experienced a step increase, rising by about 1.0 °C in the first three years, gradually warmed and completely thawed in 2005. A perennially unfrozen zone developed in 2006. Conversely, its water saturation had an exponential increase trend, reaching the maximum (1.0) in 1997, and remained constant after 2006. Similarly, there was a similar trend for permafrost at the depth of 4.0 m (Figure 5.11b) and 5.0 m (Figure 5.11c). Permafrost completely thawed in 2010 for 4.3 m, and 2016 for 6.0 depth, respectively.

Additionally, over the 1993-2018 period, mean annual soil temperature had a relatively linear ($R^2 > 0.94$) increase, at a rate of 0.19 °C·a^{-1} for 2.5 m (Figure 5.11d), 0.13 °C·a^{-1} for 4.0 m (Figure 5.11e), 0.08 °C·a^{-1} for 5.0 m (Figure 5.11f), respectively. In response to soil warming, the amount of sensible heat stored at a rectangular grid (0.2 m width × 0.25 m height) exhibited an abrupt and nonlinear increase, rising by 2 W in the thawing period (Figure 5.11d, e, and f). Once the

permafrost thawed, the amount of stored sensible energy had a relatively linear rise. The corresponding rising rates were 0.16 W·a^{-1} for the 2.5 m, 0.17 W·a^{-1} for the 4.0 m, 0.20 W·a^{-1} for the 5.0 m, respectively.
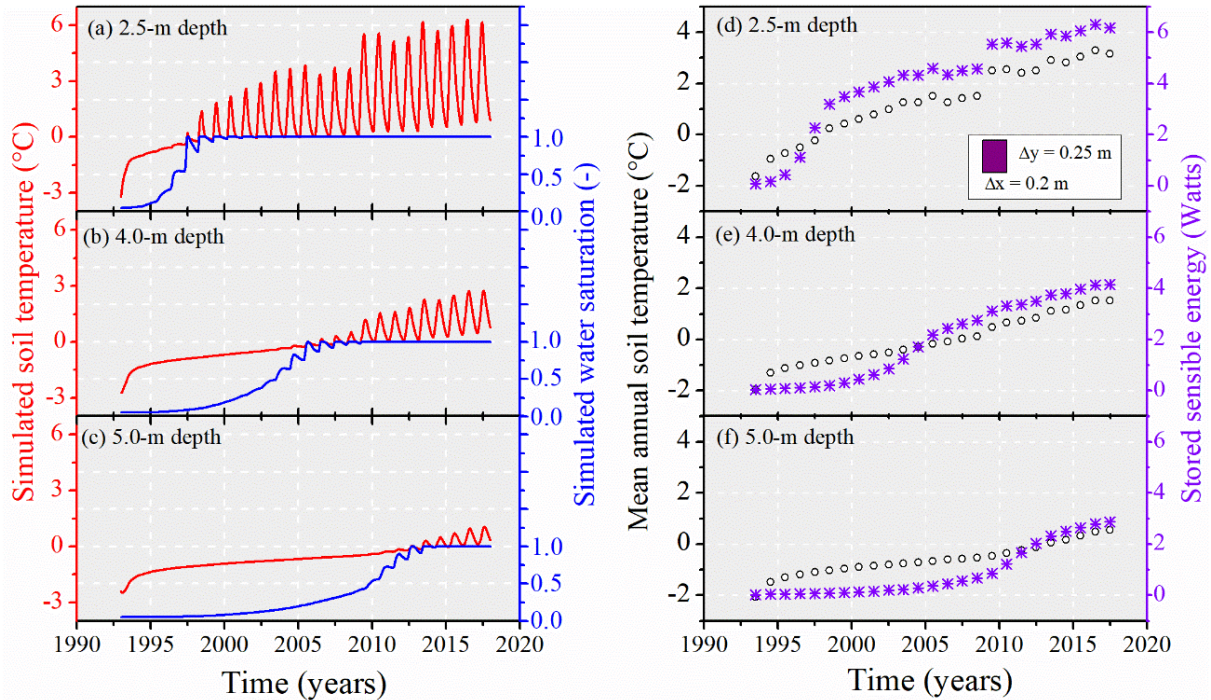
Figure 5.11. Simulated soil temperature and water saturation variations at the depth of (a) 2.5 m; (b) 4.0 m; and (c) 5.0 m, respectively, under the embankment slope at the upstream side from 1993 to 2018; and annual mean annual temperature and stored sensible energy at the depth of (d) 2.5 m; (e) 4.0 m; and (f) 5.0 m, respectively. Note: the depth is relateive to the natural ground surface; and the sizes of the rectangular grid at depth were the same with 0.2 m width and 0.25 m height, which was shown in Figure 5.11d.

5.4.2.3. Comparison between heat advection and heat conduction

Figure 5.12 presents that underlying permafrost under the road embankment of in scenario 1 was much warmer than that of scenario 2. Over the period, the permafrost warming rate in scenario 1 was 0.18 °C·a^{-1} at the depth of 1 m, about three times than that in scenario 2 (0.06 °C·a^{-1}). The mean annual soil temperature rose from -1.7 °C to 2.9 °C in scenario 1, while it remained frozen in scenario 2. The subsurface water flow roughly doubled the permafrost thawing rate (from 0.1 m·a^{-1} to 0.19 m·a^{-1}) and caused additional permafrost thaw up to 4.5 m by 2018 (Figure 5.12a), on average of 2.1 m beneath the road embankment.

Similarly, the talik zone of scenario 1 was twice larger than that of scenario 2. In general, for scenario 2, two isolated taliks were located at the upstream and downstream sides of the embankment slope, respectively. However, a connected talik was located below the embankment slope for the scenario 1. Additionally, the subsurface water flow led to higher permafrost temperature up to approximately 7 °C in October (Figure 5.12c) and about 2 °C in April (Figure 5.12d), respectively, although the corresponding value was about 1 °C lower at the top surface.
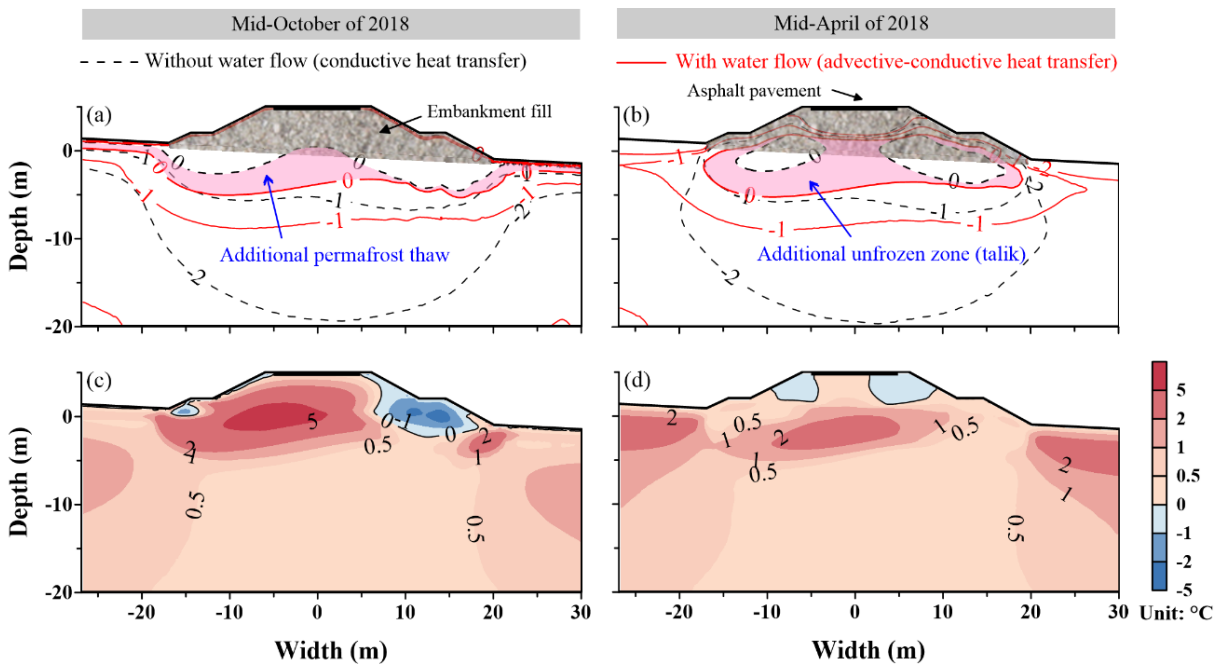
Figure 5.12. Temperature isotherms of scenario 1 (with water flow illustrated by red solid lines) and scenario 2 (without water flow showed by black dash lines) at (a) mid-October and (b) mid-April of 2018; and temperature difference (scenario 1 - scenario 2) at (c) mid-October and (d) mid-April of 2018. NOTE: mid-October was chosen to locate the permafrost table, but mid-April was characteristic of the coldest conditions of underlying permafrost.

5.5. DISCUSSION

5.5.1. Performance of integrated SUTRA-ice code and SEB model

We firstly incorporated the SEB model in SUTRA-ice code to couple the individual energy processes at the top surface and enhance the physical realism in cold regions (Figure 5.2). The combined code successfully produced the observed seasonal trends of soil temperatures with different surface cover types (i.e., undisturbed vegetated NG, snow-covered embankment slope,

and snow-free asphalt-paved surface of embankment center) (Figure 5.7). However, compared to the measured soil temperatures, simulated soil temperatures exhibited a quicker and earlier decrease trend in fall, and a slight rise in spring, respectively (Figure 5.7). The main reason is due to the lack of measurements of the inter-annual variation of snowfall date and snowmelt date. The earlier snow cover and shorter snow-covered period linearly reduce the amount of heat released to the atmosphere and warm the ground (Ishikawa 2003, Chen et al., 2021). Also, the infiltrated snowmelt water causes a step temperature rise by more than 5 °C at the ground surface (Chen et al., 2020a).

Furthermore, in comparison to the embankment center (Figure 5.7c), the combined code effectively simulated the thermal insulation effect of the snowpack, identified by the smaller amplitudes of temperature variations of the embankment slope (Figure 5.7b). Similarly, the surface offset caused by the surface albedo was clearly clarified by the difference (6.4 °C) of the summer GSTs between the embankment center and slope (Figure 5.8), due to higher albedo (0.13, Table S5.2) of asphalt-paved surface increased the amount of the solar energy absorption (Dumais and Doré 2016). Such surface offset caused by the solar absorptivity is similarly documented through the field observation (Zhang et al., 2017b, Zhang et al., 2019), the simple SEB model (Solaimanian and Kennedy 1993), and the analytical model (Krarti et al., 1995).

Furthermore, the discrepancies of simulated GSTs are mainly due to uncertainty of snow depth, followed by solar radiation and AT, and less by wind speed and rainfall (Table 5.1). The available data of the snowpack variations will improve the accuracy of the GST prediction (Kondo and Takeshi, 1990, Zhang 2005). Even if the solar radiation data is not available from the 1993-2008 period, our model is capable to estimate daily surface temperature with a reasonable accuracy (MAE < 0.4 °C, Table 5.1) by an AT-based empirical equation (Eq. 5.2). The wind speed and rainfall amount had little impact on the magnitude of the mean annual GST. Additionally, our model had considered snow depth varying and subsurface temperature feedback, which greatly improved the accuracy of GST prediction, in comparison to other approaches neglecting those processes (i.e., Lunardini 1978, Zhu 1988, Hermansson 2004, Dumais and Doré 2016). Also, the feedback of subsurface processes to the surface temperature is identified by temperature difference (about 1 °C) at the shallow ground between scenario 1 and scenario 2 (Figure 5.12). Because warmer soil

conditions at depth in scenario 1 reduce its thermal gradient with the atmosphere, and in return lower the surface temperature, which agrees with simulated results (Devoie et al., 2019).

The larger variations between the measured and simulated permafrost table and talik thickness at the downstream side (Figure 5.10) are related to uncertainties of the geometry caused by embankment subsidence, water flow direction, and temperature of recharge water. The embankment subsidence and surface movement caused by the permafrost degradation will change the embankment geometry (de Grandpré et al., 2012, Dumais & Doré 2016), but this process is not considered in the simulation. Also, the road maintenance puts the new embankment material on embankment slope, which also modify the embankment geometry. In addition, as the active layer below slopes and toes of embankment deepened over time, thawed permafrost produced ground subsidence and the road settled, unevenly, over time. As coarse embankment material (sand and gravel) with large interstitial voids subsides, it intercepts the water table, increases the permeability of the water storage media and yields more groundwater (positive feedback). The fully coupled cryohydrogeological model cannot reproduce the deformation process and mechanical characterisitcs of embankment subsidence caused by the permafrost thaw. Further, the macroscopic heterogeneity and anisotropy of embankment subgrade can also provide the preferential flow paths and control the subsurface water flow direction (Chen et al., 2020a). Moreover, although we assume that the road alignment perpendicularly intercepts the local drainage network according to the estimated from water-table elevation data (de Grandpré et al., 2012), the water flow direction may be perpendicular or sub-parallel, or parallel to the road alignment along the preferential flow paths. The preferential flow paths also redistribute the temperature of embankment subgrade and subbase.

5.5.2. Permafrost degradation and talik development

Broadly, our simulations reproduced the observed trends of talik initiation and development beneath the road embankment (Figure 5.10). Simulated results show that a combined effect of snow insulation, subsurface water flow, and climate warming contributes to a rapid permafrost degradation and talik development beneath embankment slope. We used the NG as a reference to discuss the main factors affecting these processes.

5.5.2.1. Impact of vegetation and organic layer

Even if the AT has increased by about 2.0 °C during the 1993-2018 period, the permafrost temperature remained relatively stable (Figure 5.9). The main reason relates to the thermal insulation effect of the vegetation and organic layer, which reduces heat propagation downward, buffers the impact of climate warming and restricts deepening of the active layer (Figure 5.5 and Figure 5.8). This agrees with other observation in the sub-Arctic and Arctic regions (i.e., Yi et al., 2007, Atchley et al., 2016, Fisher et al., 2016). Moreover, in summer, the heat advection by mobile water flow does not contribute significantly to permafrost degradation below the NG, which is like the simulated results in peatlands (i.e., McKenzie et al., 2007a, Kurylyk et al., 2016). The principal reason is related to the short water flow period (Figure 5.8) and the thin (~ 1.0 m) water flow path (Figure 5.9), which reduce the amount of accumulated water in the active layer. Also, the low temperature difference (Figure 5.7 and Figure 5.9) between the water flow and the underlying permafrost restricts the amount of energy absorbed by the permafrost body (Eq. 5.10).

5.5.2.2. Impact of subsurface water flow

Heat advection triggered by mobile water flow (scenario 1) provide additional heat to triple the permafrost warming rate (from 0.06 °C·a^{-1} to 0.18 °C·a^{-1}) and roughly double the thawing rate (from 0.1 m·a^{-1} to 0.19 m·a^{-1}), in comparison to the scenario 2 (without water flow) (Figure 5.11 and Figure 5.12). Mobile water flow, which is effective to transfer the heat to depth (Chen et al., 2020a), enhances the heat exchange between the underlying permafrost and overlying embankment. As a result, heat carried by mobile water flow causes the additional permafrost thaw, on average of 2.1 m beneath the embankment (Figure 5.12a) and triggers a faster warming rate of underlying permafrost. In general, the presence of mobile water flow (scenario 1) produces the most realistic thawing rate (0.2 m·a^{-1}) of permafrost observed at different test sections (350 m away) of the same study site (Chen et al., 2020a). Also, the similarity between the simulated and observed warming trends at depth (Figure 5.6 and Figure 5.11) supports the effect of water flow. Similarly, with the effect of water flow, the simulated rising rates of active layer thickness and permafrost temperature is consistent with the observations (Fortier et al., 2007, Sjöberg et al., 2016, You et al., 2017) and other simulated results of the conceptual hillslopes (Ge et al., 2011, McKenzie and Voss 2013, Jafarov et al., 2018, Dagenais et al., 2020).

Also, the simulated results in scenario 2 agrees with the observed warming rate (Wu et al., 2007), where the experimental road is mainly affected by atmospheric warming and no flow occurs.

Subsequently, as subsurface water flows beneath the embankment, the energy absorbed by the underlying permafrost increases (Figure 5.11). This process provides an additional energy source to expedite permafrost thaw, enlarges the water flow path and yields more water flow. A positive feedback linked with more water flow is created to increase the ground warming (Figure 5.11d, e, and f). Furthermore, the thicker active layer beneath embankment slope enables a large amount of the subsurface water to get trapped (Figure 5.9c). Due to the latent heat effect, trapped free and unfrozen water (Figure 5.9c) acts as a positive feedback mechanism to retard freeze back of the active layer, increases the net energy gain to the underlying permafrost body (Figure 5.11d, e, and f), and contributes to general high permafrost temperature (Figure 5.9b). Over time, the presence of water flow triggers talik initiation and development and connects the isolated talik at the upstream and downstream sides (Figure 5.12). The connections of talik layers develops new groundwater flow paths, which enlarges with time (along with permafrost degradation) (Figure 5.9). The thawing consolidation triggered by talik development may cause the pavement damages and shoulder collapse, which is consistent with drill survey along Alaska Highway (Stephani 2013) and thermal monitoring along Qinghai-Tibet Highway (Sun et al., 2018a).

Moreover, when the active layer is hydraulically active, heat advection triggered by water flow produces warming rates at depth (Figure 5.9 and Figure 5.11), but the extent of advected heat is a function of flow rate, porosity of soil media, and temperature difference between the water flow and the surrounding soils (Eq. 5.10). High inflow temperature and large hydraulic gradient enhance the thawing rate of permafrost (Devoie et al., 2019). The amount of advective heat flux shows an increasing trend in summer months when the temperature difference of the water flow and the permafrost is maximal (Kurylyk et al., 2016). Conversely, low permeability of overlying unfrozen soil limits the thermal impact of the water flow (McKenzie et al., 2007a, Ghias et al., 2017). Although the water tracks enhance water flow above permafrost, the low temperature of water flow restricts the extent of active layer deepening in high Arctic hillslope (Paquette et al., 2015, Evans et al., 2020).

Furthermore, the asymmetry temperature distribution beneath embankment subbase and subgrade (Figure 5.12) is mainly associated with the thermal impact of water flow. Mobile water firstly reaches and accumulates the upstream side, due to the thick active layer created by snow insulation (Figure 5.8 and Figure 5.11). Meanwhile, the uplifted permafrost table (1 m above the NG surface, Figure 5.11a) at the embankment centerline acts as a frozen wall and impedes the water flow. Over time, the permafrost degrades, and the thick active layer hydraulically allows water flow beneath the embankment after 2008 (Figure 5.9a). After that, the talik is observed at the downstream side (Figure 5.9b). The behavior of water accumulation at the upstream slope is similarly documented (e.g., de Grandpré et al., 2012, Mu et al., 2020b). Similar negative effect of water ponding to permafrost are observed in Qinghai-Tibet Railway (Mu et al., 2018, Mu et al., 2020b) and oil pipeline in Northeastern China (Wang et al., 2016b, Chai et al., 2019). The impact of heat advection on the permafrost thermal state is limited downstream of the embankment as most of the water trapped in the road embankment subbase has been discharged to the surface at the downstream embankment slope. These results highlight the importance of adequate drainage systems below road embankments to preserve permafrost.

5.5.2.3. Impact of snow insulation

In winter, snow insulation impedes the heat loss due to its low thermal conductivity. As a result, the ground covered with snowpack is more than 10 °C warmer, in comparison to the snow-free surface of the embankment centerline (Figure 5.8). More heat accumulates beneath embankment, while the heat loss in winter is not enough to freeze back the active layer to permafrost table and further cool the permafrost. Followed by these impacts, talik initiates and grows beneath the road embankment. Similarly, thermal insulation created by thick snowpack has been recognized elsewhere as an important factor for talik formation through the observation in the sub-Arctic roads (Fortier et al., 2011, O'Neill and Burn 2017) and through the modelling approach (i.e., Jafarov et al., 2018, Devoie et al., 2019), although the feedback of talik formation to permafrost degradation was not quantified in their study. Chen et al., (2021) present that the ground heat flux released at embankment slope exponentially decreases with the increase of snow depth and was linearly reduced with earlier snow cover and longer snow-covered period.

5.5.2.4. Impact of climate warming

The simulated GST showed a rapid response to the increasing AT due to climate change (Figure 5.8). The increasing rate (about 0.088 °C·a^{-1}) of top surface temperature is mainly related to the AT warming rate (0.072 °C·a^{-1}), as the total solar radiation remains constant over the 25-year period (SD = ± 86.9 W·m^{-2}) (Figure 5.4). Due to the absence of snow cover, the GST of embankment center exhibited stronger seasonal and inter-annual variability than the GSTs of the embankment slope and the NG (Figure 5.8). This increasing trend is similar to other simulated results produced by the SEB model (i.e., Kurylyk et al., 2016) and the long-term observation in Qinghai-Tibet Plateau (Wu et al., 2007), although the AT increasing rate was smaller (0.7 °C from 1960s to 1990s) in their study site.

Increasing AT has a certain contribution to permafrost warming and thawing. Higher AT results in the rise of GST by about 2 °C (Figure 5.8a) and simultaneously increase the embankment temperature by an average of 3.6 °C (from 2.3 °C to 5.9 °C) in mid-October, which finally result in the rise of sensible heat storage and high thermal gradient between the ground and overlying embankment. As a result, more heat propagates downwards the underlying permafrost, leads to permafrost thaw and even creates the formation of talik. Similar behavior is reported by other modelling approaches (Zhang et al., 2008a). Moreover, the increase of AT rises the thawing period of the top surface (Figure 5.8b). A longer thawing period allows more water to flow below the embankment and increases the energy absorbed by underlying permafrost (Lamontagne-Hallé et al., 2018). Also, earlier thawing period will enable more snowmelt water to reach the frozen front and may warm the ground due to the latent heat release (Hinkel et al., 2001, Kane et al., 2001), although the thermal impact of infiltrated surface water is limited by the small amount and short contact period (Chen et al., 2020a).

5.5.2.5. Impact of road construction

The simulated results demonstrate that the response of permafrost temperature to road construction is a quick and intense process, indicated by a fast-warming rate (0.7 °C·a^{-1}) in the first 3 years (Figure 5.11) and a step temperature rise (Figure 5.5c). After road construction, the low-albedo bare surface of the embankment enhances the atmospheric heat absorption, resulting in the increase of the GST by about 6.0 °C in summer (Figure 5.8). Also, the dry

embankment material favors heat propagation downward to the underlying permafrost (Chen et al., 2021). Even if the thick embankment material delays the heat propagation and uplifts the permafrost table (Sheng et al., 2002, Wu et al., 2015), asphalt pavement promotes the heat accumulation (Figure 5.3) and causes the permafrost thawing and warming (Figure 5.7). Alternatively, a relatively slow rate of the talik thickness is observed due to the latent heat effect (Figure 5.5). When the soil temperature reaches the thawing point, more heat is required to melt the pore-ice, which greatly delays the expansion of talik area. Over time, talik thickness is expected to double, once the soil in the zone of -0.2 °C isotherm thaws, and triple once the soil in the zone of -0.4 °C isotherm thaws (Figure 5.5b).

Beneath the embankment center (Figure 5.5c and Figure 5.9a), the impact of heat advection to permafrost thawing is limited by the thin water paths. The uplifted permafrost table due to the thick embankment material reduces the thickness of water flow path (less than 1.0 m, Figure 5.9a), which decreases the amount of liquid water trapped in the subsurface and further facilitates the freeze back of the active layer (Figure 5.9b). In summer, the warm road embankment, with an average temperature of 12.4 °C (Figure 5.12), serves as a heat source and loses heat to the flowing water. Also, the elevation difference of the permafrost table between the embankment center (shallower) and the slope (deeper) produces a hydraulic gradient and favors the water flow trapped at the embankment slope, instead of embankment center, identified by the unfrozen water saturation (Figure 5.9c).

5.5.3. Limitations and further study

The modelling approach in this study employed several simplifying assumptions. Firstly, snow depth is an independent variable in the SEB model. When the integrated model is used to estimate the cryohydrogeological processes in a changing climate, the coupled thermal and hydrological processes at the top surface will improve the simulation performance. The main reason is that the hydrological processes at the top surface, such as the amount of snowmelt water and duration of snow cover, are related to the energy balance at the top surface (Quinton et al., 2005, Chen et al., 2020a). While, in return, they alter the amount of the heat downward to the ground (Chen et al., 2021). Secondly, deformation caused by permafrost degradation is

neglected. The thawing ice-rich permafrost leads the coarse, permeable embankment material to intercept the water table. Though not simulated here, it is anticipated that embankment material subsidence into the water table provides a preferential flow path and results in an enhanced permafrost thawing rate, as more water flows beneath the road embankment (Chen et al., 2020a). Thirdly, the water flow direction is assumed to be perpendicular to road alignment and its impact is quantified by a two- dimensional model, which is a reasonable assumption based on the measured hydraulic gradient (Figure 5.1b) (de Grandpré et al., 2012).

For the Alaska Highway or other north road embankments, the road alignment may be perpendicular or sub-parallel or parallel to the local hydraulic gradient. The water movement results in a three-dimensional heat transfer processes of embankment subbase and subgrade. Meanwhile, the lateral heat transfer between the talik and the permafrost may accelerate permafrost degradation (Kurylyk et al., 2016). Furthermore, although our simulations are based on specific conditions at the Beaver Creek of Alaska Highway, the novel coupled model is applicable to evaluate the thermal stability of pan-Arctic infrastructure and quantify how ground surface temperatures affect groundwater discharge from hillslopes in cold regions. The employed AT-based empirical equation will reduce the required inputs of meteorological data, when solar radiation is not available.

5.6. CONCLUSIONS

This study has investigated and quantified the effects of heat advection caused by mobile water flow, snow insulation, and atmospheric warming on the permafrost degradation and talik development in a permafrost region. To our knowledge, this is the first study to integrate the SEB model into the coupled cryohydrogeological model and to quantify the heat advection on the thermal stability of road embankment, supported by long-term (1993-2018 on Alaska Highway) field observations. This novel approach of TBCs enables us to consider the inter-annual variations of meteorological data and subsurface processes. Thermal processes beneath three surface cover types were simulated, including undisturbed vegetated NG, snow-covered embankment slope, and snow-free asphalt-paved surface of embankment center.

In summer, the warm road embankment, with an average temperature of 12.4 °C, serves as a heat source and loses heat to the flowing water. Mobile water flow triggers the heat advection and provides an additional energy source to expedite permafrost thaw, which triples its warming rate and roughly doubles thawing rate. Also, the mobile water flow produces the asymmetry temperature distribution, which induces the uneven permafrost thaw and adversely affects the thermal stability of road embankment.

Talik initiated and developed versus time under a combined effect of the mobile water flow, snow cover, road construction, and climate warming. Talik formation creates a new thermal state of road embankment, resulting in acceleration of underlying permafrost. The trapped free and unfrozen water acts as a positive feedback mechanism to retard freeze back of the active layer, increases the net energy gain to the underlying permafrost body, and contributes to general high permafrost temperature.

In a warming climate condition, subsurface water flow will play a more important role in permafrost thaw and talik development, due to the more water flow produced by talik formation. The talik presence will adversely affect the structural integrity of transportation infrastructure and threaten the northern community and northern infrastructure in permafrost regions, such Alaska Highway corridor, and Qinghai-Tibet engineering corridor.

5.7. ACKNOWLEDGEMENTS

5.8. SUPPORTING MATERIALS

Figure S5.1. Linear relationship of air temperature (AT) between the BC-RES and BC-airport over the 2009-2014 period; (a) daily maximum AT; (b) daily mean AT; and (c) daily minimum AT.
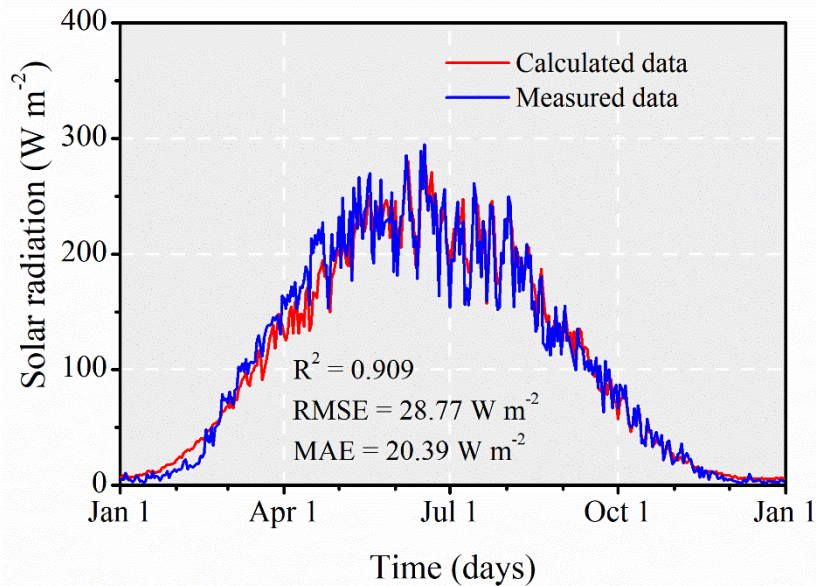
Figure S5.2. Measured and calculated mean daily solar radiation over the 2013-2018 period. Statistic values, including the root mean square error (RMSE) and mean absolute error (MAE), were presented.
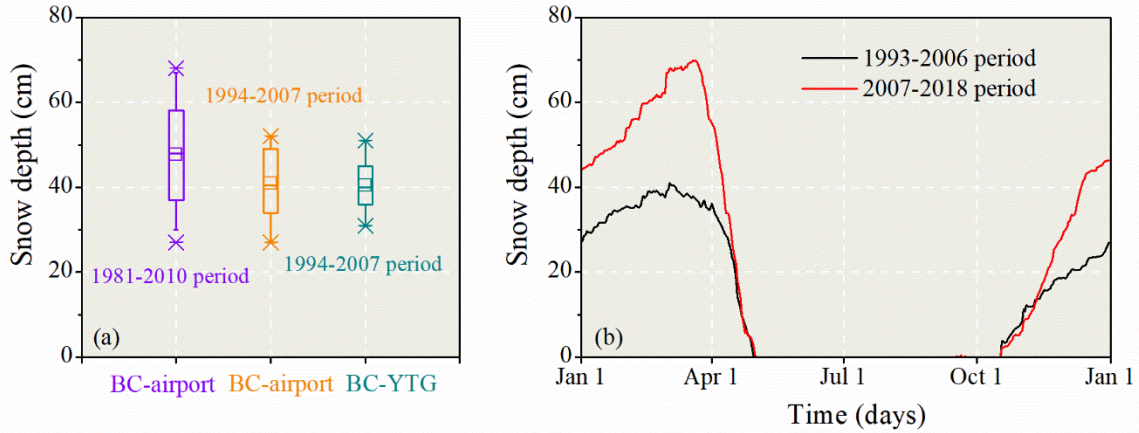
Figure S5.3. (a) Measured maximum snow depth at the BC-airport over the 1981-2010 period and at the BC-YTG over the 1994-2007 period; (b) snow regime over the three periods, including 1995-2004, 2005-2014, and 1995-2014 periods. The meteorological station at the BC-YGT (62°22' N, 140°52' W, 663.0 m above sea level,) was 4 km away from the BC-airport, which provided the available data from 1994-2007.
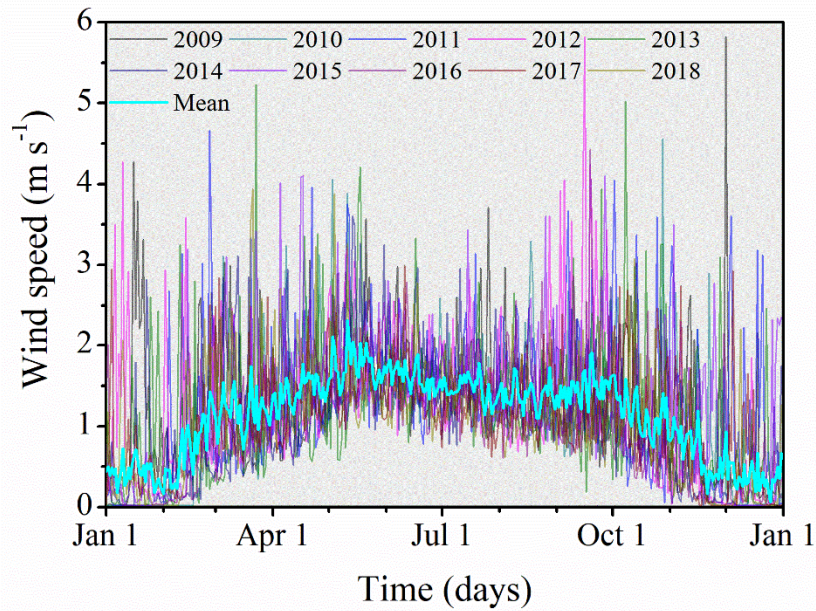
Figure S5.4. Daily wind speed variations over the 10-year period (2009-2018). The bold blue line represents the mean value of the 10-year record.
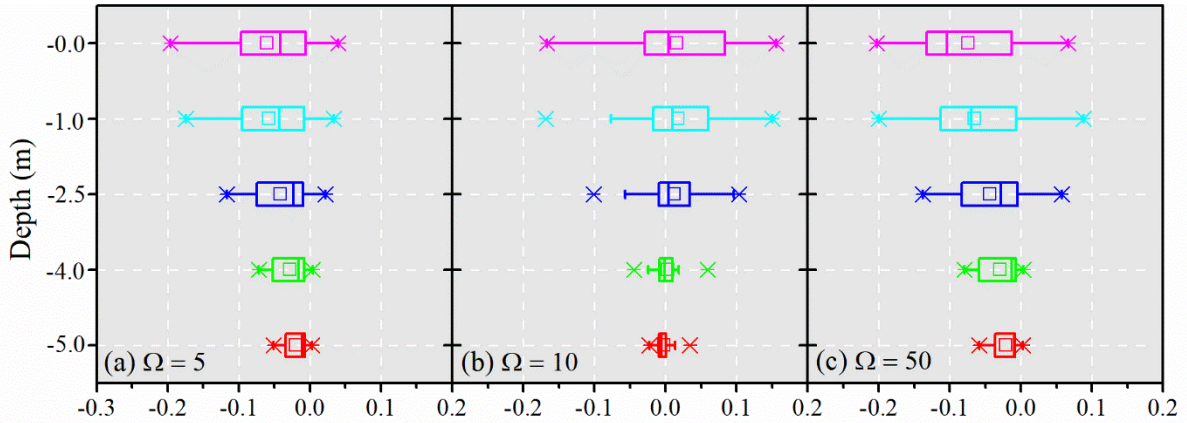
156

Figure S5.5. Sensitivity analysis of mean annual soil temperature at depth to permeability factors over the 1993-2018 period, (a) Ω = 5; (b) Ω = 10; (c) Ω = 50. The deviation was calculated by the soil temperature difference between the linear approach (PLINE) and impedance-factor (IMPE) approaches of relative permeability.

157

Table S5.1. Statistical analysis of measured and calculated solar radiation by three multiple linear regression models over the 2013-2018 period. Note: ΔT represents the diurnal temperature range; the Ra and Rs illustrate the extra-terrestrial radiation, and solar radiation, respectively; the coefficients of a, b, c, and d were calculated by the "fitlm" function in MATLAB.

	2013	2014	2015	2016	2017	2018	Mean
Linear regression model I: Rs = Ra (a$\Delta T^{0.5}$ + b)							
R^2	0.907	0.909	0.916	0.919	0.902	0.888	0.907
RMSE	30.41	28.09	28.11	26.01	30.13	31.30	29.008
MSE	924.63	788.87	790.41	676.41	907.92	979.51	844.62
MAE	20.68	20.40	18.92	19.26	21.68	23.05	20.67
SD	30.37	28.05	28.08	25.97	30.09	31.25	28.968
Multiple linear regression model II: R_s = R_a (a$\Delta T^{0.5}$ + bΔT + c)							
R^2	0.908	0.909	0.916	0.923	0.902	0.889	0.908
RMSE	30.36	28.12	28.12	25.41	30.06	31.15	28.87
MSE	921.94	790.99	790.47	645.66	903.49	970.46	837.17
MAE	20.42	20.40	18.88	18.57	21.70	22.77	20.46
SD	30.28	28.05	28.04	25.34	29.98	31.07	28.79
Multiple linear regression model III: R_s = R_a (a$\Delta T^{0.5}$ + b$\Delta T^{0.25}$ + cΔT + d)							
R^2	0.909	0.909	0.918	0.923	0.904	0.889	0.909
RMSE	30.26	28.12	27.74	25.41	29.89	31.19	28.77
MSE	915.41	790.55	769.68	645.49	893.28	972.54	831.16
MAE	20.38	20.34	18.83	18.52	21.51	22.77	20.39
SD	30.13	28.00	27.63	25.30	29.76	31.06	28.65

Table S5.2. Statistical values between measured and simulated soil temperatures at multiple depths over the 4-year period from May 1st, 2014 - April 30th, 2018.

Natural ground (seasonal snowpack covered surface)

Soil depth (m)	0.3	0.7	1.1	1.5
R^2	0.932	0.960	0.980	0.988
RMSE (°C)	1.36	0.69	0.38	0.26
MBE (°C)	-0.11	0.15	0.05	0.16
MAE (°C)	1.04	0.63	0.40	0.36
SD (°C)	1.36	0.84	0.53	0.37

Embankment slope (seasonal snowpack covered surface)

Soil depth (m)	0.1	1.0	1.3
R^2	0.930	0.975	0.992
RMSE (°C)	2.28	0.87	0.47
MBE (°C)	0.37	0.24	0.08
MAE (°C)	1.84	1.82	0.83
SD (°C)	2.28	2.16	1.00

Embankment center (snow-free surface)

Soil depth (m)	0.3	0.9	1.2	1.5
R^2	0.968	0.990	0.993	0.997
RMSE (°C)	2.39	0.99	0.74	0.47
MBE (°C)	0.67	-0.16	-0.06	0.22
MAE (°C)	2.38	1.68	1.19	0.68
SD (°C)	2.91	2.01	1.39	0.79

Table S5.3. Values/descriptions for the modelling parameter in the surface energy balance (SEB) model.

Model parameters	Value/Description	References
Albedo of asphalt	0.13	Site conditions, Dumais and Doré (2016)
Albedo of gravel/sand	0.30	Chen et al., (2021)
Albedo of vegetation	0.40	Hwang (1976)
Albedo of snow	0.90	Hwang (1976)
Surface emissivity of asphalt	0.94	Herb et al., (2008)
Surface emissivity of gravel/sand	0.91	Hwang (1976)
Surface emissivity of natural ground	0.90	Hwang (1976)
Surface emissivity of snow	0.95	Walter et al., (2005)

Table S5.4. Values/descriptions for the modelling parameter in SUTRA-ice model.

Model parameters	Value/Description	References
Hydraulic properties		
Saturated permeability of embankment fill	4.05×10^{-12} m^2	Site conditions, de Grandpré et al., (2012)
Saturated permeability of peat	9.03×10^{-13} m^2	Site conditions, de Grandpré et al., (2012)
Saturated permeability of sandy silt	1.03×10^{-13} m^2	Site conditions, de Grandpré et al., (2012)
Porosity of embankment fill	0.4	Site conditions, de Grandpré et al., (2012)
Porosity of peat	0.75	Site conditions, de Grandpré et al., (2012)
Porosity of sandy silt	0.4	Site conditions, de Grandpré et al., (2012)
Thermal properties		
Embankment fill grain thermal conductivity, λ_s	2.3 W·m^{-1}·°C^{-1}	Site conditions, Zottola et al., (2012)
Peat grain thermal conductivity, λ_s	0.45 W·m^{-1}·°C^{-1}	Site conditions, Zottola et al., (2012)
Sandy silt grain thermal conductivity, λ_s	2.0 W·m^{-1}·°C^{-1}	Site conditions, Zottola et al., (2012)
Water thermal conductivity, λ_w	0.6 W·m^{-1}·°C^{-1}	Williams and Smith (1989)
Ice thermal conductivity, λ_i	2.14 W·m^{-1}·°C^{-1}	Williams and Smith (1989)
Embankment fill grain heat capacity, $\rho_s C_s$	1.76×10^6 J·m^{-3}·°C^{-1}	Site conditions, Zottola et al., (2012)
Peat grain heat capacity, $\rho_s C_s$	4.39×10^6 J·m^{-3}·°C^{-1}	Site conditions, Zottola et al., (2012)
Sandy silt grain heat capacity, $\rho_s C_s$	2.06×10^6 J·m^{-3}·°C^{-1}	Site conditions, Zottola et al., (2012)
Water heat capacity, $\rho_w C_w$	4.18×10^6 J·m^{-3}·°C^{-1}	Williams and Smith (1989)
Ice heat capacity, $\rho_i C_i$	1.94×10^6 J·m^{-3}·°C^{-1}	Williams and Smith (1989)

Freezing functions		
Soil freezing curve	Exponential function	Lunardini (1988)
Residual liquid saturation for embankment fill	0.05	Site conditions, Zottola et al., (2012)
Residual liquid saturation for peat	0.08	Site conditions, Zottola et al., (2012)
Residual liquid saturation for sandy silt	0.08	Site conditions, Zottola et al., (2012)
Fitting parameter, *w for* embankment fill	0.25	Site conditions, Zottola et al., (2012)
Fitting parameter, *w for* peat	0.50	Site conditions, Zottola et al., (2012)
Fitting parameter, *w for* sandy silt	0.75	Site conditions, Zottola et al., (2012)
Soil relative permeability functions		
Relative permeability functions	IMPE	Jame and Norum (1980)
Impedance factor	10	Three additional scenarios were compared. (Figure S5.5)
Unsaturated parameter		
Entry capillary pressure of gravel/sand	1000 kg·m^{-1}·s^{-2}	Voss and Provost (2010)
Entry capillary pressure of peat	3000 kg·m^{-1}·s^{-2}	
Entry capillary pressure of sandy silt	5000 kg·m^{-1}·s^{-2}	
SUTRA discretization and solver settings		
Finite element mesh types	Quadrilateral element	Nodes are numbered counterclockwise
Mesh size at y direction	0.1 m to 3.3 m	Element height increases linearly with depth
Mesh size at x direction	0.2 m to 2.5 m	Element height increases linearly with distance away from the road embankment
Number of nodes	31842	4 node quadrilateral element
Number of elements	31326	4 node quadrilateral element

Time step size of stage 3	8 hours	less than 0.05 °C, compared to smaller time step size of 6 hours
Pressure solution solver	Iterative	ILU-preconditioned generalized minimum residual
Temperature solution solver	Iterative	ILU-preconditioned generalized minimum residual

Chapter 6 - CONCLUSIONS AND FUTURE WORK

6.1. CONCLUSIONS

The overall goal of this thesis is to elucidate the thermal interactions between the atmosphere, road embankment, mobile water flow, and permafrost within the context of climate change. The statistical analysis of long-term observation methodically investigates impacts of infiltration and subsurface water flow on the thermal regime of a road embankment subbase and subgrade. Moreover, understanding the pavement-atmosphere thermal processes is imperative to predict ground surface temperatures and surface energy components, particularly for snowy permafrost regions. Additionally, the quantification of the heat advected by subsurface water flow and the sensible energy stored by trapped unfrozen water provides crucial information for accelerated permafrost thaw, talik development as well as vulnerability assessment. The major findings of the three parts are summarized below.

First, I examined the anomalous temperature gradients associated with water flow, including the top-down infiltration of surface water (i.e., spring snowmelt water and summer rainfall infiltration), and lateral subsurface water flow. The results indicated that spring snowmelt water infiltration caused step temperature increases of 5.0 °C on average within a few days, down to 3 m depth. Infiltrated summer rainfall water lowered near-surface temperatures by 5.2 °C on average while warmed embankment fill materials by 1.3 °C on average, down to 3.6 m depth. In addition, temperature increase due to advective heat fluxes triggered by subsurface water flow can be up to two orders of magnitude faster than due to atmospheric warming only. The pore water flow accelerated permafrost degradation and negatively affected the structural integrity of the infrastructure.

Second, I systematically compared three different approaches to obtain ground surface temperatures, including surface energy balance model, n-factor method, and adherent-layer theory method. In comparison to other two methods, the novel surface energy balance model presented in this study showed better performance in predicting the ground surface temperatures and the thawing periods for different surface cover types and different climate

conditions, due to the consideration of land surface processes and subsurface thermal processes. The calibrated surface energy balance model indicated that the quantity of heat entering the embankment center and slope is mainly controlled by net radiation, and less by the sensible heat flux. The insulation created by the snow cover on the embankment slope reduces heat loss by three times compared with the embankment center where the snow is plowed. Furthermore, the ground heat flux released at embankment slope exponentially decreased with the increase of snow depth and was linearly reduced with earlier snow cover and longer snow-covered period. Lateral ground heat flux from the embankment center to the slopes leads to the earlier disappearance of the seasonal snow cover on the embankment slope. Furthermore, the novel surface energy balance model emphasized the importance of surface thermal processes on surface energy components of a road embankment. The outputs of the surface energy balance model, either specified ground surface temperatures or ground heat flux variations, can be fully integrated into a geothermal simulator or a cryohydrologeolocal numerical model to easily quantify the impacts of various surface disturbances on the thermal state of the underlying permafrost.

Third, I integrated a surface energy balance model and cryohydrologeolocal numerical model to better understand the surface and subsurface thermal processes of a sub-Arctic road embankment, supported by the long-term (1997-2018) thermal observation on Alaska Highway, Yukon, Canada. This coupled model had a good performance (R^2 > 0.93) to simulate the soil temperatures (MAE < 2.5 °C) and successfully reproduce the increasing trend of permafrost table depth (MAE < 0.2 m) and talik development, driven by the reconstructed meteorological data. The results show that the simulated ground surface temperatures were most sensitive to the snowpack variation, followed by solar radiation and air temperature, less by wind speed and rainfall. The simulated results demonstrate that talik initially formed and developed over time under the combined effect of the water flow, snow insulation, road construction and climate warming. The subsurface water flow promoted the development of new groundwater flow paths by connecting two isolated talik (located in the upstream and downstream sides, respectively), which enlarged with time. Talik formation created a new thermal state of road embankment, resulting in acceleration of the degradation of the underlying permafrost, due to the thermal

feedback of trapped unfrozen water. Furthermore, the application of the newly integrated surface energy balance model and cryohydrogeolocial model helps assessing the importance of conductive and convective heat transfers processes in terms of boundary conditions, rates and magnitudes at annual to decennial timescales.

The research presented in my thesis contributes to the small but growing body of literature on impacts of subsurface water flow in permafrost degradation, talik initiation and development, and thermal stability of cold-region infrastructure. Using thermal monitoring from a unique experimental section of the Alaska Highway, Yukon, Canada, I developed, calibrated, and validated a newly integrated model, which fully coupled the surface and subsurface thermal processes. This newly integrated model addresses the critical importance of surface thermal processes on the cryohydrologeolocal system and of the thermal feedback of subsurface thermal processes (i.e., talik initiation and development and trapped unfrozen water) on the thermal stability of overlying infrastructure. In addition, this study for the first time provided the evidence in support of heat advection water movement in a cold-region embankment and quantified the dominant heat exchange processes at the surface of a road embankment in a snowy permafrost region.

My research has immediate application for improving the engineered mitigation measures to accommodate subsurface water flow along the Alaska Highway. The results from my research are of interest beyond just Northern transportation infrastructure and are applicable in undisturbed grounds in high-altitude permafrost regions (e.g., polar desert and coastal plain in Arctic regions), and in high-elevation permafrost regions (e.g., alpine meadow and desertification in the QTP, China). Furthermore, the net results of my finding will be particularly important in the investigation of land-atmosphere thermal processes (e.g., heat exchange at the air-water interface), the assessment of thermal stability of transport infrastructure, as well as the quantification of subsurface cryohydrogeological processes (e.g., groundwater discharge dynamics).

6.2. FUTURE WORK

Studies have shown that the land-surface hydrologic processes are of vital importance to heat exchange between the atmosphere and the ground. In return, the lateral ground heat flux induced by uneven snow accumulation can cause earlier snowmelt. However, in this study, snow depth and surface water recharge were treated as independent variables of the meteorological inputs, while the discharge was linearly related to pressure at the boundary-condition node. Therefore, it is necessary to fully couple surface and subsurface thermal and hydrologic processes to address the importance of the hydrothermal interaction in the land-atmosphere-permafrost system. The knowledge can be applied to pan-Arctic hydrology to investigate the hillslope-stream connectivity in a permafrost watershed or to estimate the hydrothermal processes of glacier or snow melt. Additionally, the physical model should be performed in an environment simulator to study and quantify the sensitivity of thaw propagation to hydrothermal properties of subsoil (e.g., porosity, density) and boundary conditions (e.g., inputs of water temperature and pressure) for the scenarios with and without subsurface water flow.

This study investigated and quantified the influence of heat advection on the thermal stability of road embankment, without considering the thaw-induced embankment subsidence. The results have addressed the role of heat advection in accelerating the rate of permafrost thaw. While, many studies have reported that the thaw of ice-rich permafrost adversely affects the structural stability of road embankments. Recently, the thaw-induced embankment subsidence was calculated by either partially coupled thermal-mechanical model, or empirical relation between the road subsidence and the ice volume. The calculated frost heave and thaw settlement are primarily affected by an energy gain or energy loss from the ground surface, without considering uneven settlement induced by either subsurface water flow, or surface water infiltration. However, the impact of mobile water flow on the embankment subsidence have not been studied methodically. Therefore, it is imperative to develop a fully-coupled thermal-hydraulic-mechanical model to understand the vulnerability of cold-regions transportation infrastructure to permafrost thaw affected by mobile water flow. This coupled model can be implemented to predict where, when, and how road embankment failure may occur, and is applicable to evaluate

structural stability of oil pipelines and foundations, buried in the permafrost areas where the subsurface water flow is significant.

Previous studies, using numerical modelling and field observations, have demonstrated that heat advection by subsurface flow affects thermal responses along preferential water flow path by providing additional permafrost thaw and extending the duration of active layer thaw relative to the adjacent place where no water flows. Additionally, the road alignment may be perpendicular or sub-parallel or parallel to the local hydraulic gradient. These results highlight the need for coupled three-dimensional model evaluations to understand the effects of subsurface water flow and heat transport in embankment subbase and subgrade. However, in this study, the water flow direction is perpendicular to road alignment and its thermal impacts were quantified by a two-dimensional model. Therefore, it is imperative to quantify how subsurface water flow affects thermal regime of a road embankment with preferential water flow in permafrost regions by employing a three-dimensional cryohydrogeological model. The proposed investigation will be of special interest to engineers to improve the design of transportation infrastructure and the road maintenance in cold regions. Also, It is applicable to investigate the impact of the preferential water track on development of active layer thickness in the high Arctic regions or the mountain permafrost regions.

There has been much recent focus on the evaluation of the impact of climate warming on the cooling effect of mitigation techniques, aimed to increase heat extraction and reduce subsurface heat penetration. But no studies have methodically examined the adaptability of engineered mitigation measures in snowy permafrost regions where there is significant subsurface water flow in summer. There are still outstanding questions, such as: Is the air convection embankment suitable to ensure the thermal stability of road embankment affected seasonal snow cover? Alternatively, the integrated models have shown that the mobile water flow severely threatens the structural integrity of the infrastructure in the short term. Therefore, there is a necessity to develop engineered mitigation techniques to accommodate subsurface water flow and control thaw settlement of embankment. The results will also help to better understand the development of longitudinal settlement and to improve the design of mitigation techniques and drainage systems in cold regions.

REFERENCES

Aalto, J., Karjalainen, O., Hjort, J., Luoto, M. 2018. Statistical forecasting of current and future circum-Arctic ground temperatures and active layer thickness. *Geophysical Research Letters.* 45(10), 4889-4898. DOI: 10.1029/2018GL078007.

Allen, R.G., Pereira, L.S., Raes, D., Smith, M. 1998. Crop evapotranspiration: Guidelines for computing crop water requirements *In United Nations FAO, Irrigation and Drainage Paper 56, edited by J. Plummer. Rome, Italy: FAO, 300 pp.*

Alvarez-Benedi, J., Munoz-Carpena, R. 2004. Soil-water-solute process characterization: an integrated approach, CRC Press.

Anderson, E.A. 1976. A point energy and mass balance model of a snow cover*, U.S. Department of Commerce, National Oceanic and Atmospheric Administration, National Weather Service, Office of Hydrology, pp150.*

Anderson, M.P. 2005. Heat as a ground water tracer. *Ground water.* 43(6), 951-968. DOI: 10.1111/j.1745-6584.2005.00052.x.

Anisimov, O., Reneva, S. 2006. Permafrost and changing climate: the Russian perspective. *A Journal of the Human Environment.* 35(4), 169-176. DOI: 10.1579/0044-7447(2006)35[169:PACCTR]2.0.CO;2.

Anisimov, O.A., Nelson, F.E. 1996. Permafrost distribution in the Northern Hemisphere under scenarios of climatic change. *Global and Planetary Change.* 14(1), 59-72. DOI: 10.1016/0921-8181(96)00002-1.

Arenson, L.U., Sego, D.C., Newman, G. 2006. The use of a convective heat flow model in road designs for Northern regions. *2006 IEEE EIC Climate Change Conference.* 1-8. DOI: 10.1109/EICCCC.2006.277276.

Atchley, A.L., Coon, E.T., Painter, S.L., Harp, D.R., Wilson, C.J. 2016. Influences and interactions of inundation, peat, and snow on active layer thickness. *Geophysical Research Letters.* 43, 5116–5123. DOI: 10.1002/2016GL068550.

Ayers, P. 1987. Moisture and density effects on soil shear strength parameters for coarse grained soils. *Transactions of the Asae.* 30(5), 1282-1287. DOI: 10.13031/2013.30559.

Bai, Q., Li, X., Tian, Y. 2015. A method used to determine the upper thermal boundary of subgrade based on boundary layer theory. *Sciences in Cold and Arid Regions.* 7(4), 384-391. DOI: 10.3724/SP.J.1226.2015.00384.

Baranov, I.Y., Tsytovich, N. 1959. Geographical distribution of seasonally frozen ground. *Principles of geocryology.* 1, 193-219. DOI: 10.4224/20359041.

Beaulac, I., Doré, G. 2006. Permafrost Degradation and Adaptations of Airfields and Access Roads-Nunavik, Quebec, Canada. *2006 Annual conference and exhibition of the transportation association of Canada: Low-volume Roads – Beyond the Boundaries.*

Beltrami, H. 1996. Active layer distortion of annual air/soil thermal orbits. *Permafrost and Periglacial Processes.* 7(2), 101-110. DOI: 10.1002/(SICI)1099-1530(199604)7:2<101::AID-PPP217>3.0.CO;2-C.

Beltrami, H. 2001. On the relationship between ground temperature histories and meteorological records: a report on the Pomquet station. *Global and Planetary change.* 29(3), 327-348. DOI: 10.1016/S0921-8181(01)00098-4.

Beniston, M., Farinotti, D., Stoffel, M., Andreassen, L.M., Coppola, E., Eckert, N., . . . Huss, M. 2018. The European mountain cryosphere: a review of its current state, trends, and future challenges. *The Cryosphere.* 12(2), 759-794. DOI: 10.5194/tc-12-759-2018.

Bense, V., Beltrami, H. 2007. Impact of horizontal groundwater flow and localized deforestation on the development of shallow temperature anomalies. *Journal of Geophysical Research: Earth Surface.* 112(F4). DOI: 10.1029/2006JF000703.

Bense, V., Ferguson, G., Kooi, H. 2009. Evolution of shallow groundwater flow systems in areas of degrading permafrost. *Geophysical Research Letters.* 36(22), L22401. DOI: 10.1029/2009GL039225.

Berg, R.L. 1974. *Energy balance on a paved surface*, US Army Cold Regions Research and Engineering Laboratory, Hanover, New Hampshire.

Berg, R.L. 1985. *Effect of color and texture on the surface temperature of asphalt concrete pavements*, Cold Regions Research and Engineering Laboratory (US).

Biskaborn, B.K., Smith, S.L., Noetzli, J., Matthes, H., Vieira, G., Streletskiy, D.A., . . . Lantuit, H. 2019. Permafrost is warming at a global scale. *Nature Communications.* 10(1), 264. DOI: 10.1038/s41467-018-08240-4.

Boike, J., Juszak, I., Lange, S., Chadburn, S., Burke, E., Paul Overduin, P., . . . Stern, L. 2018. A 20-year record (1998–2017) of permafrost, active layer and meteorological conditions at a high Arctic permafrost research site (Bayelva, Spitsbergen). *Earth System Science Data.* 10(1), 355-390. DOI: 10.5194/essd-10-355-2018.

Boike, J., Nitzbon, J., Anders, K., Grigoriev, M., Bolshiyanov, D., Langer, M., . . . Schreiber, P. 2019. A 16-year record (2002–2017) of permafrost, active-layer, and meteorological conditions at the Samoylov Island Arctic permafrost research site, Lena River delta, northern Siberia: an opportunity to validate remote-sensing data and land surface, snow, and permafrost models. *Earth System Science Data.* 11(1), 261-299. DOI: 10.5194/essd-11-261-2019.

Bradford, J.H., McNamara, J.P., Bowden, W., Gooseff, M.N. 2005. Measuring thaw depth beneath peat-lined arctic streams using ground-penetrating radar. *Hydrological Processes.* 19(14), 2689-2699. DOI: 10.1002/hyp.5781.

Bredehoeft, J., Papaopulos, I. 1965. Rates of vertical groundwater movement estimated from the earth's thermal profile. *Water Resources Research.* 1(2), 325-328. DOI: 10.1029/WR001i002p00325.

Bronfenbrener, L. 2009. The modelling of the freezing process in fine-grained porous media: Application to the frost heave estimation. *Cold Regions Science and Technology.* 56(2), 120-134. DOI: 10.1016/j.coldregions.2008.11.004.

Brooks, R.H., Corey, A.T. 1966. Properties of porous media affecting fluid flow. *Journal of the irrigation and drainage division.* 92(2), 61-90.

Brown, J., Ferrians, O., Heginbottom, J., Melnikov, E. 2001. Circum-arctic map of permafrost and ice conditions. *Boulder, Colorado: University of Colorado, National Snow Ice Data Center for Glaciology.* DOI: 10.3133/cp45.

Brubaker, K., Rango, A., Kustas, W. 1996. Incorporating radiation inputs into the snowmelt runoff model. *Hydrological processes.* 10(10), 1329-1343. DOI: 10.1002/(SICI)1099-1085(199610)10:10<1329::AID-HYP464>3.0.CO;2-W.

Bruch Jr, J.C., Zyvoloski, G. 1974. Transient two-dimensional heat conduction problems solved by the finite element method. *International Journal for Numerical Methods in Engineering.* 8(3), 481-494. DOI: 10.1002/nme.1620080304.

Bullard, E. 1939. Heat flow in South Africa. *Proceedings of the Royal Society of London. Series A, Mathematical and Physical Sciences.* 474-502. DOI: 10.1098/rspa.1939.0159.

Burn, C.R., Mackay, J., Kokelj, S. 2009. The thermal regime of permafrost and its susceptibility to degradation in upland terrain near Inuvik, NWT. *Permafrost and Periglacial Processes.* 20(2), 221-227. DOI: 10.1002/ppp.649.

Buteau, S., Fortier, R., Delisle, G., Allard, M. 2004. Numerical simulation of the impacts of climate warming on a permafrost mound. *Permafrost and Periglacial Processes.* 15(1), 41-57. DOI: 10.1002/ppp.474.

Calmels, F., Roy, L., Laurent, C., Pelletier, M., Kinnear, L., Benkert, B., . . . Pumple, J. 2015. Vulnerability of the North Alaska Highway to permafrost thaw: a field guide and data synthesis.

Whitehorse, Yukon: Northern climate exchange, Yukon Research Centre, Yukon College, pp. 130. DOI: 10.13140/RG.2.1.3629.3284.

Campbell, G.S., Norman, J.M. 2012. *An introduction to environmental biophysics*, Springer Science & Business Media, New York. DOI: 10.1007/978-1-4612-1626-1.

Carey, S.K., Woo, M.-k. 2002. Hydrogeomorphic relations among soil pipes, flow pathways, and soil detachments within a permafrost hillslope. *Physical Geography.* 23(2), 95-114. DOI: 10.2747/0272-3646.23.2.95.

Carlson, H. 1952. Calculation of depth of thaw in frozen ground. *30th Annual Meeting of the Highway Research Board Location: Washington DC, United States, pp 192-223.*

Carsel, R.F., Parrish, R.S. 1988. Developing joint probability distributions of soil water retention characteristics. *Water Resources Research.* 24(5), 755-769. DOI: 10.1029/WR024i005p00755.

Carslaw, H.S., Jaeger, J.C. 1959. *Conduction of heat in solids*, Oxford: Clarendon Press, 2nd ed. DOI: 10.2307/3610347.

Carson, J.E. 1963. Analysis of soil and air temperatures by Fourier techniques. *Journal of Geophysical Research.* 68(8), 2217-2232. DOI: 10.1029/JZ068i008p02217.

Chai, M., Mu, Y., Li, G., Ma, W., Wang, F. 2019. Relationship between ponding and topographic factors along the China-Russia Crude Oil Pipeline in permafrost regions. *Sciences in Cold and Arid Regions* 11(6), 419-427. DOI: 10.3724/sp.J.1226.2019.00419.

Chai, T., Draxler, R.R. 2014. Root mean square error (RMSE) or mean absolute error (MAE)?– Arguments against avoiding RMSE in the literature. *Geoscientific model development.* 7(3), 1247-1250. DOI: 10.5194/gmd-7-1247-2014.

Chen, J., Wang, H., Xie, P. 2019. Pavement temperature prediction: Theoretical models and critical affecting factors. *Applied Thermal Engineering.* 158, 113755. DOI: 10.1016/j.applthermaleng.2019.113755.

Chen, L., Fortier, D., McKenzie, J.M., Sliger, M. 2020a. Impact of heat advection on the thermal regime of roads built on permafrost. *Hydrological Processes.* 1-18. DOI: 10.1002/hyp.13688.

Chen, L., Fortier, D., Sliger, M., McKenzie, J., Murchison, P. 2017a. Subsurface flow recently triggered the development of taliks under a sub-Arctic road embankment: a prelude to the collapse of the Alaska Highway? *AGU Fall Meeting.*

Chen, L., Voss, C.I., Fortier, D., McKenzie, J.M. 2021. Surface energy balance of sub-Arctic roads and highways in permafrost regions. *Permafrost and Periglacial Processes (Accepted).*

Chen, L., Yu, W., Lu, Y., Han, F., Yi, X. 2020b. Effects of desertification on permafrost environment in Qinghai-Tibetan Plateau. *Journal of Environmental Management.* 262. DOI: 10.1016/j.jenvman.2020.110302.

Chen, L., Yu, W., Lu, Y., Liu, W. 2017b. Numerical simulation on the performance of thermosyphon adopted to mitigate thaw settlement of embankment in sandy permafrost zone. *Applied Thermal Engineering.* 128(5), 1624-1633. DOI: 10.1016/j.applthermaleng.2017.09.130.

Chen, L., Yu, W., Yi, X., Hu, D., Liu, W.B. 2018. Numerical simulation of heat transfer of the crushed-rock interlayer embankment of Qinghai-Tibet Railway affected by aeolian sand clogging and climate change. *Cold Regions Science and Technology.* 155, 1-10. DOI: 10.1016/j.coldregions.2018.07.009.

Cheng, G. 2004. Influences of local factors on permafrost occurrence and their implications for Qinghai-Xizang Railway design. *Science in China Series D: Earth Sciences.* 47(8), 704-709. DOI: 10.1007/bf02893300.

Cheng, G.D. 2005a. Permafrost studies in the Qinghai–Tibet plateau for road construction. *Journal of Cold Regions Engineering.* 19(1), 19-29. DOI: 10.1061/(ASCE)0887-381X(2005)19:1(19).

Cheng, G.D. 2005b. A roadbed cooling approach for the construction of Qinghai–Tibet Railway. *Cold regions science and technology.* 42(2), 169-176. DOI: 10.1016/j.coldregions.2005.01.002.

Chiasson-Poirier, G., Franssen, J., Lafrenière, M., Fortier, D., Lamoureux, S. 2019. Seasonal evolution of active layer thaw depth and hillslope-stream connectivity in a permafrost watershed. *Water Resources Research.* 56, 1-18. DOI: 10.1029/2019WR025828.

Cho, S., Sunderland, J. 1969. Heat-conduction problems with melting or freezing. *Journal of Heat Transfer.* 91(3), 421-426. DOI: 10.1115/1.3580205.

Chou, Y., Sheng, Y., Wei, Z., Ma, W. 2008. Calculation of temperature differences between the sunny slopes and the shady slopes along railways in permafrost regions on Qinghai–Tibet Plateau. *Cold regions science and technology.* 53(3), 346-354. DOI: 10.1016/j.coldregions.2008.04.004.

Chou, Y., Sheng, Y., Zhu, Y. 2012. Study on the relationship between the shallow ground temperature of embankment and solar radiation in permafrost regions on Qinghai–Tibet Plateau. *Cold Regions Science and Technology.* 78, 122-130. DOI: 10.1016/j.coldregions.2012.01.002.

Christiansen, H.H., Etzelmüller, B., Isaksen, K., Juliussen, H., Farbrot, H., Humlum, O., . . . Ødegård, R.S. 2010. The thermal state of permafrost in the nordic area during the international polar year 2007–2009. *Permafrost and Periglacial Processes.* 21(2), 156-181. DOI: 10.1002/ppp.687.

Cichota, R., Elias, E.A., van Lier, Q.d.J. 2004. Testing a finite-difference model for soil heat transfer by comparing numerical and analytical solutions. *Environmental Modelling & Software.* 19(5), 495-506. DOI: 10.1016/S1364-8152(03)00164-6.

Comini, G., Del Guidice, S., Lewis, R., Zienkiewicz, O. 1974. Finite element solution of non-linear heat conduction problems with special reference to phase change. *International Journal for Numerical Methods in Engineering.* 8(3), 613-624. DOI: 10.1002/nme.1620080314.

Connon, R., Devoie, É., Hayashi, M., Veness, T., Quinton, W. 2018. The influence of shallow taliks on permafrost thaw and active layer dynamics in subarctic Canada. *Journal of Geophysical Research: Earth Surface.* 123(2), 281-297. DOI: 10.1002/2017JF004469.

Cook, F.A. 1955. Near surface soil temperature measurements at Resolute Bay, Northwest Territories. *Arctic.* 8(4), 237-249.

Coulombe, S., Fortier, D., Stephani, E. 2012. *Using air convection ducts to control permafrost degradation under road infrastructure: Beaver Creek experimental site, Yukon, Canada*, Cold Regions Engineering 2012: Sustainable Infrastructure Development in a Changing Cold Environment, pp. 21-31. DOI: 10.1061/9780784412473.003.

Dagenais, S., Molson, J., Lemieux, J., Fortier, R., Therrien, R. 2020. Coupled cryo-hydrogeological modelling of permafrost dynamics near Umiujaq (Nunavik, Canada). *Hydrogeology Journal.* 1-18. DOI: 10.1007/s10040-020-02111-3.

Darrow, M.M., Jensen, D.D. 2016. Modeling the performance of an air convection embankment (ACE) with thermal berm over ice-rich permafrost, Lost Chicken Creek, Alaska. *Cold Regions Science and Technology.* 130, 43-58. DOI: 10.1016/j.coldregions.2016.07.012.

Davesne, G., Fortier, D., Dominé, F., Gray, J.T. 2017. Wind driven snow conditions control the occurrence of contemporary marginal mountain permafrost in the Chic-Chocs Mountains, south-eastern Canada - a case study from Mont Jacques-Cartier. *The Cryosphere.* 11(3), 20. DOI: 10.5194/tc-11-1351-2017.

Davis, T.N. 2001. *Permafrost: a guide to frozen ground in transition*, University of Alaska Press.

de Grandpré, I., Fortier, D., Stephani, E. 2010. Impact of groundwater flow on permafrost degradation: implications for transportation infrastructures. *Proceedings of the Join 63 rd Canadian Geotechnical Conference & 6 th Canadian Permafrost Conference, Calgary, Alberta.* 534-540. DOI: 10.13140/2.1.4892.1283.

de Grandpré, I., Fortier, D., Stephani, E. 2012. Degradation of permafrost beneath a road embankment enhanced by heat advected in groundwater. *Canadian Journal of Earth Sciences.* 49(8), 953-962. DOI: 10.1139/e2012-018.

Deming, D., Sass, J.H., Lachenbruch, A.H., de Rito, R.F. 1992. Heat flow and subsurface temperature as evidence for basin-scale ground-water flow, North Slope of Alaska. *Geological Society of America Bulletin.* 104(5), 528-542. DOI: 10.1130/0016-7606(1992)104<0528:HFASTA>2.3.CO;2.

Devoie, É.G., Craig, J.R., Connon, R.F., Quinton, W.L. 2019. Taliks: A tipping point in discontinuous permafrost degradation in peatlands. *Water Resources Research.* 55, 9838–9857. DOI: 10.1029/2018wr024488.

Dincer, I., Dost, S., Li, X. 1997. Performance analyses of sensible heat storage systems for thermal applications. *International Journal of Energy Research.* 21(12), 1157-1171. DOI: 10.1002/(SICI)1099-114X(19971010)21:12<1157::AID-ER317>3.0.CO;2-N.

Domine, F., Barrere, M., Sarrazin, D. 2016. Seasonal evolution of the effective thermal conductivity of the snow and the soil in high Arctic herb tundra at Bylot Island, Canada. *The Cryosphere.* 10(6), 2573. DOI: 10.5194/tc-10-2573-2016.

Doré, G., Beaulac, I., Van Gassen, W. 2006. Performance of the Beaver Creek section of the Alaska Highway, *Cold Regions Engineering 2006: Current Practices in Cold Regions Engineering*, pp. 1-12. DOI: 10.1061/9780784408360.

Doré, G., Ficheur, A., Guimond, A., Boucher, M. 2012. *Performance and cost-effectiveness of thermal stabilization techniques used at the Tasiujaq airstrip*, Cold Regions Engineering 2012: Sustainable Infrastructure Development in a Changing Cold Environment, pp. 32-41. DOI: 10.1061/9780784412473.004.

Doré, G., Mercier, B. 2008. Expérimentation de méthodes de mitigation des effets de la fonte du pergélisol sur les infrastructures de transport du Yukon. *Groupe de recherche en ingénierie des chaussées. Département en génie civil, Université Laval, Québec, Canada, 28p.* DOI: 10.1.1.428.3505. (in French)

Doré, G., Niu, F.J., Brooks, H. 2016. Adaptation Methods for Transportation Infrastructure Built on Degrading Permafrost. *Permafrost and Periglacial Processes.* 27, 352-364. DOI: 10.1002/ppp.1919.

Dumais, S., Doré, G. 2016. An albedo-based model for the calculation of pavement surface temperatures in permafrost regions. *Cold Regions Science and Technology.* 123, 44-52. DOI: 10.1016/j.coldregions.2015.11.013.

Environment and Climate Change Canada. 2018. Climatic data of Beaver Creek, Yukon. National Climate Data and Information Archive. Available from www.climat.meteo.gc.ca (Accessed January 1st, 2018).

Eugster, W., Rouse, W.R., Pielke Sr, R.A., Mcfadden, J.P., Baldocchi, D.D., Kittel, T.G.F., . . . Vaganov, E. 2000. Land–atmosphere energy exchange in Arctic tundra and boreal forest: available data and feedbacks to climate. *Global change biology.* 6(S1), 84-115. DOI: 10.1046/j.1365-2486.2000.06015.x.

Evans, S.G., Ge, S. 2017. Contrasting hydrogeologic responses to warming in permafrost and seasonally frozen ground hillslopes. *Geophysical Research Letters.* 44(4), 1803-1813. DOI: 10.1002/2016GL072009.

Evans, S.G., Ge, S., Voss, C.I., Molotch, N.P. 2018. The role of frozen soil in groundwater discharge predictions for warming alpine watersheds. *Water Resources Research.* 54(3), 1599-1615. DOI: 10.1002/2017WR022098.

Evans, S.G., Godsey, S.E., Rushlow, C.R., Voss, C. 2020. Water tracks enhance water flow above permafrost in upland Arctic Alaska hillslopes. *Journal of Geophysical Research: Earth Surface.* 125(e2019JF005256), e2019JF005256. DOI: 10.1029/2019JF005256.

Fan, J., Chen, B., Wu, L., Zhang, F., Lu, X., Xiang, Y. 2018. Evaluation and development of temperature-based empirical models for estimating daily global solar radiation in humid regions. *Energy.* 144, 903-914. DOI: 10.1016/j.energy.2017.12.091.

Farouki, O.T. 1982. *Evaluation of methods for calculating soil thermal conductivity*, Cold Regions Research and Engineering Laboratory, Hanover, New Hampshire.

Fisher, J.P., Estop-Aragonés, C., Thierry, A., Charman, D.J., Wolfe, S.A., Hartley, I.P., . . . Phoenix, G.K. 2016. The influence of vegetation and soil characteristics on active-layer thickness of permafrost soils in boreal forest. *Global change biology.* 22(9), 3127-3140. DOI: 10.1111/gcb.13248.

Fortier, D., Allard, M., Shur, Y. 2007. Observation of rapid drainage system development by thermal erosion of ice wedges on Bylot Island, Canadian Arctic Archipelago. *Permafrost and Periglacial Processes.* 18(3), 229-243. DOI: 10.1002/ppp.595.

Fortier, D., Chen, L. 2020a. Ground temperatures of embankment subbase and subgrade at the Beaver Creek, Yukon - Road experimental section 2008 - 2018, v. 1.0 (2008-2018). *Nordicana*, 2020. D68. DOI: 10.5885/45642CE-6883D8FF051E4E4B.

Fortier, D., Chen, L. 2020b. Meteorological data at the Beaver Creek, Yukon - Road experimental section 2008 - 2018, v. 1.0 (2008-2018). *Nordicana*, 2020. D67. DOI: 10.5885/45639CE-A9A7495855214A98.

Fortier, D., Sliger, M., Rioux, K. 2018. *Performance assessment of the thermo-reflective snow-sun sheds at the Beaver Creek road experimental site*, p. 48, Université de Montréal.

Fortier, D., Veuille, S., Sliger, M., Verpaelst, M., Davesne, G., Charbonneau, S., Grandmont, K. 2016. Évaluation des impacts de l'écoulement de surface et de l'écoulement souterrain sur la degradation du pergélisol et la stabilité des infrastructures routières. *Final report prepared for Transport Canada. Cold Regions Geomorphology and Geotechnical Laboratory (Geocryolab),* Université de Montréal, Montréal, Canada. 116 pp. and annexes. (in French).

Fortier, R., LeBlanc, A.-M., Yu, W. 2011. Impacts of permafrost degradation on a road embankment at Umiujaq in Nunavik (Quebec), Canada. *Canadian Geotechnical Journal.* 48(5), 720-740. DOI: 10.1139/t10-101.

Fourier, J. 1822. *Theorie analytique de la chaleur*, Chez Firmin Didot, père et fils. (French)

Fredlund, D.G., Xing, A. 1994. Equations for the soil-water characteristic curve. *Canadian geotechnical journal.* 31(4), 521-532. DOI: 10.1139/t94-061.

French, H.M. 2017. *The periglacial environment, 4 edition*, John Wiley & Sons, Hoboken, New Jersey, United States.

Fujii, H., Okubo, H., Nishi, K., Itoi, R., Ohyama, K., Shibata, K. 2009. An improved thermal response test for U-tube ground heat exchanger based on optical fiber thermometers. *Geothermics.* 38(4), 399-406. DOI: 10.1016/j.geothermics.2009.06.002.

Gao, S., Jin, H., Bense, V.F., Wang, X., Chai, X. 2019. Application of electrical resistivity tomography for delineating permafrost hydrogeology in the headwater area of Yellow River on Qinghai-Tibet Plateau, SW China. *Hydrogeology Journal.* 27, 1725–1737. DOI: 10.1007/s10040-019-01942-z.

Gao, S., Stefan, H.G. 1999. Multiple linear regression for lake ice and lake temperature characteristics. *Journal of cold regions engineering.* 13(2), 59-77. DOI: 10.1061/(ASCE)0887-381X(1999)13:2(59).

Garnier, B., Ohmura, A. 1968. A method of calculating the direct shortwave radiation income of slopes. *Journal of Applied Meteorology.* 7(5), 796-800. DOI: 10.1175/1520-0450(1968)007<0796:AMOCTD>2.0.CO;2.

Ge, S., McKenzie, J., Voss, C., Wu, Q. 2011. Exchange of groundwater and surface-water mediated by permafrost response to seasonal and long term air temperature variation. *Geophysical Research Letters.* 38, L14402. DOI: 10.1029/2011GL047911.

Ghias, M.S., Therrien, R., Molson, J., Lemieux, J.-M. 2017. Controls on permafrost thaw in a coupled groundwater-flow and heat-transport system: Iqaluit Airport, Nunavut, Canada. *Hydrogeology Journal.* 25, 657–673. DOI: 10.1007/s1004.

Ghias, M.S., Therrien, R., Molson, J., Lemieux, J.-M. 2018. Numerical simulations of shallow groundwater flow and heat transport in a continuous permafrost setting under the impact of climate warming. *Canadian Geotechnical Journal.* 56(3), 436-448. DOI: 10.1139/cgj-2017-0182.

Glose, A., Lautz, L.K., Baker, E.A. 2017. Stream heat budget modeling with HFLUX: Model development, evaluation, and applications across contrasting sites and seasons. *Environmental Modelling & Software.* 92, 213-228. DOI: 10.1016/j.envsoft.2017.02.021.

Goering, D.J. 1998. Experimental investigation of air convection embankments for permafrost-resistant roadway design. *Proceedings of 7th International Conference on Permafrost.* 326.

Goering, D.J., Kumar, P. 1996. Winter-time convection in open-graded embankments. *Cold Regions Science and Technology.* 24(1), 57-74. DOI: 10.1016/0165-232X(95)00011-Y.

Gold, L.W. 1967. Influence of surface conditions on ground temperature. *Canadian Journal of Earth Sciences.* 4(2), 199-208. DOI: 10.1139/e67-010.

Gold, L.W., Lachenbruch, A.H. 1973. Thermal conditions in permafrost: A review of North American literature, *North American Contribution to the Second International Conference on Permafrost*, July 1973, Yakutsk, Siberia, USSR.

Goodrich, L. 1982. The influence of snow cover on the ground thermal regime. *Canadian geotechnical journal.* 19(4), 421-432. DOI: 10.1139/t82-047.

Grasby, S.E., Allen, D., Bell, S., Chen, Z., Ferguson, G., Jessop, A., . . . Moore, M. 2011. *Geothermal energy resource potential of Canada*, Geological Survey of Canada.

Grenier, C., Anbergen, H., Bense, V., Chanzy, Q., Coon, E., Collier, N., . . . Frederick, J. 2018. Groundwater flow and heat transport for systems undergoing freeze-thaw: Intercomparison of numerical simulators for 2D test cases. *Advances in Water Resources.* 114, 196-218. DOI: 10.1016/j.advwatres.2018.02.001.

Guan, X., Spence, C., Westbrook, C. 2010. Shallow soil moisture–ground thaw interactions and controls–Part 2: Influences of water and energy fluxes. *Hydrology Earth System Sciences.* 14(7), 1387-1400. DOI: 10.5194/hess-14-1387-2010, 2010.

Gui, J., Phelan, P.E., Kaloush, K.E., Golden, J.S. 2007. Impact of pavement thermophysical properties on surface temperatures. *Journal of Materials in Civil Engineering.* 19(8), 683-690. DOI: 10.1061/(ASCE)0899-1561(2007)19:8(683).

Hall, M.R., Dehdezi, P.K., Dawson, A.R., Grenfell, J., Isola, R. 2011. Influence of the thermophysical properties of pavement materials on the evolution of temperature depth profiles in different

climatic regions. *Journal of Materials in Civil Engineering.* 24(1), 32-47. DOI: 10.1061/(ASCE)MT.1943-5533.0000357.

Hansson, K., Šimůnek, J., Mizoguchi, M., Lundin, L.-C., Van Genuchten, M.T. 2004. Water flow and heat transport in frozen soil. *Vadose Zone Journal.* 3(2), 693-704. DOI: 10.2113/3.2.693.

Hargreaves, G.H., Samani, Z.A. 1982. Estimating potential evapotranspiration. *Journal of the irrigation and Drainage Division.* 108(3), 225-230.

Harlan, R. 1973. Analysis of coupled heat-fluid transport in partially frozen soil. *Water Resources Research.* 9(5), 1314-1323. DOI: 10.1029/WR009i005p01314.

Harris, C., Arenson, L.U., Christiansen, H.H., Etzelmüller, B., Frauenfelder, R., Gruber, S., . . . Humlum, O. 2009. Permafrost and climate in Europe: Monitoring and modelling thermal, geomorphological and geotechnical responses. *Earth-Science Reviews.* 92(3), 117-171. DOI: 10.1016/j.earscirev.2008.12.002.

Harris, S.A., Corte, A.E. 1992. Interactions and relations between mountain permafrost, glaciers, snow and water. *Permafrost and Periglacial Processes.* 3(2), 103-110. DOI: 10.1002/ppp.3430030207.

Harris, S.A., Pedersen, D.E. 1998. Thermal regimes beneath coarse blocky materials. *Permafrost and periglacial processes.* 9(2), 107-120. DOI: 10.1002/(SICI)1099-1530(199804/06)9:2<107::AID-PPP277>3.0.CO;2-G.

Hayashi, M., Goeller, N., Quinton, W.L., Wright, N. 2007. A simple heat-conduction method for simulating the frost-table depth in hydrological models. *Hydrological Processes.* 21(19), 2610-2622. DOI: 10.1002/hyp.6792.

Heginbottom, J., Dubreuil, M., Harker, P. 1995. Canada, Permafrost. National Atlas of Canada. *Natural Resources Canada, 5th Edition, MCR.* 4177.

Herb, W.R., Janke, B., Mohseni, O., Stefan, H.G. 2008. Ground surface temperature simulation for different land covers. *Journal of Hydrology.* 356(3-4), 327-343. DOI: 10.1016/j.jhydrol.2008.04.020.

Hermansson, Å. 2001. Mathematical model for calculation of pavement temperatures: comparison of calculated and measured temperatures. *Journal of the Transportation Research Board.* 1764(1), 180-188. DOI: 10.3141/1764-19.

Hermansson, Å. 2004. Mathematical model for paved surface summer and winter temperature: comparison of calculated and measured temperatures. *Cold regions science and technology.* 40(1-2), 1-17. DOI: 10.1016/j.coldregions.2004.03.001.

Hinkel, K., Nelson, F. 2001. Patterns of soil temperature and moisture in the active layer and upper permafrost at Barrow, Alaska: 1993–1999. *Journal of Geophysical Research: Atmospheres.* 108(D2).

Hinkel, K., Paetzold, F., Nelson, F., Bockheim, J. 2001. Patterns of soil temperature and moisture in the active layer and upper permafrost at Barrow, Alaska: 1993–1999. *Global and Planetary Change.* 29(3), 293-309. DOI: 10.1016/S0921-8181(01)00096-0.

Hinkel, K.M. 1997. Estimating seasonal values of thermal diffusivity in thawed and frozen soils using temperature time series. *Cold Regions Science and Technology.* 26(1), 1-15. DOI: 10.1016/S0165-232X(97)00004-9.

Hinkel, K.M., Klene, A.E., Nelson, F.E. 2008. Spatial and interannual patterns of winter n-factors near Barrow, Alaska. *Proceedings of the Ninth International Conference on Permafrost.* 28, 705-709.

Hinkel, K.M., Outcalt, S.I. 1993. Detection of nonconductive heat transport in soils using spectral analysis. *Water Resources Research.* 29(4), 1017-1023. DOI: 10.1029/92wr02596.

Hinkel, K.M., Outcalt, S.I. 1994. Identification of heat-transfer processes during soil cooling, freezing, and thaw in central Alaska. *Permafrost and Periglacial Processes.* 5(4), 217-235. DOI: 10.1002/ppp.3430050403.

Hinkel, K.M., Outcalt, S.I., Taylor, A.E. 1997. Seasonal patterns of coupled flow in the active layer at three sites in northwest North America. *Canadian Journal of Earth Sciences.* 34(5), 667-678. DOI: 10.1139/e06-121.

Hinzman, L.D., Bettez, N.D., Bolton, W.R., Chapin, F.S., Dyurgerov, M.B., Fastie, C.L., . . . Huntington, H.P. 2005. Evidence and implications of recent climate change in northern Alaska and other arctic regions. *Climatic Change.* 72(3), 251-298. DOI: 10.1007/s10584-005-5352-2.

Hjort, J., Karjalainen, O., Aalto, J., Westermann, S., Romanovsky, V.E., Nelson, F.E., . . . Luoto, M. 2018. Degrading permafrost puts Arctic infrastructure at risk by mid-century. *Nature Communications.* 9(1), 5147. DOI: 10.1038/s41467-018-07557-4.

Hoelzle, M., Mittaz, C., Etzelmüller, B., Haeberli, W. 2001. Surface energy fluxes and distribution models of permafrost in European mountain areas: an overview of current developments. *Permafrost and Periglacial Processes.* 12(1), 53-68. DOI: org/10.1002/ppp.385.

Hong, E., Perkins, R., Trainor, S. 2014. Thaw settlement hazard of permafrost related to climate warming in Alaska. *Arctic.* 93-103. DOI: 10.14430/arctic4368.

Hu, G., Zhao, L., Wu, X., Wu, T., Li, R., Xie, C., . . . Hao, J. 2017. A mathematical investigation of the air-ground temperature relationship in permafrost regions on the Tibetan Plateau. *Geoderma.* 306, 244-251. DOI: 10.1016/j.geoderma.2017.07.017.

Huang, J., Zhang, X., Zhang, Q., Lin, Y., Hao, M., Luo, Y., . . . Zhang, J. 2017. Recently amplified arctic warming has contributed to a continual global warming trend. *Nature Climate Change.* 7(12), 875-879. DOI: 10.1038/s41558-017-0009-5.

Huang, K., Dai, J., Wang, G., Chang, J., Lu, Y., Song, C., . . . Ye, R. 2019. The Impact of Land Surface Temperatures on Suprapermafrost Groundwater on the Central Qinghai-Tibet Plateau. *Hydrological Processes.* DOI: 10.1002/hyp.13677.

Hughes, T.J. 1977. Unconditionally stable algorithms for nonlinear heat conduction. *Computer methods in applied mechanics and engineering.* 10(2), 135-139. DOI: 10.1016/0045-7825(77)90001-9.

Hwang, C. 1976. Predictions and observations on the behaviour of a warm gas pipeline on permafrost. *Canadian Geotechnical Journal.* 13(4), 452-480. DOI: 10.1139/t76-045.

Idso, S.B., Aase, J.K., Jackson, R.D. 1975. Net radiation — soil heat flux relations as influenced by soil water content variations. *Boundary-Layer Meteorology.* 9(1), 113-122. DOI: 10.1007/bf00232257.

Ingebritsen, S.E., Sanford, W.E. 1999. *Groundwater in geologic processes*, Cambridge University Press.

IPCC. 2014. *Climate change 2014: synthesis report. Contribution of Working Groups I, II and III to the fifth assessment report of the Intergovernmental Panel on Climate Change*, Cambridge University Press, Cambridge/New York.

IPCC. 2015. *Climate change 2014: mitigation of climate change*, Cambridge University Press.

Ishikawa, M. 2003. Thermal regimes at the snow–ground interface and their implications for permafrost investigation. *Geomorphology.* 52(1), 105-120. DOI: 10.1016/S0169-555X(02)00251-9.

Ishikawa, M., Hirakawa, K. 2000. Mountain permafrost distribution based on BTS measurements and DC resistivity soundings in the Daisetsu Mountains, Hokkaido, Japan. *Permafrost and Periglacial Processes.* 11(2), 109-123. DOI: 10.1002/1099-1530(200004/06)11:2<109::AID-PPP343>3.0.CO;2-O.

Ives, J.D., Fahey, B.D. 1971. Permafrost occurrence in the Front Range, Colorado Rocky Mountains, USA. *Journal of Glaciology.* 10(58), 105-111. DOI: 10.3189/S0022143000013034.

Jafarov, E., Coon, E., Harp, D., Wilson, C.J., Painter, S., Atchley, A., Romanovsky, V. 2018. Modeling the role of preferential snow accumulation in through talik development and hillslope groundwater flow in a transitional permafrost landscape. *Environmental Research Letters.* 13(10). DOI: 10.1088/1748-9326/aadd30.

Jame, Y.W., Norum, D.I. 1980. Heat and mass transfer in a freezing unsaturated porous medium. *Water Resources Research.* 16(4), 811-819. DOI: 10.1029/WR016i004p00811.

James, M., Lewkowicz, A.G., Smith, S.L., Miceli, C.M. 2013. Multi-decadal degradation and persistence of permafrost in the Alaska Highway corridor, northwest Canada. *Environmental Research Letters.* 8(4), 045013. DOI: 10.1088/1748-9326/8/4/045013.

Jan, A., Coon, E. and Painter, S.L. 2019. Evaluating integrated surface/subsurface permafrost thermal hydrology models in ATS (v0.88) against observations from a polygonal tundra site. *Geoscientific Model Development*. 13(5), 2259-2276. DOI: 10.5194/gmd-13-2259-2020, 2020.

Jensen, M.E., Allen, R.G. 2016. Evaporation, evapotranspiration, and irrigation water requirements. *ASCE Manuals and Reports on Engineering Practices No. 70.* 1-769. DOI: 10.1061/9780784414057.

Jiang, Y., Zhuang, Q., O'Donnell, J.A. 2012. Modeling thermal dynamics of active layer soils and near-surface permafrost using a fully coupled water and heat transport model. *Journal of Geophysical Research: Atmospheres.* 117(D11110), 1-15. DOI: 10.1029/2012JD017512.

Jin, H., Yu, Q., Lü, L., Guo, D., He, R., Yu, S., . . . Li, Y. 2007. Degradation of permafrost in the Xing'anling Mountains, Northeastern China. *Permafrost and Periglacial Processes.* 18(3), 245-258. DOI: 10.1002/ppp.589.

Jin, H., Yu, Q., Wang, S., Lü, L. 2008. Changes in permafrost environments along the Qinghai–Tibet engineering corridor induced by anthropogenic activities and climate warming. *Cold Regions Science and Technology.* 53(3), 317-333. DOI: 10.1016/j.coldregions.2007.07.005.

Jordan, R. 1991. A one-dimensional temperature model for a snow cover: Technical documentation for SNTHERM. 89, Cold Regions Research and Engineering Laboratory, Hanover, New Hampshire.

Jorgenson, M.T., Shur, Y.L., Pullman, E.R. 2006. Abrupt increase in permafrost degradation in Arctic Alaska. *Geophysical Research Letters.* 33(L02503), 1-4. DOI: 10.1029/2005GL024960.

Kane, D.L., Hinkel, K.M., Goering, D.J., Hinzman, L.D., Outcalt, S.I. 2001. Non-conductive heat transfer associated with frozen soils. *Global and Planetary Change.* 29(3), 275-292. DOI: 10.1016/S0921-8181(01)00095-9.

Kane, D.L., Hinzman, L.D., Zarling, J.P. 1991. Thermal response of the active layer to climatic warming in a permafrost environment. *Cold Regions Science and Technology.* 19(2), 111-122. DOI: 10.1016/0165-232X(91)90002-X.

Kane, D.L., Stein, J. 1983. Water movement into seasonally frozen soils. *Water Resources Research.* 19(6), 1547-1557. DOI: 10.1029/WR019i006p01547.

Karjalainen, O., Luoto, M., Aalto, J., Hjort, J. 2019. New insights into the environmental factors controlling the ground thermal regime across the Northern Hemisphere: a comparison between permafrost and non-permafrost areas. *The Cryosphere.* 13(2), 693-707. DOI: 10.5194/tc-13-693-2019.

Karunaratne, K., Burn, C. 2004. Relations between air and surface temperature in discontinuous permafrost terrain near Mayo, Yukon Territory. *Canadian Journal of Earth Sciences.* 41(12), 1437-1451. DOI: 10.1139/E04-082.

Kato, T. 2016. *Prediction of photovoltaic power generation output and network operation*, Integration of Distributed Energy Resources in Power Systems, pp. 77-108, Elsevier.

Kelvin, L. 1861. The reduction of observations of underground temperature. *Trans. R. Soc. Edinb.* 22, 405-427.

Klene, A.E., Nelson, F.E., Shiklomanov, N.I., Hinkel, K.M. 2001. The n-factor in natural landscapes: variability of air and soil-surface temperatures, Kuparuk River Basin, Alaska, USA. *Arctic, Antarctic, Alpine Research.* 33(2), 140-148. DOI: 10.1080/15230430.2001.12003416.

Kondo, J., Yamazaki, T. 1990. A prediction model for snowmelt, snow surface temperature and freezing depth using a heat balance method. *Journal of applied meteorology.* 29(5), 375-384. DOI: 10.1175/1520-0450(1990)029<0375:APMFSS>2.0.CO;2.

Kondo, Junsei, and Takeshi Yamazaki. 1990. A prediction model for snowmelt, snow surface temperature and freezing depth using a heat balance method. *Journal of applied meteorology.* 29.5: 375-384. DOI: 10.1175/1520-0450(1990)029<0375:APMFSS>2.0.CO;2.

Kondratiev, V. 2002. Design and experience-controlling railroad embankment deformation on ice-rich permafrost, *Cold Regions Engineering: Cold Regions Impacts on Transportation and Infrastructure*, pp. 467-482. DOI: 10.1061/40621(254)40.

Kondratiev, V.G. 2017. Main geotechnical problems of railways and roads in Kriolitozone and Their Solutions. *Procedia engineering.* 189, 702-709. DOI: 10.1016/j.proeng.2017.05.111.

Kong, X., Doré, G., Calmels, F. 2019. Thermal modeling of heat balance through embankments in permafrost regions. *Cold Regions Science and Technology.* 158, 117-127. DOI: 10.1016/j.coldregions.2018.11.013.

Krabbenhoft, K., Damkilde, L., Nazem, M. 2007. An implicit mixed enthalpy–temperature method for phase-change problems. *Heat and mass transfer.* 43(3), 233-241. DOI: 10.1007/s00231-006-0090-1.

Krarti, M., Lopez-Alonzo, C., Claridge, D., Kreider, J. 1995. Analytical model to predict annual soil surface temperature variation. *Journal of Solar Energy Engineering.* 117(2), 91-99. DOI: 10.1115/1.2870881.

Kurylyk, B.L., Hayashi, M., Quinton, W.L., McKenzie, J.M., Voss, C.I. 2016. Influence of vertical and lateral heat transfer on permafrost thaw, peatland landscape transition, and groundwater flow. *Water Resources Research.* 52, 1286-1305. DOI: 10.1002/2015WR018057.

Kurylyk, B.L., Irvine, D.J., Carey, S.K., Briggs, M.A., Werkema, D.D., Bonham, M. 2017. Heat as a groundwater tracer in shallow and deep heterogeneous media: Analytical solution, spreadsheet tool, and field applications. *Hydrological Processes.* 31(14), 2648-2661. DOI: 10.1002/hyp.11216.

Kurylyk, B.L., MacQuarrie, K.T., Caissie, D., McKenzie, J.M. 2015. Shallow groundwater thermal sensitivity to climate change and land cover disturbances: derivation of analytical expressions and implications for stream temperature modeling. *Hydrology and Earth System Sciences.* 19, 2469–2489. DOI: 10.5194/hess-19-2469-2015.

Kwong, Y.J., Gan, T. 1994. Northward migration of permafrost along the Mackenzie Highway and climatic warming. *Climatic Change.* 26(4), 399-419. DOI: 10.1007/BF01094404.

L'Hérault, E., Allard, M., Barrette, C., Doré, G., Sarrazin, D. 2012. Investigations géotechniques, caractérisation du pergélisol et stratégie d'adaptation pour les aéroports du MTQ au Nunavik, Rapport d'étape 1: État d'avancement du projet et résultats préliminaires. Réalisé pour le compte du ministère des Transports du Québec. Centre d'études nordiques, Université Laval, Québec., p. 77. (in french)

Lai, Y., Guo, H., Dong, Y. 2009. Laboratory investigation on the cooling effect of the embankment with L-shaped thermosyphon and crushed-rock revetment in permafrost regions. *Cold Regions Science and Technology.* 58(3), 143-150. DOI: 10.1016/j.coldregions.2009.05.002.

Lai, Y., Pei, W., Zhang, M., Zhou, J. 2014. Study on theory model of hydro-thermal–mechanical interaction process in saturated freezing silty soil. *International Journal of Heat and Mass Transfer.* 78, 805-819. DOI: 10.1016/j.ijheatmasstransfer.2014.07.035.

Lai, Y., Zhang, L., Zhang, S., Mi, L. 2003. Cooling effect of ripped-stone embankments on Qing-Tibet railway under climatic warming. *Chinese Science Bulletin.* 48(6), 598-604. DOI: 10.1360/03tb9127.

Lai, Y.M., Wang, Q.S., Niu, F.J., Zhang, K.H. 2004. Three-dimensional nonlinear analysis for temperature characteristic of ventilated embankment in permafrost regions. *Cold Regions Science and Technology.* 38(2), 165-184. DOI: 10.1016/j.coldregions.2003.10.006.

Lamontagne-Hallé, P., McKenzie, J.M., Kurylyk, B., Zipper, S.C. 2018. Changing groundwater discharge dynamics in permafrost regions. *Environmental Research Letters.* 13, 084017. DOI: 10.1088/1748-9326/aad404.

Lanouette, F., Doré, G., Fortier, D., Lemieux, C. 2015. Influence of snow cover on the ground thermal regime along an embankment built on permafrost: In-situ measurements. *68th Canadian Geotechnical Conference and 7th Canadian Permafrost Conference.* 1-7. DOI: 10.13140/RG.2.1.2482.1848.

Larsen, P.H., Goldsmith, S., Smith, O., Wilson, M.L., Strzepek, K., Chinowsky, P., Saylor, B. 2008. Estimating future costs for Alaska public infrastructure at risk from climate change. *Global Environmental Change.* 18(3), 442-457. DOI: 10.1016/j.gloenvcha.2008.03.005.

Lawrence, D.M., Slater, A.G., Tomas, R.A., Holland, M.M., Deser, C. 2008a. Accelerated Arctic land warming and permafrost degradation during rapid sea ice loss. *Geophysical Research Letters.* 35, L11506. DOI: 10.1029/2008gl033985.

Lawrence, D.M., Slater, A.G., Tomas, R.A., Holland, M.M., Deser, C. 2008b. Accelerated Arctic land warming and permafrost degradation during rapid sea ice loss. *Geophysical Research Letters.* 35(11). DOI: 10.1029/2008GL033985.

Lewkowicz, A.G., Bonnaventure, P.P., Smith, S.L., Kuntz, Z. 2012. Spatial and thermal characteristics of mountain permafrost, northwest Canada. *Geografiska Annaler: Series A, Physical Geography.* 94(2), 195-213. DOI: 10.1111/j.1468-0459.2012.00462.x.

Lewkowicz, A.G., Way, R.G. 2019. Extremes of summer climate trigger thousands of thermokarst landslides in a High Arctic environment. *Nature communications.* 10(1), 1-11. DOI: 10.1038/s41467-019-09314-7.

Li, D., Wu, Z., Fang, J., Li, Y., Lu, N. 1998. Heat stability analysis of embankment on the degrading permafrost district in the East of the Tibetan Plateau, China. *Cold regions science and technology.* 28(3), 183-188. DOI: 10.1016/S0165-232X(98)00018-4.

Li, G., Wang, F., Ma, W., Fortier, R., Mu, Y., Zhou, Z., . . . Cai, Y. 2018. Field observations of cooling performance of thermosyphons on permafrost under the China-Russia Crude Oil Pipeline. *Applied Thermal Engineering.* 141, 688-696. DOI: 10.1016/j.applthermaleng.2018.06.005.

Li, S., Zhan, H., Lai, Y., Sun, Z., Pei, W. 2014. The coupled moisture-heat process of permafrost around a thermokarst pond in Qinghai-Tibet Plateau under global warming. *Journal of Geophysical Research: Earth Surface.* 119(4), 836-853. DOI: 10.1002/2013JF002930.

Liljedahl, A.K., Boike, J., Daanen, R.P., Fedorov, A.N., Frost, G.V., Grosse, G., . . . Matveyeva, N. 2016. Pan-Arctic ice-wedge degradation in warming permafrost and its influence on tundra hydrology. *Nature Geoscience.* 9(4), 312. DOI: 10.1038/ngeo2674.

Lin, Z., Gao, Z., Niu, F., Luo, J., Yin, G., Liu, M., Fan, X. 2019. High spatial density ground thermal measurements in a warming permafrost region, Beiluhe Basin, Qinghai-Tibet Plateau. *Geomorphology.* 340, 1-14. DOI: 10.1016/j.geomorph.2019.04.032.

Ling, F., Zhang, T. 2003. Impact of the timing and duration of seasonal snow cover on the active layer and permafrost in the Alaskan Arctic. *Permafrost and Periglacial Processes.* 14(2), 141-150. DOI: 10.1002/ppp.445.

Ling, F., Zhang, T. 2004. A numerical model for surface energy balance and thermal regime of the active layer and permafrost containing unfrozen water. *Cold Regions Science and Technology.* 38(1), 1-15. DOI: 10.1016/S0165-232X(03)00057-0.

Liston, G.E., Hall, D.K. 1995. An energy-balance model of lake-ice evolution. *Journal of Glaciology.* 41(138), 373-382. DOI: 10.3189/S0022143000016245.

Liu, W., Yu, W., Fortier, R., Chen, L., Lu, Y., Zhang, M., Hu, D. 2019. Thermal effect of rainwater infiltration into a replicated road embankment in a cold environmental chamber. *Cold Regions Science and Technology.* 159, 47-57. DOI: 10.1016/j.coldregions.2018.12.008.

Loranty, M.M., Abbott, B.W., Blok, D., Douglas, T.A., Epstein, H.E., Forbes, B.C., …, Walker, D.A., 2018. Reviews and syntheses: Changing ecosystem influences on soil thermal regimes in northern high-latitude permafrost regions. *Biogeosciences*, 15 (17). pp. 5287-5313. DOI: 10.5194/bg-15-5287-2018, 2018.

Lovell Jr, C. 1957. Temperature effects on phase composition and strength of partially-frozen soil. *Highway Research Board Bulletin.* 168, 74-95.

Lu, N., Ge, S. 1996. Effect of horizontal heat and fluid flow on the vertical temperature distribution in a semiconfining layer. *Water Resources Research.* 32(5), 1449-1453. DOI: 10.1029/95WR03095.

Luethi, R., Phillips, M., Lehning, M. 2016. Estimating Non-Conductive Heat Flow Leading to Intra-Permafrost Talik Formation at the Ritigraben Rock Glacier (Western Swiss Alps). *Permafrost and Periglacial Processes.* 28, 183– 194. DOI: 10.1002/ppp.1911.

Luetschg, M., Lehning, M., Haeberli, W. 2008. A sensitivity study of factors influencing warm/thin permafrost in the Swiss Alps. *Journal of Glaciology.* 54(187), 696-704. DOI: 10.3189/002214308786570881.

Lunardini, V., Varotta, R. 1981. Approximate solution to Neumann problem for soil systems. *Journal of Energy Resources Technology.* 103(1), 76-81. DOI: 10.1115/1.3230817.

Lunardini, V.J. 1978. Theory of n-factors and correlation of data. *Proceedings of the Third International Conference on Permafrost.* 1, 40-46. DOI: S0341-8162(16)30207-7/rf0230.

Lunardini, V.J. 1986. *Heat conduction with freezing or thawing*, DTIC Document.

Lunardini, V.J. 1988. *Freezing of soil with an unfrozen water content and variable thermal properties*, DTIC Document.

Lunardini, V.J. 1991. *Heat transfer with freezing and thawing*, Elsevier Science, Amsterdam, New York.

Lundin, L.-C. 1990. Hydraulic properties in an operational model of frozen soil. *Journal of Hydrology.* 118(1), 289-310. DOI: 10.1016/0022-1694(90)90264-X.

Luo, D., Jin, H., Marchenko, S.S., Romanovsky, V.E. 2018. Difference between near-surface air, land surface and ground surface temperatures and their influences on the frozen ground on the Qinghai-Tibet Plateau. *Geoderma.* 312, 74-85. DOI: 10.1016/j.geoderma.2017.09.037.

Ma, W., Cheng, G.D., Wu, Q.B. 2009. Construction on permafrost foundations: lessons learned from the Qinghai–Tibet railroad. *Cold Regions Science and Technology.* 59(1), 3-11. DOI: 10.1016/j.coldregions.2009.07.007.

Ma, W., Wen, Z., Sheng, Y., Wu, Q., Wang, D., Feng, W. 2012. Remedying embankment thaw settlement in a warm permafrost region with thermosyphons and crushed rock revetment. *Canadian Geotechnical Journal.* 49(9), 1005-1014. DOI: 10.1139/t2012-058.

Mackay, J.R. 1983. Downward water movement into frozen ground, western arctic coast, Canada. *Canadian Journal of Earth Sciences.* 20(1), 120-134. DOI: 10.1139/e2012-043.

Male, D., Granger, R. 1981. Snow surface energy exchange. *Water Resources Research.* 17(3), 609-627. DOI: 10.1029/WR017i003p00609.

Malenfant-Lepage, J. 2015. Experimentation of mitigation techniques to reduce the effects of permafrost degeradation on transportation infrastructures at Beaver Creek experimental road site Alaska Highway, Yukon, Université Laval.

Malenfant-Lepage, J., Doré, G., Fortier, D. 2012a. Thermal effectiveness of the mitigation techniques tested at Beaver Creek Experimental road site based on a heat balance analysis (Yukon, Canada), *Cold Regions Engineering 2012: Sustainable Infrastructure Development in a Changing Cold Environment*. Morse B, D.G. (ed), pp. 42-51, American Society of Civil Engineers: Reston, Virginia, USA, Quebec City, Quebec, Canada. DOI: 10.1061/9780784412473.005.

Malenfant-Lepage, J., Doré, G., Fortier, D., Murchison, P. 2012b. Thermal performance of the permafrost protection techniques at Beaver Creek experimental road site, Yukon, Canada. *Proceedings of the 10th International Conference on Permafrost.* 261-266. DOI: 10.1061/9780784412473.005.

Malenfant-Lepage, J., Doré, G., Fortier, F. 2010. Experimentation of mitigation techniques to reduce the effects of permafrost degradation on transportation infrastructures at Beaver Creek experimental road side (Alaska Highway, Yukon). *Proceedings 63rd Canadian Geotechnical Conference, Calgary, Alberta.* 526-533.

Mao, Y., Li, G., Ma, W., Mu, Y., Wang, F., Miao, J., Wu, D. 2019. Field observation of permafrost degradation under Mo'he airport, Northeastern China from 2007 to 2016. *Cold Regions Science and Technology.* 161, 43-50. DOI: 10.1016/j.coldregions.2019.03.004.

McFadden, J.P., Chapin, F.S., Hollinger, D.Y. 1998. Subgrid-scale variability in the surface energy balance of arctic tundra. *Journal of Geophysical Research: Atmospheres.* 103(D22), 28947-28961. DOI: 10.1029/98JD02400.

McKenzie, J.M., Siegel, D.I., Rosenberry, D.O., Glaser, P.H., Voss, C.I. 2007a. Heat transport in the Red Lake bog, glacial Lake Agassiz peatlands. *Hydrological Processes.* 21(3), 369-378. DOI: 10.1002/hyp.6239.

McKenzie, J.M., Voss, C.I. 2013. Permafrost thaw in a nested groundwater-flow system. *Hydrogeology Journal.* 21(1), 299-316. DOI: 10.1007/s10040-012-0942-3.

McKenzie, J.M., Voss, C.I., Siegel, D.I. 2007b. Groundwater flow with energy transport and water–ice phase change: numerical simulations, benchmarks, and application to freezing in peat bogs. *Advances in water resources.* 30(4), 966-983. DOI: 10.1016/j.advwatres.2006.08.008.

Melvin, A.M., Larsen, P., Boehlert, B., Neumann, J.E., Chinowsky, P., Espinet, X., . . . Bothner, A. 2016. Climate change damages to Alaska public infrastructure and the economics of proactive adaptation. *Proceedings of the National Academy of Sciences.* 114(2), E122-E131. DOI: 10.1073/pnas.1611056113.

Miller, G.H., Alley, R.B., Brigham-Grette, J., Fitzpatrick, J.J., Polyak, L., Serreze, M.C., White, J.W. 2010. Arctic amplification: can the past constrain the future? *Quaternary Science Reviews.* 29(15-16), 1779-1790. DOI: 10.1016/j.quascirev.2010.02.008.

Miller, T. 1979. The surface heat balance in simulations of permafrost behavior. *Journal of Energy Resources Technology.* 101(4), 240-250. DOI: 10.1115/1.3446926.

Mittaz, C., Hoelzle, M., Haeberli, W. 2000. First results and interpretation of energy-flux measurements over Alpine permafrost. *Annals of Glaciology.* 31, 275-280. DOI: 10.3189/172756400781820363.

Molson, J.W., Frind, E.O., Palmer, C.D. 1992. Thermal energy storage in an unconfined aquifer: 2. Model development, validation, and application. *Water Resources Research.* 28(10), 2857-2867. DOI: 10.1029/92WR01472.

Mu, C., Shang, J., Zhang, T., Fan, C., Wang, S., Peng, X., . . . Jia, L. 2020a. Acceleration of thaw slump during 1997–2017 in the Qilian Mountains of the northern Qinghai-Tibetan plateau. *Landslides.* DOI: 10.1007/s10346-020-01344-3.

Mu, Y., Ma, W., Li, G., Mao, Y., Liu, Y. 2020b. Long-term thermal and settlement characteristics of air convection embankments with and without adjacent surface water ponding in permafrost regions. *Engineering Geology.* 266, 105464. DOI: 10.1016/j.enggeo.2019.105464.

Mu, Y., Ma, W., Li, G., Niu, F., Liu, Y., Mao, Y. 2018. Impacts of supra-permafrost water ponding and drainage on a railway embankment in continuous permafrost zone, the interior of the Qinghai-Tibet Plateau. *Cold Regions Science and Technology.* 154, 23-31. DOI: 10.1016/j.coldregions.2018.06.007.

Nan, Z., Li, S., Cheng, G. 2005. Prediction of permafrost distribution on the Qinghai-Tibet Plateau in the next 50 and 100 years. *Science in China Series D: Earth Sciences.* 48(6), 797-804. DOI: 10.1360/03yd0258.

Nelson, F.E., Anisimov, O.A., Shiklomanov, N.I. 2001. Subsidence risk from thawing permafrost. *Nature.* 410(6831), 889-890. DOI: 10.1038/35073746.

Newman, D. 1939. The distribution of range in samples from a normal population, expressed in terms of an independent estimate of standard deviation. *Biometrika.* 31(1/2), 20-30. DOI: 10.2307/2334973.

Nishimura, S., Martin, C., Jardine, R., Fenton, C. 2009. A new approach for assessing geothermal response to climate change in permafrost regions. *Géotechnique.* 59(3), 213-227. DOI: 10.1680/geot.2009.59.3.213.

Niu, F., Liu, X., Ma, W., Wu, Q., Xu, J. 2008. Monitoring study on the boundary thermal conditions of duct-ventilated embankment in permafrost regions. *Cold Regions Science Technology.* 53(3), 305-316. DOI: 10.1016/j.coldregions.2007.07.004.

Nixon, J. 1991. Discrete ice lens theory for frost heave in soils. *Canadian Geotechnical Journal.* 28(6), 843-859. DOI: 10.1139/t91-102.

Noborio, K., McInnes, K., Heilman, J. 1996. Two-dimensional model for water, heat, and solute transport in furrow-irrigated soil: I. Theory. *Soil Science Society of America Journal.* 60(4), 1001-1009.

O'Neill, H., Burn, C. 2016. Talik formation at a snow fence in continuous permafrost, Western Arctic Canada. *Permafrost and Periglacial Processes.* 28, 558– 565. DOI: 10.1002/ppp.1905.

O'Neill, H.B., Wolfe, S.A., Duchesne, C. 2019. New ground ice maps for Canada using a paleogeographic modelling approach. *The Cryosphere.* 13(3), 753-773. DOI: 10.5194/tc-13-753-2019.

O'Neill, H.B., Burn, C.R. 2017. Impacts of variations in snow cover on permafrost stability, including simulated snow management, Dempster Highway, Peel Plateau, Northwest Territories. *Arctic Science.* 3(2), 150-178. DOI: 10.1139/as-2016-0036.

Obu, J., Westermann, S., Bartsch, A., Berdnikov, N., Christiansen, H.H., Dashtseren, A., . . . Kholodov, A. 2019. Northern Hemisphere permafrost map based on TTOP modelling for 2000–2016 at 1 km2 scale. *Earth-Science Reviews.* 193, 299-316. DOI: 10.1016/j.earscirev.2019.04.023.

Osterkamp, T. 2005. The recent warming of permafrost in Alaska. *Global and Planetary Change.* 49(3-4), 187-202. DOI: 10.1016/j.gloplacha.2005.09.001.

Osterkamp, T., Romanovsky, V. 1997. Freezing of the active layer on the coastal plain of the Alaskan Arctic. *Permafrost and Periglacial Processes.* 8(1), 23-44. DOI: 10.1002/(SICI)1099-1530(199701)8:1<23::AID-PPP239>3.0.CO;2-2.

Outcalt, S. I., Nelson, F. E., and Hinkel, K. M. 1990. The zero-curtain effect: Heat and mass transfer across an isothermal region in freezing soil, *Water Resources Research*, 26(7), 1509– 1516. DOI: 10.1029/WR026i007p01509.

Paquette, M., Fortier, D., Mueller, D.R., Sarrazin, D., Vincent, W.F. 2015. Rapid disappearance of perennial ice on Canada's most northern lake. *Geophysical Research Letters.* 42(5), 1433-1440. DOI: 10.1002/2014GL062960.

Paquette, M., Fortier, D., Vincent, W.F. 2017. Water tracks in the High Arctic: a hydrological network dominated by rapid subsurface flow through patterned ground. *Arctic Science.* 3(2), 334-353. DOI: 10.1139/as-2016-0014.

Paquette, M., Fortier, D., Vincent, W.F. 2018. Hillslope water tracks in the High Arctic: Seasonal flow dynamics with changing water sources in preferential flow paths. *Hydrological Processes.* 32(8), 1077-1089. DOI: 10.1002/hyp.11483.

Park, S.K., Moon, H.J., Min, K.C., Hwang, C., Kim, S. 2018. Application of a multiple linear regression and an artificial neural network model for the heating performance analysis and hourly prediction of a large-scale ground source heat pump system. *Energy and Buildings.* 165, 206-215. DOI: 10.1016/j.enbuild.2018.01.029.

Périer, L., Doré, G., Burn, C. 2014. The effects of water flow and temperature on thermal regime around a culvert built on permafrost. *Sciences in Cold and Arid Regions.* 6(5), 415-422.

Philip, J., De Vries, D. 1957. Moisture movement in porous materials under temperature gradients. *Eos, Transactions American Geophysical Union.* 38(2), 222-232. DOI: 10.1029/TR038i002p00222.

Pithan, F., Mauritsen, T. 2014. Arctic amplification dominated by temperature feedbacks in contemporary climate models. *Nature Geoscience.* 7, 181. DOI: 10.1038/ngeo2071.

Pomeroy, J., Gray, D., Brown, T., Hedstrom, N., Quinton, W., Granger, R., Carey, S. 2007. The cold regions hydrological model: a platform for basing process representation and model structure on physical evidence. *Hydrological Processes.* 21(19), 2650-2667. DOI: 10.1002/hyp.6787.

Provost, A.M., Voss, C.I. 2019. *SUTRA, a model for saturated-unsaturated, variable-density groundwater flow with solute or energy transport—Documentation of generalized boundary conditions, a modified implementation of specified pressures and concentrations or temperatures, and the lake capability*, U.S. Geological Survey Techniques and Methods. DOI: 10.3133/tm6A52.

Putkonen, J. 1998. Soil thermal properties and heat transfer processes near Ny-Alesund, northwestern Spitsbergen, Svalbard. *Polar research.* 17(2), 165-179. DOI: 10.1111/j.1751-8369.1998.tb00270.x.

Qin, Y., Hiller, J.E. 2014. Understanding pavement-surface energy balance and its implications on cool pavement development. *Energy and Buildings.* 85, 389-399. DOI: 10.1016/j.enbuild.2014.09.076.

Qin, Y., Hiller, J.E., Bao, T. 2012. Modeling cold region ground temperatures with a heat flux upper boundary model. *Journal of Cold Regions Engineering.* 27(1), 29-43. DOI: 10.1061/(ASCE)CR.1943-5495.0000051.

Qin, Y., Liang, J., Tan, K., Li, F. 2017a. The amplitude and maximum of daily pavement surface temperature increase linearly with solar absorption. *Road Materials and Pavement Design.* 18(2), 440-452. DOI: 10.1080/14680629.2016.1162732.

Qin, Y., Long, X., Ma, X., Huang, H. 2017b. Theoretical models for the solar absorptivity of a roadway embankment. *Cold Regions Science and Technology.* 137, 30-35. DOI: 10.1016/j.coldregions.2017.02.009.

Qiu, Y., Fu, B., Wang, J., Chen, L. 2003. Spatiotemporal prediction of soil moisture content using multiple-linear regression in a small catchment of the Loess Plateau, China. *Catena.* 54(1-2), 173-195. DOI: 10.1016/S0341-8162(03)00064-X.

Quinton, W., Baltzer, J. 2013. The active-layer hydrology of a peat plateau with thawing permafrost (Scotty Creek, Canada). *Hydrogeology Journal.* 21(1), 201-220. DOI: 10.1007/s10040-012-0935-2.

Quinton, W., Shirazi, T., Carey, S., Pomeroy, J. 2005. Soil water storage and active-layer development in a sub-alpine tundra hillslope, southern Yukon Territory, Canada. *Permafrost and Periglacial Processes.* 16(4), 369-382. DOI: 10.1002/ppp.543.

Raleigh, M.S., Landry, C.C., Hayashi, M., Quinton, W.L., Lundquist, J.D. 2013. Approximating snow surface temperature from standard temperature and humidity data: New possibilities for snow model and remote sensing evaluation. *Water Resources Research.* 49(12), 8053-8069. DOI: 10.1002/2013WR013958.

Rampton, V. 1971. Late Quaternary vegetational and climatic history of the Snag-Klutlan area, southwestern Yukon Territory, Canada. *Geological Society of America Bulletin.* 82(4), 959-978. DOI: 10.1130/0016-7606(1971)82[959:LQVACH]2.0.CO;2.

Ran, Y., Li, X., Cheng, G. 2018. Climate warming over the past half century has led to thermal degradation of permafrost on the Qinghai-Tibet Plateau. *The Cryosphere.* 12(2). DOI: 10.5194/tc-12-595-2018.

Reimchen, D., Doré, G., Fortier, D., Walsh, R. 2009. Cost and constructability of permafrost test sections along the Alaska Highway, Yukon, p. 20, Vancouver, Canada.

Richard, C., Dore, G., Lemieux, C., Bilodeau, J.-P., Haure-Touze, J. 2015. Albedo of pavement surfacing materials: in situ measurements. *16th International Conference on Cold Regions Engineering.* 181-192. DOI: 10.1061/9780784479315.017.

Richards, L.A. 1931. Capillary conduction of liquids through porous mediums. *Physics.* 1(5), 318-333. DOI: 10.1063/1.1745010.

Riseborough, D., Shiklomanov, N., Etzelmüller, B., Gruber, S., Marchenko, S. 2008. Recent advances in permafrost modelling. *Permafrost and Periglacial Processes.* 19(2), 137-156. DOI: 10.1002/ppp.615.

Romanovsky, V., Drozdov, D., Oberman, N., Malkova, G., Kholodov, A., Marchenko, S., . . . Abramov, A. 2010. Thermal state of permafrost in Russia. *Permafrost and Periglacial Processes.* 21(2), 136-155. DOI: 10.1002/ppp.683.

Romanovsky, V., Osterkamp, T. 1995. Interannual variations of the thermal regime of the active layer and near-surface permafrost in northern Alaska. *Permafrost and Periglacial Processes.* 6(4), 313-335. DOI: 10.1002/ppp.3430060404.

Romanovsky, V., Osterkamp, T., Duxbury, N. 1997. An evaluation of three numerical models used in simulations of the active layer and permafrost temperature regimes. *Cold Regions Science and Technology.* 26(3), 195-203. DOI: 10.1016/S0165-232X(97)00016-5.

Roth, K., Boike, J. 2001. Quantifying the thermal dynamics of a permafrost site near Ny-Ålesund, Svalbard. *Water resources research.* 37(12), 2901-2914. DOI: 10.1029/2000WR000163.

Roux, N., Costard, F., Grenier, C. 2017. Laboratory and numerical simulation of the evolution of a river's talik. *Permafrost and Periglacial Processes.* 28(2), 460-469. DOI: 10.1002/ppp.1929.

Rowland, J., Travis, B., Wilson, C. 2011. The role of advective heat transport in talik development beneath lakes and ponds in discontinuous permafrost. *Geophysical Research Letters.* 38(17), L17504. DOI: 10.1029/2011GL048497.

Rühaak, W., Anbergen, H., Grenier, C., McKenzie, J., Kurylyk, B.L., Molson, J., . . . Sass, I. 2015. Benchmarking numerical freeze/thaw models. *Energy Procedia.* 76, 301-310. DOI: 10.1016/j.egypro.2015.07.866.

Rutten, M.M., Steele-Dunne, S.C., Judge, J., van de Giesen, N. 2010. Understanding heat transfer in the shallow subsurface using temperature observations. *Vadose Zone Journal.* 9(4), 1034-1045. DOI: 10.2136/vzj2009.0174.

Sadeghi, M., Tuller, M., Warrick, A. W., Babaeian, E., Parajuli, K., Gohardoust, M. R., & Jones, S. B. (2019). An analytical model for estimation of land surface net water flux from near-surface soil moisture observations. *Journal of hydrology*, 570, 26-37. DOI : 10.1016/j.jhydrol.2018.12.038.

Saito, H., Šimůnek, J., Mohanty, B.P. 2006. Numerical analysis of coupled water, vapor, and heat transport in the vadose zone. *Vadose Zone Journal.* 5(2), 784-800. DOI: 10.2136/vzj2006.0007.

Satterlund, D.R. 1979. An improved equation for estimating long-wave radiation from the atmosphere. *Water Resources Research.* 15(6), 1649-1650. DOI: 10.1029/WR015i006p01649.

Schmidt, R., Gluns, D.R. 1991. Snowfall interception on branches of three conifer species. *Canadian Journal of Forest Research.* 21(8), 1262-1269. DOI: 10.1139/x91-176.

Serreze, M.C., R.G. Barry, Processes and impacts of Arctic amplification: A research synthesis. *Global and Planetary Change*, 2011. 77(1): p. 85-96. DOI: 10.1016/j.gloplacha.2011.03.004.

Shen, M. 1988. Numerical analysis of temperature field in a thawing embankment in permafrost. *Canadian Geotechnical Journal.* 25(1), 163-166. DOI: 10.1139/t88-017.

Sheng, Y., Ma, S., Cao, W., Wu, J. 2020. Spatiotemporal changes of permafrost in the Headwater Area of the Yellow River under a changing climate. *Land Degradation & Development.* 31(1), 133-152. DOI: 10.1002/ldr.3434.

Sheng, Y., Zhang, J., Liu, Y., Wu, J. 2002. Thermal regime in the embankment of Qinghai–Tibetan Highway in permafrost regions. *Cold Regions Science and Technology.* 35(1), 35-44. DOI: 10.1016/S0165-232X(02)00026-5.

Shiklomanov, N.I., Streletskiy, D.A., Swales, T.B., Kokorev, V.A. 2017. Climate change and stability of urban infrastructure in Russian permafrost regions: prognostic assessment based on GCM climate projections. *Geographical review.* 107(1), 125-142. DOI: 10.1111/gere.12214.

Shur, Y., Jorgenson, M. 2007. Patterns of permafrost formation and degradation in relation to climate and ecosystems. *Permafrost and Periglacial Processes.* 18(1), 7-19. DOI: 10.1002/ppp.582.

Šimůnek, J., Šejna, M., van Genuchten, M.T. 1998. *The HYDRUS-1D software package for simulating water flow and solute transport in two-dimensional variably saturated media. Version 2.0*, IGWMC-TPS-70. International Ground Water Modeling Center, Colorado School of Mines, Golden, Colorado, 202 pp., 1998.

Šimůnek, J., Van Genuchten, M.T., Sejna, M. 2005. *The Hydrus-1D software package for simulating the one-dimensional movement of water, heat, and multiple solutes in variably-saturated media*. Version 3.0, HYDRUS Software Series 1, Department of Environmental Sciences, University of California Riverside, Riverside, CA, 270 pp.

Sippel, S., Meinshausen, N., Fischer, E.M., Székely, E. and Knutti, R., 2020. Climate change now detectable from any single day of weather at global scale. *Nature Climate Chang*. 10, 35–41. DOI: 10.1038/s41558-019-0666-7

Sjöberg, Y., Coon, E., Sannel, K., Britta, A., Pannetier, R., Harp, D., . . . Lyon, S.W. 2016. Thermal effects of groundwater flow through subarctic fens: A case study based on field observations and numerical modeling. *Water Resources Research.* 52, 1591– 1606. DOI: 10.1002/2015WR017571.

Sliger, M. 2016. Structure et évolution du pergélisol depuis le Pléistocène Tardif, Beaver Creek, Yukon, Université de Montréal. (in French)

Sliger, M., Fortier, D., deGrandpré, I., Lapointe-Elmrabti, L. 2015. Incidence of Late Pleistocene-Holocene Climate on the Concurrent Landscape and Permafrost Development of the Beaver Creek Region, Southwestern Yukon, Canada. *Proceedings of the 7th Canadian Conference on Permafrost and the 68th Canadian Conference on Geotechnic.* DOI: 10.13140/RG.2.1.2180.2644.

Smerdon, J.E., Beltrami, H., Creelman, C., Stevens, M.B. 2009. Characterizing land surface processes: A quantitative analysis using air-ground thermal orbits. *Journal of Geophysical Research: Atmospheres.* 114, D15102. DOI: 10.1029/2009JD011768.

Smerdon, J.E., Pollack, H.N., Enz, J.W., Lewis, M.J. 2003. Conduction-dominated heat transport of the annual temperature signal in soil. *Journal of Geophysical Research: Solid Earth.* 108(B9). DOI: 10.1029/2002JB002351.

Smith, M., Riseborough, D. 1983. Permafrost sensitivity to climate change. *Proceedings of the 4th International Conference on Permafrost.* 1178-1183.

Smith, M., Riseborough, D. 1996. Permafrost monitoring and detection of climate change. *Permafrost and Periglacial Processes.* 7(4), 301-309. DOI: 10.1002/(SICI)1099-1530(199610)7:4<301::AID-PPP231>3.0.CO;2-R.

Smith, S., Romanovsky, V., Lewkowicz, A., Burn, C.R., Allard, M., Clow, G., . . . Throop, J. 2010. Thermal state of permafrost in North America: a contribution to the international polar year. *Permafrost and Periglacial Processes.* 21(2), 117-135. DOI: 10.1002/ppp.690.

Smith, S.L., Roy, L.-P., Lewkowicz, A.G., Chartrand, J. 2017. *Ground thermal data collection along the Alaska Highway easement (KP 1559-1895) Yukon, summer 2016*, p. 29, Natural Resources Canada. DOI: 10.4095/306304.

Solaimanian, M., Kennedy, T.W. 1993. Predicting maximum pavement surface temperature using maximum air temperature and hourly solar radiation. *Journal of Transportation Research Record.* 1-11. DOI: isbn/0309055652.

Spaans, E.J., Baker, J.M. 1995. Examining the use of time domain reflectometry for measuring liquid water content in frozen soil. *Water Resources Research.* 31(12), 2917-2925. DOI: 10.1029/95WR02769.

Statistics Canada. 2018. Ecological Land Classification (ELC), Available form www.statcan.gc.ca/eng/subjects/standard/environment/elc/2017-1 (Release data: March 1, 2018).

Stephani, E. 2013. Permafrost Geosystem Assessment at the Beaver Creek Road Experimental Site (Alaska Highway, Yukon, Canada), University of Alaska Fairbanks.

Stephani, E., Drage, J., Miller, D., Jones, B.M., Kanevskiy, M. 2020. Taliks, cryopegs, and permafrost dynamics related to channel migration, Colville River Delta, Alaska. *Permafrost and Periglacial Processes.* 1-16. DOI: 10.1002/ppp.2046.

Stephani, E., Fortier, D., Shur, Y., Fortier, R., Doré, G. 2014. A geosystems approach to permafrost investigations for engineering applications, an example from a road stabilization experiment, Beaver Creek, Yukon, Canada. *Cold Regions Science and Technology.* 100, 20-35. DOI: 10.1016/j.coldregions.2013.12.006.

Stone, R., Dutton, E., Harris, J., Longenecker, D. 2001. The advancing date of spring snowmelt in the Alaskan Arctic. *Proc. 11th Atmospheric Radiation Measurement (ARM) Science Team Meeting.*

Streletskiy, D.A., Shiklomanov, N.I., Nelson, F.E. 2012. Permafrost, infrastructure, and climate change: a GIS-based landscape approach to geotechnical modeling. *Arctic, antarctic, and Alpine research.* 44(3), 368-380. DOI: 10.1657/1938-4246-44.3.368.

Streletskiy, D.A., Suter, L.J., Shiklomanov, N.I., Porfiriev, B.N., Eliseev, D.O. 2019. Assessment of climate change impacts on buildings, structures and infrastructure in the Russian regions on permafrost. *Environmental Research Letters.* 14(2), 025003. DOI: 10.1088/1748-9326/aaf5e6.

Sturm, M., Johnson, J.B. 1992. Thermal conductivity measurements of depth hoar. *Journal of Geophysical Research: Solid Earth.* 97(B2), 2129-2139. DOI: 10.1029/91JB02685.

Sturm, M., Perovich, D.K., Holmgren, J. 2002. Thermal conductivity and heat transfer through the snow on the ice of the Beaufort Sea. *Journal of Geophysical Research: Oceans.* 107(8043), 1-17. DOI: 10.1029/2000JC000409.

Sun, Z., Ma, W., Zhang, S., Mu, Y., Yun, H., Wang, H. 2018a. Characteristics of thawed interlayer and its effect on embankment settlement along the Qinghai-Tibet Railway in permafrost regions. *Journal of Mountain Science.* 15(5), 1090-1100. DOI: 10.1007/s11629-017-4643-1.

Sun, Z., Ma, W., Zhang, S., Wen, Z., Wu, G. 2018b. Embankment Stability of the Qinghai–Tibet Railway in Permafrost Regions. *Journal of Cold Regions Engineering.* 32(1), 04018001. DOI: 10.1061/(ASCE)CR.1943-5495.0000153.

Suter, L., Streletskiy, D.A., Shiklomanov, N. 2019. Assessment of the cost of climate change impacts on critical infrastructure in the circumpolar Arctic. *Polar Geography.* 42(4), 267-286. DOI: 10.1080/1088937X.2019.1686082.

Tai, B., Wu, Q., Zhang, Z., Xu, X. 2020. Study on thermal performance of novel asymmetric crushed-rock-based embankment on the Qinghai-Tibet Railway in permafrost region. *International Journal of Thermal Sciences.* 152, 106333. DOI: 10.1016/j.ijthermalsci.2020.106333.

Tan, X., Chen, W., Wu, G., Yang, J. 2013. Numerical simulations of heat transfer with ice–water phase change occurring in porous media and application to a cold-region tunnel. *Tunnelling and Underground Space Technology.* 38, 170-179. DOI: 10.1016/j.tust.2013.07.008.

Tank, SE, Vonk, JE, Walvoord, MA, McClelland, JW, Laurion, I, Abbott, BW. 2020. Landscape matters: Predicting the biogeochemical effects of permafrost thaw on aquatic networks with a state factor approach. *Permafrost and Periglacial Process*. 31: 358-370. DOI:10.1002/ppp.2057.

Taylor, G.S., Luthin, J.N. 1978. A model for coupled heat and moisture transfer during soil freezing. *Canadian Geotechnical Journal.* 15(4), 548-555. DOI: 10.1139/t78-058.

Teng, J., Kou, J., Yan, X., Zhang, S., Sheng, D. 2019. Parameterization of soil freezing characteristic curve for unsaturated soils. *Cold Regions Science and Technology.* 170, 102928. DOI: 10.1016/j.coldregions.2019.102928.

Teubner, I.E., Haimberger, L., Hantel, M. 2015. Estimating snow cover duration from ground temperature. *Journal of Applied Meteorology and Climatology.* 54(5), 959-965. DOI: 10.1175/JAMC-D-15-0006.1.

Thibault, S., Payette, S. 2009. Recent permafrost degradation in bogs of the James Bay area, northern Quebec, Canada. *Permafrost and Periglacial Processes.* 20(4), 383-389. DOI: 10.1002/ppp.660.

Thomas, H.R., Cleall, P.J., Li, Y., Harris, C., Kern-Luetschg, M. 2009. Modelling of cryogenic processes in permafrost and seasonally frozen soils. *Geotechnique.* 59(3), 173-184. DOI: 10.1680/geot.2009.59.3.173.

Throop, J., Lewkowicz, A.G., Smith, S.L. 2012. Climate and ground temperature relations at sites across the continuous and discontinuous permafrost zones, northern Canada. *Canadian Journal of Earth Sciences.* 49(8), 865-876. DOI: 10.1139/e11-075.

Trochu, F. 1993. A contouring program based on dual kriging interpolation. *Engineering with computers.* 9(3), 160-177. DOI: 10.1007/BF01206346.

US Army Corps of Engineers. 1956. Snow Hydrology: Summary Report of the Snow Investigations. *North Pacific Division, Corps of Engineers.* 3, 437. DOI: 10.3189/S0022143000024503.

Van Dam, J., Feddes, R. 2000. Numerical simulation of infiltration, evaporation and shallow groundwater levels with the Richards equation. *Journal of Hydrology.* 233(1-4), 72-85. DOI: 10.1016/S0022-1694(00)00227-4.

Vandenberghe, J., French, H. M., Gorbunov, A., Marchenko, S., Velichko, A. A., Jin, H., ... & Wan, X. 2014. The L ast P ermafrost M aximum (LPM) map of the N orthern H emisphere: permafrost

extent and mean annual air temperatures, 25–17 ka BP. *Boreas*, 43(3), 652-666. DOI: 10.1111/bor.12070.

van Everdingen, R. 1988. Multi-language glossary of permafrost and related ground-ice terms. National Snow and Ice Data Center/World Data Center for Glaciology, Boulder, CO. World Wide Web Address: http://nsidc.org/fgdc/glossary.

Van Genuchten, M.T. 1980. A closed-form equation for predicting the hydraulic conductivity of unsaturated soils. *Soil science society of America journal.* 44(5), 892-898. DOI: 10.2136/sssaj1980.03615995004400050002x.

Van Vuuren, D. P., Edmonds, J., Kainuma, M., Riahi, K., Thomson, A., Hibbard, K., ... & Masui, T. (2011). The representative concentration pathways: an overview. *Climatic change*, 109(1-2), 5. DOI: 10.1007/s10584-011-0148-z

Veuille, S., Fortier, D., Verpaelst, M., Grandmont, K., Charbonneau, S. 2015. Heat advection in the active layer of permafrost: physical modelling to quantify the impact of subsurface flow on soil thawing. *Proceedings of the 7th Canadian Conference on Permafrost and 68th Canadian Conference on Geotechnic.* 20-23. DOI: 10.13140/RG.2.1.3622.0563.

Voss, C., Provost, A. 2010. *SUTRA—a model for saturated-unsaturated, variable-density ground-water flow with solute or energy transport*, US Geological Survey Water-Resources Investigations report. DOI: 10.3133/wri024231.

Walter, M.T., Brooks, E.S., McCool, D.K., King, L.G., Molnau, M., Boll, J. 2005. Process-based snowmelt modeling: does it require more input data than temperature-index modeling? *Journal of Hydrology.* 300(1-4), 65-75. DOI: 10.1016/j.jhydrol.2004.05.002.

Walvoord, M.A., Voss, C.I., Ebel, B.A., Minsley, B.J. 2019. Development of perennial thaw zones in boreal hillslopes enhances potential mobilization of permafrost carbon. *Environmental Research Letters.* 14(1), 015003. DOI: 10.1088/1748-9326/aaf0cc.

Wang, F., Li, G., Ma, W., Mu, Y., Zhou, Z., Mao, Y. 2018a. Permafrost thawing along the China-Russia Crude Oil Pipeline and countermeasures: A case study in Jiagedaqi, Northeast China. *Cold Regions Science and Technology.* 155, 308-313. DOI: 10.1016/j.coldregions.2018.08.018.

Wang, K., Jafarov, E., Overeem, I., Romanovsky, V., Schaefer, K., Clow, G., . . . Schwalm, C. 2018b. A synthesis dataset of permafrost-affected soil thermal conditions for Alaska, USA. *Earth System Science Data.* 10, 2311–2328. DOI: 10.5194/essd-10-2311-2018.

Wang, L., Wu, Q., Jiang, G. 2019. The effect of desertification on frozen soil on the Qinghai-Tibet Plateau. *Science of The Total Environment.* 711, 134640. DOI: 10.1016/j.scitotenv.2019.134640.

Wang, Y.-p., Li, G.-y., Jin, H.-j., Lu, L.-z., He, R.-x., Zhang, P. 2016a. Thermal state of soils in the active layer and underlain permafrost at the kilometer post 304 site along the China-Russia Crude Oil Pipeline. *Journal of Mountain Science.* 13(11), 1984-1994. DOI: 10.1007/s11629-016-3908-4.

Wang, Y., Jin, H., Li, G. 2016b. Investigation of the freeze–thaw states of foundation soils in permafrost areas along the China–Russia Crude Oil Pipeline (CRCOP) route using ground-penetrating radar (GPR). *Cold Regions Science and Technology.* 126, 10-21. DOI: 10.1016/j.coldregions.2016.02.013.

Way, R.G., Lewkowicz, A.G. 2018. Environmental controls on ground temperature and permafrost in Labrador, northeast Canada. *Permafrost and Periglacial Processes.* DOI: 10.1002/ppp.1972.

Wen, Z., Niu, F., Yu, Q., Wang, D., Feng, W., Zheng, J. 2014. The role of rainfall in the thermal-moisture dynamics of the active layer at Beiluhe of Qinghai-Tibetan plateau. *Environmental earth sciences.* 71(3), 1195-1204. DOI: 10.1007/s12665-013-2523-8.

Wen, Z., Yu, S., Wei, M., Jilin, Q., Wu, J. 2005. Analysis on effect of permafrost protection by two-phase closed thermosyphon and insulation jointly in permafrost regions. *Cold Regions Science and Technology.* 43(3), 150-163. DOI: 10.1016/j.coldregions.2005.04.001.

Wen, Z., Zhang, M., Ma, W., Wu, Q., Niu, F., Yu, Q., . . . Sun, Z. 2015. Thermal–moisture dynamics of embankments with asphalt pavement in permafrost regions of central Tibetan Plateau. *European Journal of Environmental and Civil Engineering.* 19(4), 387-399. DOI: 10.1080/19648189.2014.945043.

Westermann, S., Boike, J., Langer, M., Schuler, T., Etzelmüller, B. 2011. Modeling the impact of wintertime rain events on the thermal regime of permafrost. *The Cryosphere.* 5, 1697-1736. DOI: 10.5194/tcd-5-1697-2011.

Westermann, S., Lüers, J., Langer, M., Piel, K., Boike, J. 2009. The annual surface energy budget of a high-arctic permafrost site on Svalbard, Norway. *The Cryosphere.* 3(2), 245. DOI: 10.5194/tc-3-245-2009.

Williams, P.J. 1964. Unfrozen water content of frozen soils and soil moisture suction. *Geotechnique.* 14(3), 231-246. DOI: 10.1680/geot.1964.14.3.231.

Williams, P.J., Smith, M.W. 1989. *The frozen earth: fundamentals of geocryology*, Cambridge University Press.

Williams, T.J., Pomeroy, J.W., Janowicz, J.R., Carey, S.K., Rasouli, K. and Quinton, W.L. 2015. A radiative–conductive–convective approach to calculate thaw season ground surface temperatures for modelling frost table dynamics. *Hydrological Processes.* 29(18), 3954-3965. DOI: 10.1002/hyp.10573

Winton, M. 2006. Amplified Arctic climate change: What does surface albedo feedback have to do with it? *Geophysical Research Letters.* 33(3). DOI: 10.1029/2005GL025244.

Woo, M.-k. 2012. *Permafrost hydrology*, Springer-Verlag, Berlin Heidelberg. DOI: 10.1007/978-3-642-23462-0.

Wu, Q., Cheng, G., Ma, W., Niu, F., Sun, Z. 2006. Technical approaches on permafrost thermal stability for Qinghai–Tibet Railway. *Geomechanics and Geoengineering.* 1(2), 119-127. DOI: 10.1080/17486020600777861.

Wu, Q., Dong, X., Liu, Y., Jin, H. 2007. Responses of permafrost on the Qinghai-Tibet Plateau, China, to climate change and engineering construction. *Arctic, Antarctic, and Alpine Research.* 39(4), 682-687. DOI: 10.1657/1523-0430(07-508)[WU]2.0.CO;2.

Wu, Q., Hou, Y., Yun, H., Liu, Y. 2015. Changes in active-layer thickness and near-surface permafrost between 2002 and 2012 in alpine ecosystems, Qinghai–Xizang (Tibet) Plateau, China. *Global Planetary Change.* 124, 149-155. DOI: 10.1016/j.gloplacha.2014.09.002.

Wu, Q., Liu, Y., Zhang, J., Tong, C. 2002. A review of recent frozen soil engineering in permafrost regions along Qinghai-Tibet Highway, China. *Permafrost and Periglacial Processes.* 13(3), 199-205. DOI: 10.1002/ppp.420.

Wu, Q., Yu, W., Jin, H. 2017. No protection of permafrost due to desertification on the Qinghai–Tibet Plateau. *Scientific Reports.* 7. DOI: 10.1038/s41598-017-01787-0.

Wu, Q., Zhang, Z., Liu, Y. 2010. Long-term thermal effect of asphalt pavement on permafrost under an embankment. *Cold Regions Science and Technology.* 60(3), 221-229. DOI: 10.1016/j.coldregions.2009.10.007.

Yang, M., Wang, S., Yao, T., Gou, X., Lu, A., Guo, X. 2004. Desertification and its relationship with permafrost degradation in Qinghai-Xizang (Tibet) plateau. *Cold Regions Science and Technology.* 39(1), 47-53. DOI: 10.1016/j.coldregions.2004.01.002.

Yao, J., Zhao, L., Gu, L., Qiao, Y., Jiao, K. 2011. The surface energy budget in the permafrost region of the Tibetan Plateau. *Atmospheric research.* 102(4), 394-407. DOI: 10.1016/j.atmosres.2011.09.001.

Yen, Y.-C. 1965. *Heat transfer characteristics of naturally compacted snow. US Army Cold Regions Research and Engineering Laboratory, Research Report 166, Hanover, NH, 9 pp.*

Yi, S., Woo, M.k., Arain, M.A. 2007. Impacts of peat and vegetation on permafrost degradation under climate warming. *Geophysical Research Letters.* 34(16). DOI: 10.1029/2007GL030550.

Yoshikawa, K., Hinzman, L.D. 2003. Shrinking thermokarst ponds and groundwater dynamics in discontinuous permafrost near Council, Alaska. *Permafrost and Periglacial Processes.* 14(2), 151-160. DOI: 10.1002/ppp.451.

Yoshioka, M., Takakura, S., Ishizawa, T., Sakai, N. 2015. Temporal changes of soil temperature with soil water content in an embankment slope during controlled artificial rainfall experiments. *Journal of Applied Geophysics.* 114, 134-145. DOI: 10.1016/j.jappgeo.2015.01.009.

Yotsukura, N., Jackman, A.P., Faust, C.R. 1973. Approximation of heat exchange at the air-water interface. *Water resources research.* 9(1), 118-128. DOI: 10.1029/WR009i001p00118.

You, Y., Wang, J., Wu, Q., Yu, Q., Pan, X., Wang, X., Guo, L. 2017. Causes of pile foundation failure in permafrost regions: The case study of a dry bridge of the Qinghai-Tibet Railway. *Engineering Geology.* 230, 95-103. DOI: 10.1016/j.enggeo.2017.10.004.

You, Y., Yu, Q., Guo, L., Wang, X., Hu, J., Qian, J., Zhang, H. 2016. In-situ monitoring the thermal regime of foundation backfill of a power transmission line tower in permafrost regions on the Qinghai–Tibet Plateau. *Applied Thermal Engineering.* 98, 271-279. DOI: 10.1016/j.applthermaleng.2015.12.042.

Yu, W., Che, F., Feng, W., Guo, M., Zhou, G. 2012. *Properties of subgrade and construction techniques of mobei expressway*, GeoCongress 2012: State of the Art and Practice in Geotechnical Engineering, pp. 1410-1417. DOI: 10.1061/9780784412121.145.

Yu, W.B., Lai, Y.M., Zhang, X.F., Zhang, S.J., Xiao, J.Z. 2004. Laboratory investigation on cooling effect of coarse rock layer and fine rock layer in permafrost regions. *Cold Regions Science and Technology.* 38(1), 31-42. DOI: 10.1016/S0165-232X(03)00061-2.

Yu, W.B., Liu, W.B., Lai, Y.M., Chen, L., Yi, X. 2014. Nonlinear analysis of coupled temperature-seepage problem of warm oil pipe in permafrost regions of Northeast China. *Applied Thermal Engineering.* 70(1), 988-995. DOI: 10.1016/j.applthermaleng.2014.06.028.

Yumashev, D., Hope, C., Schaefer, K., Riemann-Campe, K., Iglesias-Suarez, F., Jafarov, E., . . . Whiteman, G. 2019. Climate policy implications of nonlinear decline of Arctic land permafrost and other cryosphere elements. *Nature Communications.* 10(1), 1900. DOI: 10.1038/s41467-019-09863-x.

Zeng, Y., Su, Z., Wan, L., Wen, J. 2011. A simulation analysis of the advective effect on evaporation using a two-phase heat and mass flow model. *Water Resources Research.* 47(10), W10529. DOI: 10.1029/2011WR010701.

Zhang, T.J. 2005. Influence of the seasonal snow cover on the ground thermal regime: An overview. *Reviews of Geophysics*. 43.4. DOI: 10.1029/2004RG000157.

Zhang, H., Zhang, J., Wang, E., Zhang, Z., Cao, W., Zhou, P. 2017a. Thermal and settlement analyses under a riverbank over permafrost. *Computers and Geotechnics.* 91, 48-57. DOI: 10.1016/j.compgeo.2017.07.002.

Zhang, K.C., Qu, J.J., Liao, K.T., Niu, Q.H., Han, Q.J. 2010. Damage by wind-blown sand and its control along Qinghai-Tibet Railway in China. *Aeolian Research.* 1(3), 143-146. DOI: 10.1016/j.aeolia.2009.10.001.

Zhang, M., Lai, Y., Zhang, J., Sun, Z. 2011. Numerical study on cooling characteristics of two-phase closed thermosyphon embankment in permafrost regions. *Cold Regions Science and Technology.* 65(2), 203-210. DOI: 10.1016/j.coldregions.2010.08.001.

Zhang, M., Min, K.H., Wu, Q., Zhang, J., Harbor, J. 2012. A New Method to Determine the Upper Boundary Condition for a Permafrost Thermal Model: An Example from the Qinghai-Tibet Plateau. *Permafrost and Periglacial Processes.* 23(4), 301-311. DOI: 10.1002/ppp.1755.

Zhang, M., Wang, J., Lai, Y. 2019. Hydro-thermal boundary conditions at different underlying surfaces in a permafrost region of the Qinghai-Tibet Plateau. *Science of The Total Environment.* 670, 1190-1203. DOI: 10.1016/j.scitotenv.2019.03.090.

Zhang, M., Wen, Z., Xue, K., Chen, L., Li, D. 2016a. A coupled model for liquid water, water vapor and heat transport of saturated–unsaturated soil in cold regions: model formulation and verification. *Environmental Earth Sciences.* 75(8), 1-19. DOI: 10.1007/s12665-016-5499-3.

Zhang, M., Zhang, J., Lai, Y. 2005. Numerical analysis for critical height of railway embankment in permafrost regions of Qinghai–Tibetan plateau. *Cold Regions Science and Technology.* 41(2), 111-120. DOI: 10.1016/j.coldregions.2004.09.001.

Zhang, Y., Chen, W., Cihlar, J. 2003. A process-based model for quantifying the impact of climate change on permafrost thermal regimes. *Journal of Geophysical Research: Atmospheres.* 108(D22). DOI: 10.1029/2002JD003354.

Zhang, Y., Chen, W., Riseborough, D.W. 2008a. Disequilibrium response of permafrost thaw to climate warming in Canada over 1850–2100. *Geophysical Research Letters.* 35, L02502,. DOI: 10.1029/2007GL032117.

Zhang, Y., Wang, S., Barr, A.G., Black, T. 2008b. Impact of snow cover on soil temperature and its simulation in a boreal aspen forest. *Cold Regions Science and Technology.* 52(3), 355-370. DOI: 10.1016/j.coldregions.2007.07.001.

Zhang, Z., Wu, Q., Liu, Y., Gao, S. 2017b. Characteristics of water and heat changes in near-surface layers under influence of engineering interface. *Applied Thermal Engineering.* 125, 986-994. DOI: 10.1016/j.applthermaleng.2017.07.087.

Zhang, Z., Wu, Q., Liu, Y., Zhang, Z., Wu, G. 2018. Thermal accumulation mechanism of asphalt pavement in permafrost regions of the Qinghai–Tibet Plateau. *Applied Thermal Engineering.* 129, 345-353. DOI: 10.1016/j.applthermaleng.2017.10.065.

Zhang, Z., Wu, Q., Xun, X. 2016b. Radiation and energy balance characteristics of asphalt pavement in permafrost regions. *Environmental Earth Sciences.* 75(3), 221. DOI: 10.1007/s12665-015-4975-5.

Zhongqiong, Z., Qingbai, W., Xueyi, X., Yuncheng, L. 2019. Spatial distribution and changes of Xing'an permafrost in China over the past three decades. *Quaternary International.* 523, 16-24. DOI: 10.1016/j.quaint.2019.06.007.

Zhu, L. 1988. Study of the adherent layer on different types of ground in permafrost regions on the Qinghai-Xizang Plateau. *Journal of Glaciology and Geocryology.* 1, 35-39. (in Chinese)

Zhu, L., Wu, Z., Liu, Y., Li, D. 1996. Permafrost degeneration in the east of Qinghai-Xizang Plateau. *Chinese Geographical Science.* 6(3), 231-238. DOI: 10.1007/s11769-996-0025-2.

Zipper, S.C., Lamontagne-Hallé, P., McKenzie, J.M., Rocha, A.V. 2018. Groundwater controls on postfire permafrost thaw: water and energy balance effects. *Journal of Geophysical Research: Earth Surface.* 123(10), 2677-2694. DOI: 10.1029/2018JF004611.

Zottola, J., Darrow, M., Daanen, R., Fortier, D., de Grandpré, I. 2012. Investigating the effects of groundwater flow on the thermal stability of embankments over permafrost. *Proceedings of the 15th International Specialty Conference on Cold Regions Engineering.* 601-611. DOI: 10.1061/9780784412473.060.

Zou, D., Zhao, L., Sheng, Y., Chen, J., Hu, G., Wu, T., . . . Pang, Q. 2017. A new map of the permafrost distribution on the Tibetan Plateau. *The Cryosphere.* 11, 2527–2542. DOI: 10.5194/tc-11-2527-2017.

APPENDIX

APPENDIX 1: MATLAB code used to plot the image

```
% =========================================================================
% Lin Chen, 2020-02-01

% The following code was programmed to draw the graphs by using the "image" and "plot" functions in MATLAB.

% ========== Load Dataset of Daily Air Temperature 1993-2018 ===============
load BC_Road_AT_Mean_LF_93_18.mat;
load BC_Road_MAAT_Mean.mat;


cdata1_AT = BC_Road_AT_Mean_LF_93_18;
Y1_AT    = BC_Road_MAAT_Mean;


% ========== Load Dataset of Daily Solar Radiation 1993-2018 ===============
load SR_calculated_93_18_LF.mat;
load BC_Road_Solar_mean_LF.mat;


cdata1_Solar = SR_calculated_93_18_LF;
Y1_Solar    = BC_Road_Solar_mean_LF;


% =========== Load Dataset of Daily Rainfall 1993-2018 =====================
load BC_Road_Rainfall_93_18_max20.mat;
load BC_Road_Rainfall_93_18_mean.mat;


cdata1_Rain = BC_Road_Rainfall_93_18_max20;
Y1_Rain    = BC_Road_Rainfall_93_18_mean;


createfigure(cdata1_Solar, Y1_Solar,cdata1_AT, Y1_AT,cdata1_Rain, Y1_Rain);% Function createfigure, described at the end of the file.


function createfigure(cdata1_Solar, Y1_Solar,cdata1_AT, Y1_AT,cdata1_Rain, Y1_Rain)


% Create figure
figure1 = figure;
colormap(jet);


% ========== Polt Daily Air Temperature 1993-2018 =====================
```

218

```matlab
% ======================== Subplot #1  ============================
% Create axes
axes1 = axes('Parent',figure1,...
    'Position',[0.1 0.75 0.45 0.2]); % [X Y Width Height]
hold(axes1,'on');

% Create image
image(cdata1_AT,'Parent',axes1,'CDataMapping','scaled');

% % Create ylabel
% ylabel('Time (days)');
% % Create xlabel
% xlabel('Time (years)');

% Uncomment the following line to preserve the X-limits of the axes
xlim(axes1,[0.5 26.5]);
% Uncomment the following line to preserve the Y-limits of the axes
ylim(axes1,[0.5 365.5]);
% Uncomment the following line to preserve the Z-limits of the axes
% zlim(axes1,[-1 1]);
box(axes1,'on');
axis(axes1,'ij');
% Set the remaining axes properties
set(axes1,'FontName','Times New Roman','Layer','top','LineWidth',1,...
    'TickDir','out','XTick',[3 8 13 18 23 ],'XTickLabel',...
    {''},'YTick',[1 90 181 273 365],...
    'YTickLabel',{'Jan.','Apr.','Jul.','Oct.','Jan.'},'ZTick',[-1 0 1]);
% Create colorbar
colorbar(axes1,'TickLength',0.02,'TickLabels',{'-40','-20','0','20'},...
    'LineWidth',1,...
    'FontSize',8,...
    'FontName','Times New Roman');

% ======================== Subplot #2  ============================
% Create axes
axes2 = axes('Parent',figure1,...
    'Position',[0.61 0.75 0.37 0.2]); % [X Y Width Height]
hold(axes2,'on');

% Create plot
plot(Y1_AT,'Parent',axes2,'MarkerFaceColor',[1 1 1],'MarkerSize',4,...
    'Marker','o',...
```

```matlab
    'LineWidth',1,...
    'Color',[1 0 0]);

% Create ylabel
ylabel('MAAT (°C)');

% Create xlabel
% xlabel('Time (years)');

% Uncomment the following line to preserve the X-limits of the axes
% xlim(axes2,[0 30]);
% Uncomment the following line to preserve the Y-limits of the axes
 ylim(axes2,[-8 0]);
% Uncomment the following line to preserve the Z-limits of the axes
% zlim(axes2,[-1 1]);
box(axes2,'on');
% Set the remaining axes properties
set(axes2,'FontName','Times New Roman','LineWidth',1,'TickDir','out',...
    'XTick',[3 8 13 18 23 28],'XTickLabel',{''},...
    'YTick',[-8 -6 -4 -2 0],...
    'YTickLabel',{'-8','-6','-4','-2','0'},'ZTick',[-1 0 1]);

%CREATEFIGURE(cdata1, Y1)
%  CDATA1:  image cdata
%  Y1:  vector of y data

% =========== Polt Daily Solar Radiation 1993-2018 ====================
% ========================= Subplot #3   ==============================
colormap(jet);

% Create axes
axes3 = axes('Parent',figure1,...
    'Position',[0.1 0.51 0.45 0.2]); % [X Y Width Height]
hold(axes3,'on');

% Create image
image(cdata1_Solar,'Parent',axes3,'CDataMapping','scaled');

% Create ylabel
ylabel('Time (days)','FontSize',10);
```

```matlab
% % Create xlabel
% xlabel('Time (years)');


% Uncomment the following line to preserve the X-limits of the axes
xlim(axes3,[0.5 26.5]);
% Uncomment the following line to preserve the Y-limits of the axes
ylim(axes3,[0.5 365.5]);
% Uncomment the following line to preserve the Z-limits of the axes
% zlim(axes3,[-1 1]);
box(axes3,'on');
axis(axes3,'ij');
% Set the remaining axes properties
set(axes3,'FontName','Times New Roman','Layer','top','LineWidth',1,...
    'TickDir','out','XTick',[3 8 13 18 23 ],'XTickLabel',...
    {''},'YTick',[1 90 181 273 365],...
    'YTickLabel',{'Jan.','Apr.','Jul.','Oct.','Jan.'},'ZTick',[-1 0 1]);
% Create colorbar
colorbar(axes3,'TickLength',0.02,'TickLabels',{'100','200','300'},...
    'LineWidth',1,...
    'FontSize',8,...
    'FontName','Times New Roman');


% ========================= Subplot #4   =============================


% Create subplot
axes4 = axes('Parent',figure1,...
    'Position',[0.61 0.51 0.37 0.2]); % [X Y Width Height]
hold(axes4,'on');


% Create plot
plot(Y1_Solar,'Parent',axes4,'MarkerFaceColor',[1 1 1],'MarkerSize',4,...
    'Marker','o',...
    'LineWidth',1,...
    'Color',[1 0 0]);


% Create ylabel
ylabel('MASR (W/m^2)');


% Create xlabel
% xlabel('Time (years)');
```

```matlab
% Uncomment the following line to preserve the X-limits of the axes
% xlim(axes4,[0 30]);
% Uncomment the following line to preserve the Y-limits of the axes
ylim(axes4,[100 130]);
% Uncomment the following line to preserve the Z-limits of the axes
% zlim(axes4,[-1 1]);
box(axes4,'on');
% Set the remaining axes properties
set(axes4,'FontName','Times New Roman','LineWidth',1,'TickDir','out',...
    'XTick',[3 8 13 18 23 28],'XTickLabel',{''},...
    'YTick',[100 110 120 130],...
    'YTickLabel',{'100','110','120','130'},'ZTick',[-1 0 1]);




% =========== Polt Daily Rainfall 1993-2018 ====================
% ========================= Subplot #5   ============================
colormap(jet);

% Create axes
axes5 = axes('Parent',figure1,...
    'Position',[0.1 0.27 0.45 0.2]); % [X Y Width Height]
hold(axes5,'on');

% Create image
image(cdata1_Rain,'Parent',axes5,'CDataMapping','scaled');
%
% % Create ylabel
% ylabel('Time (days)','FontSize',10);
%
% Create xlabel
xlabel('Time (years)','FontSize',10);

% Uncomment the following line to preserve the X-limits of the axes
xlim(axes5,[0.5 26.5]);
% Uncomment the following line to preserve the Y-limits of the axes
ylim(axes5,[0.5 365.5]);
% Uncomment the following line to preserve the Z-limits of the axes
% zlim(axes5,[-1 1]);
box(axes5,'on');
axis(axes5,'ij');
% Set the remaining axes properties
set(axes5,'FontName','Times New Roman','Layer','top','LineWidth',1,...
```

```matlab
    'TickDir','out','XTick',[3 8 13 18 23 ],'XTickLabel',...
    {'1995','2000','2005','2010','2015'},'YTick',[1 90 181 273 365],...
    'YTickLabel',{'Jan.','Apr.','Jul.','Oct.','Jan.'},'ZTick',[-1 0 1]);

% Create colorbar
colorbar(axes5,'TickLength',0.02,'TickLabels',{'0','5','10','15','>20'},...
    'LineWidth',1,...
    'FontSize',8,...
    'FontName','Times New Roman');

% ========================= Subplot #6   =============================
% Create axes
axes6 = axes('Parent',figure1,...
    'Position',[0.61 0.27 0.37 0.2]); % [X Y Width Height]
hold(axes6,'on');

% Create plot
plot(Y1_Rain,'Parent',axes6,'MarkerFaceColor',[1 1 1],'MarkerSize',4,...
    'Marker','o',...
    'LineWidth',1,...
    'Color',[1 0 0]);

% Create ylabel
ylabel('TAR (mm)'); % Total annual rainfall

% Create xlabel
xlabel('Time (years)','FontSize',10);

% Uncomment the following line to preserve the X-limits of the axes
% xlim(axes6,[0 30]);
% Uncomment the following line to preserve the Y-limits of the axes
 ylim(axes6,[100 500]);
% Uncomment the following line to preserve the Z-limits of the axes
% zlim(axes6,[-1 1]);
box(axes6,'on');
% Set the remaining axes properties
set(axes6,'FontName','Times New Roman','LineWidth',1,'TickDir','out',...
    'XTick',[3 8 13 18 23 28],'XTickLabel',...
    {'1995','2000','2005','2010','2015','2020'},'YTick',[100 200 300 400 500],...
    'YTickLabel',{'100','200','300','400','500'},'ZTick',[-1 0 1]);
end
```

APPENDIX 2: MATLAB code used in data analysis

```
% =====================================================================
% The following code was programmed by Lin Chen, 2020-02-15.

% Statistic analysis
% The key difference between the functions of "fitlm" and "regress" is:
% "fitlm(x,y)" function uses intercept by default;
% "regress(y,x)" function uses no intercept by default. The user can add intercept by adding "ones" matrix.

% matrix ST_BC
% [1] Coefficient of Determination (R-Squared)
% [2] Root mean square error (RMSE)
% [3] Mean squared error (MSE)
% [4] Mean absolute error (MAE)
% [5] Standard deviation (SD)

N_length  = length(LF_coeff_BC_Mean);
%-------- Mean AT -----------
% Linear regression model:
ST_mdl_Mean = fitlm(LF_coeff_BC_Mean(:,1),LF_coeff_BC_Mean(:,2));

% Coefficient of Determination (R-Squared)
ST_BC(1,1) = ST_mdl_Mean.Rsquared.Ordinary;
% Root mean square error (RMSE)
ST_BC(2,1) = ST_mdl_Mean.RMSE;
% Mean squared error (MSE)
ST_BC(3,1) = ST_mdl_Mean.MSE;
% Mean absolute error (MAE)
ST_BC(4,1)  =  mean(abs(LF_coeff_BC_Mean(:,1) - LF_coeff_BC_Mean(:,2)));
% Standard deviation (SD)
ST_Diff_01 = LF_coeff_BC_Mean(:,1) - LF_coeff_BC_Mean(:,2);
ST_BC(5,1) = (sum((ST_Diff_01 - mean(ST_Diff_01)).^2)/(N_length-1))^0.5;


%-------- Max AT -----------
ST_mdl_Max = fitlm(LF_coeff_BC_Max(:,1),LF_coeff_BC_Max(:,2));

% Coefficient of Determination (R-Squared)
ST_BC(1,2) = ST_mdl_Max.Rsquared.Ordinary;
% Root mean square error (RMSE)
ST_BC(2,2) = ST_mdl_Max.RMSE;
```

```matlab
% Mean squared error (MSE)
ST_BC(3,2) = ST_mdl_Max.MSE;
% Mean absolute error (MAE)
ST_BC(4,2)  = mean(abs(LF_coeff_BC_Max(:,1) - LF_coeff_BC_Max(:,2)));
% Standard deviation (SD)
ST_Diff_02 = LF_coeff_BC_Max(:,1) - LF_coeff_BC_Max(:,2);
ST_BC(5,2) = (sum((ST_Diff_02 - mean(ST_Diff_02)).^2)/(N_length-1))^0.5;


%-------- Min AT -----------
ST_mdl_Min = fitlm(LF_coeff_BC_Min(:,1),LF_coeff_BC_Min(:,2));


% Coefficient of Determination (R-Squared)
ST_BC(1,3) = ST_mdl_Min.Rsquared.Ordinary;
% Root mean square error (RMSE)
ST_BC(2,3) = ST_mdl_Min.RMSE;
% Mean squared error (MSE)
ST_BC(3,3) = ST_mdl_Min.MSE;
% Mean absolute error (MAE)
ST_BC(4,3)  = mean(abs(LF_coeff_BC_Min(:,1) - LF_coeff_BC_Min(:,2)));
% Standard deviation (SD)
ST_Diff_03 = LF_coeff_BC_Min(:,1) - LF_coeff_BC_Min(:,2);
ST_BC(5,3) = (sum((ST_Diff_03 - mean(ST_Diff_03)).^2)/(N_length-1))^0.5;
```

APPENDIX 3: MATLAB code used to combine the multiple-decadal meteorological data

```
% =====================================================================
% The following code was programmed by Lin Chen, 2019-12-15.

% Data are available from Environment and Climate Change Canada (see
http://climate.weatheroffice.ec.gc.ca/climate_normals).
% The meteorological data in each year was placed in a single ".csv" file.
% The following code was used to combine the multiple-decadal meteorological data and to automatically calculate
the mean annual air temperature (MAAT) over the 1968-2014 period.


BC_files = dir('*.csv');
BC_len   = length(BC_files);


for i=1:BC_len
    [DATA_old_BC,txt_BC] = xlsread(BC_files(i).name,'A25:AA391');
    [a_BC,b_BC] = size(DATA_old_BC);
    BC_DATA(1:a_BC,1:b_BC,i) = DATA_old_BC(1:a_BC,1:b_BC);
end


save('BC_DATA');


for jj = 1:BC_len
    BC_Max_temp(:,jj)       = BC_DATA(:,5,jj);   % Units: degreee
    BC_Min_temp(:,jj)       = BC_DATA(:,7,jj);   % Units: degreee
    BC_Mean_temp(:,jj)      = BC_DATA(:,9,jj);   % Units: degreee
    BC_Thaw_index(:,jj)     = BC_DATA(:,11,jj);  % Units: degreee days
    BC_Freeze_index(:,jj)   = BC_DATA(:,13,jj);  % Units: degreee days
    BC_Total_rain(:,jj)     = BC_DATA(:,15,jj);  % Units: mm
    BC_Total_snow(:,jj)     = BC_DATA(:,17,jj);  % Units: cm
    BC_Total_precip(:,jj)   = BC_DATA(:,19,jj);  % Units: mm
    BC_Total_Snow_Grnd(:,jj) = BC_DATA(:,21,jj);  % Units: cm
```

```
end


M_days_Leap1 = [31,29,31,30,31,30,31,31,30,31,30,31];
M_days_Leap2 = [0, 31,29,31,30,31,30,31,31,30,31,30,31];


M_days_common1 = [31,28,31,30,31,30,31,31,30,31,30,31];
M_days_common2 = [0,31,28,31,30,31,30,31,31,30,31,30,31];



for ij = 1:BC_len
    No_day1 = 0; % initial number of the days
    No_day2 = 0; % initial number of the days


    MAAT_0 = BC_Mean_temp(366,ij);


    if MAAT_0 == 0
        bb = BC_Max_temp(1:365,ij);
        cc = BC_Min_temp(1:365,ij);
        aa = BC_Mean_temp(1:365,ij);
        Mark_Yleap = 0;
    else
        bb = BC_Max_temp(1:366,ij);
        cc = BC_Min_temp(1:366,ij);
        aa = BC_Mean_temp(1:366,ij);
        Mark_Yleap = 1;
    end


    No_NAN = numel(find(isnan(aa)));
    if No_NAN < 10
        BC_MAAT(ij) = nanmean(aa);
    else
        BC_MAAT(ij) = mean(aa);
```

228

```matlab
    end



if Mark_Yleap == 0
   for M_j = 1:12 % 12 months
      No_day1 = No_day1 + M_days_common1(M_j);
      No_day2 = No_day2 + M_days_common2(M_j);


      MAT_month_0 = 0;
      MAT_month_0 = aa(1 + No_day2:No_day1);
      No_NAN = numel(find(isnan(MAT_month_0)));


      if No_NAN < 5
         MAT_month(M_j,ij) = nanmean(MAT_month_0);
      else
          MAT_month(M_j,ij) = mean(MAT_month_0);
      end
   end
else
   for M_j = 1:12 % 12 months


      No_day1 = No_day1 + M_days_Leap1(M_j);
      No_day2 = No_day2 + M_days_Leap2(M_j);
      MAT_month_0 = 0;
      MAT_month_0 = aa(1 + No_day2:No_day1);
      No_NAN = numel(find(isnan(MAT_month_0)));


      if No_NAN < 5
         MAT_month(M_j,ij) = nanmean(MAT_month_0);
      else
          MAT_month(M_j,ij) = mean(MAT_month_0);
      end
   end
```

```matlab
    end


%---------------------------------------------
% Precipitation


    BC_MAP(ij,1) = sum(BC_Total_precip(:,ij));
    BC_MAR(ij,1) = sum(BC_Total_rain(:,ij));
    BC_MAS(ij,1) = sum(BC_Total_snow(:,ij));
end


BC_DATA_period = textread('Data_period_BC.txt');
BC_period = BC_DATA_period(1):BC_DATA_period(2);
save('BC_period');


for jj = 1:BC_len
    for ii = 1:366
        BC_Snow_Grnd0(ii+366*(jj-1),1) = BC_Total_Snow_Grnd(ii,jj);
    end
end
% =======================================================================
% Plot mean annual air temperatures


figure;
plot(BC_period,BC_MAAT,'r','LineWidth',2);
hold on;
xlabel('Time (years)','Fontname', 'Times New Roman','FontSize',16);
ylabel('Temperature (℃)','Fontname', 'Times New Roman','FontSize',16);
legend('AT of Beaver Creek','Fontname', 'Times New Roman','FontSize',14);
set(gca, 'XTick',[1960:10:2020],'Fontname', 'Times New Roman','FontSize',14);
set(gca, 'YTick',[-10:2:0],'Fontname', 'Times New Roman','FontSize',14);
ylim([-10 0]);
hold off;
```

```matlab
% =====================================================================
% Plot snow regimes


figure;
plot(BC_Snow_Grnd0,'r','LineWidth',2);
hold on;
xlabel('Time (years)','Fontname', 'Times New Roman','FontSize',16);
ylabel('Snow depth (cm)','Fontname', 'Times New Roman','FontSize',16);
legend('Snow depth of Beaver Creek','Fontname', 'Times New Roman','FontSize',14);
set(gca, 'XTick',[0:366*5:17202],'Fontname', 'Times New Roman','FontSize',14);
set(gca, 'YTick',[0:20:120],'Fontname', 'Times New Roman','FontSize',14);
hold off;
```

APPENDIX 4: MATLAB code used to generate the inputs of SUTRA-ice code

```
% ====================================================================
% The following code was programmed by Lin Chen, 2020-01-15.
% The following code was programmed to create the DATA Set 14b and 15b of the input file of SUTRA-ice code.
 load('DATA_Set_14b.mat') % Nodewise Data
load('DATA_Set_15b.mat') % Elementwise Data

load('DATA_Set_18.mat')  % '+' time independent QBC
load('DATA_Set_20.mat')  % '-' time dependent TBC

load('DATA_Set_22.mat')  % Element Incidence Data

Node_up = -DATA_Set_20(:,1);
Node_down = DATA_Set_18(:,1);

Node_total_ST = length(DATA_Set_14b);

Node_ST = length (Node_up);
Node_SQ = length (Node_down);

X_coord = DATA_Set_14b(:,3);
Y_coord = DATA_Set_14b(:,4);

DATA_Set_14b_Mod = DATA_Set_14b;

for i = 1 : Node_total_ST
   Index(i) = 1;
   DATA_Set_14b_Mod(i,2) = 1;   % zone 1: embankment fill
   DATA_Set_14b_Mod(i,6) = 0.001;% porosity
```

```matlab
        DATA_Set_14b_Mod(i,7) = 0.999;% specific heat capacity
    for j = 1:Node_ST
        if ((DATA_Set_14b(i,1) <= Node_down(j))&& (DATA_Set_14b(i,1) >= Node_up(j)))
            Y_rel =  60 - X_coord(i) * 0.05;


            if (Y_coord(i) >= Y_rel -0.35)% zone 2:  0.35 m
                Index(i) = 2;
                DATA_Set_14b_Mod(i,2) = 2;   % region number
                DATA_Set_14b_Mod(i,6) = 0.75;% porosity
                DATA_Set_14b_Mod(i,7) = 2090;% specific heat capacity


            elseif ((Y_coord(i) < Y_rel - 0.5)&& (Y_coord(i) >= Y_rel - 25))
                % zone 3:  0.35 - 25 m


                Index(i) = 3;
                DATA_Set_14b_Mod(i,2) = 3;   % region number
                DATA_Set_14b_Mod(i,6) = 0.40;% porosity
                DATA_Set_14b_Mod(i,7) = 840; % specific heat capacity


            elseif (Y_coord(i) < Y_rel - 25)% zone 4:  0.35 - 25 m


                Index(i) = 4;
                DATA_Set_14b_Mod(i,2) = 4;   % region number
                DATA_Set_14b_Mod(i,6) = 0.30;% porosity
                DATA_Set_14b_Mod(i,7) = 840; % specific heat capacity
            end
            break;
        end
    end
end


Node_total_SH = length(DATA_Set_15b);
DATA_Set_15b_Mod = DATA_Set_15b;
```

```matlab
for i = 1 : Node_total_SH
        i_DS22  = DATA_Set_22(i,2);


    if ((Index(i_DS22)) == 1)
        DATA_Set_15b_Mod(i,2) = 1;       % zone 1: embankment fill
        DATA_Set_15b_Mod(i,3) = 4.50e-19; % maximum permeability
        DATA_Set_15b_Mod(i,4) = 4.50e-19; % minmum  permeability
        DATA_Set_15b_Mod(i,10)= 0.0099;   % thermal conductivity


    elseif (Index (i_DS22) == 2)


        DATA_Set_15b_Mod(i,2) = 2;       % region number
        DATA_Set_15b_Mod(i,3) = 9.030e-13; % maximum permeability
        DATA_Set_15b_Mod(i,4) = 9.030e-13; % minmum  permeability
        DATA_Set_15b_Mod(i,10)= 0.5;      % thermal conductivity


    elseif (Index (i_DS22) == 3)


        DATA_Set_15b_Mod(i,2) = 3;        % region number
        DATA_Set_15b_Mod(i,3) = 1.0e-13;  % maximum permeability
        DATA_Set_15b_Mod(i,4) = 1.0e-13;  % minmum  permeability
        DATA_Set_15b_Mod(i,10)= 1.4;      % thermal conductivityty

    else

        DATA_Set_15b_Mod(i,2) = 4;        % region number
        DATA_Set_15b_Mod(i,3) = 1.02e-16; % maximum permeability
        DATA_Set_15b_Mod(i,4) = 1.02e-16; % minmum  permeability
        DATA_Set_15b_Mod(i,10)= 1.4;      % thermal conductivity
    end
end
```